

# **Design and Analyses of Porous Concrete for Safety Applications**

## **Proefschrift**

ter verkrijging van de graad van doctor  
aan de Technische Universiteit Delft,  
op gezag van de Rector Magnificus prof.ir. K.C.A.M. Luyben;  
voorzitter van het College voor Promoties,  
in het openbaar te verdedigen op  
23 november 2016 om 15:00 uur

Door

Ayda Şafak AĞAR ÖZBEK  
Master of Science in Civil Engineering  
Istanbul Boğaziçi University, Turkije  
geboren te Istanbul, Turkije

This dissertation has been approved by the

promotor: Prof. Dr. Ir. K. van Breugel

copromotor: Dr. Ir. J. Weerheijm

Composition of the doctoral committee:

Rector Magnificus

Promotor : Prof. Dr. Ir. K. van Breugel Faculty of Civil Engineering and Geosciences, TU Delft

Copromotor : Dr. Ir. J. Weerheijm Faculty of Civil Engineering and Geosciences, TU Delft  
TNO, Defence, Safety and Security

Independent members:

Prof. Dr. Ir. L.J. Sluijs Faculty of Civil Engineering and Geosciences, TU Delft

Prof. Dr. Ing. V. Mechtcherine Technische Universität Dresden, Germany

Prof. Dr. Ir. E. Schlangen Faculty of Civil Engineering and Geosciences, TU Delft

Prof. Dr. M.A. Taşdemir Istanbul Technical University, Turkey

Prof. Dr. A.V. Metrikine Faculty of Civil Engineering and Geosciences, TU Delft

The research presented in this thesis has been carried out at the Faculty of Civil Engineering and Geosciences, Delft University of Technology and supported by the Nederlandse Defensie Academie and TNO.

## Summary

In an explosion taking place close to or inside a concrete structure, apart from the dangers of the explosive itself, the hazard due to the large debris originating from the concrete structure is an important threat. Protective structures with high probability to experience such extreme loadings during their service lives, such as protection walls outside important buildings or munition magazines for storing explosives, have to be designed to mitigate the effects of a probable explosion. With this goal, a PhD project was undertaken on designing and analyzing a cementitious material with sufficient static strength to carry the service loads and fractures into small-size fragments when subjected to an explosion. This thesis presents the design procedure of such a material, the experimental and numerical investigations and the results of the project.

In the last decades, extensive research has been focused on understanding the behavior of concrete structures under extreme dynamic loadings. While most studies aim at designing materials that resist impact loading, the objective of this project was developing a cementitious material that is expected to fracture and disintegrate under impact. During the research, a sensitivity study was conducted on various forms of cementitious materials (Chapter 2). Porous concretes with enhanced strength, fracturing into small fragments when exposed to impact loading, were obtained and analyzed. In the process of modifying the porous concrete properties the main goal was to enhance the static strength while maintaining a high porosity. By modifying the mixture composition as well as the method of compaction, porous concretes with improved static strengths (at the range of 30-50 MPa) were produced as presented in detail in Chapter 3.

In order to better understand the properties of the porous concretes produced, mechanical tests at macro and meso-scales were performed. Computer tomography, electron microscopy and X-ray diffraction analyses were also conducted to better explain the effective parameters which were summarized in Chapter 3. Among all the parameters that have been investigated, aggregate properties have the most significant effect on the mechanical properties of porous concrete. On the other hand, intense compaction in thin layers (to ensure good control of the production process), which directly affects the packing of the particles and the porosity, is essential to attain porous concretes with substantial strengths. The contribution of microsilica to the mechanical properties of porous concrete was not significant, even though the tests on the interfacial transition zone (ITZ) clearly showed that microsilica improved the strength of the ITZ phase. The reason for this ‘contradiction’ was better explained by the CT scans of partially fractured samples. These scans revealed that in porous concretes crack patterns are very much influenced by the distinct porous structure and the aggregate skeleton. The cracks are forced to propagate into locations guided by the geometry of the present phases and the path does not always go through the weakest phase i.e. the ITZ.

In the process of designing a material with desired dynamic performance, efficient dynamic testing techniques were highly required. In Chapter 4, dealing with the dynamic testing and evaluation of the experimental research, various experimental configurations were adapted or introduced for determining the dynamic response of porous concretes in a drop weight impact test. Different types of porous concretes and a mixture of normal concrete were subjected to drop

weight impact tests. When the experimental configurations that have been used are compared, it can be concluded that stress gauge measurements have the advantage of direct measurement of the transmitted stress, while no analyses are needed afterwards to obtain the impact strength data. Among the other two monitoring and measuring techniques (LDV and high speed photography) that have been applied, LDV proved to be more accurate due to its higher sampling rate compared to high speed photography. It also has the advantage of being independent of factors such as the intensity of the light source. High speed photography, however, has its own advantage of also facilitating the visualization of the fracture process, which provides important qualitative information on the crack patterns. On the other hand, both techniques have the advantage of being non-contact methods.

In the analyses of the drop weight impact test results, obtained using LDV and high-speed photography, the reverberation application of the impedance mismatch method was used. The analysis method proved to be very suitable to investigate the drop weight impact behavior of porous concretes. It also had the advantage of involving only the well-known dynamic impedance properties and the velocity measurements of the impactor, while the properties of the tested target specimen are not directly involved in the measurements and the analysis.

The focus of the numerical part of the research was simulating and assessing the dynamic behavior of different porous concretes under impact loading. To achieve this goal, analyses were conducted both on real porous concretes and on fictitious (model) porous materials. The latter models were used to demonstrate better the individual factors affecting the porous concrete properties. In the research, explicit time integration was selected as the analysis method. For the realistic representation of the real concretes that were produced and tested, the aggregates present in the mixtures were directly determined through 3D computed tomography. A mesh generation program was developed for generating realistic finite element meshes. In the analyses, porous concrete was considered as a four-phase material consisting of aggregates, bulk cement paste, interfacial transition zones (ITZ) and meso-size air pores.

When analyzing real porous concretes, the influences of the different parameters such as pore and aggregate size distributions and total porosity, are usually coupled. For distinguishing the sole effect of each parameter, virtual or model porous concretes were analyzed. The primary objectives of these analyses were computing the impact strength and examining the fragmentation behavior. The pore structures parameters are the most dominant factors affecting the mechanical properties of porous concretes. Therefore, model porous concretes having regularly and irregularly distributed circular pores of different radii and total porosity were analyzed. From the comparison of the impact responses of model porous concretes with different size pores, it could be concluded that for all porosities analyzed the impact strength of the concretes increased with decreasing pore size (at constant total porosity). It could also be concluded that for constant total porosity the sizes of the fragments that were formed drastically decreased when the pore size decreased. The results obtained from the analyses on the concretes with randomly distributed pores showed that for mixtures with larger pore sizes the scatter in impact strengths was larger. To understand the effect of aggregate size on the porous concrete



properties, circular aggregate model porous concretes were analyzed. The results showed that the impact strengths of porous concretes with 8 mm and 4 mm particles (same porosity) were approximately the same, while the impact strength of the model porous concrete with 2 mm particles was lower. Reasons for this were explained in detail in Chapter 5: in different mixtures several factors influenced the results in opposite ways.

In the numerical analyses of real porous concretes, the simulations were quite realistic. This result was achieved by applying proper finite element meshes resembling the actual porous concretes and accurate input data for the cementitious phases of the materials being quantified in the experiments at the meso-scale. Comparison of the peak values of the impact stress time histories showed that impact strengths of the samples obtained numerically (presented in Chapter 5) were in a good agreement with the experimental results. Pore and fragment size distributions of real porous concretes were also computed using the numerical models. This provided valuable information for better understanding of the fragmentation of the different mixtures.

This thesis comprises experimental and numerical investigations performed on porous concretes meant to be used in safety applications. The results obtained from the enhanced strength porous concretes that have been produced were promising. The impact test monitoring methods proposed as well as the numerical analyses can be used in experimental and numerical investigation of the dynamic behavior of porous concretes.

## Samenvatting

In een explosie die dichtbij of in een betonnen constructie plaatsvindt is er, naast het gevaar door de directe explosie-effecten als de blast en de vuurbal, ook het gevaar van weggeslingerde grote brokstukken (fragmenten of puin). Beschermingsconstructies met een grote kans om aan explosies te worden blootgesteld, zoals betonnen beschermingswanden, bij ministeries, ambassades en munitie magazijnen, moeten de explosie-effecten minimaliseren. Tegen deze achtergrond is een PhD-onderzoek uitgevoerd naar het ontwikkelen en analyseren van een cementgebonden materiaal dat bij een explosie opbreekt in kleine fragmenten, maar tegelijkertijd voldoende statische sterkte heeft. Dit proefschrift beschrijft de ontwerpprocedure, de verrichte experimentele- en numerieke onderzoeken en de resultaten van het project.

Om inzicht te krijgen in het gedrag van betonconstructies onder extreme dynamische belastingen zijn er in de laatste decennia uitgebreide studies verricht. Terwijl de meeste studies gericht waren op het ontwerpen van materialen die bestand zijn tegen schokbelasting, is het doel van dit project het ontwikkelen van een cementgebonden materiaal dat onder de schokbelasting juist verbrijzelt en desintegreert. In het onderzoek is eerst een literatuurstudie uitgevoerd naar de eigenschappen van verschillende typen cementgebonden materialen. De resultaten zijn in hoofdstuk 2 samengevat. Met deze kennis is een poreus beton ontwikkeld en geanalyseerd met een voldoende sterkte en dat bij blootstelling aan impactbelasting in kleine fragmenten opbreekt.

Tijdens het proces om de eigenschappen van het poreuze beton te verbeteren lag de nadruk op het ontwikkelen van de statische sterkte met behoud van de hoge porositeit. Door wijziging van de mengselsamenstelling en de methode van verdichten is een poreus beton met een verbeterde statische sterkte (in het bereik van 30-50 MPa) ontwikkeld. Het ontwerpproces van het materiaal en de resultaten zijn gedetailleerd uiteengezet in hoofdstuk 3.

Om de eigenschappen van het geproduceerde poreuze beton beter te begrijpen en te kwantificeren, zijn mechanische testen op macro- en meso-schaal uitgevoerd. Daarnaast zijn computertomografie, elektronenmicroscopie en röntgendiffractie onderzoeken uitgevoerd om de dominante parameters, zoals beschreven in hoofdstuk 3, nader te onderzoeken. Van alle parameters die zijn onderzocht, zijn de eigenschappen van de grindkorrels het meest bepalend voor de mechanische eigenschappen van poreus beton. Daarnaast geldt dat storten in dunne lagen en intensieve verdichting, waardoor de dichtheid van het korrelskelet wordt verhoogd en de porositeit wordt verlaagd, van essentieel belang is voor het realiseren van poreus beton met hogere sterkte. De bijdrage van microsilica aan de mechanische eigenschappen van poreus beton bleek niet erg significant, ofschoon in de proeven op meso-schaal van de korrel-pasta overgangszone (Interfacial Transition Zone, ITZ), duidelijk bleek dat microsilica de sterkte van de ITZ fase verbetert. De reden voor deze ‘tegenstrijdigheid’ kon worden afgeleid uit de CT scans van gedeeltelijk gebroken monsters. Hieruit bleek dat de scheurpatronen in poreuze beton sterk worden beïnvloed door de poriestructuur en het korrelskelet. Deze zijn bepalend voor het uiteindelijke scheurpad, dat niet altijd via de ITZ loopt.

Voor het ontwerpen van het materiaal met specifieke dynamische prestaties waren efficiënte, dynamische testtechnieken noodzakelijk. Dynamisch proeven en de evaluatie van deze proeven

zijn zijn beschreven in hoofdstuk 4. Verschillende meetmethoden en opstellingen zijn onderzocht en toegepast voor het bepalen van de dynamische respons van poreus beton in een impact proef (drop weight impact test). Op verschillende soorten poreus beton en een gewoon beton zijn impact testen uitgevoerd. Uit de vergelijking van de onderzochte meetmethoden blijkt dat de “stress gauge” metingen het voordeel biedt dat hiermee direct de dynamische sterkte kan worden bepaald. Van de andere twee toegepaste registratie- en meettechnieken (Laser Doppler Velocimetry, LDV, en hoge snelheid fotografie), bleek LDV het meest accuraat te zijn vanwege de hogere testfrequentie in vergelijking met hoge snelheid fotografie. De LDV techniek heeft ook het voordeel onafhankelijk te zijn van factoren zoals de lichtbronsterkte. Hoge snelheid fotografie heeft echter ook het specifieke voordeel dat daarmee het breukproces direct wordt gevisualiseerd en vastgelegd, waarmee belangrijke kwalitatieve informatie kan worden verkregen. Voor beide technieken geldt het voordeel dat het contactloze methoden zijn en geen instrumentatie van proefstuk nodig is.

Bij de analyse van de resultaten van de valgewichtproef, verkregen met behulp van LDV en hoge snelheid fotografie, is de ‘impedantie-mismatch-methode’ gebruikt om de dynamische sterkte te bepalen. De methode heeft als groot voordeel dat het uitsluitend gebruik maakt van de bekende dynamische impedantie-eigenschappen van het valgewicht en de snelheidsmetingen, en niet van de materiaaleigenschappen van het te onderzoeken proefstuk.

Het doel van het numerieke deel van het onderzoek was het simuleren en beoordelen van het dynamisch gedrag van verschillende poreuze betonsamenstellingen onder impact belasting. Om dit doel te bereiken zijn analyses uitgevoerd voor zowel modellen van de echte betonsamenstellingen als voor modellen van fictieve samenstellingen en korrelstructuren. De laatste modellen zijn gebruikt om de invloed van de individuele mengselparameters op de eigenschappen te kunnen onderzoeken. In de numerieke analyses is voor expliciete tijdtintegratie gekozen. Voor een realistische weergave van de het werkelijk geproduceerde en geteste beton is de korrelstructuur direct bepaald door middel van 3D computertomografie. Een mesh-generator programma is ontwikkeld voor het genereren van eindige elementen meshes. In de analyses is poreus beton beschouwd als een vier-fase materiaal bestaande uit korrels, bulk cement, toeslagmatrix overgangszones (ITZ) en (lucht-)poriën tussen de korrels.

Bij het analyseren van testresultaten van poreus beton worden de invloeden van de verschillende parameters zoals porie- en korrelgrootteverdeling en totale porositeit meestal niet afzonderlijk beschouwd. Om een onderscheid te kunnen maken in het effect van de individuele parameters is een analyse van virtueel of modelbeton nodig, waarin deze parameters onafhankelijk van elkaar worden geanalyseerd.

Het belangrijkste doel van de numeriek analyse is het berekenen van de impactsterkte en het onderzoeken van het breukproces en de uiteindelijke fragmentatie. De parameters die de uiteindelijke poriestructuur bepalen behoren tot de belangrijkste factoren die invloed hebben op de mechanische eigenschappen van poreus beton. Daarom is met modellen van fictief poreus beton het effect van regelmatig en onregelmatig verdeelde ronde poriën met verschillende stralen en de totale porositeit op de dynamische respons geanalyseerd. Uit de analyses bleek dat

voor alle mengsels die onderzocht zijn geldt dat naarmate de poriegrootte in het mengsel kleiner is (bij gelijke totale porositeit) de impactsterkte van het beton groter is. Ook blijkt dat naarmate de poriegrootte kleiner is en het aantal poriën toeneemt, bij gelijkblijvende porositeit, de de fragmenten die gevormd worden aanzienlijk kleiner zijn. Uit de analyseresultaten van het beton met willekeurig verdeelde poriën blijkt echter dat naarmate de poriegrootte toeneemt dit geen eenduidig effect heeft op de impactsterkte.

Om het effect van korrelgrootte op de betoneigenschappen te onderzoeken, zonder de invloed pakking en korrelvorm, zijn modellen toegepast van fictief poreus beton met ronde korrels . Uit de analyse volgde dat de impactsterkte van poreus beton met 8 mm en 4 mm deeltjes (bij een zelfde porositeit) ongeveer gelijk is, terwijl de impactsterkte van het (model-)beton met deeltjes van 2 mm lager was. De achterliggende mechanismen en de wisselwerking tussen de verschillende parameters, en hoe deze het uiteindelijk dynamisch gedrag bepalen, is in detail beschreven in hoofdstuk 5.

De numerieke simulaties van de impactproeven op het poreuze beton kwamen zeer goed overeen met de resultaten van de uitgevoerde proeven. . Deze goede overeenkomst is bereikt dankzij het realistisch modelleren van de werkelijke korrelstructuur en gebruik van de materiaalgegevens van het cementsteen en de ITZ zoals die bepaald zijn met de materiaalproeven op meso schaal. De gemeten en berekende piekwaarden en het spannings-tijd verloop zijn met elkaar vergeleken. Beiden blijken zeer goed met elkaar overeen te komen. Verdelingen van de fragmentgrootte konden ook worden afgeschat met behulp van de numerieke resultaten. Deze resultaten onderstrepen het belang van de numerieke analyses, omdat hiermee waardevolle informatie wordt verkregen over de invloed van verschillende betonsamenstellingen op de impactsterkte en fragmentatie en helpen om de onderliggende mechanismen te begrijpen.

Dit proefschrift omvat experimenteel en numeriek onderzoek uitgevoerd op poreus beton dat werd ontwikkeld voor veiligheidstoepassingen. De dynamische eigenschappen van het ontwikkelde beton zijn veelbelovend. De geïnstrumenteerde impactproef zoals die is voorgesteld en de numerieke modellen zijn zeer geschikt voor experimenteel en numeriek onderzoek naar het dynamische gedrag van poreus beton.

## Table of Contents

Summary .....	3
Samenvatting.....	6
1 CHAPTER 1 .....	12
GENERAL INTRODUCTION.....	12
1.1 Background .....	12
1.2. Research Objective .....	13
1.3. Research Outline .....	13
References .....	14
2 CHAPTER 2 .....	16
RESEARCH STEPS FOLLOWED TO OBTAIN A MULTIPLE FRAGMENTING “SAFETY” CONCRETE .....	16
2.1. Introduction.....	16
2.2. Cementitious Material with Network of Microcracks .....	16
2.2.1. Autogenous Shrinkage .....	16
2.2.2. Lowering the Water to Cement Ratio .....	17
2.2.3. Surface Tension Increasing Agent : Agar .....	17
2.2.4. Flash Set.....	18
2.3. Sand Concrete .....	19
2.4. Enhanced Strength Porous Concrete.....	20
References .....	21
3 CHAPTER 3 .....	23
STATIC PROPERTIES OF POROUS CONCRETES INVESTIGATED AT DIFFERENT SCALES.....	23
3.1. Introduction.....	23
3.2. Experimental Procedures .....	24
3.2.1. Macro-Scale Testing .....	25
3.2.2. Meso-Scale Testing.....	25
3.2.3. Complementary Characterization Techniques Used.....	29
3.3. Experimental Investigations.....	32
3.3.1 Materials .....	32
3.3.2 Test Results for the Selected Porous Concrete Mixtures at Macro-Scale .....	36
3.3.3 Meso-Scale Tests Results and the Complementary Analyses .....	51

3.4. General Overview of the Factors Affecting Porous Concrete Strength.....	59
3.5. Conclusions.....	60
References.....	62
4 CHAPTER 4 .....	66
IMPACT PROPERTIES OF POROUS CONCRETES AND THE DYNAMIC TESTING TECHNIQUES USED .....	66
4.1. Introduction.....	66
4.2. Planar Impact Measurement Techniques .....	66
4.2.1. Laser Doppler Velocimetry.....	68
4.2.2. High-Speed Photography .....	68
4.2.3. Direct Stress Measurements Using Piezoresistive Stress Gauges .....	69
4.3 Impact Strength Analysis Techniques .....	70
4.3.1 Analysis of One-Dimensional Wave Propagation .....	70
4.3.2 Impedance Mismatch Method.....	74
4.3.3 Reverberation Technique .....	75
4.4. Experimental Investigations.....	79
4.4.1 Materials .....	79
4.4.2 Measuring Impact Stress Using a Piezoresistive Gauge.....	81
4.4.3 Laser Doppler Velocimetry (LDV) Investigations .....	84
4.4.4 Laser Doppler Velocimetry Results and Discussion .....	90
4.4.5. Hi-Speed Photography Investigations.....	100
4.4.6 High-Speed Photography Results and Discussion.....	105
4.4.7 Ultrasonic Wave Velocity Testing of Porous Concretetes .....	111
4.4.8. Particle Size Analysis of Post-Failure Fragments.....	112
4.5. Conclusions.....	115
References.....	116
5 CHAPTER 5 .....	123
EXPLICIT FINITE ELEMENT ANALYSIS OF THE IMPACT BEHAVIOR OF POROUS CONCRETE .....	123
5.1. Introduction.....	123
5.2. Explicit Finite Element Analysis .....	123
5.3. Fracture Behavior of Porous Materials .....	124
5.4. Finite Element Analyses of the Impact Behavior of Porous Concrete .....	131
5.4.1. Finite Element Model .....	132
5.4.2 Mesh Generation.....	137

5.4.3. Numerical Analyses on a Single Pore.....	142
5.4.4. Numerical Analyses on Model Porous Concretes .....	146
5.4.5. Numerical Analyses on Real Porous Concretes.....	175
5.4.6. Determination of Pore Size Distribution.....	187
5.4.7. Determination of Fragment Size Distribution.....	190
5.4.8. Conclusions .....	194
References .....	196
6 CHAPTER 6 .....	200
HIGHLIGHTS AND GENERAL CONCLUSIONS .....	200
6.1 Highlights of the Thesis .....	200
6.2. General Conclusions .....	201
6.3. Further research .....	202
ACKNOWLEDGEMENTS .....	203
CURRICULUM VITAE .....	205

# CHAPTER 1

## GENERAL INTRODUCTION

### 1.1 Background

Explosion is broadly defined as a high amplitude and sudden release of energy (Nolan 2010). In case of an explosion taking place close to or inside a concrete structure, apart from the dangers of the explosive itself, the hazard due to the flying debris from the concrete construction is an important threat as seen in Figure 1.1. Protective structures such as safety walls outside important buildings that have to be protected, or munition magazines for storing explosives carry higher risks of experiencing such extreme loadings during their service lives. Therefore, they are of particular interest in terms of mitigating the effects of a probable explosion. In order to accomplish this goal, a research project was undertaken by Delft University of Technology in collaboration with TNO (Organisation for Applied Scientific Research) and the Netherlands Defense Academy (Netherlands Ministry of Defense), also inspired by the pioneering idea of Jennings and Thomas on designing a cementitious material fracturing into small size fragments in an explosion while having sufficient static strength to carry the service loads of the structure, named as “safety concrete” (O’Neil et al. 2004).



Figure 1.1 Flying debris generated by explosions

Responses of cementitious materials to dynamic loading are significantly different from those under static loading mainly due to the complexities associated with strain-rate sensitivity. Especially in the last decades, extensive research efforts have been focused on understanding the behavior of concrete structures under extreme dynamic loadings (Reinhardt 1982, CEB 1988, Weerheijm et al. 2007, Weerheijm et al. 2013). While most studies aim at designing materials that resist impact loading, developing a cementitious material that is expected to fracture and



disintegrate and is therefore “weak” under impact, but at the same time remains intact during its service life and is therefore also “strong” was the main challenge of this project.

To accomplish that aim, an organized sensitivity study was conducted on various forms of cementitious materials. As a result, porous concretes with enhanced strength, that facilitate the formation of multiple cracks and subsequently fracture into small fragments when exposed to impact loading, were attained. Porous concrete is a construction material that has already been used in various applications mainly as a water permeable, noise absorbing or heat insulating cementitious material (Yang and Jiang 2003, Chindaprasirt et al. 2008, Ghafoori 1995, Marolf 2004). However, its dynamic performance was not of very much interest due to its weak mechanical properties as a consequence of its intentionally increased meso-scale porosity. Due to the high percentage of its meso-size air pores, porous concrete normally has a moderate static strength compared to plain concrete, while owing to its porous structure and aggregate distribution; it has a favorable characteristic of forming multiple cracks. The formation of multiple cracks also facilitates more energy dissipation throughout the material. Therefore, in the process of modifying the material, the main focus was to enhance the static strength properties while maintaining the high porosity.

## **1.2. Research Objective**

The main goal of this research project was to develop a special type of concrete that shows a multiple fragmentation behavior under impact loading. The objective of the experimental work was obtaining and modifying the aimed material and thoroughly examining its unknown properties. The objective of the numerical work was to analyze different types of model and real porous concretes at mesoscopical level in order to better understand the parameters that influence the dynamic behavior of porous concretes.

## **1.3. Research Outline**

The thesis comprises experimental and numerical investigations that have been performed in the scope of the research project. The detailed descriptions of the measurement techniques that have been developed in order to analyze porous concretes are also presented in the corresponding chapters.

This current chapter presents the general introduction.

Chapter 2 summarizes the research steps followed to develop a multiple fragmenting cementitious material, starting from the early stages of the project where the focus was on designing a cementitious material containing an intentionally introduced network of microcracks to the final steps of designing porous concretes with enhanced strength that fracture into small fragments.

Chapter 3 focuses on the macroscopic and mesoscopic as well as some complementary microscopic properties of different porous concretes.

Chapter 4 aims to demonstrate the dynamic characteristics of the porous concretes that have been designed and produced, as well as two new measurement techniques that have been introduced to test porous concretes.

Chapter 5 presents the dynamic numerical analyses conducted on model (with circular pores or circular aggregates) and real porous concretes in order to individually and collectively investigate the different factors that influence the impact performance of porous concretes.

The content of the thesis can be grouped under the following broad headings presented in Figure 1.2.

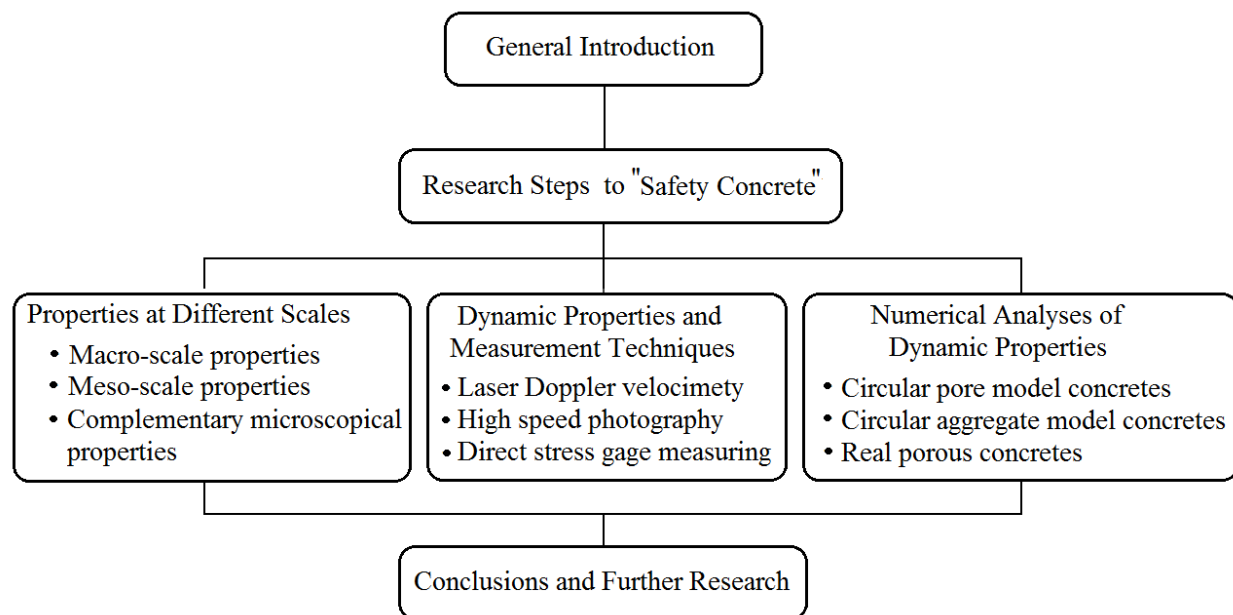


Figure 1.2 Outline of the thesis

## References

Chindaprasirt P, Hatanaka S, Chareerat T, Mishima N, Yuasa Y. (2008), *Cement paste characteristics and porous concrete properties*, Construction and Building Materials, 22(5), 894-901.

Comité Euro-International du Béton, (1988), *Concrete Structures under Impact and Impulsive Loading*, CEB Bulletin 187, Lausanne, Switzerland.

Ghafoori N, Dutta S. (1995), *Building and nonpavement applications of no-fines concrete*, Journal of Materials in Civil Engineering, 7(4), 286-9.

Marolf A, Neithalath N, Sell E, Wegner K, Weiss J, Olek J. (2004), *Influence of aggregate size and gradation on the acoustic absorption of enhanced porosity concrete*, ACI Materials Journal, 101(1), 82-91.

Nolan, D. P. (2010), *Handbook of Fire and Explosion Protection Engineering Principles*, Elsevier, UK.

O'Neil, E. F., Jennings, H., Thomas, J., Shen, W., Cummins, T. (2004), *Safety concrete-development of a frangible concrete to reduce blast-related casualties*, Northwestern Univ., Infrastructure Technology Institute, Evanston, USA.

Reinhardt, H.W., (1982), *Concrete under Impact Loading - Tensile Strength and Bond*, HERON, 27(3), 2-43.

Weerheijm, J., Vegt, I., Breugel, K. van (2007), *Research developments and experimental data on dynamic concrete behavior* C.U. Grosse (ed.), in: *Advances in construction materials*, Berlin: Springer, 765-773.

Weerheijm, J., (2013), *Understanding the Tensile Properties of Concrete*, Woodhead Publishing, Cambridge, UK.

Yang J, Jiang G. (2003), *Experimental study on properties of pervious concrete*, *Cement and Concrete Research*, 33(3), 381-6.

## **CHAPTER 2**

### **RESEARCH STEPS FOLLOWED TO OBTAIN A MULTIPLE FRAGMENTING “SAFETY” CONCRETE**

#### **2.1. Introduction**

In order to reach the objective of obtaining a special type of concrete that fractures into small fragments under impact loading while having sufficient static properties as a building material, various forms of cementitious materials have been investigated in the scope of the research project. As a starting point, designing of a cementitious material that incorporates a network of microcracks, which are idle under the service loads of the structure, but propagate under impact loading, was initially the main focus of the research. Therefore, certain mechanisms, that have been known to be potential causes of cracking in concrete, were re-investigated in the counter direction with the aim of enhancing them. After gaining some experience in trying to place a homogeneously distributed weak phase in concrete (network of microcracks) that can facilitate multiple fragmenting, the research direction was decided to be shifted to including another form of weak phase in concrete. This time placing a weak phase in the form of air pores, that can be better controlled by modifying the mixture content and compaction, was aimed. Therefore, at the rest of the research, porous concrete was the focal point while enhanced strength porous concretes, which comply with the initially defined requirements of the project and which can therefore, perhaps be termed as “safety concrete”, have been designed and produced. The research steps, which have been followed, can briefly be summarized as follows, starting from the initial idea of a microcracks network.

#### **2.2. Cementitious Material with Network of Microcracks**

##### **2.2.1. Autogenous Shrinkage**

The research study has started with investigating the potential effects of autogenous shrinkage and how they can be enhanced. Autogenous shrinkage was selected because of the well-known property of autogenous shrinkage cracks being evenly distributed in the bulk cement paste phase forming a homogenous structure. In a cementitious material, the amount of free water in the reacting body gradually decreases due to the hydration reaction of cement while fine pores are formed in the hardened cement paste. As the hydration continues, the amount of free water decreases and micropores are further shaped by the hydration reaction. Consequently, the water vapor pressure reduces and the relative humidity in the fine pore decreases under the isolated conditions which is called self-desiccation. The reduction in internal relative humidity goes along with an increase in the tension in the capillary water which results in shrinkage. In concretes with low water to binder ratios (about 0.3), autogenous shrinkage can be significant. Consequently, shrinkage results in tensile stresses in the cement paste due to aggregate restraint

and causes the formation of microcracks (Tazawa 1998, Lura 2003, Lura et al. 2003, Holt 2005, Igarashi 2000, Koenders 1997).

### 2.2.2. Lowering the Water to Cement Ratio

In order to enhance the already known effect of a low water to cement ratio on the degree of autogenous shrinkage, the water to cement ratio was further decreased to very low values that had not been investigated so far due to their low feasibility. Cement pastes were produced in which the water to cement ratio was decreased to extremely low values (w/c of 0.15 and 0.17). In these mixtures, a great portion of the cement grains were expected not to hydrate due to the insufficiency of water, i.e. at those w/c's, only approximately 36 % and 40 % by mass of the cement were expected to get a chance to hydrate, respectively. To be able to get a mixture that is workable enough, the percentage of superplasticizer used had to be raised up to 10 %. For having a better control over the restraining effect of aggregates on the shrinking cement paste, a mold with the dimensions of 15x15x1 cm was used in which prismatic brass aggregates with different cross-sectional shapes and sizes (circular or hexagonal) were fixed in the mold as seen in Figure 2.1. Starting from locating only one aggregate in the sample and by increasing the number of aggregates along with varying the distance between them, the restraining effect of aggregates was also tried to be controlled.

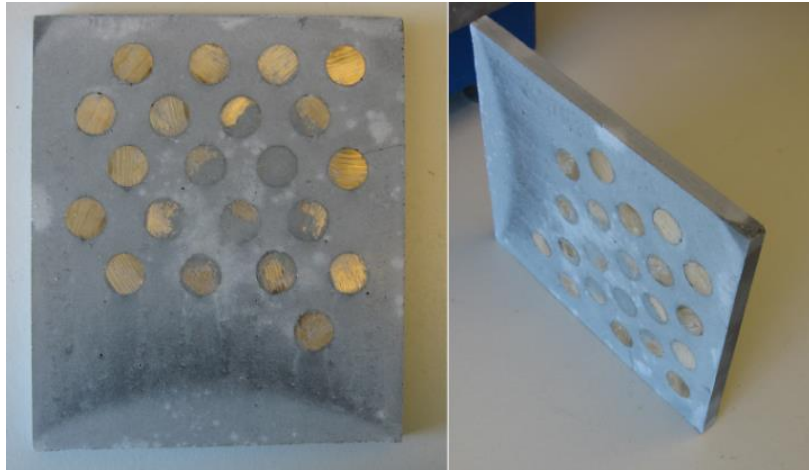


Figure 2.1 Cement paste samples with metal aggregates used in shrinkage investigation

### 2.2.3. Surface Tension Increasing Agent : Agar

In order to further enhance the autogenous shrinkage without further decreasing the w/c, the possibility of increasing the surface tension of the capillary water was investigated. Based on the Kelvin equation and Raoult's law the RH is calculated as follows:

$$\ln(RH) = \frac{-2\gamma V_m}{rRT} \quad (2.1)$$

where  $\gamma$  is the surface tension of pore water,  $V_m$  is the molar volume of water,  $r$  is the radius of the meniscus (the radius of the largest water-filled cylindrical pore),  $R$  is the universal gas constant and  $T$  is the absolute (Kelvin) temperature where a contact angle of 0 (complete wetting) is assumed (Jensen and Hansen 2002, Bentz and Jensen 2004). Decreasing the surface tension of the pore solution to mitigate shrinkage was a previously applied method where generally organic admixtures were used (Tazawa and Miyazawa 1995, Rongbing and Jian 2004). Since the objective of the research was enhancing shrinkage, the opposite of what has been done for mitigation purposes was therefore, applied. A material that could be added to the mixing water of cement paste (mortar or concrete), which was stable at varying temperatures and which did not react with the cement, aggregates or the conventional admixtures e.g. superplasticizers, was explored. Therefore, agar which is a gelatinous hydrophilic colloid being usually used as an additive in food products was investigated (Williams and Phillips 2000).



Figure 2.2 Agar as additive to increase surface tension (Fankhauser 2010)

The promising properties of agar were that once it has melted in water, it was stable up to temperatures around 85°C. The difference between setting and melting temperatures was much greater in agar than in any other reversible gelling agent. It did not require the presence of other products or ions for gelation and it could be used over a wide range of pH (Imeson 1997). To see the effect on shrinkage, solutions of water having different concentrations of agar (0.2, 0.4, 0.6, 1.0 % by mass of water) were prepared, where cement pastes with the water to cement ratio of 0.3 were produced using only the agar gel solutions as mixing water and increasing the amount of superplasticizer to maintain the workability.

#### 2.2.4. Flash Set

In order to weaken the matrix (the cement paste) and promote the formation of cracks, a special type of cement that performs a flash set was also tried. In the hydration of Portland cement in the presence of gypsum, ettringite is formed followed by the formation of monosulfate during the later stages of hydration. In the lack of gypsum,  $C_3A$  starts hydrating and voluminous hexagonal aluminates hydrates form instead of combining with sulfate to form ettringite. The interlocking aluminates hydrates fill up the water-filled space, causing stiffening and a quick set often called “flash set” occurs. This situation usually results in a poor strength development because the large hydration plates weaken the paste microstructure. This also retards the hydration of the silicates

and inhibits strength development (Hills and Tang 2004). Autogenous shrinkage is also known to depend on the contents and degree of hydration of  $C_3A$  and  $C_4AF$  (El Elaoui and Benkaddour 1997).

To be able achieve flash set, a cement that contained no gypsum was used in the experiments. Since that type of cement is not commercially preferred, the clinker of CEMI 32.5 was taken from the cement plant in its non-ground form and was ground at the Mining Department at Delft University of Technology. The ground clinker that did not contain any gypsum was used instead of cement in the experiments to obtain a very weak and highly shrinking cement paste phase. Mixtures were produced again using agar this time with ground clinker instead of Portland cement keeping the water to cement ratio at 0.3. In order to provide restraint to generate cracking, aggregates at various gradings were also used in the mixtures instead of artificial metal aggregates.

### 2.3. Sand Concrete

Next, a different cementitious material that can be called a “sand concrete” was produced with a very wide range of water/cement and aggregate/cement ratios up to 2 and 10, respectively to be able to obtain mechanically weak mortars. The aim was, starting from the very weak state, modifying the properties step by step to obtain the aimed cementitious material. In the mixtures, cements with and without gypsum were used to try weak and stronger matrices. The fine aggregate used was either at 0.125-0.25 or 0.25-0.50 mm standard size ranges. Initially, some of the mixtures were produced to again investigate shrinkage. The weak matrix was believed to crack more readily under the effect of shrinkage. While consistent cracking could not be obtained, it was realized that with a low cement content, the material becomes very porous and weak. High water/cement ratio, very low cement content mixtures were then produced to introduce additional porosity to the mixture in a controlled way. In Figure 2.3, a sample of sand concrete with low cement (high water) content can be seen.



Figure 2.3 “sand concrete”

Because the workability of the mixtures was very low, the pouring and placing of the material had to be done by compacting in layers with a steel weight. The specimens had to be demolded not before two days. It was not possible to demold them after one day because they were

fracturing during demolding due to insufficient strength gain in one day. While some samples were hit by a drop weight without quantifying the impact stress, it was seen that they fracture into small fragments, as seen in Figure 2.3. Therefore, in terms of fragmentation under impact, the preliminary observations were found to be promising for further research and the research direction was shifted to including pores instead of microcracks in concrete.

## 2.4. Enhanced Strength Porous Concrete

After gaining experience on sand concrete and deciding to focus on porous concretes, several modifications were made step by step in the mixture contents and the production technique. The details of the mixture design and production are presented in Chapter 3. The general evolution of the stress-strain curves of the porous concretes produced in this research project can be summarized with the graph in Figure 2.4. This figure shows some selected mixtures that have been produced in subsequent steps of modifying the material. In the process of strength enhancement starting from static compressive strengths less than 10 MPa to reaching more than 50 MPa, the dominant parameters can be summarized as intensive compaction, lower aggregate/cement (a/c) and water/cement (w/c) ratios, using set retarding admixture and altering the aggregate grading.

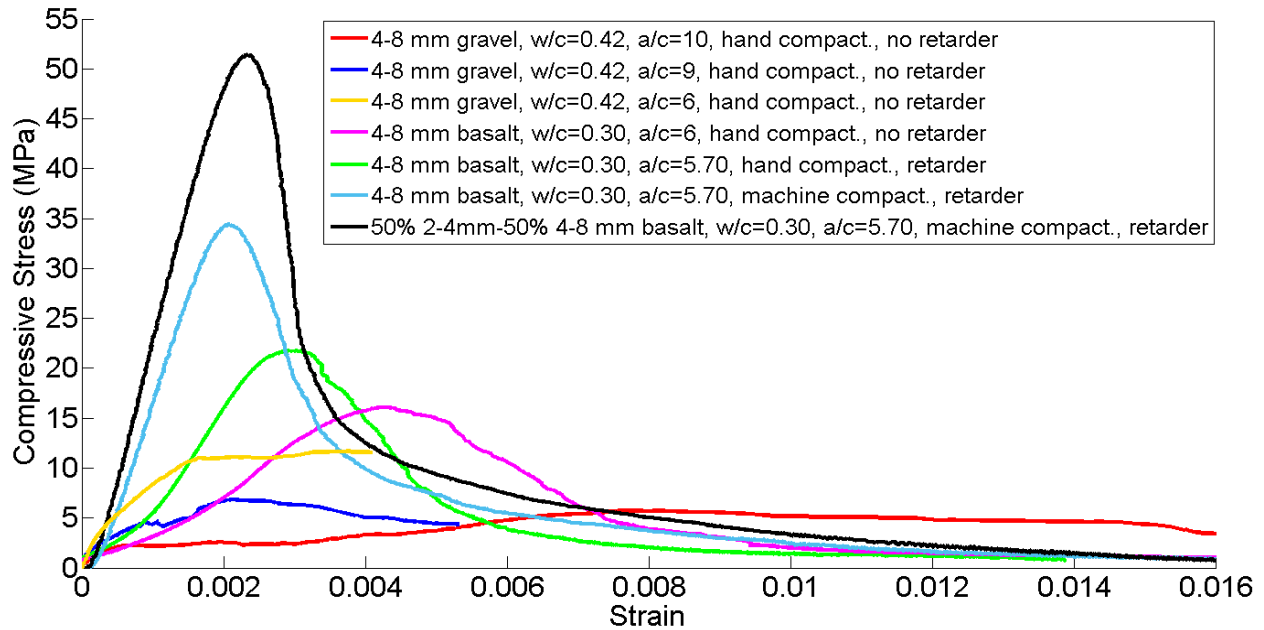


Figure 2.4 Evolution of porous concretes in the scope of the research project



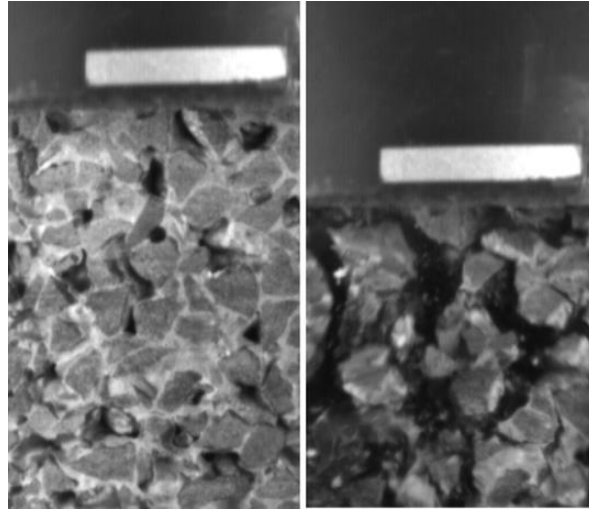


Figure 2.5 Example of a multiple fragmenting porous concrete under impact loading

While the static as well as the dynamic strengths were enhanced, the fragmentation behavior of the material which was also one of the main focuses of the project was continuously investigated (as seen in an example in Figure 2.5) and modified. As will be presented in detail in Chapter 3, different porous concrete mixtures with improved strength properties were designed and tested both statically and dynamically in order to obtain the desired cementitious material.

## References

- Bentz, D.P., Jensen, O.M. (2004), *Mitigation Strategies for Autogenous Shrinkage Cracking*, Cement and Concrete Composites, 26(6), 677-685.
- El Elaoui, B., Benkaddour, M. (1997), *Hydration of  $C_3A$  in the Presence of  $CaCO_3$* , Journal of Thermal Analysis, 48, 893-901.
- Fankhauser, D.B. (2010), [http://biology.clc.uc.edu/fankhauser/Labs/Microbiology/Bacterial\\_Inhibition/Agar\\_Overlay.htm](http://biology.clc.uc.edu/fankhauser/Labs/Microbiology/Bacterial_Inhibition/Agar_Overlay.htm)
- Hills, L., Tang, F. (2004), *Manufacturing Solutions for Concrete Performance*, World Cement, 35, 115-121.
- Holt, E. (2005), *Contribution of Mixture Design to Chemical and Autogenous Shrinkage of Concrete at Early Stages*, Cement and Concrete Research, 35(3), 464-472.
- Igarashi, S. I., Kubo, H. R., Kawamura, M. (2000), *Long-Term Volume Changes and Microcracks Formation in High Strength Mortars*, Cement and Concrete Research, 30(6), 943-951.

Imeson, A. (1997), *Thickening and Gelling Agents for Food*, Blackie Academic & Professional, Imprint of Chapman & Hall, New York, USA.

Jensen, O. M., Hansen, P. F. (2002), *Water-Entrained Cement-Based Materials II. Experimental Observations*, Cement and Concrete Research, 32(6), 973-978.

Koenders, E. A. B. (1997), *Simulation of Volume Changes in Hardening Cement-Based Materials*, Faculty of Civil Engineering, Delft University of Technology, Delft, PhD.

Lura, P. (2003), *Autogenous Deformation and Internal Curing of Concrete*, Faculty of Civil Engineering, Delft University of Technology, Delft, PhD.

Lura, P., Jensen, O.M., Breugel, K. van (2003), *Autogenous Shrinkage in High-Performance Cement Paste: An evaluation of Basic Mechanisms*, Cement and Concrete Research, 33(2), 223-232.

Rongbing, B., Jian, S. (2004), *Synthesis and Evaluation of Shrinkage-Reducing Admixture for Cementitious Materials*, Cement and Concrete Research, 35(3), 445-448.

Tazawa, E. I., Miyazawa, S. (1995), *Influence of Cement and Admixture on Autogenous Shrinkage of Cement Paste*, Cement and Concrete Research, 25(2), 281-287.

Tazawa, E. (ed.) (1998), *AUTOSHRINK'98: Proceedings of International Workshop on Autogenous Shrinkage of Concrete*, Japan Concrete Institute, Hiroshima, Japan.

Williams, P. W., Phillips, G. O. (2000), *Handbook of hydrocolloids*, Woodhead Publishing, Cambridge, UK.

## **CHAPTER 3**

### **STATIC PROPERTIES OF POROUS CONCRETES INVESTIGATED AT DIFFERENT SCALES**

#### **3.1. Introduction**

Porous concrete is a special type of cementitious material that incorporates a high amount of meso-size air pores. Due to its high porosity, it is used in various applications that require permeability, noise absorption or thermal insulation (Yang and Jiang 2003, Chindaprasirt et al. 2008, Ghafoori and Dutta 1995-1, Ghafoori and Dutta 1995-2, Marolf et al. 2004). In order to attain the porous structure, both the mixture design and the casting procedure of porous concrete have to be different from those of normal concrete. Namely, the aggregates are gap-graded or in one standard size range, the cement paste content is highly decreased and compaction in layers is essential during casting due to the very low workability of the mixture (Ghafoori and Dutta 1995-2).

Within the scope of the PhD project on designing a cementitious material, that fractures into small fragments when exposed to impact loading while having a sufficient static strength, different types of porous concretes were designed and investigated at various scales i.e. macro, meso and micro-scales (Agar Ozbek et al. 2013-1, Agar Ozbek et al. 2013-2). Aiming to enhance the mechanical properties, a sensitivity study was conducted where factors that affect the properties of porous concrete were considered along with their interactions. As the mixture designs and the production techniques of the porous concretes were modified, experiments at different scales were planned and performed to determine the effectiveness of the various factors. The outcome of the tests guided the modification process of the material. As a consequence, different types of porous concretes were produced and tested while some were selected to be presented in this chapter as representative mixtures. Because pores are essential for the required dynamic performance of the material, the main focus was to enhance the static strength properties while maintaining the high porosity. This chapter aims to summarize the static and some microscopical characteristics of the porous concretes that have been designed as well as the techniques used to understand their behaviors. In order to produce porous concretes with improved static strength and the target dynamic properties, composition characteristics such as aggregate properties, grading and cement paste properties as well as the compaction technique had to be modified.

Among all the parameters, aggregate properties have a significant effect on the rheological as well as the mechanical properties of porous concrete. It is accepted also for normal concrete that aggregates, with a particle size distribution of a wide range of sizes, increase the packing up to a threshold, provided that there is sufficient cement paste present in the mixture (Erdogan and Fowler 2005, Klieger and Lamond 1994). In porous concretes, the aggregate particle size also influences the pore size distribution. The relationship between the porosity and strength has been thoroughly investigated by researchers both theoretically and experimentally (Chindaprasirt et al.

2008, Deo and Neithalath 2011, Lian et al. 2011). For both mono-size and graded aggregate distributions, an increase in aggregate size results in an increased median pore size. On the other hand, for mono-sized aggregate mixtures, there is no significant difference in total porosity as the aggregate size changes (Marolf et al. 2004). The morphological properties of aggregate particles also affect the rheology and the mechanical properties of normal and porous concretes. Rounded aggregates result in an increased packing. On the contrary, as surface smoothness increases, the contact and, therefore, the bond area decreases compared to those of a rough particle. Therefore, smoother particles also require and tend to hold a lower amount of cement paste than a rough particle. This should additionally be considered in adjusting the cement paste viscosity in the mixture. It should also be considered that texture and angularity contribute to concrete strength due to particle-to-particle mechanical interlock and increased total surface area available for the adherence of the cement paste. The different mechanical properties of the aggregates also have an influence on the strength of porous concrete even for aggregates that have the same texture (Erdogan and Fowler 2005, Crouch et al. 2007, Lian and Zhuge 2010).

Because fresh porous concrete has a low workability, in order to provide a better aggregate packing, applying special compaction techniques is essential during casting. Meanwhile, because of the prolonged compaction time and the moisture loss due to the large amount of air exposed surface of porous concrete, the possibility of cement paste setting during casting should also be considered (Crouch et al. 2007, Kevern et al. 2009). Therefore, the admixtures used in a porous concrete mixture should be precisely adjusted. Different from normal concretes, porous concretes lack nearly all fine aggregates. Therefore, the effects of widely known mixture modifications, such as adding mineral admixtures, may also differ when porous concrete is of concern. Although the enhancing effect of microsilica on the mechanical properties of concrete is well accepted, there is controversy as to whether the enhancement is due to its effect on the ITZ (Cohen et al. 1994, Bentz et al. 1992, Toutanji and El-Korchi 1995) or in large part because of the improved strength of its bulk cement paste constituent (Cong et al. 1992). The situation in porous concrete is more complicated and less known due to its different mixture design and the distribution and relative amounts of its phases, as it will be explained in more detail in the following sections of the chapter as well as Chapter 5.

In this chapter, the effects of different factors on enhancing the mechanical properties of porous concretes are summarized. The experimental procedures that were followed in order to acquire information on the properties of the material at different scales are described. The results, which were obtained at smaller scales, enable a better interpretation of the global behavior of the different types of porous concretes with improved strength.

### **3.2. Experimental Procedures**

In the scope of the research, the compressive and tensile tests were performed at macro-scale (testing of porous concrete) while the tensile tests were also conducted at meso-scale (testing of ITZ and cement paste phases). The samples that have gone through mechanical testing were also analyzed through computed tomography (CT) to visualize the crack patterns and better

understand the fracturing behavior. Meso-scale porosity was also measured through CT scanning coupled with image processing. The fracture surfaces of the samples, which have been tested at meso-scale ITZ testing, were observed under environmental scanning electron microscope (ESEM) to be able to see a relation between the ITZ strength and the fracture surfaces formed. The macro scale samples were also observed using ESEM to be able to characterize the materials more thoroughly and support the mechanical test results. X-ray diffraction (XRD) analysis has also been performed on the gravel samples that have shown a strong bonding in the meso-scale ITZ testing.

### 3.2.1. Macro-Scale Testing

At macro-scale, deformation controlled uni-axial compression and tension tests were performed at the loading rate of 1 and 0.1  $\mu\text{m}/\text{sec}$ , respectively. The deformation measurements were made over the whole height of the samples at both tensile and compressive tests and the average of four LVDTs were used as the feed-back signal, as shown in Figure 3.1. In the tests, 83 mm diameter, 160 mm height and 83 mm diameter, 80 mm height cylindrical specimens were used in compression and tension tests, respectively. 55 mm diameter, 70 mm height cylindrical samples were also tested at the initial sets of experiments. Before testing, the cylinder ends were sawn parallel and capping was applied. For the tensile test, the samples were glued to non-rotating steel plates using an epoxy based glue. Because porous concrete readily incorporates numerous notches due to its porous nature, no notches were made on the tensile test samples. To be able to prevent the snap-back behavior, the tensile sample height was kept at 80 mm for the large size samples. During the tensile tests, the specimens failed at one visible major crack.



Figure 3.1 Deformation controlled uni-axial compression test set-up

### 3.2.2. Meso-Scale Testing

In order to understand the global behavior of porous concrete as a composite material, the properties of its different phases should also be investigated separately at a lower scale. Data on the mechanical properties of the interfacial transition zone (ITZ) was, therefore, essential. There is a considerable amount of information in the literature that clearly demonstrates the formation and the microscopic structure of the ITZ (Scrivener et al. 2004). Although its microscopic structure is investigated widely in detail, the experimental data available on its mechanical properties is relatively limited. In order to measure the load-displacement response of the aggregate-cement paste bond, various testing techniques have been designed and investigated (Alexander 1993, RILEM 1996). In one of the studies on the subject, the bond strength for different aggregate types and surface roughnesses were found to be between 0.2-1.2 MPa (Zimbelmann 1985) while in another study the bond strength was on average 2 MPa (Hsu and Slate 1963). In a study, where chevron-notched beam composite specimens were produced to perform SEM investigation using stereo pairs, relationships between the fracture surfaces and the interfacial transition zone properties were found (Diamond and Mindess 1992). The effect of aggregate type on the ITZ properties were also explored in other studies (Qian et al. 2010, St John 1998).

Among the three phases of concrete, ITZ is the one that has the lowest mechanical properties. The properties of the bulk cement paste phase can be an indication for the properties of the interface formed between that cement paste and an inclusion such as an aggregate. However, such a relation is not definite especially if mineral admixtures such as microsilica, that are known to influence the ITZ and bulk cement paste phase properties at different extents, are involved. Therefore, the proper material design considerations require specific knowledge on the ITZ phase itself.

While the testing of pure cement paste at a smaller scale is relatively more straightforward, testing of the mechanical properties of the interfacial transition zone is challenging due to the complexities of testing a phase that has a micro-scale thickness. A standard testing method to determine the mechanical properties of the interfacial transition zone has not yet been established. In the scope of this research, a systematic approach was followed to modify the geometry of the meso-size samples in order to reach a reproducible and feasible ITZ testing method.

Using two spherical half aggregates glued together with a small fixed amount of cement paste (amount controlled by a dropper) was initially tried in order to produce meso-scale specimens as seen in Figure 3.2. In the figure, the half aggregates as well as the computed tomography image of a sample are shown. To be able to keep the sample not damaged by its self-weight during hardening, an electrical magnet mechanism was used to keep the top aggregate hung until hardening, as can also be seen in Figure 3.2.

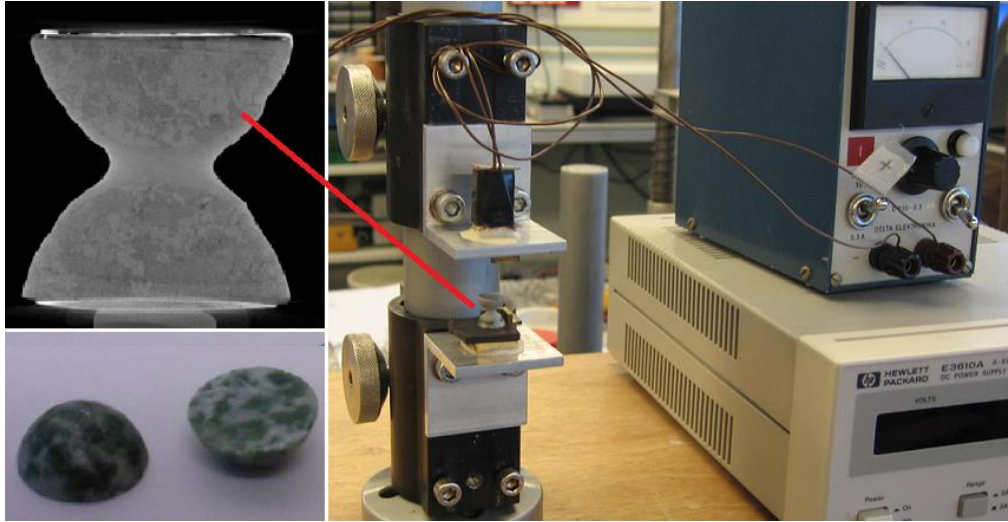


Figure 3.2 Meso-scale composite ITZ specimens with spherical half aggregates and the production set-up

The meso-scale sample was also analyzed numerically to be able to see the stress distributions as shown in Figure 3.3.

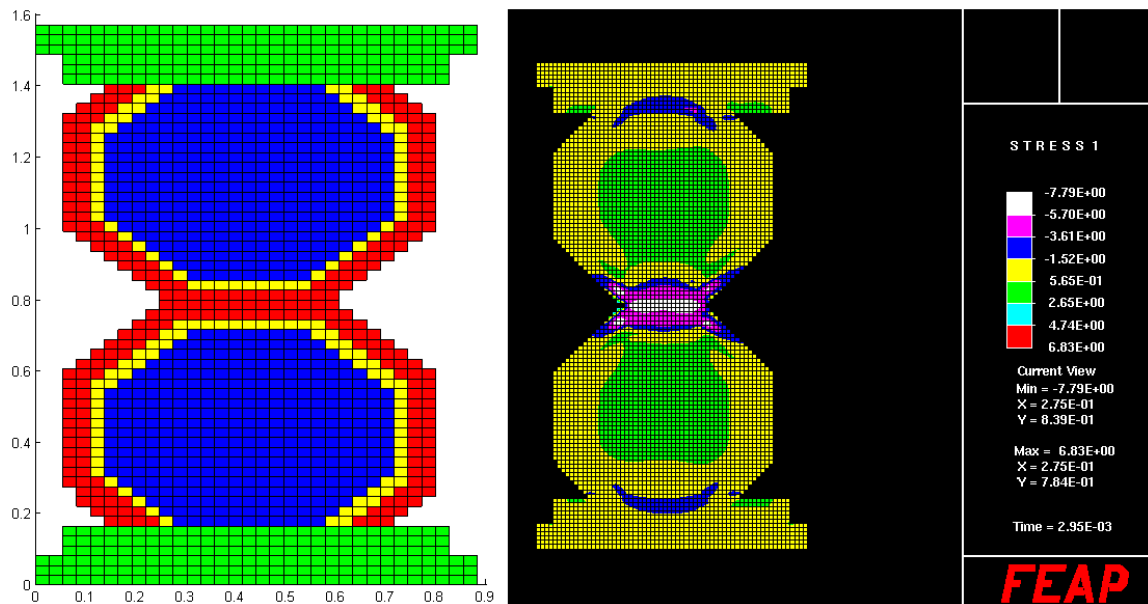


Figure 3.3 Preliminary numerical analyses on stress distributions of two aggregate specimens

Because the production of such samples is complex and extracting information solely on the ITZ phase was not very straightforward, the samples were further simplified. Cylindrical steel aggregates with various diameters in a sandwich form, where a cement paste is poured between the metal aggregates, that have been tightly located into plastic pipes of corresponding diameters (which were removed after hardening), as seen in Figure 3.4, were used next. These samples

were better reproducible and straightforward to evaluate. However, because of the presence of two ITZ layers in each sample and also because the texture of polished metal aggregates did not resemble those of natural aggregates very accurately, further modifications on the samples were needed.

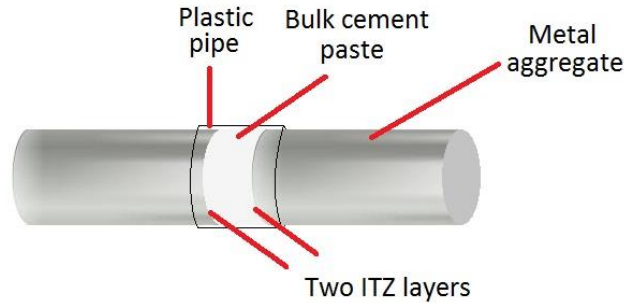


Figure 3.4 Meso-scale composite ITZ specimen with cylindrical metal aggregates

Finally, natural aggregates (basalt and different types of river gravel), with an 8 mm by 8 mm square cross-section, were used, taking the 4-8 mm aggregate size range of the porous concrete as reference. The size of the cement paste parts of the samples were therefore, comparable with the cement paste bridges present between the aggregates in macro size porous concrete samples. Owing to this, the cement paste in the samples was affected by similar conditions in terms of shrinkage. Preserving the natural surface of the aggregates, as they exist in the macro-size samples, was an important feature of the samples in order to have a realistic ITZ structure. The aggregates with square shaped cross sections were cut from the special aggregate-glue composite samples (see Figure 3.5, the top image). Aggregate-glue composite samples were prepared using an epoxy based glue at the bottom to be able to have a horizontal surface on top, while having the flat surface of the glue at the bottom. The lateral surfaces of the aggregates were covered with a type of wax in order not to have any cement paste adhesion at the lateral surfaces that may have affected the results. The 8 mm by 8 mm square aggregates were then placed at the bottom of steel molds onto which cement paste was poured. The molds were vibrated on a normal size vibration table. Because the aggregate-glue composites were made by placing large size natural aggregates on a liquid glue and then by cutting it into a square prism, each composite sample had a different height and a proportion of glue and aggregate. The samples were then glued to the testing device. After the sample was connected to the compression-tension testing machine with again the liquid glue, the testing device was temporarily set to load control until the glue hardens. Owing to that, the sample was not exposed to tension due to the shrinkage of the glue while hardening. In all the composite ITZ samples tested, the failure occurred in the immediate vicinity of the aggregate at the ITZ phase. Thus, the peak load that is measured can be used to determine the tensile strength of the ITZ phase itself. However, due to the different proportions of glue and aggregate components, the displacement values are insignificant and cannot be compared with each other. The samples were wrapped with aluminum and plastic foils and kept at 20 °C at the



laboratory conditions exactly like the macro-size samples. The meso-size cement paste samples, with a section of 8 mm x 8 mm and a height of about 15 mm were also tested under tension.

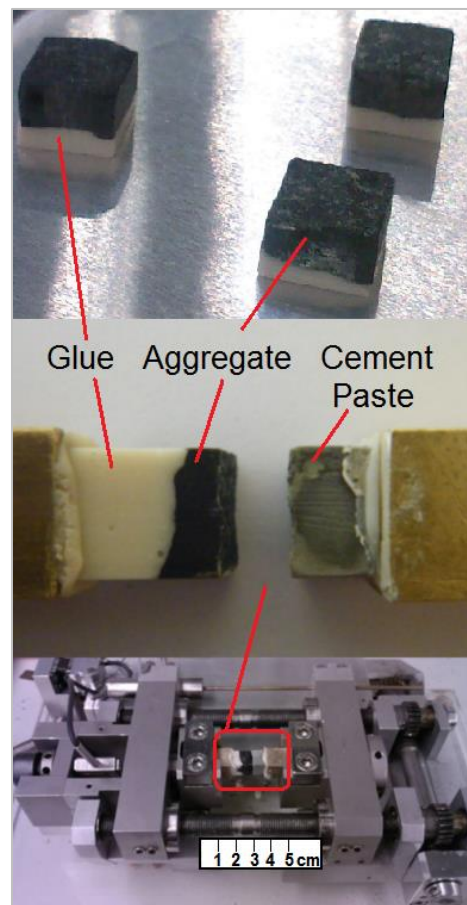


Figure 3.5 Square shaped basalt aggregates, composite sample for ITZ testing and meso-scale compression-tension test setup

Testing of the cement paste and composite ITZ samples was done with a displacement controlled small-scale compression-tension testing machine as shown in Figure 3.5. Cement paste samples were also tested with the same setup. During the tests, the loading rate was 0.1  $\mu\text{m}/\text{sec}$  as in the macro-scale tensile testing.

### 3.2.3. Complementary Characterization Techniques Used

#### 3.2.3.1. Environmental Scanning Electron Microscopy

Electron microscopy is an increasingly used technique for analyzing the microstructure of cementitious materials. (Diamond 2004, Scrivener 2004, Bentz and Stutzman 1995, Copuroglu 2010). SEM imaging techniques have the common feature of focusing a high-velocity electron beam on an extremely fine spot where the focused beam executes a raster pattern over the limited area of the surface (Diamond 2004). In the analyses, a Philips XL30 environmental scanning

electron microscope (ESEM) was used. The ESEM was also equipped with energy-dispersive X-ray spectroscopy (EDS) that provides specific chemical compositional information on any desired spot or area.

### 3.2.3.2 Computed Tomography (CT)

Computed tomography has been used as a tool for examining the properties of cement based materials (Erdogan et al. 2006, Suzuki et al. 2010, Persson and Östman 1986). In the CT image, different materials are detected and indicated by different shades of gray according to their densities. In conducting the CT scans, a Phoenix Nanotom X-ray computed tomography machine (as shown in Figure 3.6) was used. The resolution was  $0.5\text{ }\mu\text{m/voxel}$ , depending on the sample size. During the computed tomography application, two dimensional X-ray images are taken while rotating the specimen 360 degrees around an axis. The two dimensional images are subsequently reconstructed to generate a three-dimensional image of the specimen. The three-dimensional image is then separated into virtual slices enabling the analysis of the specimen at any section taken both vertically and horizontally at any angle.



Figure 3.6 Computed Tomography (CT) machine for testing building materials

CT analyses can be used for visualizing crack patterns as well as determining the porosity. Measuring the meso-size porosity of the mixtures was done by converting the acquired images of the sample to binary mode. An example is shown in Figure 3.7. By using the image processing toolbox of MATLAB, the ratio of the solid and air phases, i.e. the numbers of black and white pixels, is determined.

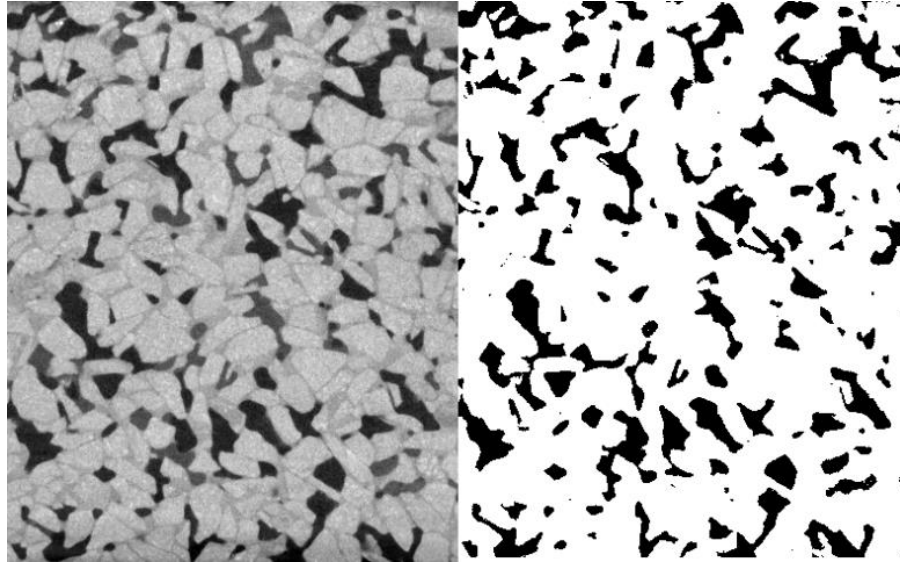


Figure 3.7 Determination of porosity: a) (left) CT image of a section, b) (right) Image converted to binary mode

For inspecting cracks formed at a uni-axial compression test, macro-size samples were loaded under compression up to slightly beyond the peak stress and then unloaded (Figure 3.8 (right)). The partially fractured samples were afterwards impregnated with epoxy resin to stabilize the cracks. In CT inspections, the pieces of the samples that are cut from the macro-size samples were 3-4 centimeters. Numerous sections inside the sample can be visualized with a resolution of about  $23\text{ }\mu\text{m}/\text{voxel}$ . The effect of sample preparation on the cracks observed is minimized.

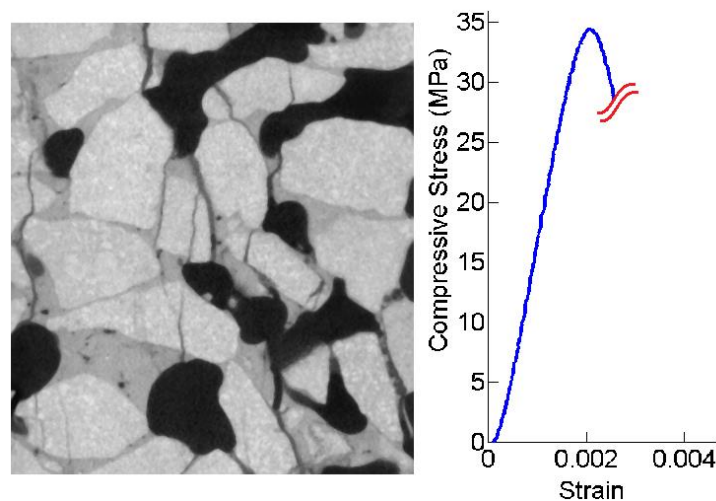


Figure 3.8 CT imaging of partially fractured porous concrete

### **3.3. Experimental Investigations**

The results obtained from experimental analyses at different scales (macro, meso and micro if needed) were evaluated and will be discussed in separate sections. In the macro-scale testing, the compressive and tensile properties of different types of porous concretes and full concretes were investigated. The effects of different compositional factors on the mechanical properties of porous concrete were evaluated. At the meso-scale tests, the properties of the ITZ of samples made with different types of aggregates were analyzed. The meso-scale cement paste samples were tested in order to determine the properties of cement pastes under shrinkage conditions that are similar to those of the thin cement paste bridges between aggregates in real porous concretes. In real porous concretes, the cement paste bridges gluing the aggregates are also exposed to air on all lateral surfaces as in meso-scale samples. The results of computed tomography (CT), environmental scanning electron microscopy (ESEM) and X-ray diffraction analyses are also presented in order to explain the mechanical test results.

#### **3.3.1 Materials**

In the process of modifying the mixture properties, a large number of different porous concrete mixtures were produced and tested. The compositions of the selected representative mixtures are given in Table 3.1. It should be noted that most of these mixtures are produced in parallel with the mixtures used for investigating the dynamic properties given in Chapter 4.

The specimens were wrapped with multiple layers of plastic and aluminum foils and kept at 20°C at the laboratory conditions until their testing dates. The water-cured samples were kept in tap water until one day before their testing dates and dried at the laboratory environment until their testing day. Cylindrical specimens that were 83 mm in diameter and 170 mm in height were used for compression tests. Half samples, with 83 mm diameter and 80 mm height, were used for tension testing to eliminate the snap-back behavior as much as possible. It should be noted that 83 mm diameter samples were mixed, cast and compacted one by one with the aim to mitigate the scatter in test results. 50 mm diameter and 70 mm height hand-compacted samples were also used in some of the initial tests.

In the scope of this research, production of concretes incorporating meso-size air pores and having a static strength at the range of 30-50 MPa was accomplished by adjusting the mixture design and applying enhanced compaction. Even though the mixture components and the casting method may vary for different application fields, the main principle of making a concrete with meso-size air pores is excluding fine aggregates from the mixture. In the process of enhancing the static strength, while complying with this main principle of not including fine aggregates, the rest of the mixture components were adjusted and the compaction technique was modified.

Table 3.1 Compositional properties of selected representative porous and full concrete mixtures

Mixture code	PRC1	PRC2	PRC3	PRC4	PRC5	PRC6	PRC7	PRC8	PRC9	PRC10	PRC11	FC1	FC2
Crushed basalt (2-4 mm) (gr)	-	2000	1000	-	-	2000	1000	-	-	-	-	-	-
Crushed basalt (4-8 mm) (gr)	2000	-	1000	-	2000	-	1000	2000	-	2000	2000	2000	2000
River gravel (4-8 mm) (gr)	-	-	-	2000	-	-	-	-	2000	-	-	-	-
Cement (gr)	351	351	351	351	298	298	298	351	351	351	263	951	808
Microsilica (gr)	-	-	-	-	53	53	53	-	-	-	-	-	144
Water (gr)	105	105	105	105	105	105	105	105	105	105	79	285	285
Superplasticizer (gr)	0.97	0.97	0.97	0.97	1.30	1.30	1.30	1.00	1.00	1.00	0.73	4.20	5.71
Set retarder (gr)	1.20	1.20	1.20	1.20	1.20	1.20	1.20	-	-	1.00	0.90	2.22	2.22
Compaction	high	high	high	high	high	high	high	low	low	low	high	high	high
Curing	No curing, wrapping with multi-layers of plastic and aluminum foils												

In porous concrete applications, where high permeability is aimed at, compaction is partly restricted due to the fact that it also reduces pore connectivity. In this current application, porosity was essential, but pore connectivity was not a requirement. Therefore, different compaction techniques were experienced in order to optimize the compaction. Because the pores of the concretes produced in this research were not necessarily connected, the concretes cannot be classified as pervious, but rather as porous.

To be able to produce a porous concrete that incorporates an evenly distributed cement paste phase throughout the specimen without accumulation at any location especially at the bottom portion, the consistency of the cement paste has to be adjusted. The required consistency of the cement paste for porous concrete can be defined as the consistency which facilitates a uniform cement paste distribution in the material even under the intensive compaction applied. The consistency is dependent on various parameters such as the type of binder, the water to cement ratio and the admixtures. The amount of superplasticizer and the water to cement ratio are the most decisive parameters affecting the consistency. The amounts and types of admixtures were adjusted according to the types of binders used in the mixture. The set retarder also has a key role in maintaining the workability throughout the prolonged compaction which is also essential. Without using a set retarder, the cement paste starts to set during the casting process. The cement paste bridges between the aggregates, that have already started setting, are broken as the compaction process continues, which drastically lowers the strength. Obtaining a porous concrete with improved strength properties is, therefore, not possible without a set retarder, as it was also experienced in the preliminary samples that were tested. In order to have a cement paste with a high strength, which strongly binds the coarse aggregates together, the water to cement ratio has to be kept low. Water to cement ratio was finally selected to be 0.30 in the mixtures after different combinations of varying water to cement ratios, amounts of superplasticizer and set retarder were tried.

In the mixtures, the aggregates were either in one (2-4 mm or 4-8 mm) or two (2-4 mm and 4-8 mm, each 50 percent by mass) standard size ranges (three different aggregate gradings). Two different types of aggregates (crushed basalt and river gravel) and two binders (cement and microsilica) were mainly involved in the productions. The summary of the compositional properties of the selected representative mixtures is presented in Table 3.1. The cement used was CEM I 52.5 Rapid hardening Portland cement with a specific gravity of  $3.13 \text{ g/cm}^3$  and Blaine fineness of  $5330 \text{ cm}^2/\text{g}$ . An undensified type of microsilica, with a  $\text{SiO}_2$  content of 97%, was used for partial replacement of cement in some mixtures. A polycarboxylic ether type of superplasticizer and a set retarder that provides a workability time of up to 3 hours were used as admixtures. Crushed basalt with a specific gravity of  $3.0 \text{ g/cm}^3$  and river gravel with a specific gravity of  $2.60 \text{ g/cm}^3$  were sieved in size groups of 2-4 mm and 4-8 mm before use.

The mixing of the porous concrete was done following a very standardized procedure (which was established after numerous trials of different mixing techniques). In the mixtures containing both cement and microsilica, the binders were first mixed at the dry state in a high power food processor for five minutes prior to mixing with water. This was a critical and essential step in

order to eliminate the agglomerates in the microsilica. The usage of microsilica without dry mixing have shown unfavorable results due to the presence of agglomerates both in macro and meso-size samples, which was detected through both microscopy and CT scanning and will be presented in the following sections. In the preliminary porous concrete mixtures, it was seen that even though a long duration mixing is applied, the agglomerates of microsilica could not be eliminated without prior dry mixing of the binders. After dry mixing, the binders were mixed with water, the superplasticizer and the set retarder in a separate mixer for three minutes to make the cement paste. Subsequently, the cement paste was mixed with the aggregates in a third and larger size rotary mixer for three minutes.

The type of compaction technique used is very critical for modifying the porous concrete properties. In the current study, initially two compaction techniques were used, which were hand compaction using a steel cylinder and a special compaction technique using an impact hammer that moves in vertical direction and vibrates at the same time while it also rotated. In this compaction technique, also because the hammer end is covered with a layer of a soft type of rubber, the aggregate particles are arranged, which remarkably modifies the aggregate orientations and packing. Casting was done in thin layers where each 2.5 cm layer was compacted. The static strength of hand compacted samples was relatively low due to insufficient aggregate packing. Using the special compaction technique with an impact hammer, high strength values were obtained. Therefore, that compacting method was adopted as a part of the standard casting procedure. In both methods, some of the weak aggregates in river gravel fractured while no fracturing happened when basalt aggregates were used. Because the mixing and compacting procedures were time consuming, the use of a set retarder was essential.

The samples that are named “full concrete” (FC1 and FC2) were produced with the same amount and type of aggregates as in the porous concrete samples (PRC1 and PRC5) while the compaction was also applied in a similar way. After compaction, cement paste was added to the samples and the samples were further vibrated to remove the meso-scale air pores. These mixtures do not contain any fine aggregates and, therefore, their structure is also different from that of a normal concrete. The only difference between full and porous concretes was the higher amount of cement paste and consequently the lack meso-size air pores.

The same cement paste mixtures (plain cement paste and cement paste with 15 percent by mass cement replacement by microsilica) that were produced for making porous concretes (PRC1 and PRC5) were also used for making meso-scale composite specimens, with slightly higher amounts of superplasticizer. Consequently, ITZ properties as similar as possible to the porous concrete samples were aimed to be obtained. The same cement paste mixtures were also used for casting meso-size cement paste samples.

With the aim to design porous concretes having higher static strengths, various parameters of the mixture design and the production technique were evaluated by testing different types of porous concretes. Therefore, series of macro-scale deformation controlled compression and tension tests were conducted. According to the results obtained, it can generally be said that the grading, morphological and mechanical properties of the aggregates have a pronounced effect on the

properties of hardened porous concrete, because the coarse aggregates are dominant in the formation of the final material structure. Results of the mechanical tests of the selected representative mixtures are summarized in Table 3.2 at the end of (the macro-scale testing) section 3.3.2.2. It should be noted that while the tests of porous concrete mixtures were done mostly at the age of 28 days (later ages for leaching samples), full concrete specimens were tested at the age of 56 days.

### 3.3.2 Test Results for the Selected Porous Concrete Mixtures at Macro-scale

#### 3.3.2.1 Effect of Aggregate Properties and Compaction

Results showed that if two sizes of aggregates (2-4 and 4-8 mm) were used instead of single sized aggregates, both the compressive and the tensile strengths of porous concretes increased. PRC3 and PRC7, having aggregates of two sizes, are the mixtures that reached the highest strength values in the tests, i.e. 50.5 MPa and 48.8 MPa, respectively. This can be attributed to the fact that the grading including two aggregate sizes provides a better packing and lower porosities (18.8% and 18.6%, respectively), which contributes to the strengths of the mixtures irrespective of the changes in cement paste composition. Therefore, aggregate grading, that also determines the total porosity, is the main factor that affects the strength which was also found in the numerical analyses in Chapter 5. This can be explained by the particles having varying sizes being more densely packed. When compaction is applied, particles of different sizes pack even more densely as small particles flow better into the voids between larger ones.

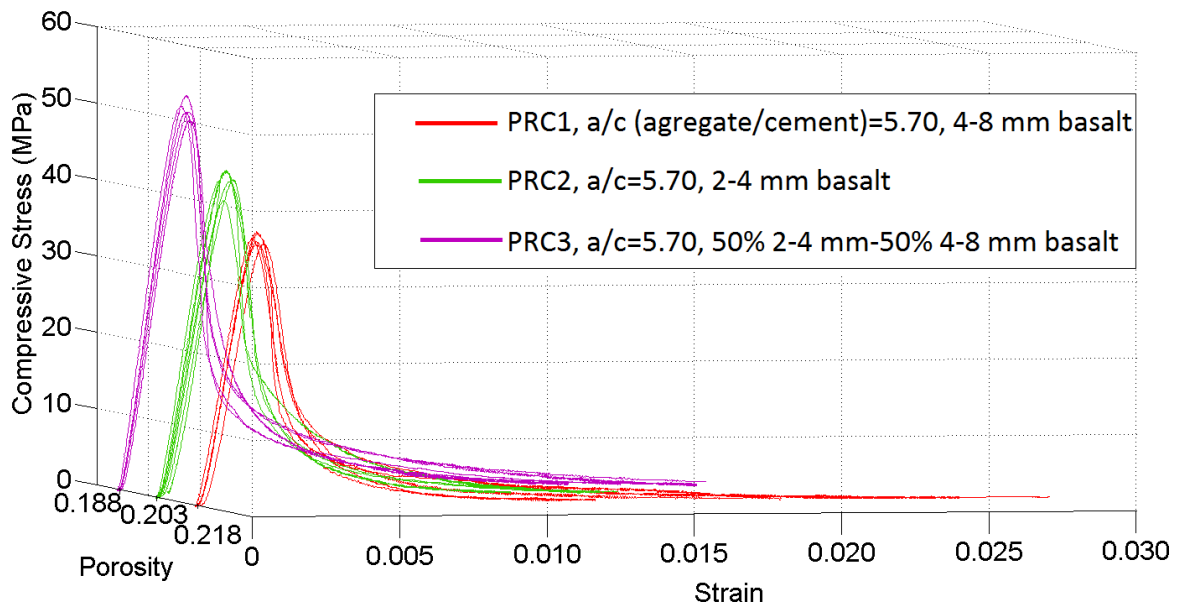


Figure 3.9 Representative compressive stress-strain curves of mixtures with different aggregate gradings



In Figure 3.9, the representative compressive stress-strain curves of different mixtures with the same aggregate/cement ratios, varying only in aggregate grading, are presented in terms of their compressive strengths and porosities. The figure clearly shows that aggregate grading determines the porosity in a porous concrete mixture which dominantly affects the strength of the material. Tensile test results exhibit the same trend as seen in Figure 3.10.

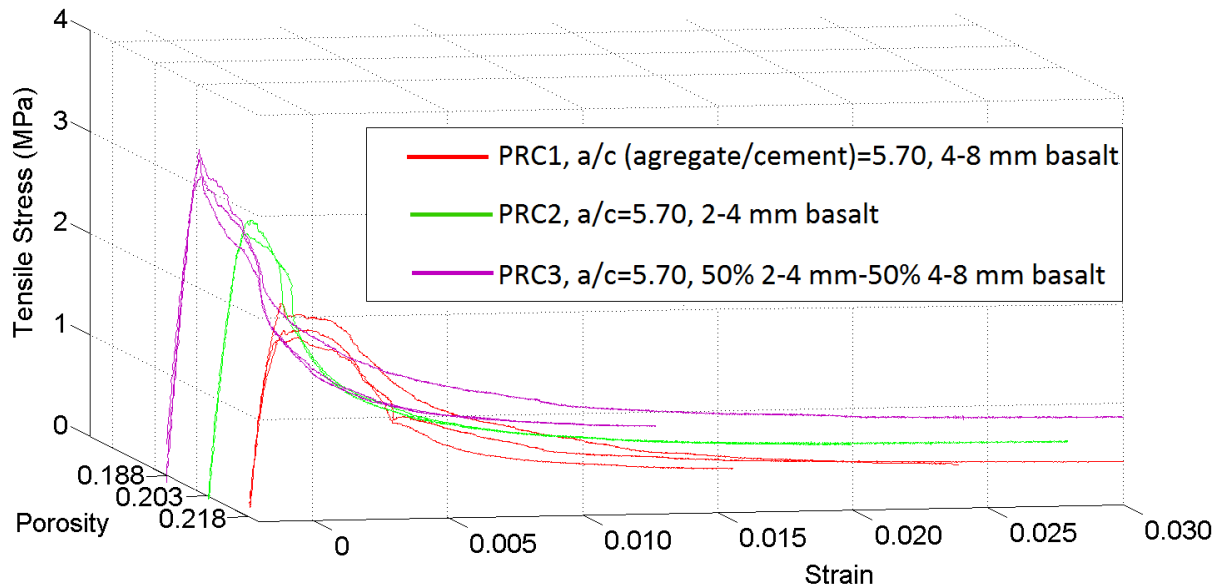


Figure 3.10 Representative tensile stress-strain curves of mixtures with different aggregate gradings

When the compressive strengths of mixtures PRC1 and PRC2 (or PRC5 and PRC6) having single size range aggregates at different sizes (either 4-8 mm or 2-4 mm) are compared, it can be said that as the aggregate size decreases (from 4-8 mm to 2-4 mm) the strengths increase. When the porosity values of the mixtures are compared, it is seen that the porosities of mono-sized aggregate mixtures are almost the same, irrespective of the aggregate size. Therefore, the increase in strengths can be explained by the increase in contact or bonding areas with decreasing size of the aggregates (this trend however could not be seen in the numerical results, which will be presented in Chapter 5) and a better interlocking of smaller irregularly shaped, crushed particles.

The mixtures PRC1 and PRC4 have the same mixture compositions except that river gravel was used in PRC4 instead of crushed basalt. River gravel tends to have a more equi-dimensional and rounded shape compared to crushed basalt having a more elongated and angular shape. Crushed basalt aggregates not only have irregular shapes, but also have a rough texture. Due to these differences in shape and texture, the river gravel facilitates a better packing. Therefore, mixtures incorporating river gravel (PRC4) have a 17.9 % porosity, which is lower than those of the mixtures with basalt. On the contrary, a rough texture and high angularity contribute to porous

concrete strength due to enhanced mechanical interlock, increased total surface area and increased contact points. As it will be explained in section 3.3.3 on meso-scale testing, the different mineralogical types of rocks present in river gravel also have very different levels of adherence to cement paste. While there are particles that have very weak bonds with the matrix, there are also particles that have very strong bonds with cement paste. As a result of all the factors present, PRC4 containing river gravel had lower strength than mixtures with the same composition, but containing crushed aggregate, as seen in Figure 3.11. It should also be noted that some of the different types of aggregates present in river gravel blend have very low strengths themselves such that they fracture and break into pieces during the compaction process already, which also surely affects the performance of the concrete produced with those aggregates. This was not a concern for basalt aggregates.

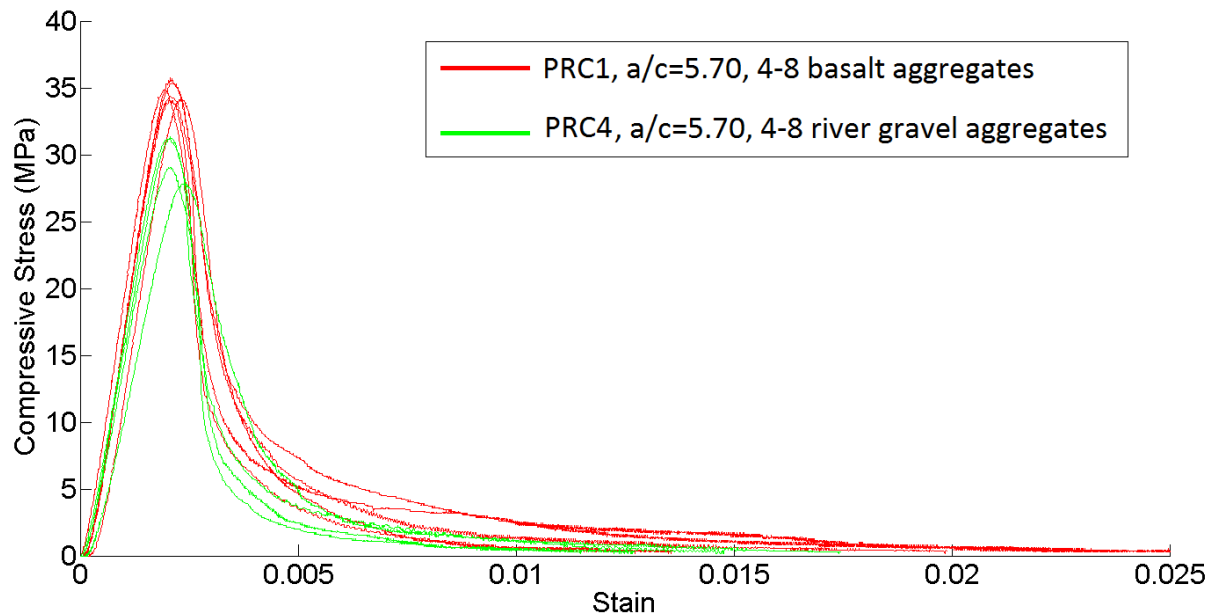


Figure 3.11 Representative compressive stress-strain curves of mixtures with crushed and gravel aggregates

It should also be mentioned that in the preliminary porous concrete mixtures produced, where the compaction was performed through hand compaction using a steel hammer, compressive strengths up to 20 MPa were obtained. With special machine compaction using an impact hammer, the strength values were drastically increased to values in the range of 35-55 MPa. This can be seen in Table 3.2, which shows that machine compaction in thin layers is strongly required in making porous concrete with enhanced mechanical properties.

### 3.3.2.2 Effect of Cement Paste Composition and Amount

While aggregate properties were dominantly affecting the porous concrete properties, the effect of changing the cement paste composition by adding microsilica did not have a very significant

effect. The representative compressive stress-strain curves of different mixtures with different microsilica contents are presented in Figure 3.12. In the figure, all mixtures contained the same amount of basalt aggregates. The grading of the aggregates, on the other hand, were 4-8 mm, 2-4 mm or 50% 4-8mm-50% 2-4 mm from top to bottom. In each graph, the red curves show the mixtures containing only cement as a binder while the black ones show the mixtures with 15% replacement by microsilica.

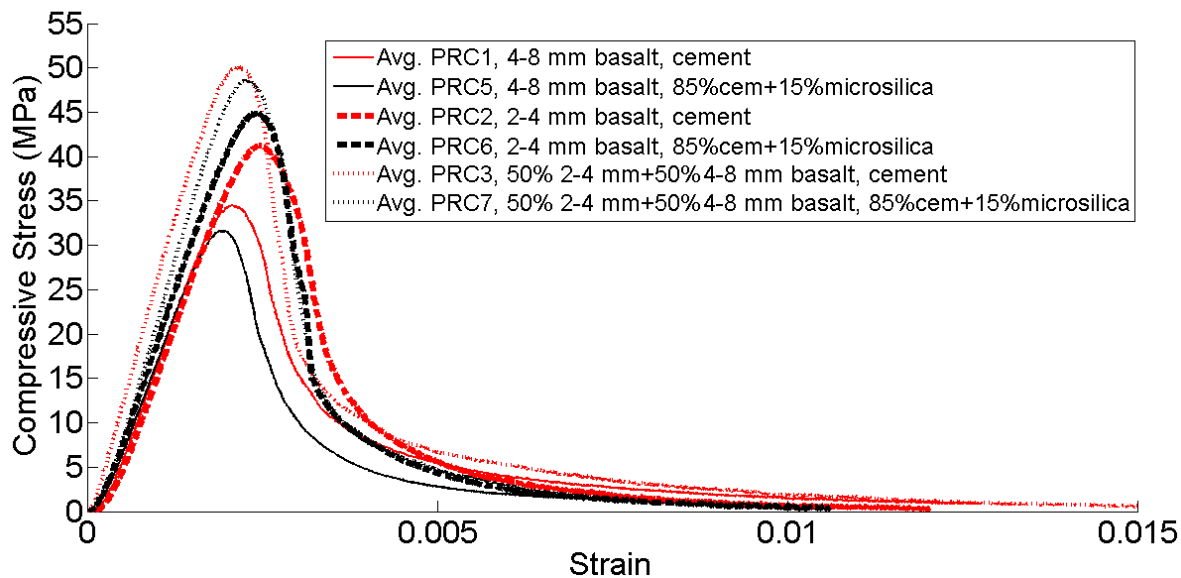


Figure 3.12 Average compressive stress-strain curves for the effect of microsilica on porous concretes having aggregates of different grading

Replacing 15 percent by mass of cement by microsilica did not enhance and even slightly decreased the strengths of most of the porous concrete mixtures, even though dry mixing was applied to the binders (dry mixing to eliminate agglomeration). Similarly, in full concretes it did not increase the strength. The total amount of ITZ present in porous concrete mixtures (and in the full concretes, FC1 and FC2), that include only 4-8 mm coarse aggregates and no fine aggregates, is very low compared to normal concrete. Microsilica, which is generally known to improve the ITZ properties in normal concrete, may, therefore, not have a strong effect on porous concretes. While the strengths of mixtures with microsilica were generally a little lower, for mixtures PRC2 and PRC6 a small increase in strength was observed. The probable reasons for this are also presented in the calculated tomography observations, presented in the chapter explaining the fracture patterns of porous concretes. In those patterns, cracks tend to go more through the ITZ when the aggregates are finer while they have more tendency to go through the aggregates as the aggregates are very coarse. It can be said that microsilica, that densifies the ITZ and improves its mechanical properties, has a small strength improving effect on porous concretes with finer aggregates while it does not have that effect when the aggregates are coarser. When the tensile strengths of porous concretes with 2-4 mm basalt aggregates, with and

without microsilica (PRC2 and PRC6) are compared, as shown in Figure 3.13, it can be seen that the results are very close and no significant effect of microsilica is evident.

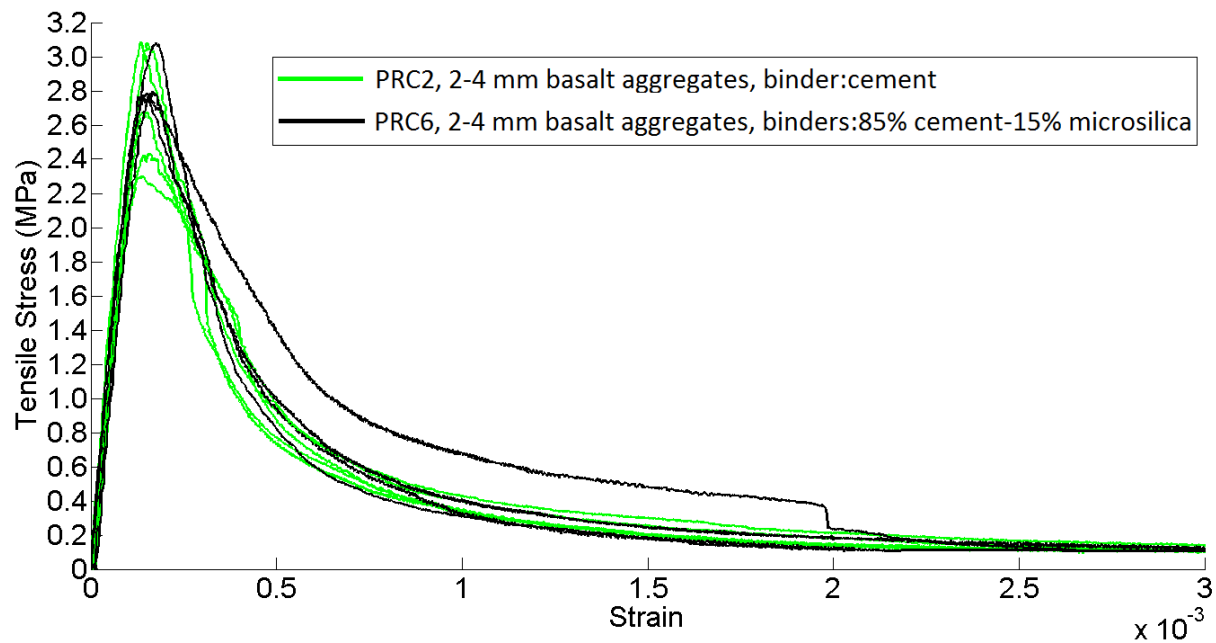


Figure 3.13 Representative tensile stress-strain curves for the effect of microsilica on porous concretes with 2-4 mm basalt aggregates

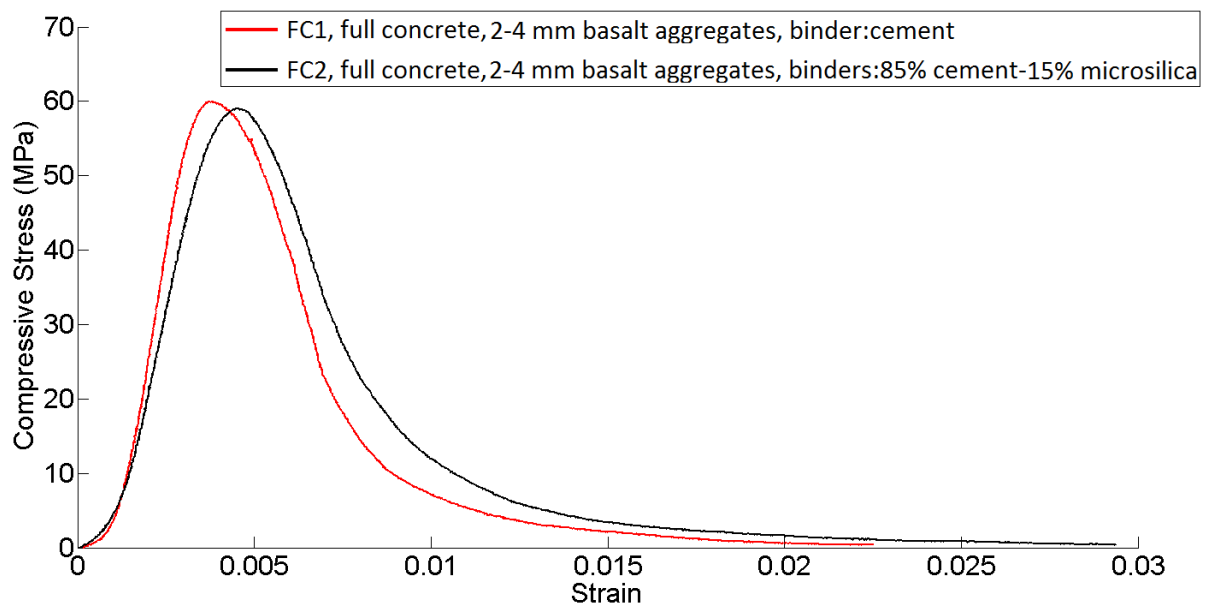


Figure 3.14 Representative compressive stress-strain curves for the effect of microsilica on full concretes

The behaviors of full concretes with and without microsilica under compressive loading are presented in Figure 3.14. The full samples with microsilica showed approximately the same strength. The difference in strength is not significant and too small to see a trend of increasing strength with the inclusion of microsilica.

Mixture PRC11, having the same composition as PRC1, except a lower amount of cement paste, was produced to see whether similar strength properties can also be reached with a reduced amount of cement paste. The results showed that the amount of cement paste that is present in the mixtures is also critical. Decreasing it significantly lowers the strength down to 24.6 MPa, while increasing it too much causes the accumulation of cement paste at the bottom part of the samples during compaction, even when an appropriate viscosity of cement paste is attained.

Macro-scale tests were also conducted on cement paste samples of 55 mm diameter and 70 mm height to provide information on the compressive behavior of the bulk cement paste phases of porous concrete specimens with and without microsilica. The compressive strengths of cement pastes with and without 15 percent microsilica were 112.2 and 111.8 MPa, respectively.

Visualizing the structure and the crack patterns of porous concrete using the Computed Tomography (CT) images of the specimens that have partially fractured under uni-axial compression gives us a better insight in how the material behaves. For that purpose, the specimens, that were loaded in uni-axial compression and unloaded after the peak, were visually inspected. In porous concrete, it is expected that stress concentrations form at the contact locations between the aggregate particles like in normal concrete. Because there are no fine aggregates present, there is a relatively small number of aggregates present. Therefore, the amount of contact regions around each aggregate compared to the complete aggregate surface is much lower than in normal concrete.

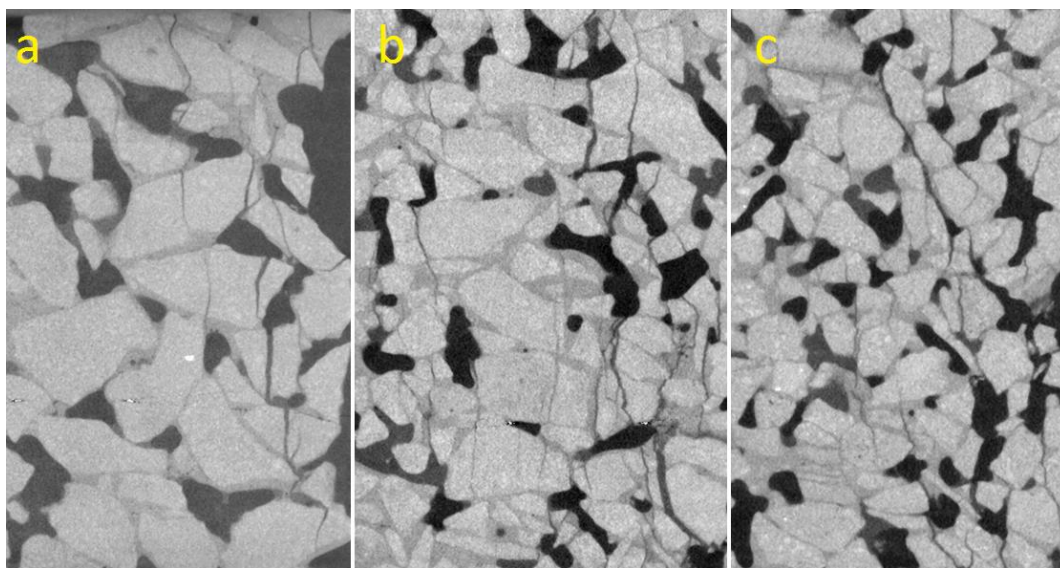


Figure 3.15 CT images of partially fractured porous concretes having different aggregate gradings a) PRC1, 4-8mm basalt, b) PRC3, 50% 2-4mm-50% 4-8mm, c) PRC2 2-4mm basalt

The sections of samples that are shown in Figure 3.15 were taken from the outer mid-height region of the specimens, approximately from the same location of each sample in order to make a better comparison. The three images show the samples from mixtures PRC1, PRC3 and PRC2. They are from porous concretes having the same cement paste properties with the only difference of including 4-8 mm aggregates, 50% 2-4 mm - 50% 4-8 mm aggregates or 2-4 mm aggregates, respectively. The partially cracked sections of the specimens reveal that the crack patterns caused by compressive loading are usually tensile cracks parallel to the direction of loading. Subsequent shear cones underneath the aggregates are observed as in normal concrete. As a general observation for the whole specimens, shear cracks formed close to the ends of the samples due to the frictional forces generated at the boundaries with the loading plates were also typical. However, different from normal concretes, the crack patterns are very much influenced by the distinct porous structure where the cracks are forced to propagate into locations guided by the geometry of the skeleton structure. Because there is only a very small portion of ITZ and bulk cement paste connecting the aggregates, the cracks have to propagate according to the geometry of the phases that are physically present. Cracks also initiate from the poles of pores because of the tensile stress concentrations at those locations. Because the cement paste bridges that bind coarse aggregates are very thin, those numerous weak bridges tend to fail as well. This also makes its ultimate behavior different from normal concrete. From the images in Figure 3.15, the reasons behind the macro-scale test results can be understood better. When the mixtures with coarse and relatively finer mono-sized aggregates are compared, it can be seen that in the porous concrete with finer aggregates (Figure 3.15 c) the cracks go through the ITZ more than they do in the coarse aggregate one (Figure 3.15 a). The tendency is surely to go through the path with the lowest resistance. However, when a crack meets with a very coarse aggregate it goes through it rather than the whole distance around it. Even though cracks initiating from ITZ are commonly expected, the propagation of cracks varies according to the aggregate grading and the local pore structure. Cracks tending to go more through the ITZ when aggregates are fine may also help to explain the effect of microsilica on the strength of the porous concretes. Microsilica, that is known to increase the strength of ITZ, had a small effect on the strength of porous concretes with finer aggregates, while it does not have such an effect on the mixtures with coarser aggregates. The total volume of ITZ, being smaller in coarse aggregate mixtures, is also another reason for the effect of microsilica being insignificant in such mixtures.

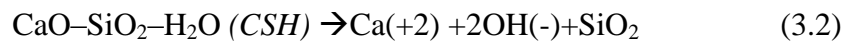
Table 3.2 Summary of the static mechanical tests results of selected representative mixtures

Mixture code	Compressive strength (MPa)	Meso-scale Porosity (%)	Tensile strength (MPa)	Young's Modulus (MPa)	Fracture energy (N/m)
PRC1	34.8	21.8	1.91	23413	105.1
PRC2	41.9	20.3	2.73	26644	110.0
PRC3	50.5	18.8	2.95	32177	110.3
PRC4	29.6	17.9	1.98	24841	115.4
PRC5	31.6	22.0	1.85	23361	101.2
PRC6	44.8	20.1	2.80	26487	120.3
PRC7	48.8	18.6	2.67	29605	107.0
PRC8	15.9	-	-	-	-
PRC9	13.1	-	-	-	-
PRC10	21.7	-	-	-	-
PRC11	24.6	26.7	1.69	22791	96.7
FC1	61.1	0	3.51	30117	163.7
FC2	59.3	0	3.08	27908	181.6

### 3.3.2.3 Effect of Water Curing and Leaching

In the preliminary mechanical tests conducted on porous concrete samples that have been cured in water, unexpectedly unfavorable results were obtained. The curing process, which has since long been widely known to enhance the mechanical properties, works in the opposite direction and causes a decrease in both compressive and tensile strengths and drastically reduces the stiffness. This will be demonstrated in the following test results. After making some microscopical observations, it was found that the change in mechanical behavior was caused by the leaching of ions from the cement paste matrix into the curing water. Calcium ion leaching, which also occurs in normal concretes, was exceptionally influential in case of porous concretes due to their large external surface areas accessible for water.

When a cement based material is placed in distilled (or tap) water, the large concentration gradients between the pore solution within cement paste and the tap water cause the diffusion of free ions from the pore solution to the surrounding curing water. Such a movement drastically affects the chemical equilibrium that exists between the main hydrates ( $\text{Ca(OH)}_2$  and CSH) in cementitious materials and the free ions from these components in the pore solution (Carde and François 1999, Wee et al. 2001).



If the concentrations of calcium ( $\text{Ca}^{+2}$ ) or hydroxyl ( $\text{OH}^{-1}$ ) ions in the pore solution decrease, the chemical equilibrium (3.1) shifts to the right and the dissolution of  $\text{Ca}(\text{OH})_2$  occurs, thus supplying additional  $\text{Ca}^{+2}$  or  $\text{OH}^{-}$  to maintain the equilibrium. Upon the complete dissolution of  $\text{Ca}(\text{OH})_2$ ,  $\text{Ca}^{+2}$  from CSH begins to dissolve causing the degradation of CSH into silica gel ( $\text{SiO}_2$ ) (Wee et al. 2001).

Leaching in cement based materials and its effects on their mechanical and physical properties have been investigated by several researchers (Wee et al. 2001, Carde and François 1997). In those studies, which mainly concentrate on the leaching of  $\text{Ca}^{2+}$  ions from  $\text{Ca}(\text{OH})_2$  and the progressive decalcification of CSH, it is emphasized that the peripheral degraded zone that has gone through leaching becomes more porous than the bulk sample. In leaching studies, it is usually assumed that the decalcification process leads to the development of two separated zones; a peripheral zone, which is degraded, and the bulk zone, which is still sound. This was also observed in the ESEM images of porous concrete samples that have gone through leaching as presented below in Figure 3.21 and Figure 3.22. In a literature study, the compressive stress-longitudinal strain behavior of constant diameter samples that have gone through leaching were analyzed.  $\text{Ca}^{+2}$  ions are monitored by microprobe analysis, which allows to plot the calcium profile along the samples (residual calcium content in solid phase), and the removal of  $\text{Ca}(\text{OH})_2$  is confirmed by the plot of XRD (Cobalt radiation) curves at different depths. By using these techniques, the area of peripheral degraded zone is calculated using the degraded thickness, which is measured from the edge of the cylindrical samples (with 10 mm diameter/20 mm height), exposed to leaching. In Figure 3.16, the stress-strain curves obtained are presented based on the ratio of the peripheral degraded area ( $A_d$ ) over the total area  $A_t$  of the sample (Carde and François 1997). The curves show that the behavior of the material becomes more plastic as a result of the degradation process. The increase in the degraded ratio  $A_d/A_t$  corresponds to a decrease in strength as well as a significant increase in the ductility.

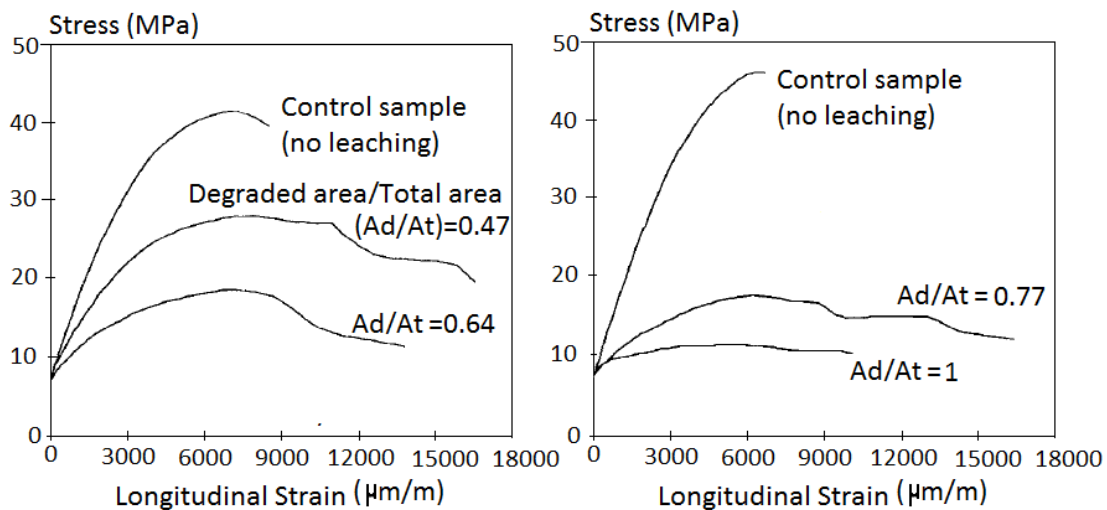


Figure 3.16 Compressive behavior of 10 mm diameter/20 mm height cylindrical samples that have gone through  $\text{Ca}^{2+}$  leaching (Carde and François 1997)



In a study where the leaching of cement paste samples with and without microsilica were compared, the results revealed that in pure pastes, the dissolution of the calcium hydroxide was the reason for sometimes very high reductions in strength. Meanwhile, for such samples, the decalcification of CSH has less effect on the mechanical properties. In pastes containing microsilica in which much less calcium hydroxide is present, the decalcification of CSH is the main mechanism (Carde and François 1999). In another study it was again shown that the dissolution of  $\text{Ca(OH)}_2$  generally occurs more easily, while decalcification of CSH only occurs when  $\text{Ca(OH)}_2$  is inaccessible or locally depleted (Chen et al. 2006).

In the uniaxial compressive tests that have been applied on the preliminarily produced porous concretes in this current research (4-8 mm aggregates, no microsilica,  $w/c=0.30$ , aggregate/cement=6, hand compacted, no set retarder), it was seen that curing in water for 40 days had detrimental effects on the mechanical behavior. If the graphs given at the top (not cured, kept in open air) and bottom (water cured) of Figure 3.17 are compared, it can be seen that both the peak strength and the stiffness of the material are negatively affected by water curing.

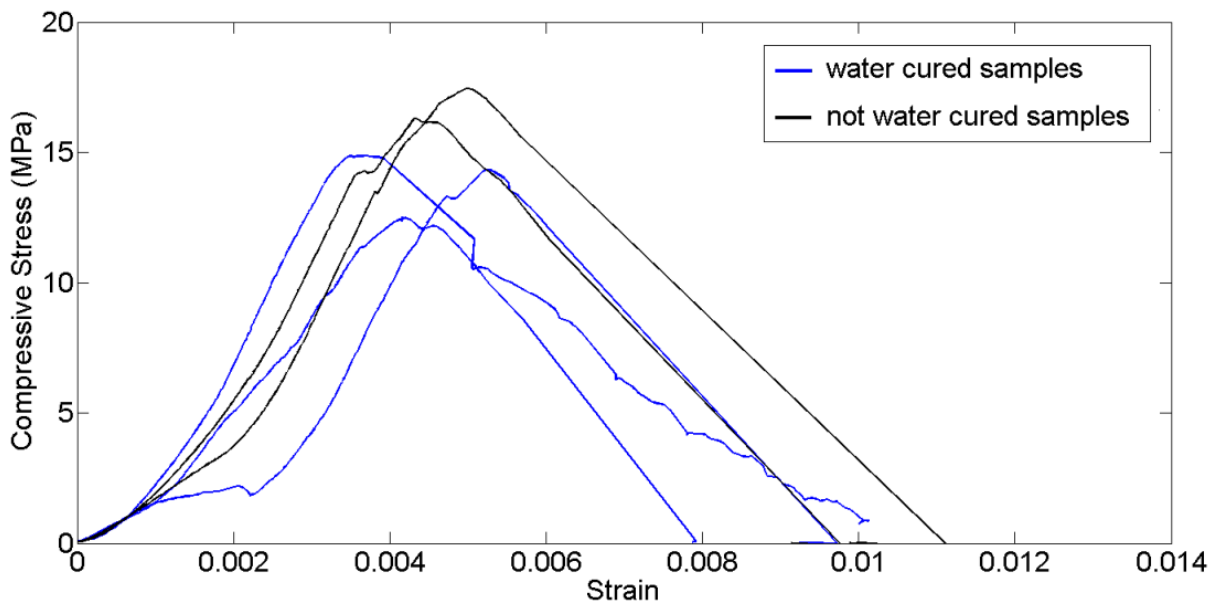


Figure 3.17 Compressive behavior of porous concrete samples that were a) not cured, kept in open air and b) water-cured

The effect of water curing is even more pronounced when the amount of cement paste in the mixture is lower. An example of this can be seen in Figure 3.18 where preliminary porous concretes (4-8 mm aggregates,  $w/c=0.30$ , aggregate/cement=8, hand compacted) at 40 days (a) without and (b) with water curing are shown.

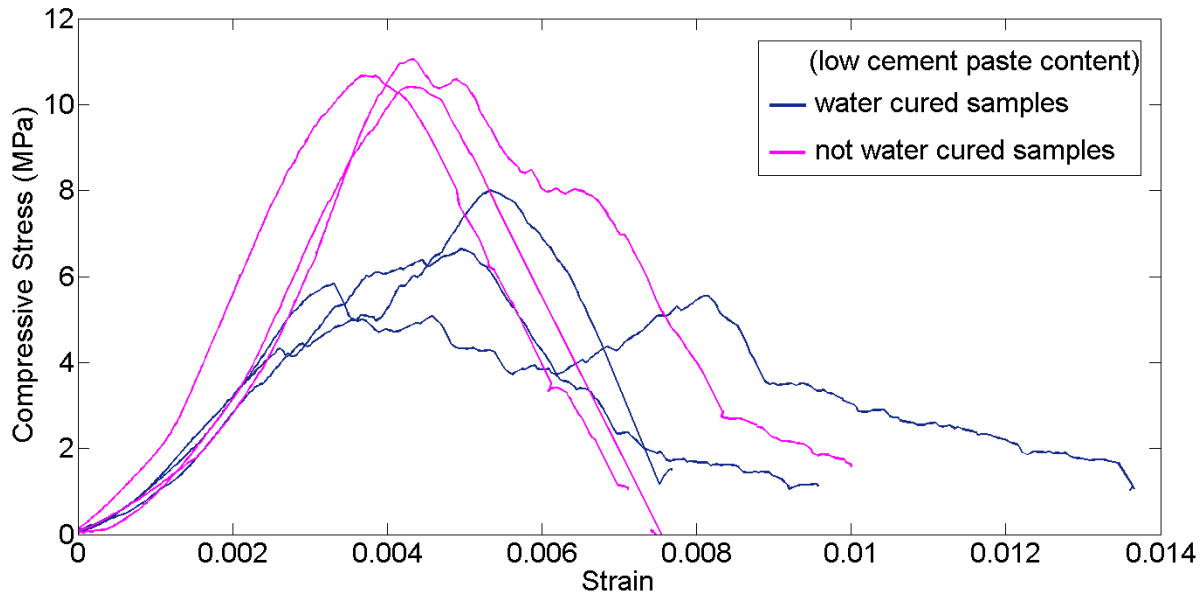


Figure 3.18 Compressive behavior of porous concrete samples (with lower cement paste content) that were a) not cured, kept in open air and b) water-cured

In samples that also contain microsilica (4-8 mm aggregates, with microsilica,  $w/c=0.30$ , aggregate/cement=6, hand compacted, with set retarder), at the end of 56 days of water curing, a similar trend is observed both in terms of peak strengths and the stiffnesses, as can be seen in Figure 3.19.

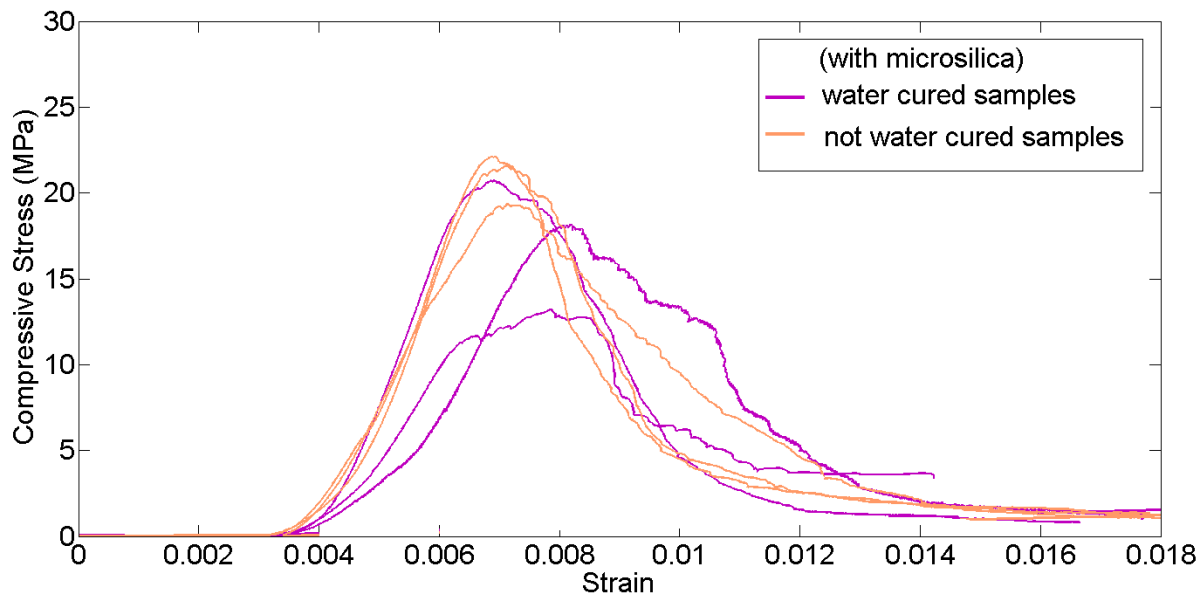


Figure 3.19 Compressive behavior of porous concrete samples (with microsilica) that were a) not cured, kept in open air and b) water-cured

For the machine compacted and higher strength porous mixtures such as PRC1 (see Table 3.1), the unfavorable effects of water curing are less. In these specimens, the leaching of  $\text{Ca}^{2+}$  ions from the outer surface of the sample is less compared to the hand compacted samples or the samples containing less cement paste. Consequently, the samples that have gone through water curing performed similar to the ones that are not cured in water as seen in Figure 3.20.

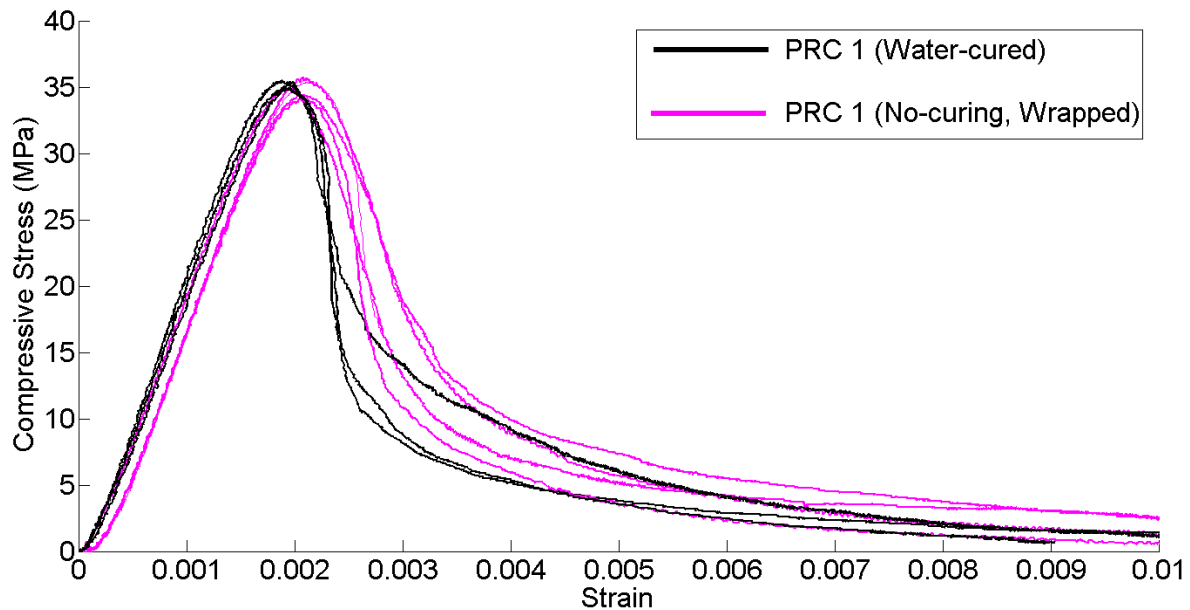


Figure 3.20 Compressive behavior of machine compacted porous concrete samples with and without water curing

When the samples that have gone through water curing were investigated using ESEM, the effects of leaching could clearly be detected. In the analyses, samples that were prepared by taking sections from the macro-scale concrete specimens (Figures 3.21 and 3.22) were polished. The outer surfaces of the samples that have gone through leaching (Figure 3.23) were not polished, not to lose the delicate formations that existed on those surfaces. No coating was applied to the samples.

The samples cured in water for about 40 days, showed clear signs of calcium ion leaching at the vicinity of the pores that are accessible for water (Figure 3.21). The top figure shows a sample from a porous concrete containing only cement as the binder. The bottom figure is from a specimen that contains 15 % microsilica.

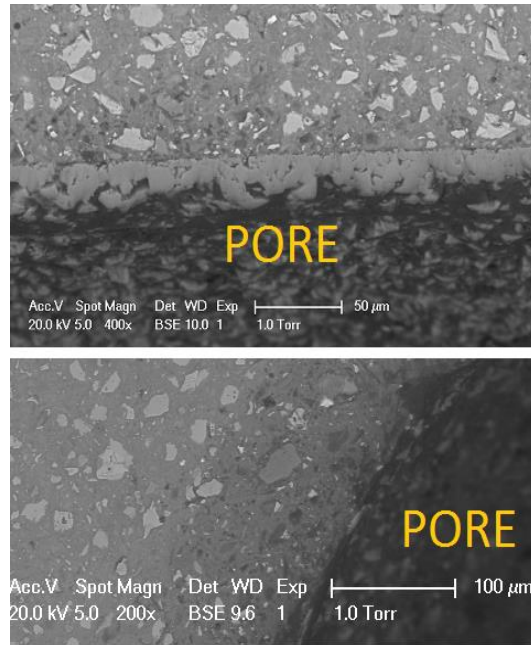


Figure 3.21 ESEM images of porous concrete samples without (top) and with microsilica (bottom) showing signs of Ca leaching

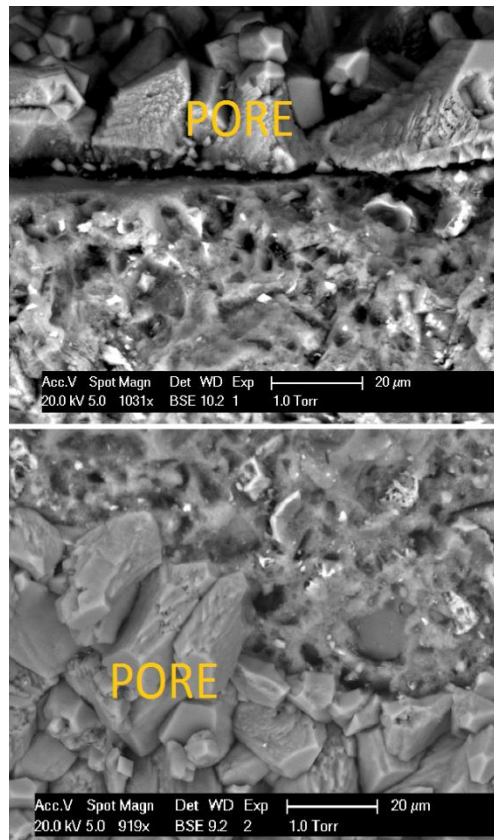


Figure 3.22 ESEM images of porous concrete samples without (top) and with microsilica (bottom) showing signs of Ca leaching

Figure 3.22 presents samples from two mixtures with (bottom image) and without (top image) microsilica that had been kept in tap water for about 70 days. In all the images, the change into a more porous cement paste structure is clearly seen. In this figure, the crystals that have formed and accumulated on the concrete surface due to leaching and subsequently the carbonation of the calcium hydroxide, which is a well-known and widely investigated reaction, can also be seen (Lamond and Pielert 2006). These crystals formed on the outside surface of the pores are more clearly demonstrated in Figure 3.23.

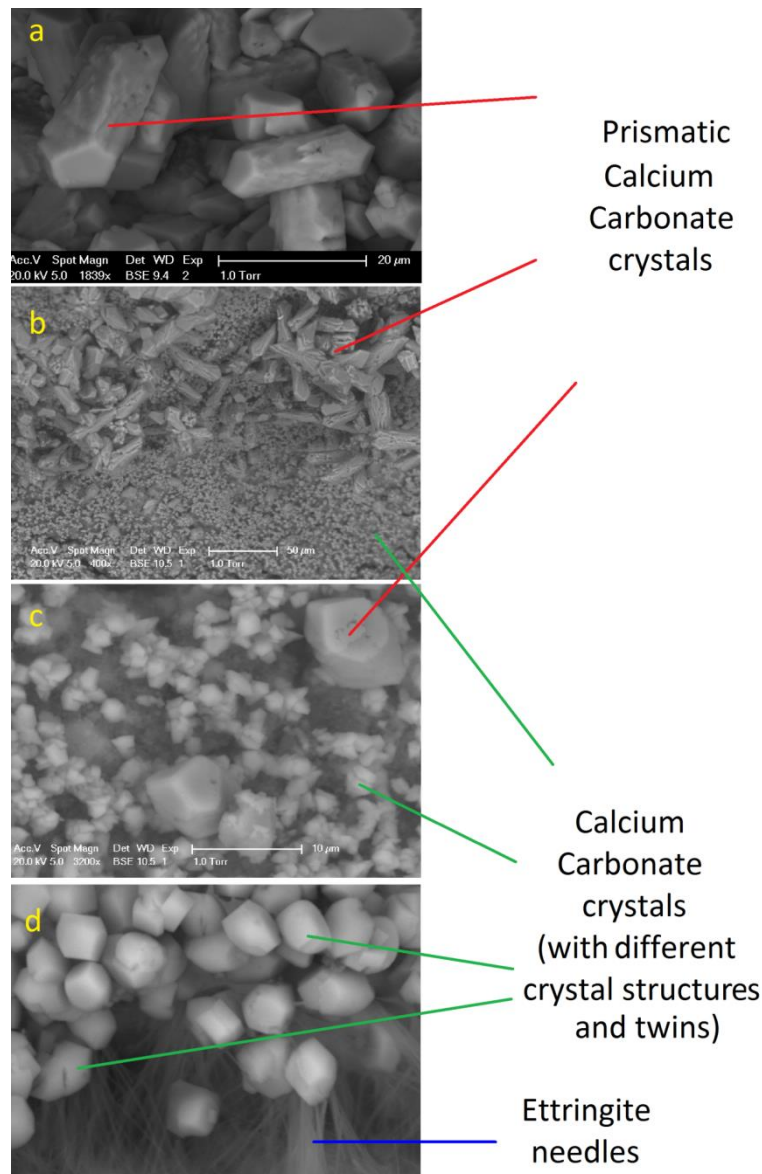


Figure 3.23 Formations observed on the surfaces of porous concrete samples that had gone through Ca leaching

The images of the outer surfaces of porous concrete samples acquired using ESEM are given in Figure 3.23. In the images, the different types of crystals that are observed are mainly the products of the carbonation reaction of Calcium hydroxide that had leached from and precipitated on the surface of the porous concrete samples. Even though it was not possible to quantify them, during the ESEM analyses it was observed that when the amount of crystals that have precipitated on the samples increased, the mechanical properties of the samples were more drastically affected. These precipitates are mainly calcium carbonate and ettringite crystals. Crystals of calcium carbonate show a wide variety of shapes. They usually exist as combinations of some main crystal forms such as prismatic, scalenohedral, pinacoid etc., as well as corresponding twinned forms (Britannica 2015). Different forms of calcium carbonate (as also seen in images a and b from literature in Figure 3.24) can clearly be observed in the ESEM images in Figure 3.23. In the images, the larger precipitates formed on the surfaces of the porous concrete samples, as in (a) and (b) and partly in (c) of Figure 3.23 can be identified as prismatic calcium carbonate crystals (Mineral shows website 2009). The smaller crystals, seen in (c) and (d) of the images are more similar to Figure 3.24(c), which is a combination of a rhombohedron and a pinacoid type of calcium carbonate (Britannica 2015). Several of such crystals can be observed to co-exist as twinned crystals, as also seen in Figure 3.24(d) (Crystalclassics website 2007). In the last image of Figure 3.23, the ettringite needles that have precipitated on the concrete surface can also be identified. The presence of ettringite in the images can be explained by sulphates being very frequently found in natural water. The reaction of sulphur ions with the products of cement hydration principally leads to ettringite. The solubility of ettringite in water depends on various factors such as the concentration of  $\text{Ca(OH)}_2$ . If the concentration of  $\text{Ca(OH)}_2$  in the solution is high, the solubility of ettringite decreases and crystals start to form and accumulate on the concrete surface and inside the pores. This is the case with the curing water of porous concretes that contains a high concentration of leached  $\text{Ca(OH)}_2$ . Thus, the secondary ettringite forms in the water involved in leaching (Walker 1992, Cerny and Rovnanikova 2002).

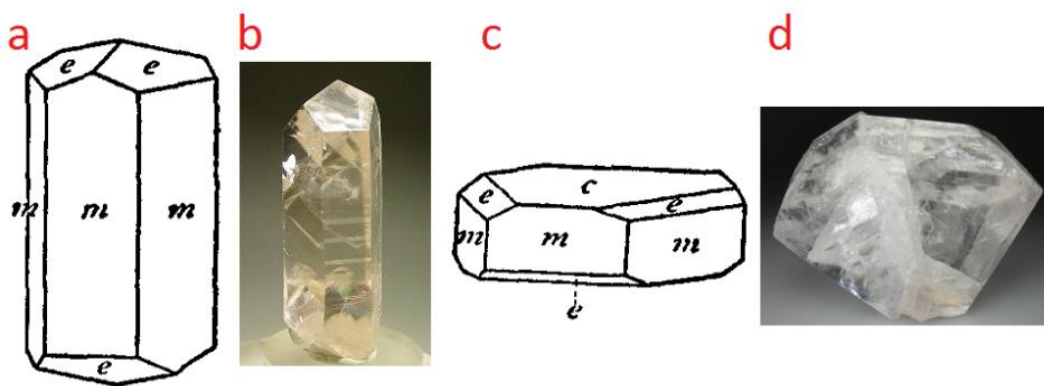


Figure 3.24 Different forms of calcium carbonate crystals (Britannica 2015, Mineral shows 2009, Crystal classics 2007)



### 3.3.3 Meso-scale Tests Results and the Complementary Analyses

The meso-scale tests were conducted using a micro tension-compression testing device (by Kammrath & Weiss) with a 50 N load cell. Closed loop displacement controlled meso-scale tests were conducted on composite samples consisting of aggregate (either basalt (Figure 3.25(b)) or different types of river gravel (Figure 3.25(c)), cement paste and the ITZ phase, and on meso-size cement paste samples (Figure 3.25(a)). The composite samples were especially required to be able to better understand how the ITZ phase of porous concrete behaves. The tests were performed to investigate the load displacement data of the ITZ phase under uni-axial tension while the testing was done at the loading rate of 0.1  $\mu\text{m}/\text{sec}$ , which was the same as the loading rate at the macro-scale tension tests. In the composite samples, two types of cement pastes with and without 15 % microsilica were used, as in the macro-size samples.

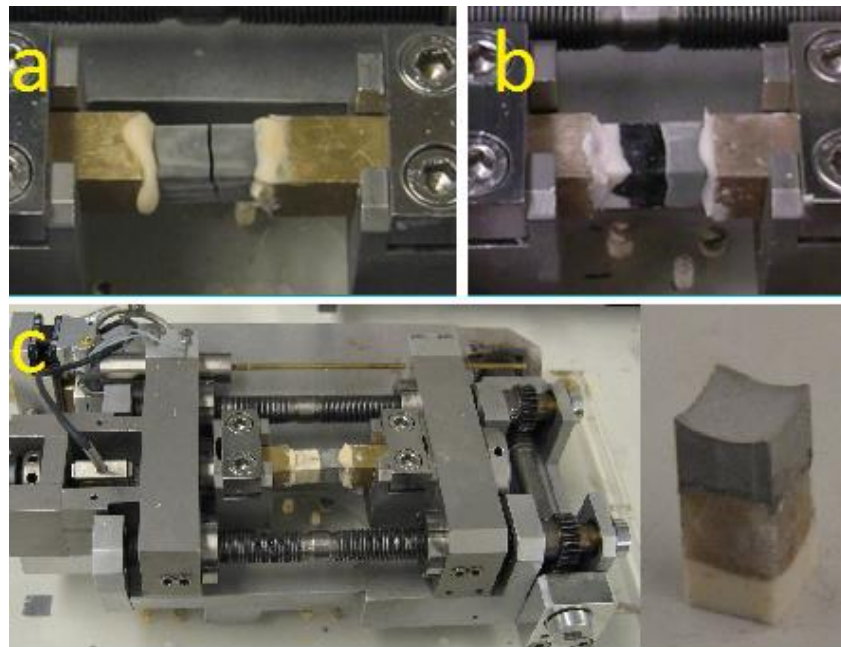


Figure 3.25 Meso-scale (a) cement paste sample , (b) composite ITZ sample with basalt and (c) composite ITZ samples with different types of river gravels

In all the composite ITZ samples tested, the failure occurred in the immediate vicinity of the aggregate, which showed that the failure happened at the ITZ. Therefore, the peak load that is measured can be used to determine the tensile strength of the ITZ phase. Acquisition of the complete load-displacement response was not possible during testing because of the snap-back behavior immediately after the peak. Therefore, the descending branch could not be captured. Representative meso-scale ITZ tensile test graphs of composite samples consisting of plain cement paste-basalt aggregate are presented in Figure 3.26. A mean ITZ tensile or bond strength of 0.95 MPa was found in the tests of plain cement paste-basalt aggregate samples. Because the composite aggregates used in the samples had different heights and contained different amounts of glue at their base, the results of the tests are presented separately. It should be noted that

meso-scale testing is very challenging in the sense that the sample can sometimes be damaged during demolding or gluing to the testing device before testing due to its very small size. While a high number of basalt ITZ samples with and without silica fume were tested, for a few types of gravel samples with weak ITZ phases, two or three successful tests could be conducted.

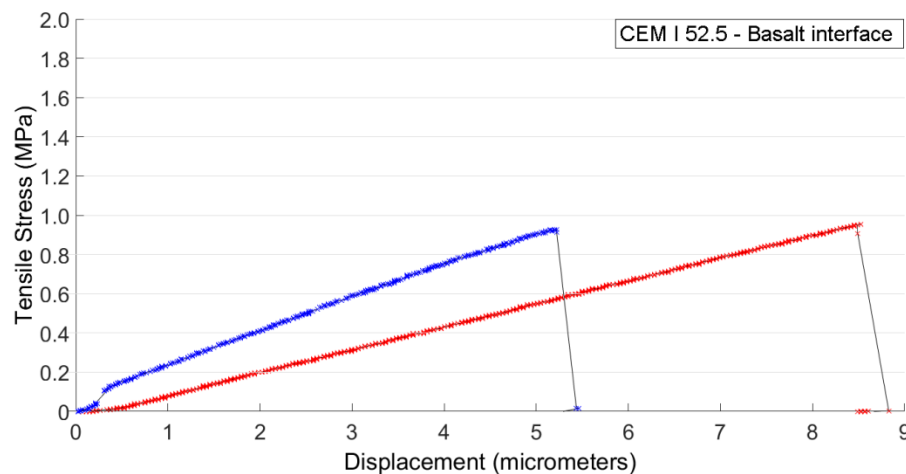


Figure 3.26 Two representative meso-scale ITZ test results of plain cement paste-basalt aggregate

When 15% by mass of cement is replaced by microsilica, the strength values increased as can be seen by comparing Figure 3.26 and Figure 3.27. As in the mixtures produced for macro-scale samples containing both cement and microsilica, the binders were first dry mixed in a separate mixer for mixing powders to eliminate agglomeration of the microsilica. The samples containing 15 percent microsilica provided a mean bond strength value of 1.3 MPa. A clear increase of bond strength was found in the results for samples containing microsilica. This information can also be used to better interpret the macro-scale porous concrete data. They showed that the ITZ phase is not the reason for no increase and sometimes even a slight decrease in the compressive and tensile strengths of coarse aggregate porous concretes with microsilica.

As explained in detail in section 3.3.2.1., the behavior of porous concrete is dominated by its aggregate grading. Cracks tend to go more through the ITZ when the aggregates are finer while they have more tendency to go through the aggregates when the aggregates are coarse. It can be said that microsilica, that densifies the ITZ and improves its mechanical properties, has a slight strength improving effect on porous concretes with finer aggregates while it does not have that effect when the aggregates are coarser.



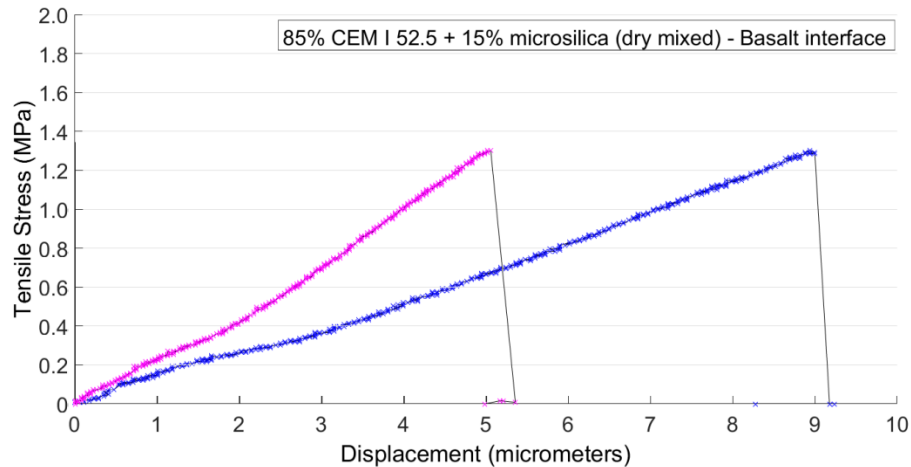


Figure 3.27 Representative meso-scale ITZ test results of (dry mixed) cement paste with 15 percent microsilica-basalt aggregate

It should also be noted that composite samples containing 15 percent microsilica, that were produced without dry binder mixing prior to wet mixing, were also tested. In those samples the bond strength was found to be on average 1.05 MPa, which is lower than the strength obtained when dry mixing is applied. The physical explanation for this is the formation of microsilica agglomerates. These agglomerates were detected in CT scans, as shown in Figure 3.28. Apparently, the large agglomerates also disrupt the packing of the cement grains causing the formation of a zone adjacent to the agglomerate which is more porous due to the deficit of cement grains. Due to the presence of more porosity, the agglomerates are seen as relatively darker spots even though microsilica (having a density of about  $2.2 \text{ g/cm}^3$ ) itself has a higher density compared to hardened cement paste (which has a density of about  $1.9 \text{ g/cm}^3$  for the w/c ratio of 0.3) (Lamond and Pielert 2006). If the color of those spots are compared with the air pores present in the glue layer at the bottom part of the sample (CT images in Figure 3.28), it is also seen that the spots in the cement paste are much lighter in color. Therefore, they are actually not air pores themselves, but agglomerates that are surrounded by a zone of high porosity.

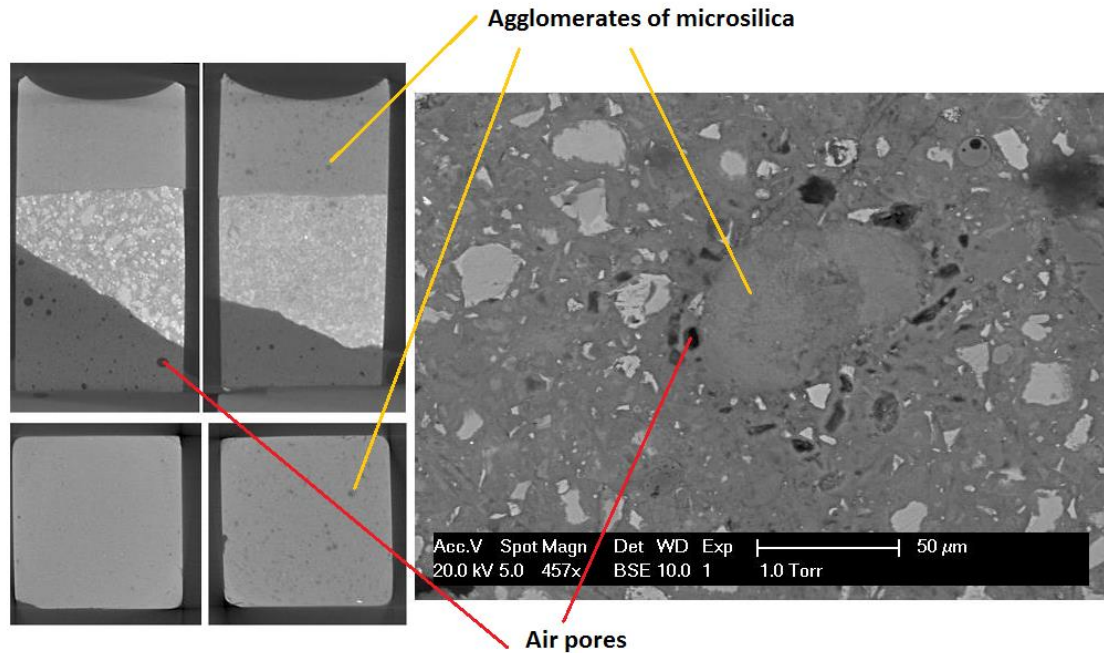


Figure 3.28 CT images of composite samples with and without agglomerates and an ESEM image from a macro-scale porous concrete sample containing agglomerates

The agglomerates break down only partially during wet mixing and remain in that form in the paste (Diamond and Sahu 2006). In porous concretes, the lack of fine aggregates, the very low percentage of superplasticizer as well as the low cement paste content negatively affects the sufficient blending of all the ingredients during mixing. Therefore, the dispersion of microsilica in between cement particles is even more difficult to attain. Agglomerates that remain, cannot fully participate in the expected filler and pozzolanic effects (Diamond and Sahu 2004). In the meso-scale tests however, there was a small increase in bond strengths of samples containing microsilica with agglomerates, as can also be seen in Figure 3.29, when compared to samples with plain cement paste in Figure 3.26. This means that microsilica, even with agglomerates, is still partially in function in strengthening the ITZ.

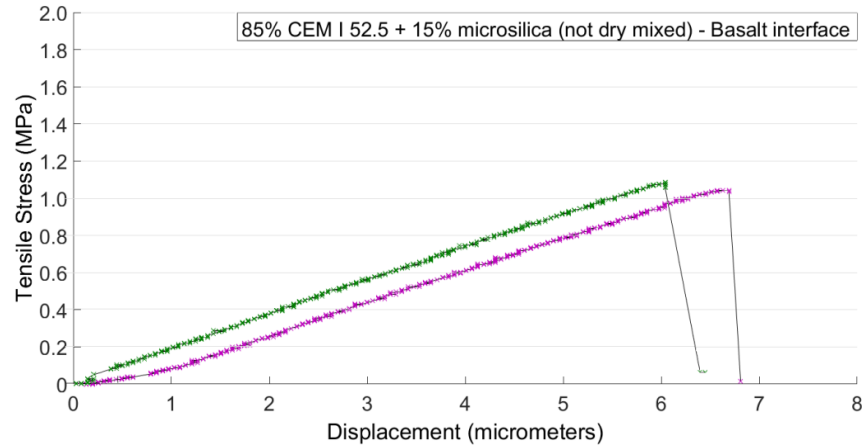


Figure 3.29 Representative meso-scale ITZ test results of (not dry-mixed) cement paste with 15 percent microsilica-basalt aggregate

Besides the basalt aggregates, river gravel aggregates have been tested as well because they were also used in macro scale samples. River gravel is actually a batch of aggregates with different mineralogical properties. The aggregate particles have a smooth texture. In the river gravel batch tested, there were aggregates that cause the formation of very weak interfaces while there were also ones that form much stronger bonds with the cement paste. Thus, very different results were obtained from the same batch of river gravel aggregates used in composite mixtures with river gravel. Aggregate particles from feldspar and chert, which are very common among the different types of gravel, gave bond strengths around 0.5 MPa. The presence of aggregates that form very weak bonds with cement paste is the reason for lower strengths in macro-scale tests. Representative results from river gravel testing are presented in Figure 3.30. Among the aggregates that were tested at meso-scale, there was a specific type of gravel that gave very high bond strength (an average of 1.7 MPa) in the test. Figure 3.30 (a) shows a representative test result for a sample made with quartz aggregate. The XRD analysis of that specific gravel is given in section 3.3.3.2.

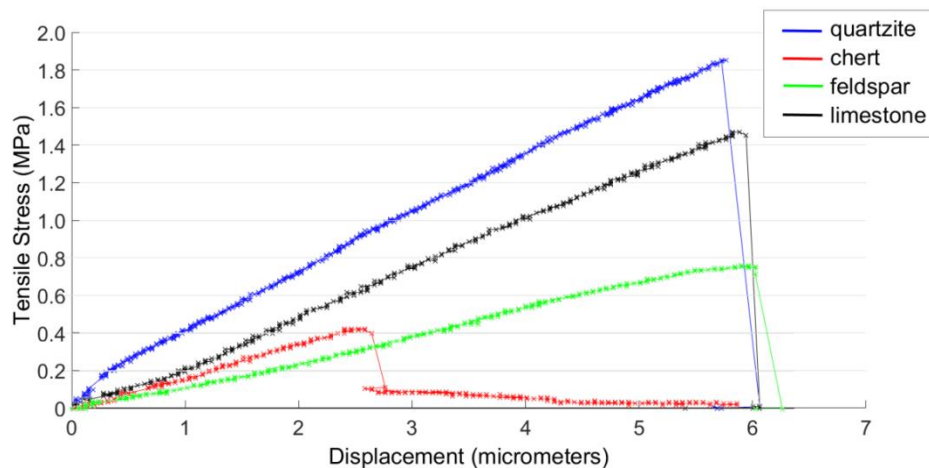


Figure 3.30 Representative meso-scale ITZ test results of cement paste- different gravel aggregates (quartzite, chert, feldspar, limestone)

Displacement controlled uni-axial tensile tests were also conducted on 4 mm by 4 mm section cement paste samples using the micro tension-compression testing device. The cement paste compositions were the same as those of the macro-size samples (as given in Table 3.1). Mean tensile strengths of 3.12 MPa and 2.59 MPa were found for plain cement paste and cement paste with 15 percent microsilica, respectively. It should again be noted that the cement pastes with and without microsilica had similar tensile strengths, similar to the compressive strengths obtained from macro-size samples as presented in section 3.3.2.2. The meso-scale tensile testing samples of cement pastes with microsilica had even slightly lower strengths as can also be seen in Figure 3.31 and Figure 3.32.

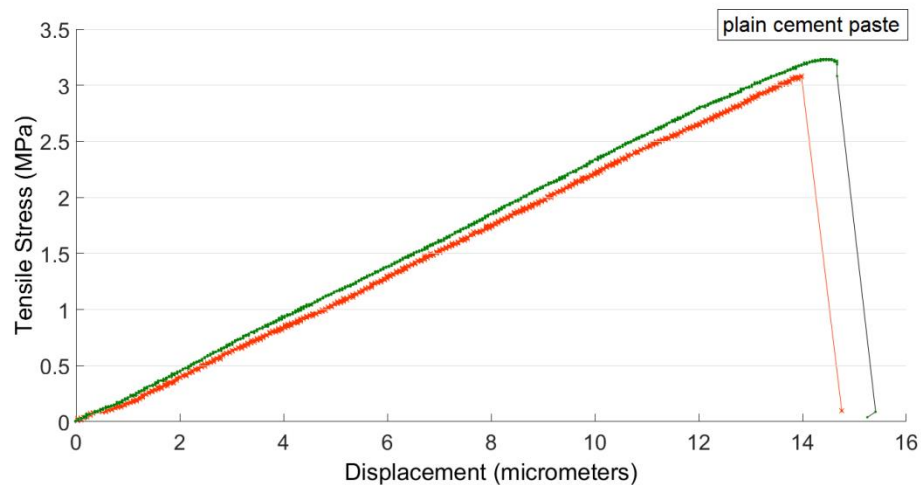


Figure 3.31 Representative meso-scale tensile test results of plain cement paste

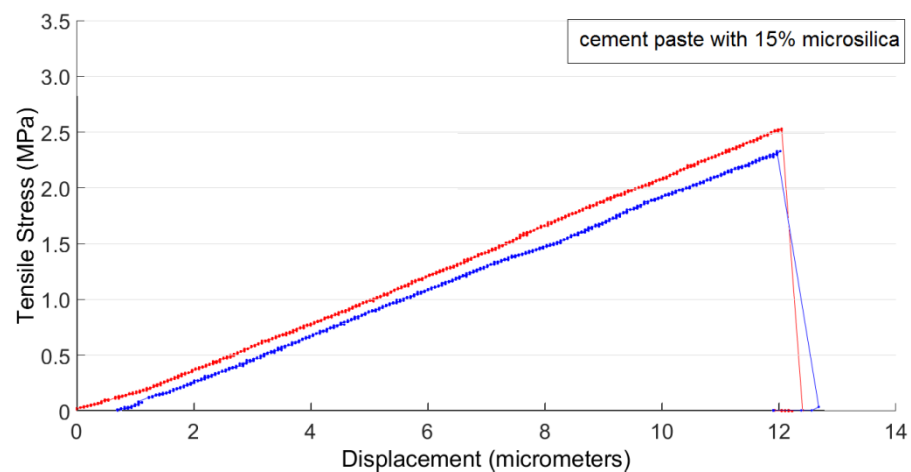


Figure 3.32 Representative meso-scale tensile test results of cement paste with 15 percent microsilica

### 3.3.3.1. ESEM examinations of meso-scale samples

The 4 mm x 4 mm cross-section meso-scale ITZ samples, which have failed during the tensile tests, were also analyzed microscopically. Both the cement paste and the aggregate surfaces of the interface were characterized using ESEM, to be able to find a relation between the ITZ strength and the properties of the aggregate surfaces. The images were captured using a Philips XL30 environmental scanning electron microscope. The images presented in Figure 3.33 were taken from the aggregate surface of the fractured samples. The fractured surfaces were not polished, not to lose the delicate formations that existed on those surfaces. No coating was applied to the samples. The three images from the top to the bottom correspond to the aggregate surfaces of plain cement paste-basalt aggregate, cement paste with 15 percent microsilica-basalt aggregate and plain cement paste-river gravel (feldspar) aggregate composite samples, respectively. Even though a quantitative evaluation was not possible, it could be concluded that for composite samples with only cement as binder in the cement paste (Figure 3.33 (a)), the aggregate surface contains a very small amount of cement paste after the fracture. In samples where the cement paste includes microsilica, large pieces of cement paste are present on the aggregate surface (Figure 3.33 (b)). Figure 3.33 (c) is an image taken from the aggregate surface of a composite sample containing feldspar aggregate and plain cement paste, which gave very low bonding strength values in the tests. The picture shows that there are hardly remains of cement paste present on the aggregate surface.

EDS spot analyses were performed at the selected areas for checking the chemical composition to verify whether those parts belong to cementitious phases or aggregates themselves, which showed that the remains in the images belong to cementitious phases. ESEM observations and the EDS checks revealed that as bond strength between the ITZ and the aggregate increases, fracturing not always occurs at the immediate vicinity of the aggregate. Therefore, more amounts of ITZ or cement paste phases remain on the aggregate side of the fractured surface. Likewise, for very weak bonds as in image c (about 0.4 MPa), breaking takes place immediately near the aggregate surface.

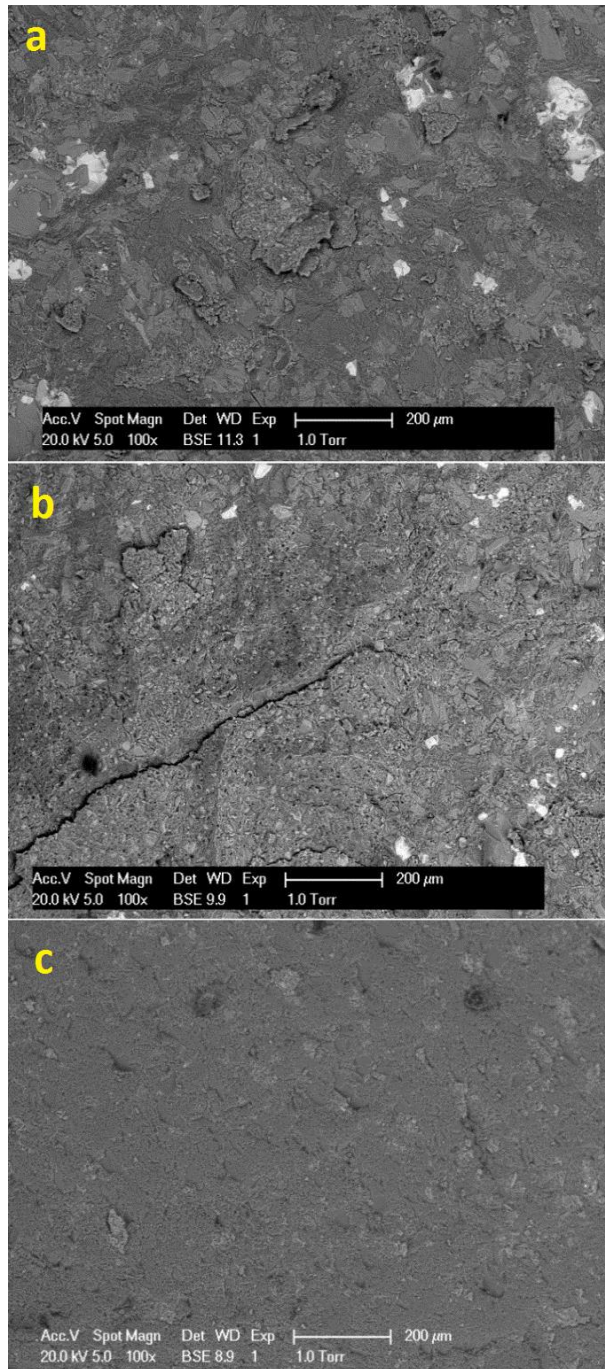


Figure 3.33 ESEM images of the aggregate surfaces of fractured meso-size composite samples of: (a) plain cement paste-basalt aggregate, (b) cement paste with 15 percent microsilica-basalt aggregate, (c) plain cement paste-river gravel (feldspar)

### 3.3.3.2. X-Ray diffraction of gravel aggregate

To be able to better identify the specific type of gravel that gave significantly higher bond strength compared to any other aggregate, X-ray diffraction analyses were conducted on these

gravel samples. For this purpose, the gravel was ground into powder form. Thin sections of the gravel were also prepared. The X-ray diffraction analyses showed numerous peaks of quartz and a peak of calcite, as presented in Figure 3.34. The rock was found to be consisting of quartz (95%) with the inclusions of calcite (5%). The X-ray pattern as well as the optical microscope observations indicate that the type of river gravel, that have formed the strongest bond with the cement paste (ITZ with highest strength) among all the different types of gravel and basalt aggregates that have been tested, was a type of quartz that hosted layers of calcite.

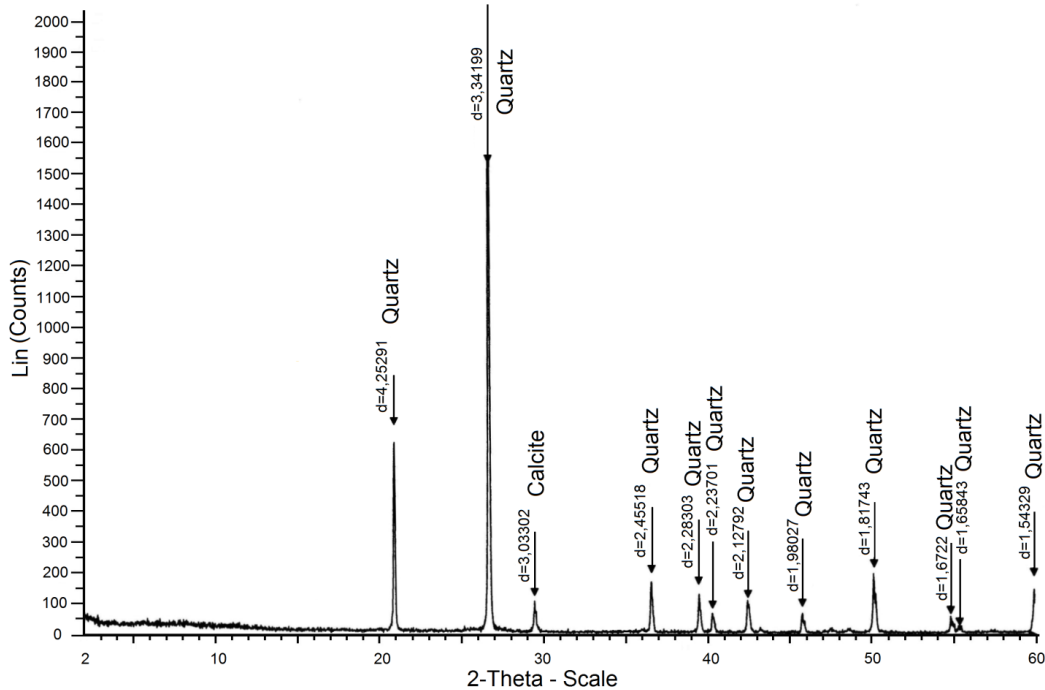


Figure 3.34 XRD analysis result of the gravel aggregate

### 3.4. General Overview of the Factors Affecting Porous Concrete Strength

As presented in Figure 3.35, numerous factors affect the mechanical properties of porous concrete. Some of them were also coupled to each other and, therefore, affect the ultimate properties in a combined way. Testing at different scales is helpful in investigating the separate factors and in understanding their effects on the global behavior of the porous concrete material.



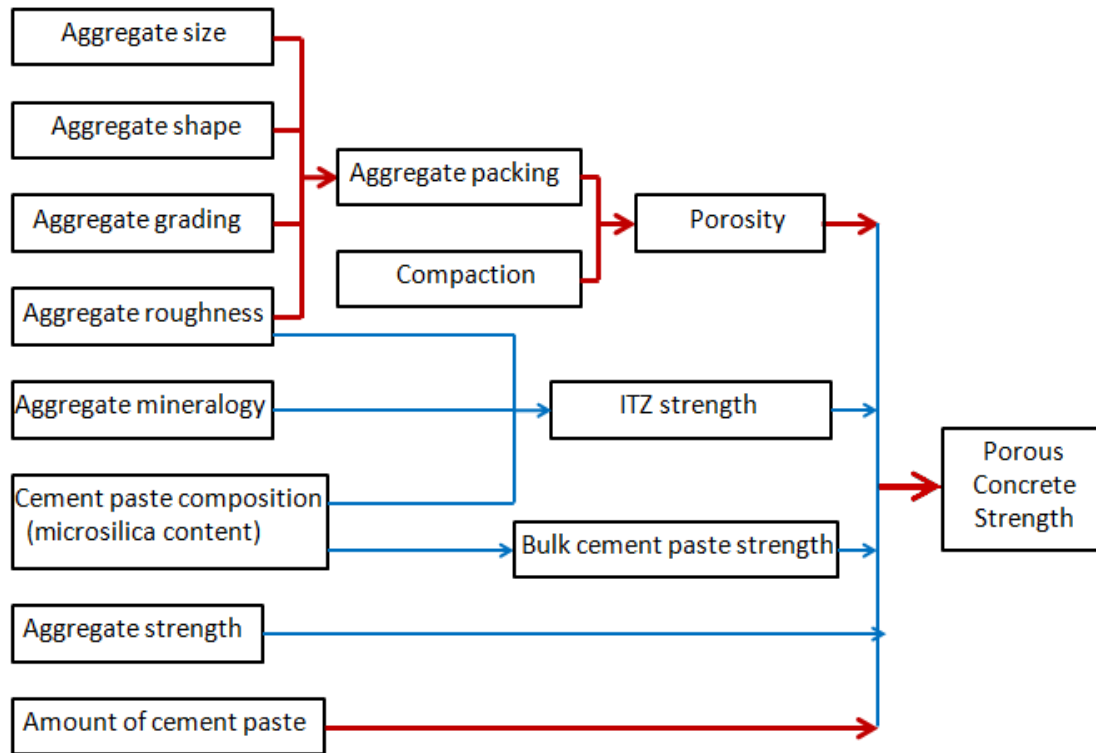


Figure 3.35 Summary of the factors affecting porous concrete strength

According to the results obtained from the tests conducted in the scope of this research, the factors that affect the aggregate packing, the orientation of the particles and the porosity of the final material, which are mainly dominated by the aggregate properties and compaction, are the most controlling factors. The amount of cement paste present in the mixture is another dominating factor. As an extreme, the available space between the aggregates infilled with cement paste as in the full concretes (FC1 and FC2) gives high strengths. Using too low amounts of cement paste (as in PRC11) on the other hand, drastically lowers the strength as expected. It was seen in the meso-scale tests that mechanical properties of the ITZ phase can be improved by changing the cement paste composition, e.g. by using microsilica. However, according to the macro-scale test results obtained, the effects of these variations on the resulting strengths of porous concretes are not significant. The only exception to that was the low strength porous concretes with river gravel due to very weak ITZ bonds formed with river gravel. In Figure 3.35, the highly effective factors are emphasized with red arrows while, the parameters that are less significant are indicated with blue.

### 3.5. Conclusions

In the scope of this research project, with the aim to design porous concretes that fracture into small fragments and have relatively high static strength, a sensitivity study was conducted where many factors that affect the properties of porous concrete were investigated. Experiments at



different scales were performed to determine the effectiveness of the various factors while the outcome of the tests guided the process of modification of the material. By modifying the mixture composition as well as the method of compaction, porous concretes with improved static strengths (at the range of 30-50 MPa) were produced. In order to better understand the properties of these porous concretes, mechanical tests at macro and meso-scales were performed. Computed tomography, electron microscopy and X-ray diffraction analyses were also conducted to explain the results. Based on the results obtained, the following conclusions are drawn:

Among all the parameters that have been investigated, aggregate properties have the most significant effect on the mechanical properties of porous concrete. The coarse aggregates dominate the formation of the skeleton structure of the material. Macro-scale experimental results clearly indicate that the aggregate grading and, therefore, the meso-scale pore size distribution had a predominant effect on the properties of porous concretes. The decrease in aggregate size (when using aggregates in a single size range) also increases the strength of porous concretes.

Increased roughness and angularity also contribute to porous concrete strength due to enhanced mechanical interlock, increased total surface area available for the adherence of cement paste and increased number of contact points.

Intense compaction in very thin layers, which directly affects the orientation and the packing of the particles and the porosity, is essential to attain porous concretes with higher strengths, provided that the setting time of cement paste is controlled with a set retarder.

The contribution of microsilica to the mechanical properties of porous concrete was not significant. It even slightly lowered both the compressive and the tensile strengths of most of the mixtures with the exception of finer aggregate mixtures. The presence of microsilica also slightly lowered the tensile strength values of meso-size cement paste samples, whereas it did not have a significant effect on the compressive strengths of macro-size cement paste samples.

Otherwise than expected, water curing (in tap water) caused the cementitious phases of porous concrete to significantly degrade. The reason for this degrading was the calcium leaching. In the ESEM observations, it was found that the cement paste that had gone through leaching became significantly more porous. Consequently, the mechanical tests on porous concretes showed lower strengths and stiffnesses due to water curing.

Meso-scale ITZ testing provided important information on the effects of cement paste composition and aggregate type on the mechanical properties of the ITZ. According to the meso-scale testing results, it was clearly seen that microsilica improved the strength of ITZ. This effect, however, was not seen in porous concretes where the amount of ITZ phase is highly reduced compared to normal concrete. Along with the reason that the total amount of ITZ phase is drastically less, the CT scans of fractured samples revealed that in porous concretes crack patterns are very much influenced by the distinct porous structure where the cracks are forced to propagate into locations guided by the geometry of the aggregate skeleton. When the aggregates are finer, cracks tend to go more through the ITZ, while they go more often through the

aggregates with increasing aggregate size. This also supports the explanation that microsilica, which enhances the ITZ properties, has a slight enhancing effect on the porous concrete with finer aggregates while it does not have such an effect on the mixtures with coarser aggregates. A river gravel batch contains particles having different mineralogical properties. In the meso-scale tests of composite samples containing gravel aggregates, for different types of gravels, bonds of very different strengths were found. The presence of the types of gravels that form very weak bonds with cement paste is the reason behind the lower strengths of macro-scale porous concrete mixtures containing river gravel. The smooth texture of river gravel also weakens the bond, due to reduced total surface area and less mechanical interlock. In meso-scale ITZ testing of composite samples with river gravel, a specific gravel aggregate that is a type of quartzite including very thin layers of calcite gave the highest bonding strength values.

## References

- Agar Ozbek A.S., Weerheijm J., Schlangen E., van Breugel K. (2013), *Dynamic behavior of porous concretes under drop weight impact testing*, Cement and Concrete Composites, 39, 1-11.
- Agar Ozbek A.S., Weerheijm J., Schlangen E., van Breugel K. (2013), *Investigating porous concrete with improved strength: Testing at different scales*, Construction and Building Materials 41, 480-490.
- Alexander M.G. (1993), *Two experimental techniques for studying the effects of the interfacial zone between cement paste and rock*, Cement and Concrete Research, 23, 567-575.
- Bentz D.P., Stutzman P.E., Garboczi E.J. (1992), *Experimental and simulation studies of the interfacial zone in concrete*, Cement and Concrete Research, 22, 891-902.
- Bentz D.P. and Stutzman P.E. (1995), *SEM Analysis and Computer Modelling of Hydration of Portland Cement Particles*, Petrography of Cementitious Materials, 60-73, Philadelphia, USA.
- Carde C., François R. (1997), *Effect of the leaching of calcium hydroxide from cement paste on mechanical and physical properties*, Cement and Concrete Research, 27(4), 539-550.
- Carde C., François R. (1999), *Modeling the loss of strength and porosity increase due to the leaching of cement pastes*, Cement and Concrete Composites 21(3), 181-188.
- Chen J.J., Thomas J. and Jennings H. M. (2006), *Decalcification shrinkage of cement paste*, Cement and Concrete Research, 36(5), 801-809.
- Cerny R. and Rovnanikova P. (2002), *Transport Processes in Concrete*, Taylor & Francis Spon Press, London, UK.
- Chindaprasirt P., Hatanaka S., Chareerat T., Mishima N., Yuasa Y. (2008), *Cement paste characteristics and porous concrete properties*, Construction and Building Materials, 22(5), 894-901.

Cohen M.D., Goldman A., Chen W. (1994), *The role of microsilica in mortar: Transition zone versus bulk paste modification, Part II: Toughness characterization*, Cement and Concrete Research, 24, 95-98.

Cong X., Gong S., Darwin D., McCabe S.L. (1992), *Role of microsilica in compressive strength of cement paste, mortar, and concrete*, ACI Materials Journal, 89(4), 375-387.

Copuroglu O. (2010), *Effect of silica dissolution on the mechanical characteristics of alkali-reactive aggregates*, Journal of Advanced Concrete Technology, 8(1), 5-14.

Crouch L.K., Pitt J., Hewitt R. (2007), *Aggregate effects on pervious Portland cement concrete static modulus of elasticity*, Journal of Materials in Civil Engineering, 19(7), 561-568.

Deo O., Neithalath N. (2011), *Compressive response of pervious concretes proportioned for desired porosities*, Construction and Building Materials, 25(11), 4181-4189.

Diamond S., Mindess S. (1992), *SEM Investigations of fracture surfaces using stereo pairs: I. Fracture surfaces of rock and of cement paste*, Cement and Concrete Research, 22(1), 67-78.

Diamond S. (2004), *The microstructure of cement paste and concrete-a visual primer*, Cement and Concrete Composites, 26, 919-933.

Diamond S., Sahu S. (2006), *Densified microsilica: particle sizes and dispersion in concrete*, Materials and Structures, 39(9), 849-59.

Diamond S., Sahu S., Thaulow N. (2004), *Reaction products of densified microsilica agglomerates in concrete*, Cement and Concrete Research, 34(9), 1625-1632.

Erdogan S.T., Fowler D.W. (2005), *Determination of aggregate shape properties using X-ray tomographic methods and the effect of shape on concrete rheology*, Research Report, International Center for Aggregates Research, Austin, Texas, USA.

Erdogan S.T., Quiroga P.N., Fowler D.W., Saleh H.A., Livingston R.A., Garboczi E.J., Ketcham P.M., Hagedorn J.G., Satterfield S.G. (2006), *Three-dimensional shape analysis of coarse aggregates: New techniques for and preliminary results on several different coarse aggregates and reference rocks*, Cement and Concrete Research, 36(9), 1619-1627.

Ghafoori N., Dutta S. (1995), *Building and nonpavement applications of no-fines concrete*, Journal of Materials in Civil Engineering, 7(4), 286-9.

Ghafoori N., Dutta S. (1995), *Development of no-fines concrete pavement applications*, Journal of Transport Engineering, 121, 283-8.

Hsu T.T.C., Slate F.O. (1963), *Tensile bond strength between aggregate and cement paste or mortar*, ACI Journal Proceedings, 60(4), 465-86.

<https://crystalclassics.co.uk/news-story.php?id=18>

<http://global.britannica.com/EBchecked/topic/88899/calcite>

<http://www.mineralshows.com/denver2009/specials.shtml>

Kevern J.T., Schaefer V.R., Wang K. (2009), *Evaluation of pervious concrete workability using gyratory compaction*, Journal of Materials in Civil Engineering, 21(12), 764-770.

Klieger P., Lamond J.F., (1994), *Significance of tests and properties of concrete and concrete-making*, ASTM special technical publication, Philadelphia, USA.

Lamond J. F. and Pielert J. H. (2006), *Significance of tests and properties of concrete and concrete making materials*, ASTM 169D.

Lian C., Zhuge Y. (2010), *Optimum mix design of enhanced permeable concrete-An experimental investigation*, Construction and Building Materials, 24(12), 2664-2671.

Lian C., Zhuge Y., Beecham S.. (2011), *The relationship between porosity and strength for porous concrete*, Construction and Building Materials, 25(11), 4294-4298.

Marolf A., Neithalath N., Sell E., Wegner K., Weiss J., Olek J. (2004), *Influence of aggregate size and gradation on the acoustic absorption of enhanced porosity concrete*, ACI Materials Journal, 101(1), 82-91.

Persson S., Ostman E. (1986), *The use of computed tomography in non-destructive testing of polymeric materials, aluminium and concrete: Part 1-basic principles*, Polymer Testing, 6(6), 407-414.

Qian C, Dong H, Liu Y. (2010), Comparisons of ITZ characteristics of marble and sandstone aggregates. Magazine of Concrete Research, 62(9), 609-15.

RILEM (1996), *Interfacial transition zone in concrete*, Chapman and Hall, London, UK.

Scrivener K.L. (2004) *Backscattered electron imaging of cementitious microstructures-Understanding and quantification*, Cement and Concrete Composites, 26, 935-945.

Scrivener K.L., Crumbie A.K., Laugesen P. (2004), *The interfacial transition zone (ITZ) between cement paste and aggregate in concrete*, Interface Science, 12, 411-421.

Suzuki T., Ogata H., Takada R., Aoki M., Ohtsu M. (2010), *Use of acoustic emission and X-ray computed tomography for damage evaluation of freeze-thawed concrete*, Construction and Building Materials, 24(12), 2347-2352.

St John D.A., Poole A.B., Sims I. (1998), *Concrete Petrography*, John Wiley and Sons, New York, USA.

Toutanji H.A., El-Korchi T. (1995), *The influence of microsilica on the compressive strength of cement paste and mortar*, Cement and Concrete Research, 25(7), 1591-1602.

Walker H. N., (1992), *Petrographic Methods of Examining Hardened Concrete: A Petrographic Manual*, Virginia Transportation Research Council, USA.

Wee T. H., Zhu J. Chua H. T., Wong S. F. (2001), *Resistance of blended cement pastes to leaching in distilled water at ambient and higher temperatures*, ACI Materials Journal, 98(2), 184-193.

Yang J, Jiang G. (2003), *Experimental study on properties of pervious concrete*, Cement and Concrete Research, 33(3), 381-386.

Zimbelmann R. (1985), *A contribution to the problem of cement-aggregate bond*, Cement and Concrete Research, 15, 801-808.

## **CHAPTER 4**

### **IMPACT PROPERTIES OF POROUS CONCRETES AND THE DYNAMIC TESTING TECHNIQUES USED**

#### **4.1. Introduction**

Numerous testing techniques have been proposed by researchers to characterize the dynamic behaviours of engineering materials. The capabilities of different measurement techniques and how they can be adapted to an impact testing configuration for porous concrete were among the main concerns of this research project. Therefore, various testing techniques have been considered and investigated for feasibility. While some of those techniques have been directly adopted, some were modified in order to accomplish an accurate, repeatable and fast testing method that can be used in the process of designing a special type of cementitious material that fractures into small size fragments under dynamic loading. This chapter aims to summarize the dynamic characteristics of the porous concretes that have been designed and produced in the scope of this research project as well as the testing and analysis techniques that have been utilized to understand their dynamic behaviours.

In the experiments, the dynamic loading configuration was a drop weight impact set-up. Three different measurement and monitoring techniques have been utilized, each with its own specific analysis method. The three applied techniques are laser Doppler velocimetry, high speed photography and direct impact stress measurements using piezoresistive (manganin) stress gauges. These techniques were compared and their applicability for the impact tests on porous concrete was validated by evaluating the results.

#### **4.2. Planar Impact Measurement Techniques**

New monitoring methods used in impact experiments made an extensive contribution to the research on the dynamic properties of cementitious materials. In planar impact experiments, there are various measurement techniques involved to quantify the velocity and pressure for defining the dynamic performance of a material (Espinosa 2000). Laser interferometry has become generally accepted as a competent tool for monitoring the motion of the surfaces of shocked specimens using different experimental configurations. The system called velocity interferometer system for any reflector (VISAR) is the most widely used interferometer configuration for shock profile measurements (Barker and Hollenbach 1972). It has been effectively used in measuring free surface velocity-time histories, where various materials have been tested and analyzed for hyper-velocity collisions (Grady 1996; Hereil and Buzaud 2006; Reinhart et al. 1999; Furnish et al. 1999; Hall et al. 1999; Gebbeken et al. 2006; Grady 1998; Chhabildas et al. 2002). In

velocity interferometry systems, velocity measurements are usually performed at the stress free back surface of the target or at the interface of a transparent window attached to the back of the target (Chen et al. 2004). Particle velocity wave profiles are also captured using electromagnetic velocity gauges embedded at various depths within the sample to derive the impact stress (Gustavsen et al. 1999). Accelerometers are used to monitor the impactor and consequently the target specimen where the results are compared with laser displacement measurements (Sukontasukkul et al. 2004). Contact electrical resistance measurement is conducted to monitor concrete–concrete pressure contacts in real time during dynamic pressure application (Luo and Chung 2000). Doppler-radar is an alternative technique to obtain surface velocity histories (Unosson and Nilsson 2006).

Plate impact experiments using flyer plate technique has been used to determine the Hugoniot curves of many materials including concrete (the main principles of Hugoniot curves will be described in more detail in the impact strength analysis techniques section of this chapter.) (Grady 1996, Gebbeken et al. 2001). Plate impact experiments can even be used for testing liquids. As special applications, impact properties of liquids such as liquid deuterium which is also known as heavy hydrogen are determined. In those applications, the experimental configuration is designed to facilitate the symmetric impact of a magnetically driven aluminum flyer plate onto an aluminum front plate.

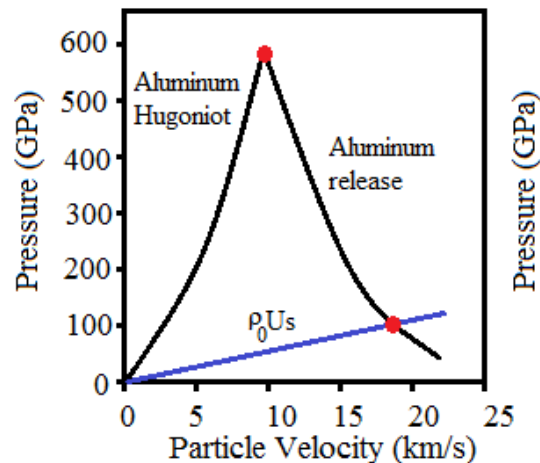


Figure 4.1 Impedance mismatch graph of symmetric impact for finding the Hugoniot of liquid deuterium (Chhabildas et al. 2005)

In the configuration, the cell of the liquid is confined by the front plate. Since Hugoniot data of aluminum is known up to stresses around 500-600 GPa, such testing techniques involving aluminum can reach very high stress levels, where in the mentioned testing configuration, stresses in the range of 30-100 GPa are of concern. In such an experiment, the Hugoniot response of liquid deuterium is obtained using impedance matching technique as the analysis method which is illustrated Figure 4.1 (Chhabildas et al. 2005).

This method, which is also applied in this current research, will be described in more detail in the section on impedance mismatch method of this chapter.

Among the wide variety of dynamic testing techniques that are being employed in shock wave experiments, laser Doppler velocimetry, high speed photography and direct stress measuring using piezoresistive stress gauges were selected to be used for the impact testing of porous concrete for this research project.

#### **4.2.1. Laser Doppler Velocimetry**

Laser Doppler velocimetry (LDV), also known as laser Doppler anemometry (LDA), is a non-contact diagnostic technique, based on the Doppler principle, for measuring transient velocity. The technique has been used in various applications after its first introduction (Yeh and Cummins 1964). Doppler effect is based on monitoring the change in the wavelength of the reflected laser light, which is a function of the relative velocity of the moving object that the laser beam meets. The vibrometer used in the measurements is a two beam laser interferometer that measures the frequency difference between the internal reference beam and the measuring beam. A Doppler velocimeter system is capable of measuring the motion of a particle or surface which has a rapidly changing velocity. This property can, therefore, be employed to measure the motion of a free-falling projectile throughout an impact test to obtain the full velocity-time history. In research studies where LDV is used, the velocity signals captured are either differentiated to obtain the acceleration and multiplied by the impactor mass to attain the load-time relationship or used in energy calculations based on the change in kinetic energy (Wu et al. 1994; Birch and Jones 1990; Hodgkinson et al. 1982). LDV has been selected as the monitoring technique in this research to capture the velocity history data of the impacted surface of the impactor.

#### **4.2.2. High-Speed Photography**

High-speed photography has been used for acquiring a wide range of fast-changing events and has been employed in numerous scientific applications. After the first known experiment using high speed photography, conducted by Talbot in 1851, high speed photography has been a topic of research that involves several disciplines. Since then, a rapid development in the high speed photography techniques and devices has taken place (Lee and Swallow 2004). The introduction of digital technology has also greatly supported the new advances in the area.

In some research studies using high speed photography, dynamic failure mechanisms are examined to better understand the failure modes that are present and in some of those studies the output is also compared with results from photoelasticity (Xu and Rosakis 2003, Xu and Rosakis 2005, Majzoub and Chaudhri 2000, Duffy 1991). Similarly, high speed photography is also being used to acquire and quantify the deformation history of the whole specimen itself or particularly the vicinity of a dynamically growing crack-tip



in impact tests (Lee et al. 2009, Kajberg et al. 2004, Sharma et al. 2002). There are also investigations that have been carried out to investigate plate impact experiments in which a planar compression that induces a uniform region of strain behind a shock front in the target medium is visualized based upon high-speed photography (Bourne et al. 1995).

High speed photography has been effectively used in the mechanical tests of concrete since a long period of time. In the pioneering applications, it was being used in examining the crack patterns and failure modes (Bhargava 1975, Mindess 1985). Since then, it has been used in concrete testing, especially in ballistic impact studies (Field et al. 2004). In high speed photography studies, digital image correlation is frequently used to evaluate the digital image output with the aid of displacement and strain field estimation algorithms (Pan et al. 2009). High speed photography measurements were conducted in this research in order to compare and validate the results obtained by LDV measurements as well as visualizing the fragmentation behavior of the material.

#### **4.2.3. Direct Stress Measurements Using Piezoresistive Stress Gauges**

Piezoresistive gauges have been used extensively in the last decades as in-material stress transducers in planar stress studies (Rosenberg 1985-I). Using piezo-resistive stress gauges in measuring the dynamic stress is one of the most important direct techniques where the dynamic characteristics of the materials are acquired by doing series of tests at different stress ranges (Rosenberg 1981; Ishiguchi et al. 2000).

Manganin and ytterbium are the most widely preferred types of gauges among all. Manganin is a copper-manganese-nickel alloy having a high sensitivity to pressure. Manganin alloy has a relatively high and almost constant piezoresistance together with low temperature sensitivity as a dynamic transducer (Rosenberg et al. 1980-I). These stress gauges work with the same principle as strain gauges where the thickness and therefore the electrical resistance of the gauge change as exposed to stress. The gauge is placed such that the active gauge element is normal to the direction of wave propagation. When a shock wave passes through the gauge plane, the recorded voltage increases with pressure applied to the gauge. Usually in such applications, a resistance bridge is used.

All stress gauges require calibration so that their output can be related to stress in the specimen. Quasi-static loading-unloading cycles are performed on the gauges for calibration where data on shock stresses versus relative resistance change showing the behavior of the gauge is found (Yaziv et al. 1980). For manganin gauges, the change in resistance as a function of applied pressure is linear to extremely high pressures. There are numerous researches conducted to determine the characteristics of piezoresistive and especially manganin gauges themselves and the corresponding calibration data (Gupta 1980, Rosenberg et al. 1983, Rosenberg and Partom 1985-I).

Investigations on the performance of stress gauges in plane shock experiments based on the measurement of uniaxial strain and in experiments to determine Hugoniot data were also conducted by researchers (Rosenberg et al. 1980-I, Rosenberg 1981, Millett et al.

1998). The direct measuring of the lateral stress in a shocked specimen was also done by using thin piezoresistance stress gauges inserted laterally inside the shocked target. The principle of using such stress gauges for lateral measurements is based on the foil being very thin so that the stress across its thickness direction equalizes the lateral stress in the surrounding (Rosenberg and Partom 1985-II, Appleby-Thomas et al. 2009).

The purpose of using manganin stress gauge is to measure the stress normal to the direction of the shock wave. However in practice, piezoresistive gauges respond to both stress and strain along the gauge plane (Antoun et al. 2003). The efforts to separate the stress component of the measured change in resistance from the strain component in this research project are described in section 4.4.2.1 on measuring impact stress using a piezoresistive gauge.

### **4.3 Impact Strength Analysis Techniques**

The analyses of the plate impact experiments are usually performed based on the theoretical principles of one-dimensional motion of compressible media. The analyses of wave propagation in one dimensional media are primarily built on the laws of conservation taken in one dimensional planar form and the equation of state (EOS) of the material (Antoun et al. 2003, Meyers 1994, Drumheller 1998). Therefore, to be able to conduct the analyses of the experimental results, conservation equations in combination with the EOS of the materials used in the experiments have to be understood and elaborated. Equations for the conservation laws are valid for all materials. Equation of state, however, identifies the material itself and is also unique in the sense that the state is independent of the path taken to reach it. In wave propagation research, the general thermodynamic EOS expression is usually reduced to a relation between the parameters of pressure, density and internal energy. Additionally, because such state parameters are very challenging to directly measure during experiments, when analyzing shock waves, EOS is more frequently expressed in terms of velocity values i.e. particle and wave velocities (Antoun et al. 2003).

#### **4.3.1 Analysis of One-Dimensional Wave Propagation**

The one-dimensional shock wave propagation situation, which is also the concept that the analyses conducted for the drop-weight experiments of this research are based on, can be represented by a shock tube or a moving piston, which is analogous to a long hollow cylinder filled with a compressible material as shown in Figure 4.2. Initially, the material has a pressure  $P_0$ , density  $\rho_0$  and internal energy  $E_0$ . Because it is at rest, the velocity of its particles is  $u_0=0$ . At time  $t=0$ , the piston which has been at rest is suddenly released and starts to move at the particle velocity of  $u_p$ . The motion of every portion of the compressible material is parallel to the axis of the tube. At any instant in time, the velocity at any point in the tube is only a function of its position along the axis of the piston. Thus, the flow of the compressible material in the tube is assumed to be one

dimensional. At any instant in time, the pressure  $P$  at any point in the tube is also a function of its position along the piston.

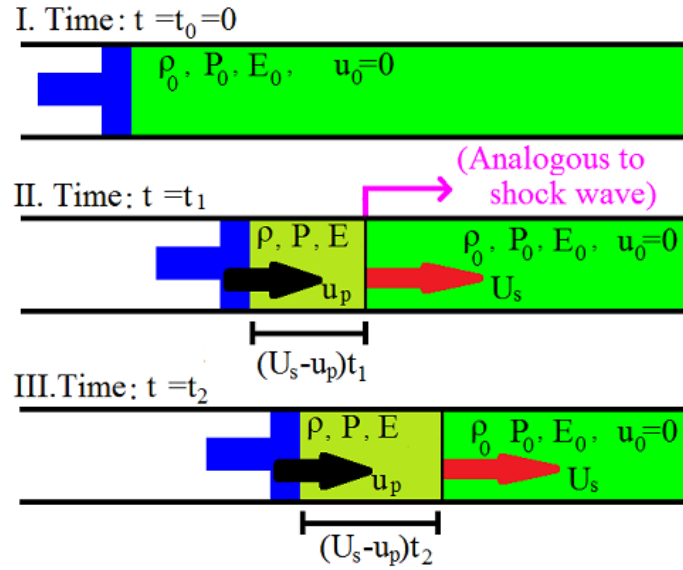


Figure 4.2 One-dimensional shock tube representation (Meyers 1994)

At time  $t=t_1$ , the compressed portion of the material ahead of the piston has a pressure  $P$ , density  $\rho$  and internal energy  $E$ , and has moved a distance of  $U_s t_1$  where  $U_s$  is the shock wave velocity. Meanwhile, the displacement of the piston itself is  $u_p t_1$ . The velocity of the front of the compressed region, which is analogous to the velocity of shock front is much higher than the velocity of the piston i.e. the particle velocity. Consequently, the portion of compressed material increases drastically in time as illustrated in Figure 4.2 (Meyers 1994, Drumheller 1998).

A shock wave is characterized by a rapid change in density, pressure, internal energy and particle velocity. The application of conservation equations i.e. the balance of mass, balance of linear momentum and balance of energy conditions to the shock wave gives the following adapted forms (Ramesh 2009).

#### Conservation of mass:

(The initial state is denoted by the subscript 0.)

Mass moving toward the shock front:  $A\rho_0(U_s - u_0)dt$

Mass moving away from the front:  $A\rho(U_s - u_p)dt$

(Equation of the conservation of mass)

$$A\rho_0(U_s - u_0)dt = A\rho(U_s - u_p)dt \quad (4.1)$$

$$\rho_0 U_s = \rho(U_s - u_p) \quad (4.2)$$

#### Conservation of linear momentum:

Difference in linear momentum=Impulse per unit cross-sectional area

$$A \rho (U_s - u_p) u_p dt - A \rho_0 (U_s - u_0) u_0 dt = (P - P_0) A dt \quad (4.3)$$

The material is initially at rest,  $u_0=0$ .

For shock waves travelling in solids, the shock pressure  $P$  is much greater than the initial pressure  $P_0$ , which is the ambient atmospheric pressure. Therefore, the  $P_0$  is usually neglected and removed from the conservation equations involving solids (Kanel et al. 2004; Meyers 1994).

$$\text{The equation therefore becomes: } (P - P_0) = P = \rho_0 U_s u_p \quad (4.4)$$

#### Conservation of energy:

Difference in work done by  $P$  and  $P_0$  = difference in the totals of kinetic and internal energies between the two sides of the wave front (force x distance)

$$\text{(Equation of the conservation of energy) } E - E_0 = \frac{1}{2} (P + P_0) (V_0 - V) \quad (4.5)$$

On the other hand, the relationship between the shock and particle velocities are expressed in the equation of state (EOS) of the material (Meyers 1994, Antoun et al. 2003, Drumheller 1998). Because it describes the variation of shock velocity with particle velocity, the gradient of the curve for metals is constant up to very high stresses. Therefore, usually only  $S_1$  (see Eq. 4.6 below) is given for metals and higher order terms can be neglected. In the equation,  $U_0$  and  $S$  are material-specific parameters where  $U_0$  is the speed of sound in the material.

$$U_s = U_0 + S_1 u_p \quad (4.6)$$

For concrete, it is not possible to neglect the higher order terms even for moderate speed impacts. However, because the impact calculations will be done based on the behavior of the steel (or aluminum) impactors in the experiments conducted in this research project, the linear EOS relations of the metals are applicable (Ramesh 2009), which will be explained in more detail in the impedance mismatch method section. The EOS relations for steel and aluminum are presented in Figure 4.3 and Figure 4.4, respectively (Furnish et al. 2014, Jordan and Melvin, 2012).

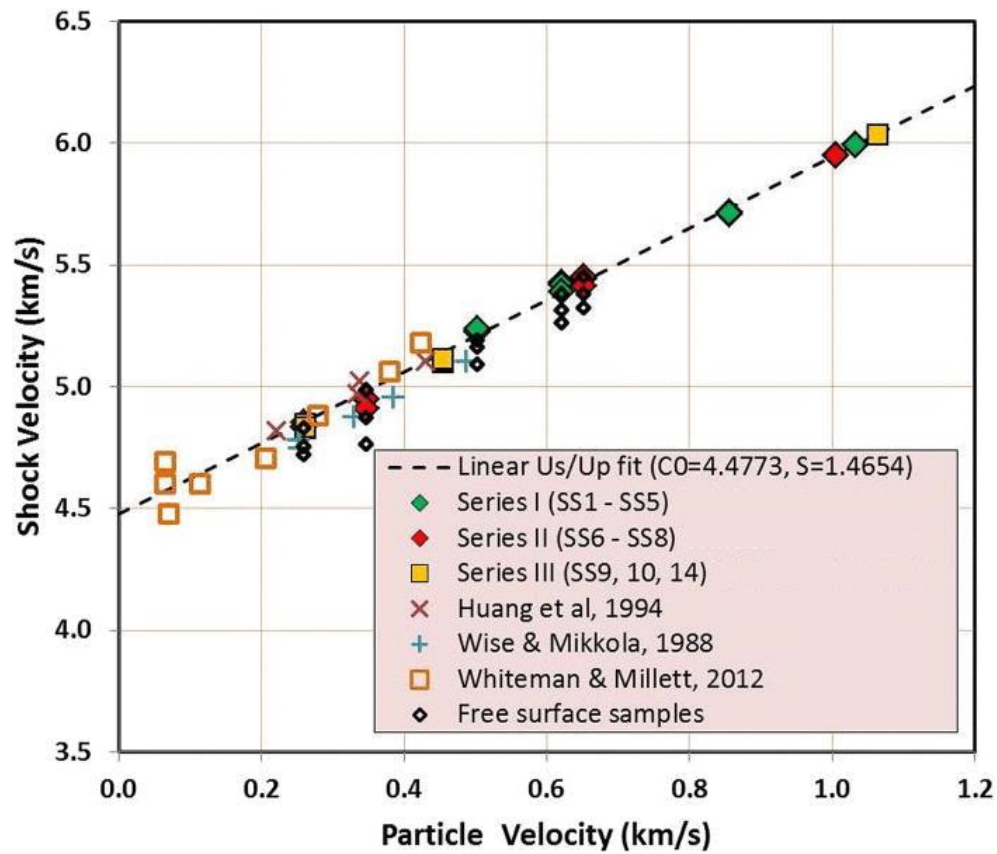


Figure 4.3 Equation of state plot for steel (Furnish et al. 2014)

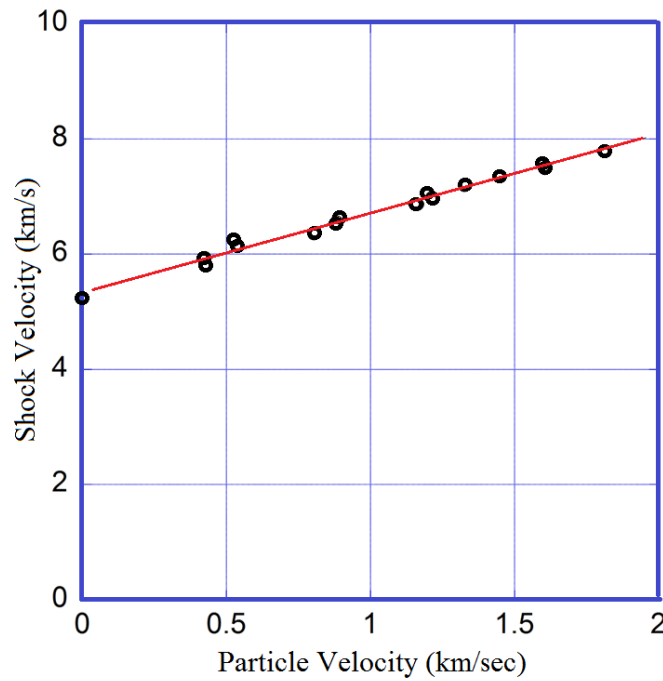


Figure 4.4 Equation of state plot for aluminum (Jordan and Melvin, 2012)

In view of the results presented in these figures and concerning the particle velocity values that are valid for this research, the shock wave velocity can confidently be taken to be equal to the speed of sound  $U_0$  for steel and aluminum in the calculations,  $U_s=U_0$ .

The conservation of energy expression above, providing a relation between pressure  $P$  and density  $\rho$ , is generally named as the Rankine-Hugoniot equation also known as the Hugoniot of the material. When analyzing shock waves in solids, it is widely accepted to approximate compression paths with the Hugoniot curve. The Hugoniot can be represented in any two dimensional plane where the most useful representations are either pressure-particle velocity or pressure-specific volume planes. The pressure-particle velocity Hugoniot is not a path that is followed, but rather the locus of all the possible states that can be achieved when a single shock wave passes through a material at a given initial state (Kanel et al. 2004; Meyers 1994). In application, the weak shock assumption is usually made, which is valid until shock waves are encountered with very large jumps in stress. The weak shock assumption can be made until a jump in stress around 270 GPa for steel. When the material obeys the weak shock assumption, the response path of the compression wave is coincident with the Hugoniot (Drumheller 1998). The weak shock assumption is, therefore, valid for the current study where the metal impactors that are involved in the analyses are exposed to much lower stresses.

The shock wave does not cause the material to move along the Hugoniot. Instead, the shock causes the material to jump between two points on the Hugoniot curve. These points are located at the intersections of the Hugoniot curve and the chord, which is named the Rayleigh line, connecting the initial state ( $P_0, u_0$ ) and final shocked state ( $P_1, u_1$ ) which is also shown in Figure 4.5 The slope of this Rayleigh line is equal to the dynamic impedance ( $Z$ ) of the material  $Z=\pm\rho_0U_0$ , which is one of the main parameters defining the dynamic properties of a material where  $\rho_0$  and  $U_0$  are the density and the sound wave velocity of the material, respectively.

Hugoniots with slope discontinuities due to transition from elastic to plastic behavior can thus have regions for which the initial state cannot be connected to the final state with a single Rayleigh line. In such cases the final state is reached by a series of two or more Rayleigh lines. At moderate pressures, Hugoniots of many materials are in their linear range (Drumheller 1998; Kanel et al. 2004; Meyers 1994).

### **4.3.2 Impedance Mismatch Method**

The pressure in a shock front follows the Rayleigh line, which corresponds to a discontinuity that can also be used in explaining the planar impact situation. When an impactor strikes a target with an impact velocity, the impact surface between the impactor and the target constitutes a discontinuity in particle velocity. The particle velocity ( $u_p$ ) is zero inside the target and is equal to the impact velocity ( $u_i$ ) inside the flyer plate, while the pressure is the ambient atmospheric pressure ( $P_0$ ) as can be seen in Figure 4.5. How the method was applied in a special form in this research will be explained in more detail

in section 4.4.3.2. Decomposition of the discontinuity causes the formation of two shock waves that propagate from the impact surface into the impactor and the concrete target, travelling in opposite directions (Meyers 1994). The states behind these shock waves must lie on the corresponding Hugoniot. In most planar impact studies, the pressure versus particle velocity relationship is analyzed using the main features of a method where the Hugoniot curves are intersected, which is called the impedance mismatch method. The graphical presentation of the impedance mismatch method is illustrated in Figure 4.5. The principle of equal pressures and particle velocities at the interface is satisfied at point  $P=P_I$ ,  $u_p=u_I$  (Meyers 1994).

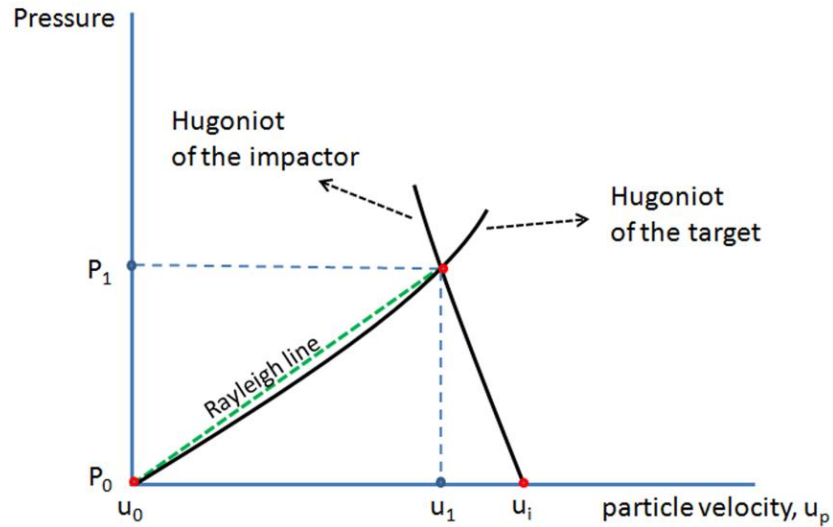


Figure 4.5 Graphical presentation of the impedance mismatch method (Meyers 1994)

### 4.3.3 Reverberation Technique

The experimental configuration in the tests performed for this study was slightly different from the impact situation described above, where there is one interface present. In the tests conducted for this investigation, the low impedance target materials, porous and normal concretes, are hit by a higher impedance impactor (steel or aluminum). The steel base structure of the set-up constitutes a second interface with the target material and causes the compression wave to reflect back into the specimen. Therefore, the situation in these tests can be considered to be a low impedance material that is impacted while being located between two high impedance media. A one-dimensional stress wave propagating in different media can be presented using a Lagrangian diagram where  $x$  is the spatial coordinate and  $t$  is time. Stress and particle velocity measurements in shock wave experiments are normally performed in Lagrangian coordinates because the position of the sensor relative to the material particle is fixed (Antoun et al. 2003). Even though the interface between the impactor and the target moves downwards with the particle velocity ( $u_p$ ), this should not be observable in the diagram when compared to the speed of the wave itself (Zukas 1990).

However, because the motion of the interface between the impactor and the target is measured during the experiments, the displacement of the interface is also shown in the diagram given in Figure 4.6. In the diagram, time  $t=0$  corresponds to the instant of collision.

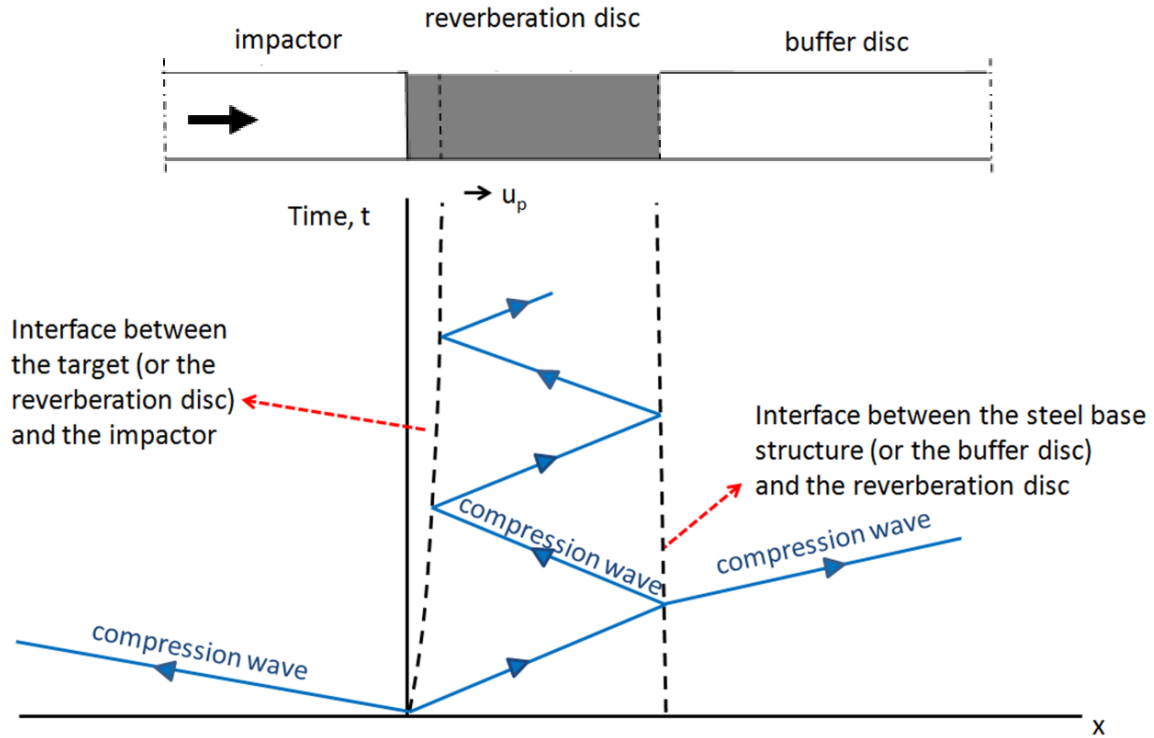


Figure 4.6 Lagrangian diagram for a low impedance material impacted between two high impedance media

The configuration where the sample is impacted between two materials of higher dynamic impedances has been investigated by several researchers (Kanel et al. 2004; Lysne et al. 1969; Kondo et al. 1981). In those experiments, a projectile disc (or impactor) is impacted onto a stationary target, which is also called the reverberation disc. The reverberation disc is made of a linear elastic material having a lower dynamic impedance than the disc that strikes it. The schematic presentation of the discs is also included in Figure 4.6. The target is backed by a buffer disc having a dynamic impedance again higher than the dynamic impedance of the target itself. With the collision, two compression waves propagate away from the interface between the projectile disc and the target. The dynamic impedances of the target and the other two disks determine how the compression wave is reflected from the two interfaces, namely the interface between the projectile disc and one end of the target and the interface between the other end of target and the buffer disk. The reflection and transmission of a wave at an interface between two materials depend upon the ratio of their dynamic impedances  $K = Z^{MAT I} / Z^{MAT II}$ . The reflected wave keeps the sign of the incident wave when the dynamic impedances of the



materials from which it reflects are higher than the dynamic impedance of the material it propagates in. Therefore, depending on the relative values of the impedances of the target and the two discs that are in contact with it, each reflection successively increases the amplitude of the compression wave propagating in the target.

Because the target has a much shorter height compared to the heights of the projectile and buffer discs, many wave reflections take place after the collision. In the corresponding reverberation studies presented in literature, the target is a linear elastic material with a dynamic strength that is sufficient to withstand the maximum stress that can be applied by that test configuration at that impact velocity. This maximum stress corresponds to the intersection of the Hugoniot curves of the projectile and buffer disc materials. Therefore, stress continues to increase until that final value is reached through multiple reverberations which is also considered to be a state of equilibrium in pressure (Kanel et al. 2004; Lysne et al. 1969; Kondo et al. 1981). This situation is illustrated in Figure 4.7 where the impedance mismatch technique is applied in a special manner because of the repetitive reflections and the presence of two interfaces. Different from the typical impedance mismatch representation illustrated in Figure 4.5, in Figure 4.7 the two main inclined lines are the Hugoniot of the impactor and the buffer disc materials, while the lines that travel between those two Hugoniot represent the behavior of the reverberation disc material that is compacted in between. The Hugoniot lines of the impactor and the buffer material intersect at stress ( $P_e$ ) and particle velocity ( $u_e$ ) values that can be considered to be an equilibrium for pressure. The figure also illustrates how the amplitude of a compressive shock wave in the target specimen increases, where the compressive stress is taken positive.

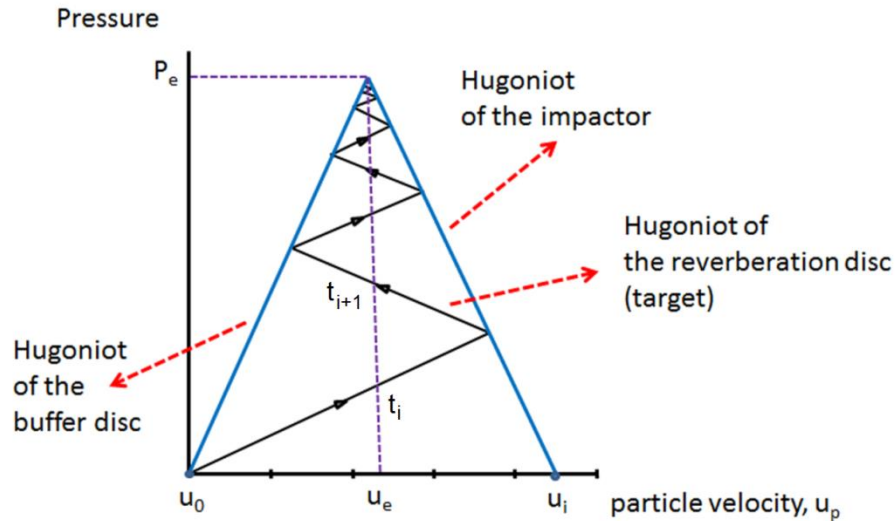


Figure 4.7 Impedance mismatch graph for a linear elastic reverberation disc (Kondo et al.1981)

This analysis can also be applied when testing nonlinear materials with dynamic strengths that are not sufficient to withstand the maximum stress that can be applied by the test

configuration. In the tests conducted in this research, the targets being either porous concrete or normal concrete, slightly changes the properties of the reverberation process. Similar to the case described above, the target has a small height compared to the impactor and the steel base structure.

Therefore, the shock wave that travels in the target makes again some reflections before waves that travel in the impactor and the set-up reflect back as tension waves from the top surface of the impactor and the bottom surface of the test set-up, respectively. Because of its height (more than 80 cm), the steel base structure can even be considered as a wave sink. The reverberation process that occurs in the concrete impact tests mentioned above are different from the case when a strong linear elastic material is tested. The reverberation situation, when testing concrete, continues until the stress within the concrete specimen reaches a value that generates substantial inelastic strains in the material beyond which further wave propagation within the specimen can be neglected. The amplitude of the subsequent wave fronts will be very small (Ramesh 2009). This situation and the related wave reverberations can be seen in the impedance mismatch figure illustrated in Figure 4.8. The red spots indicated on the Hugoniot of the impactor represent the points where the Hugoniot of the impactor and the target material intersect i.e. the points where the stress and particle velocities of the target and the impactor are equal. In the figure, those points eventually come to an equilibrium level that corresponds to a constant value of stress ( $P_e$ ). The velocity values of those points are measured by the Doppler laser velocimeter during the test when the falling impactor and the target come into contact and with the subsequent reverberations, the pressure come to an equilibrium. Because the particle velocity of the impactor is measured at its interface, it reaches an approximately constant value when the pressure reaches equilibrium, as seen in Figure 4.8. This velocity value is named equilibrium velocity ( $u_e$ ).

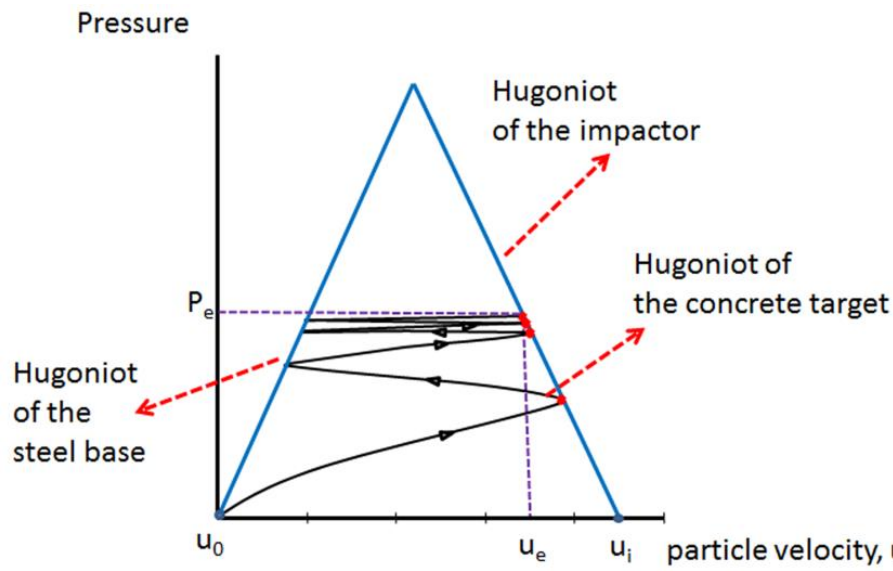


Figure 4.8 Impedance mismatch graph for a concrete target impacted between two metals

## 4.4. Experimental Investigations

### 4.4.1 Materials

For the dynamic experimental investigation, nine different types of porous concretes were cast. To be able to compare their properties with normal concrete, a moderate strength plain concrete was also produced. Since data on the dynamic properties of plain concretes is available in the literature, testing normal concrete also contributed to the validation of the testing techniques by comparing the results with the literature. The properties of the porous concrete mixtures produced for the dynamic analyses are presented in Table 4.1 while the composition of the normal concrete is given in Table 4.2. It should be noted that these mixture compositions are the same as those of the mixtures of the samples used for investigating the static properties given in Chapter 3 in order to compare the static and dynamic properties along with the fragmentation behavior.

Table 4.1 Compositional properties of the porous concrete mixtures (The content for one sample is presented because one porous concrete sample was cast from each batch.)

Mixture code	PRC1	PRC2	PRC3	PRC4	PRC5	PRC6	PRC7	PRC8	PRC9
Aggregate composition									
Crushed basalt (2-4 mm) (gr)	-	2000	1000	-	-	2000	1000	-	-
Crushed basalt (4-8 mm) (gr)	2000	-	1000	-	2000	-	1000	2000	-
River gravel (4-8 mm) (gr)	-	-	-	2000	-	-	-	-	2000
Cement paste composition									
Cement (gr)	351	351	351	351	298	298	298	351	351
Silica fume (gr)		-	-	-	53	53	53	-	-
Water (gr)	105	105	105	105	105	105	105	105	105
Superplast. (gr)	0.97	0.97	0.97	0.97	1.30	1.30	1.30	1.00	1.00
Set retarder (gr)	1.20	1.20	1.20	1.20	1.20	1.20	1.20	-	-
Cement paste code	cp1	cp1	cp1	cp1	cp2	cp2	cp2	cp3	cp3
Compaction	high	high	High	high	high	high	high	low	low

Table 4.2 Compositional properties of the normal concrete mixture (NC1)

NC1 composition	Amounts (g per 2.5 dm <sup>3</sup> )
CEM I 42.5N	1033
0.125-0.250 mm sand	440
0.250-0.500 mm sand	813
0.500-1 mm sand	940
1-2 mm sand	940
2-4 mm sand	1253
4-8 mm river gravel	1880
Water	583
superplasticizer	19

Both porous and normal concrete specimens were wrapped with plastic and aluminum foils directly after demolding and kept at 20°C at the laboratory conditions until their testing dates of 28 days. Cylindrical specimens that were 83 mm in diameter, 170 mm in height were cast. Two core samples of 60 mm diameter were then drilled from the specimens and cut at the fixed height of 70 mm to be tested at the drop weight impact test.

The two impactors used at the tests were made of steel and aluminum. The material properties of the impactors used are critical in the sense that they are directly involved in the impact stress calculations. Using the elasticity modulus and the Poisson's ratio values provided by the manufacturer, the shear and bulk moduli were calculated. With these values, the longitudinal wave velocities of the materials of the impactors were calculated with Eq. 4.7. The material properties of the impactors are presented in Table 4.3.

$$C_l = \sqrt{\frac{K + \frac{4G}{3}}{\rho}} \quad (4.7)$$

Table 4.3 Properties of the materials used in the impactors

Material properties	Steel	Aluminum
Elasticity modulus, $E$ (GPa)	200	69
Density, $\rho$ (g/cm <sup>3</sup> )	7.9	2.7
Poisson's ratio, $\nu$	0.28	0.33
Shear modulus, $G$ (GPa)	78.1	25.9
Bulk modulus, $K$ (GPa)	151.5	67.7
Longitudinal wave velocity, $C_l$ (m/sec)	5690	6155

#### 4.4.2 Measuring Impact Stress Using a Piezoresistive Gauge

As a starting point for finding a measurement technique for determining the impact strengths of the porous concretes, piezoresistive manganin stress gauges were used. By making direct measurements using the stress gauges, stress histories in shock-loaded specimens were obtained without further analyses.

##### 4.4.2.1 Test Set-up and Instrumentation for Stress Gauge Measurements

The impact stress measurement system consisted of the manganin stress gauge/gauges implemented on the specimen, a voltage box that also included an amplifier and the oscilloscope itself as the data recorder.

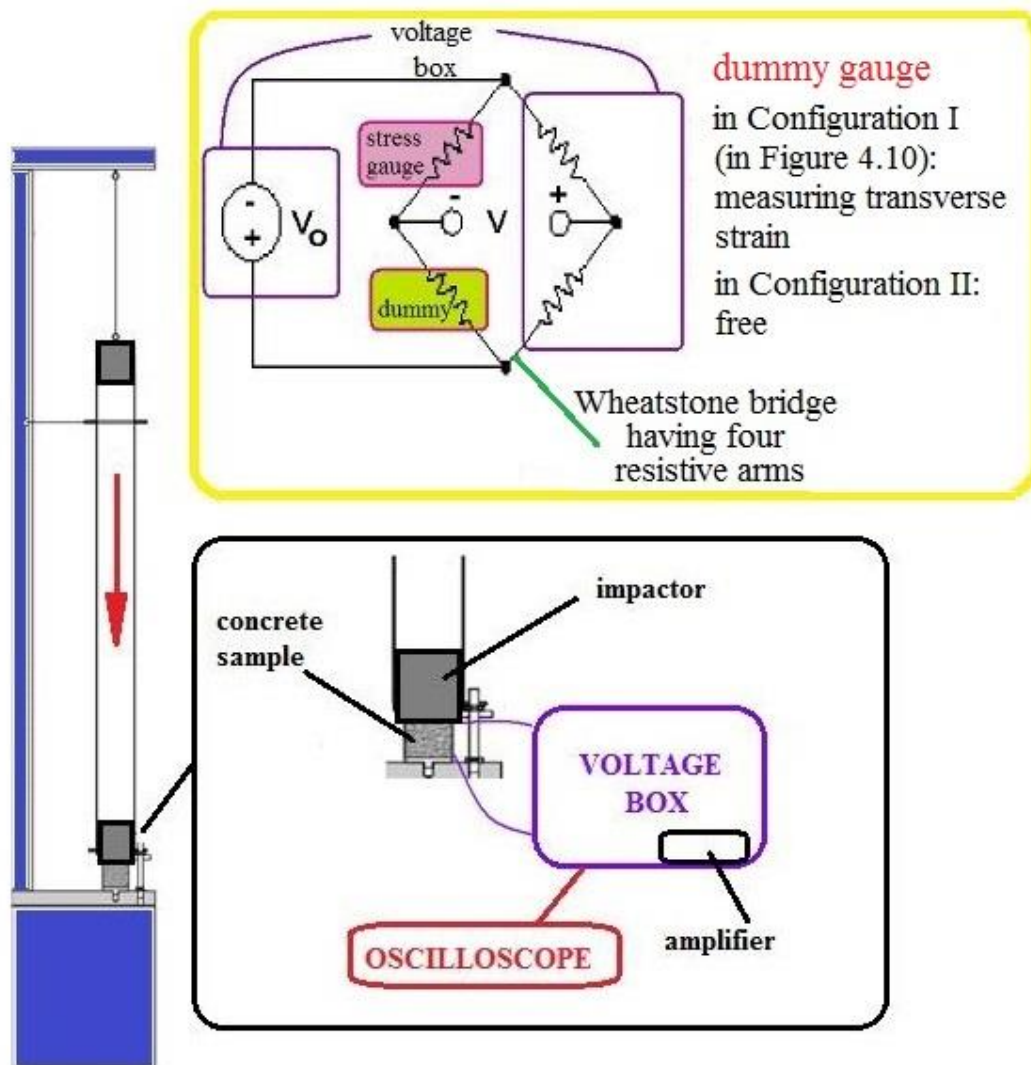


Figure 4.9 Stress gauge measurement test set-up

The manganin gauges were organized in a bridge system. The amplifier worked as a signal conditioner, which was selected depending on the specific type of gauge used, in order to get a relevant voltage signal that can be recorded by the oscilloscope. LM-SS-125CH-048 Micro-Measurements manganin stress gauges were used in the experiments. All stress gauges have to be calibrated before testing in order to relate the resistance to stress. Therefore, static calibration tests based on loading-unloading cycles were performed on the gauges using a test cell where a stress-resistance relation of 6.6 mV/kN was found. In the presented test results, both the voltage output and the calculated stress values are given on different axes. The testing configuration is shown in Figure 4.9.

A thin layer of rubber was placed on the specimens to transfer the load applied by the impactor to the specimen without breaking the stress gauge. After trying different thicknesses and types of rubbers, a 2 mm thickness soft rubber was found to give the best results (see also Figure 4.10). The purpose of using manganin stress gauge is to measure the stress normal to the direction of the shock wave. In practice, piezoresistive gauges also respond to both stress and strain along the gauge plane (Antoun et al. 2003). Therefore, an attempt was made also to record the strain data by placing the dummy gauge into the hollow space that had been prepared in the capping material. The hollow space was prepared so that the dummy gauge is not exposed to any normal stress while it responds to the transverse strain because it is bonded to the upper surface of the specimen as in configuration I in Figure 4.10.

Normally, the dummy gauge is left free of any stress and strain, as in configuration II in Figure 4.10. When the results of the two options are compared, there was not a significant difference between the values, so the tests were performed with configuration II where the dummy gauge of the Wheatstone bridge (see Figure 4.9) is left free, not glued on the specimen.

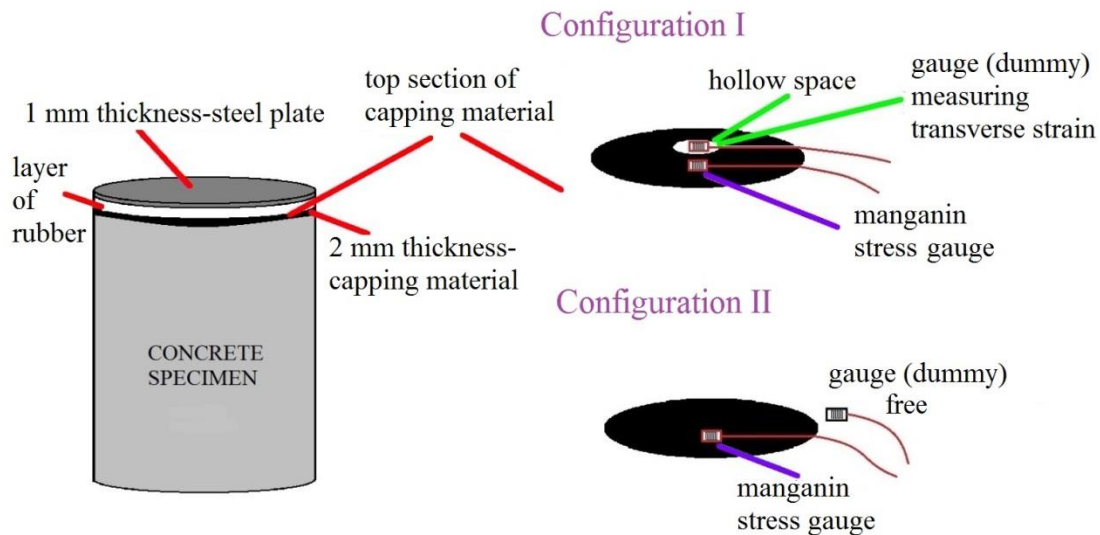


Figure 4.10 Target sample - stress gauge configurations

Initially, an aluminum specimen (as shown in Figure 4.11) was prepared with stress gauge/gauges installed on the specimen. The complete experimental configuration have been tried repeatedly in order to check the consistency of the results. An aluminum sample was chosen because it has a lower dynamic impedance compared to the steel impactor. Therefore, the impact situation where a high impedance impactor hits a lower impedance target still holds (as in the case where the target is concrete). Additionally as an advantage, the aluminum specimen is strong enough to stay intact during the experiments, which is not the case when testing concrete samples. Therefore, the tests were repeated many times and showed that the gauges are damaged only after many hits. After the aluminum trial tests, real porous concrete samples with installed stress gauges were prepared and tested.

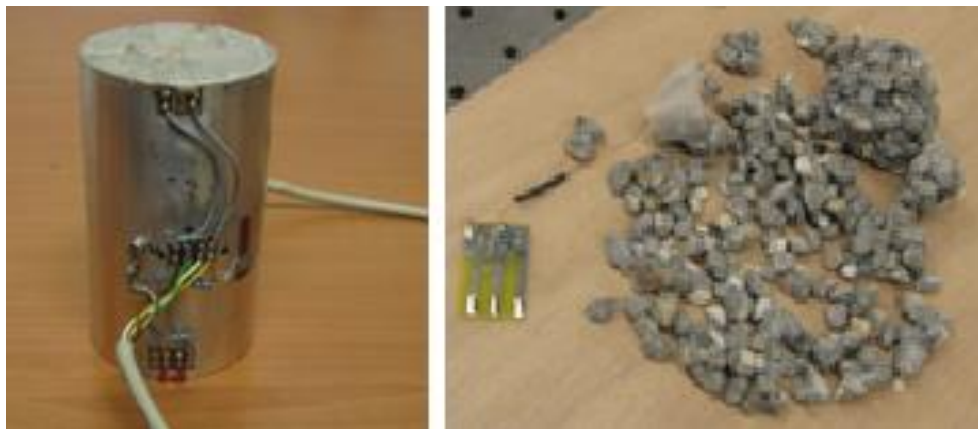


Figure 4.11 Photographs of aluminum and porous concrete samples after testing

The representative stress (also resistance) histories of three porous concrete specimens from mixture PRC9 are given in Figure 4.12. The curves present the impact stresses that are exerted by the impactor to the samples. All the samples failed and fractured into small fragments during the tests as seen in Figure 4.11. The peak stresses obtained at the porous concrete tests are the impact strengths of the samples.



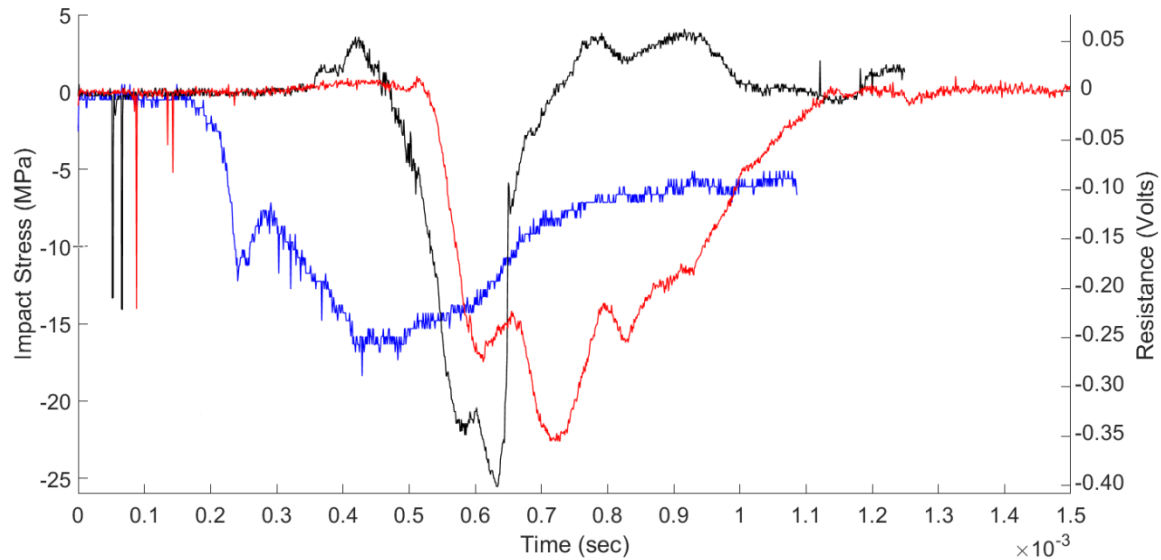


Figure 4.12 Stress (also resistance) histories of three PRC9 porous concrete specimens

Because the target porous concrete samples, that are being tested, drastically fracture into small pieces during the experiment, at nearly half of the tests, the stress gauge or the wires were damaged. Therefore, it was not possible to obtain any measurement data from those tests. This was the main problem in adapting this method to the drop weight testing of porous concrete. Another difficulty was that preparing each sample by precisely making a capping, installing the gauges and all the wiring was very time consuming. Since a very high number of samples has to be tested, it was not feasible to continue using this testing system for the project.

Important to mention is that the peak stresses obtained from the stress gauge records are close to the average values obtained from laser Doppler velocimetry (21.84 MPa) and high speed photography (23.07 MPa) for the same concrete mixture (PRC9). This was a verification for the LDV and high-speed photography testing configurations (the results of which will be presented in sections 4.4.4 and 4.4.6). Stress gauge measurements can be taken as reference because they provide a direct way of obtaining the impact stress. The curves appear to have similar characteristics. Local high stresses exist may be because of large aggregates that are present in the porous concrete mixture.

#### 4.4.3 Laser Doppler Velocimetry (LDV) Investigations

In the scope of this research, an experimental configuration for the determination of the dynamic response of porous concretes in a drop weight impact test was introduced based on Laser Doppler Velocimetry. The main features of the measurement method are presented in Figure 4.13. In the drop weight impact tests the particle velocity histories of the interface (between the impactor and the concrete target) were captured using LDV. The data was analyzed using a special application of the reverberation technique where the dynamic impedance of the impactor was required as input. As a result of the analyses,



the impact strengths of the target concrete samples were obtained (Agar Ozbek et al. 2012).

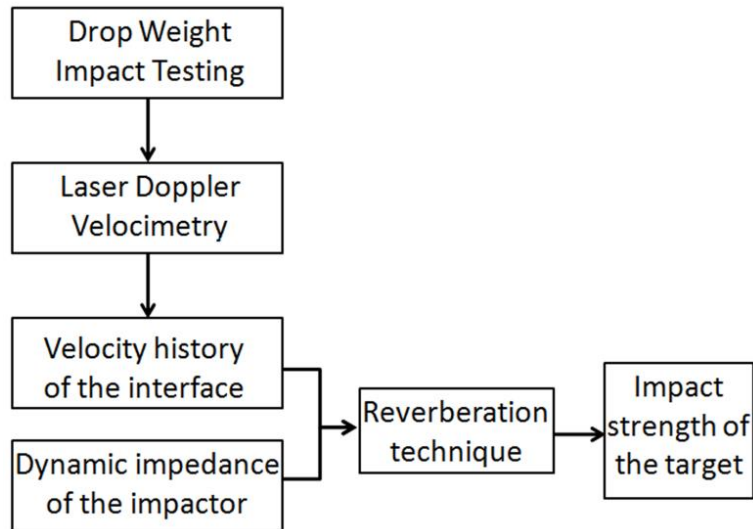


Figure 4.13 The main features of the method used

#### 4.4.3.1 LDV Test Set-up and Instrumentation

The impact tests were carried out using an instrumented drop-weight impact test set-up. In the experiment, the specimen was placed vertically on a steel base structure, which also serves as a steel buffer plate that functions as a wave sink at the impact experiments. The impactor was dropped from approximately 1.2 m to provide striking velocities ranging between 4.0 - 4.7 m/sec. The selection of the impactor material and the magnitude of the impact velocity determine the pressure applied to the concrete sample. Therefore, by varying those properties, the input pressure could be controlled. The impactors that were made of either steel or aluminum were 110 mm in diameter and 220 mm in height.

A Doppler laser vibrometer was utilized to measure the velocity of the falling impactor. The schematic figure showing the general view of the testing system and an enlarged view of the orientations of the retro-reflective sticker and the 45-degree mirror are presented in Figure 4.14.

For the purpose of measuring the velocity of the interface between the impactor and the target, an easily applicable measurement method has been introduced and verified in this study. The impactor diameter (110 mm) was selected to be larger than the diameter of the target (60 mm) so that there was an outer rim of 25 mm present to take velocity measurements at the interface. The point where the laser beam hits the impactor was adjusted to be as close as possible to the specimen perimeter, in the inside locations of the rim (which is indicated with a red arrow in Figure 4.15). The laser beam coming from the laser head following a horizontal path was reflected by an angle of 90° from a 45-degree

mirror such that it was directed vertically upwards. The reflected vertical beam hitting the retro-reflective sticker attached to the bottom surface of the impactor rim was then reflecting and following the same path back to the laser head. The captured particle velocity time histories of the interface between the target and the impactor were subsequently processed to determine the impact stress applied on the target.

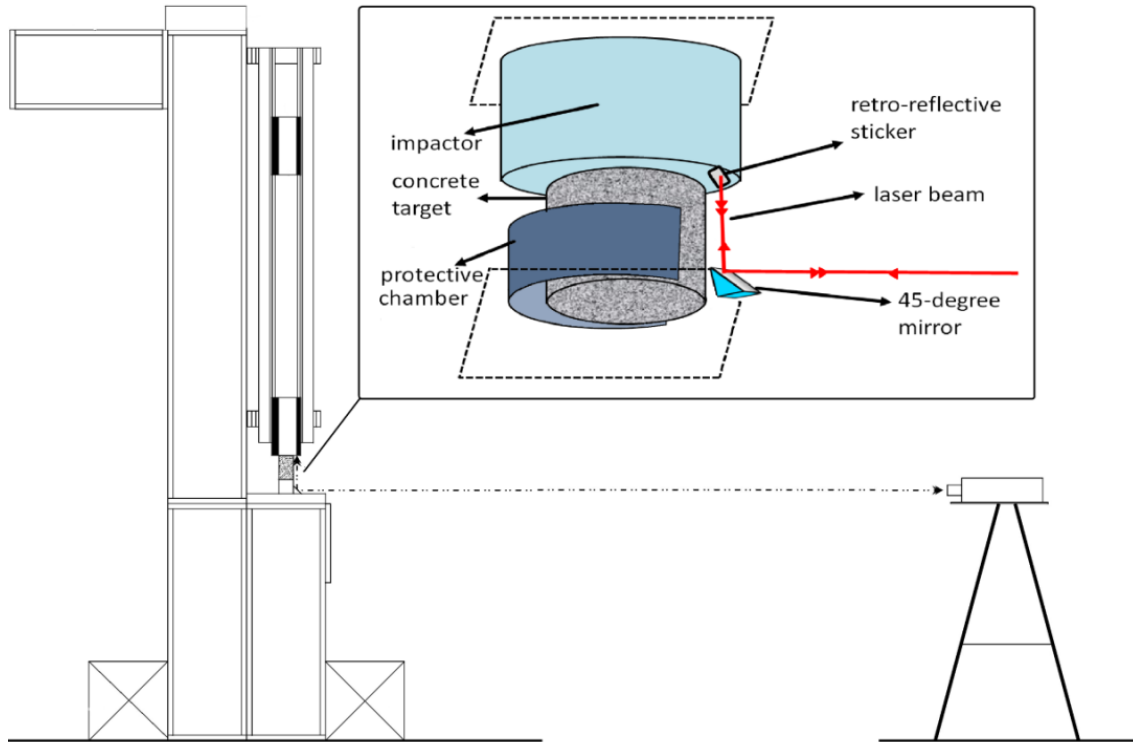


Figure 4.14 Schematic view of the measurement configuration

The photographs of the Doppler vibrometer sensor head and the drop weight impact test set-up are shown in Figure 4.15. The bottom surface of the impactor is also shown in detail in the photograph where the retro-reflective sticker at the bottom surface that looks very shiny even when exposed to camera flash light and the reflecting laser beam (seen as a red point indicated by the red arrow in the figure) are also visible.



Figure 4.15 Test set-up, laser vibrometer sensor head and the bottom surface of the impactor

During the test, after the free falling impactor hits the stationary target specimen with the impact velocity, it starts to decelerate as expected. After its velocity is decreased due to its contact with the target, the impactor is subsequently brought to rest by a protective chamber, which acts as a stopper (shown in Figure 4.14). The height of the protective chamber was approximately 2.5 cm shorter than the specimen height. After the collision with the target, the impactor was stopped by the protective chamber to protect the target, which had already failed due to the stress waves. This is done especially because the sizes of the broken fragments are critical in evaluating the feasibility of using porous concretes for safety applications and also to protect the 45-degree mirror that is placed under the impactor. The horizontal dimensions of the chamber (110 x 120 mm) were selected to be larger than the cross-section (60 mm diameter) of the sample. Therefore the chamber could accommodate specimens without forming any lateral confinement.

A Polytec OFV 505 laser head and OFV 5000 controller with VD 06 velocity decoder were used in the experiments. The laser light involved in the measurements was an eye-safe He-Ne laser with a wavelength of 633 nm. The OFV 5000 controller had a sampling frequency capacity of 2 GHz. Measurements with sampling frequencies of 500 kHz and 400 kHz were taken by using a LeCroy Wavesurfer 432 digital oscilloscope. The trigger threshold was set at the velocity of 3 m/sec, where the measurement block length and trigger delay time were set at 2 sec and -1 sec, respectively. Therefore, the saving of the data was done starting from 1 sec before the velocity reaches the value of 3 m/sec until 1 sec after that value. This period is sufficient to capture the whole impact process along with the free fall of the impactor before the collision.

#### 4.4.3.2 Analysis of particle velocity histories

The particle velocity becoming nearly constant as the pressure reaches equilibrium can be seen in the velocity histories measured during the tests. In Figure 4.16, a typical Doppler laser velocimetry signal from a drop weight impact experiment of porous concrete impacted by a steel impactor is given. In the figure, the first part that seems horizontal corresponds to the free fall of the impactor and has a slope that is close to the gravitational acceleration. Due to the friction between the impactor and the set-up, the acceleration at that portion of the curve was measured to be slightly lower than the gravitational acceleration. After the free fall part, there is the collision followed by wave reverberations that end up at the equilibrium of the stress that also corresponds to a nearly constant particle velocity. The plateau corresponding to this equilibrium state is clearly observed in all the tests that have been conducted on porous concretes and the normal concrete that have been impacted with a steel impactor.

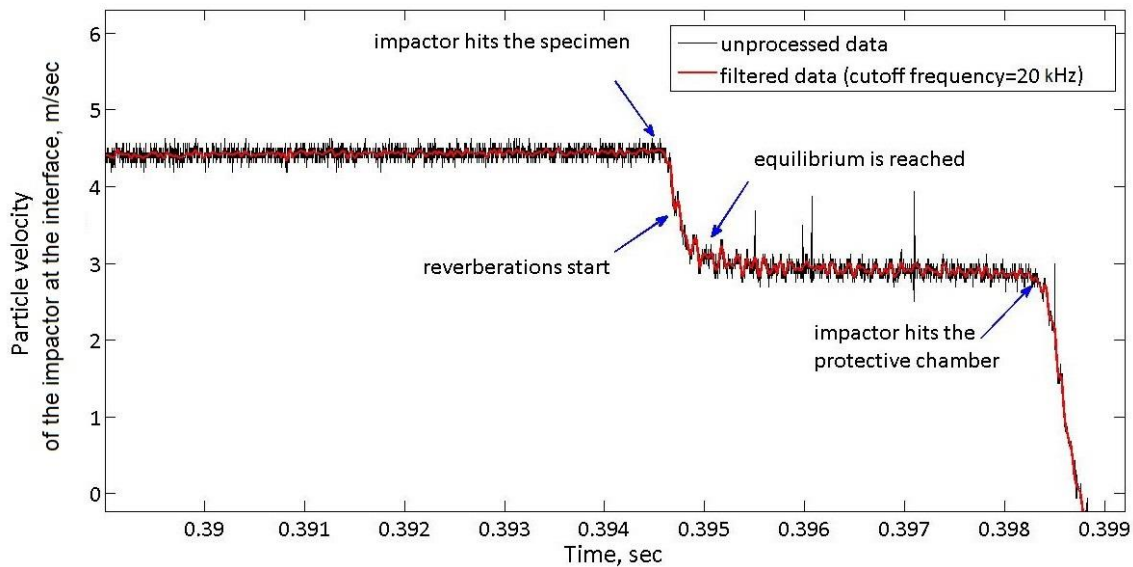


Figure 4.16 Doppler laser velocimetry signal from a drop weight impact test of porous concrete

The last part of the plateau in the figure corresponds to the part, at which the impactor hits the protective chamber (shown in Figure 4.16) that has a shorter height than the specimen, where the particle velocity very rapidly becomes zero. Afterwards it bounces back. Since the particle velocity value that corresponds to equilibrium in pressure, i.e. the equilibrium velocity, is extracted from the very beginning of the plateau, this last portion of the data has already no significance. The relative heights of the protective chamber and the target determine the interval of time before the impactor contacts the stopper and therefore the length of the plateau. Along with the raw data that is measured with the frequency of 400 kHz, the filtered data with a cutoff frequency of 20 kHz is presented in the figure.

Considering the time at which the equilibrium velocity is reached after the impact, about 0.5 msec, it can be seen that this time is larger than the time at which the peak forces are reached in the studies of very high speed impact testing reported in literature. This is caused by the low impact velocity and, therefore, the low strain rate of the drop weight impact test performed. It was presented in low velocity impact studies that the peak impact force was reached earlier as the velocity of the projectile increased, i.e. a shorter period of time to reach the peak force after the impact. For velocities varying between 26-93 m/sec the peak force was reached after 0.05-0.60 msec, respectively (Wu et al.1994, Perez-Castellanos 1997). Therefore, the time to reach the equilibrium velocity in the drop weight tests conducted for the current study is consistent with the results presented in the related studies (Wu et al.1994, Perez-Castellanos 1997).

Reverberation application of the dynamic impedance technique was used in the analyses. In the calculations, as explained in the section on analysis of one-dimensional wave propagation, the shock wave velocities of steel and aluminum impactors were taken to be equal to the speed of sound  $U_s=U_0$  according to the equation of state (EOS) of the materials, which are also presented in Figures 4.3 and 4.4. The conservation laws are actually the principles behind the Hugoniot relations and the impedance mismatch technique. To be able to obtain the stress from the particle velocity measurements, conservation of momentum law is used where the stress is calculated using the equilibrium velocity and the slope of the pressure-particle velocity Hugoniot of the impactor using Eq. 4.8. According to the conservation equation, the pressure  $P$  applied to the target material is determined by the momentum transferred by the impactor to the target per unit time as shown in Eq. 4.8 (see also Eq. 4.4).

$$P_e - P_0 = \rho_0 U_0 (u_i - u_e) \quad (4.8)$$

where,  $P$ ,  $P_0$ ,  $\rho_0$ ,  $U_0$ ,  $u_i$  and  $u_e$  are the shock pressure, initial pressure, initial density, wave velocity, impact velocity and the equilibrium velocity, respectively. For shock waves travelling in solids, the shock pressure  $P$  is much greater than the initial ambient atmospheric pressure  $P_0$ . Therefore,  $P_0$  is usually neglected and removed from the conservation equations involving solids (Kanel et al. 2004; Meyers 1994). When the equilibrium in pressure is reached, the target material with zero velocity reaches an approximately constant particle velocity corresponding to the equilibrium in pressure and the impactor with the impact velocity decelerates down to the same velocity (Kanel et al. 2004). The analyses of the particle velocity histories were done by first extracting the impact and equilibrium velocities from the experimental graph as in Figure 4.16. Then, by using Eq. 4.8, the impact stress was obtained. Since the concretes that were tested had reached their dynamic strength values, the stress that is calculated is also the dynamic strength of the specimen tested.

#### **4.4.4 Laser Doppler Velocimetry Results and Discussion**

In the experiments, the particle velocity histories were measured for nine different types of porous concretes and one normal concrete (Agar-Ozbek et al. 2012, Agar-Ozbek et al. 2013). All the specimens that were tested failed during the impact.

The first series of LDV measurements were conducted to demonstrate how the proposed experimental technique can be used to analyze the performance of porous and normal concretes under impact loading. In the first series, two different types of porous concretes were tested by impacting each type with two different types of impactors (steel and aluminum). The purpose of performing these tests was validating the consistency of the technique by testing the specimens from the same mixture with two different impactors having different dynamic impedances. In the tests, it was proven that the same dynamic strength values are obtained through using different impactors. Before the concrete tests, in order to verify the measurement set-up, a set of tests with, the collision of an impactor and a target that were made of the same material (aluminum) was also performed. This is also known as symmetric impact. This test is important in the sense that when identical material discs collide, the equilibrium reached should be at a velocity of exactly half the impact velocity. It was possible to capture this behavior at the half of the impact velocity owing to the high sampling frequency of the experiment i.e. the high number of data points measured.

In summary, the impact strengths of nine different types of porous concretes and one mixture of normal concrete were investigated. The measurement method was verified and the effects of different compositional factors on the properties of porous concrete were evaluated.

##### **4.4.4.1 Impact test results of porous concretes tested with different impactors**

In the first series of tests, each of the two types of porous concretes was tested by using steel and aluminum impactors of the same geometrical size. The results of the first series of tests are presented in Table 4.4. The averages of the dynamic strength results were 26.26 (with a standard deviation (std) of 2.61 MPa) and 25.48 MPa (std 1.71 MPa) for PRC8 tested with steel and aluminum impactors, respectively. The average results for PRC9 were 21.84 (std 2.22 MPa) and 22.93 MPa (std 1.29 MPa) again for steel and aluminum impactor tests, respectively. The results obtained for the same mixture, when tested with two impactors having different dynamic impedances, were approximately the same for both porous concrete mixtures. This proves that the measurement principle is sufficient irrespective of the type of metal selected for the impactor. From the comparison of the test results obtained with steel and aluminum impactors it can be said that, as the dynamic impedance of the impactor increases, the equilibrium velocity is also higher and the difference between impact velocity and the equilibrium velocity is lower. However, it should also be noted that both impactors are suitable for testing porous concrete since the

dynamic impedance for both aluminum and steel are much higher than that of porous concrete.

Table 4.4 Results of impact tests on porous concretes tested with different impactors

Mixture code	Impactor	Sample no	Impact velocity ( $u_i$ ) (m/sec)	Particle velocity at pressure equilibrium ( $u_e$ ) (m/sec)	$\Delta$ Particle velocity ( $\Delta u$ ) (m/sec)	Dynamic strength (from Eq. 4.8) (MPa)
PRC8	steel	1	4.46	3.90	0.56	25.17
PRC8	steel	2	4.34	3.72	0.62	27.86
PRC8	steel	3	4.30	3.67	0.63	28.31
PRC8	steel	4	4.34	3.73	0.61	27.42
PRC8	steel	5	4.33	3.84	0.49	22.02
PRC8	aluminum	1	4.58	2.91	1.67	27.75
PRC8	aluminum	2	4.59	3.08	1.51	25.09
PRC8	aluminum	3	4.65	3.13	1.52	25.25
PRC8	aluminum	4	4.52	2.94	1.58	26.24
PRC8	aluminum	5	4.56	3.17	1.39	23.09
PRC9	steel	1	4.43	3.95	0.48	21.57
PRC9	steel	2	4.40	3.88	0.52	23.37
PRC9	steel	3	4.47	4.02	0.45	20.22
PRC9	steel	4	4.49	3.94	0.55	24.72
PRC9	steel	5	4.55	4.12	0.43	19.33
PRC9	aluminum	1	4.46	3.03	1.43	24.19
PRC9	aluminum	2	4.49	3.07	1.42	23.56
PRC9	aluminum	3	4.54	3.28	1.26	20.85
PRC9	aluminum	4	4.34	2.93	1.41	23.43
PRC9	aluminum	5	4.41	3.11	1.30	22.63

#### 4.4.4.2. Symmetric impact test results

In the second series of experiments, symmetric impact tests by impacting an aluminum target with an aluminum impactor were conducted. The data acquisition and analysis procedures were identical to those of concrete testing. In these tests, a protective chamber was not present. A typical velocity-time history acquired at a symmetric impact experiment, also showing the equilibrium velocity portion, is demonstrated in Figure 4.17. In the figure, the unprocessed data measured with the frequency of 500 kHz and the filtered data with a cutoff frequency of 20 kHz are presented. The sudden peaks in Figure 4.17, which are formed due to the noise that is captured because of the high sampling

frequency of the testing technique, are therefore removed by the filter. In these tests, long plateaus were no longer observed. It should also be noted that the horizontal portion seen at the bottom part of Figure 4.17 is not a plateau, but only the part that shows the velocity of the impactor travelling upwards in the opposite direction after hitting and bouncing back from the aluminum target.

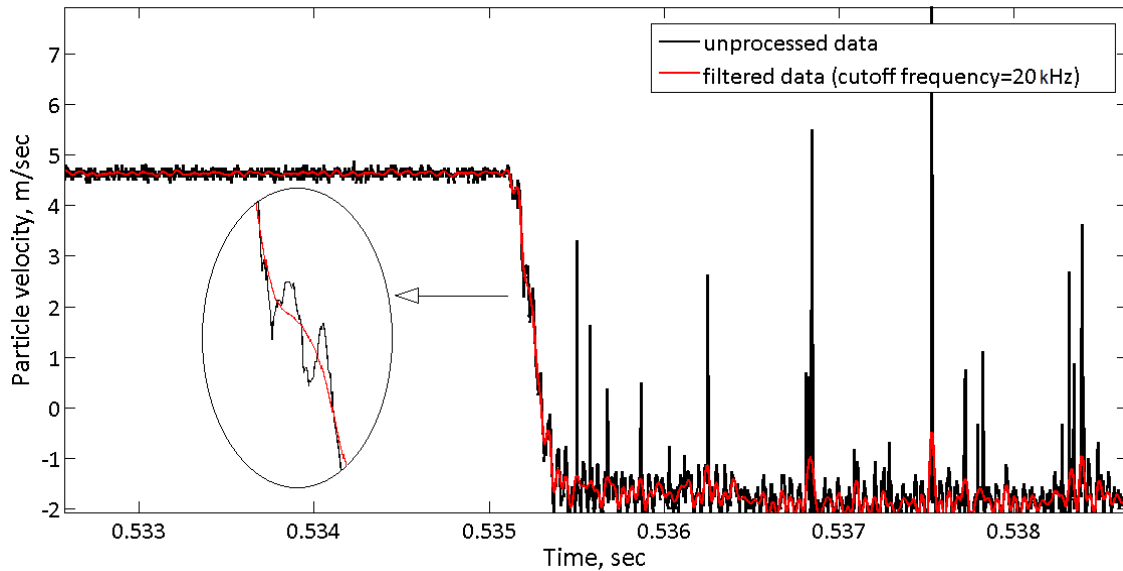


Figure 4.17 Velocity time history acquired at a symmetric impact experiment

The results of the symmetric impact experiments are given in Table 4.5. In the table, impact velocity and equilibrium velocity values along with their ratios are presented. When the target and the flyer plate are made of the same material, because the Hugoniot are symmetrical to each other (see Figure 4.18), equilibrium velocity i.e. the x coordinate of the intersection of the two Hugoniot, should be equal to half of the impact velocity. In Table 4.5, it can be seen that the equilibrium velocity is reached approximately at the half of the impact velocity. This confirms that the symmetric impact could be measured using the experimental configuration.



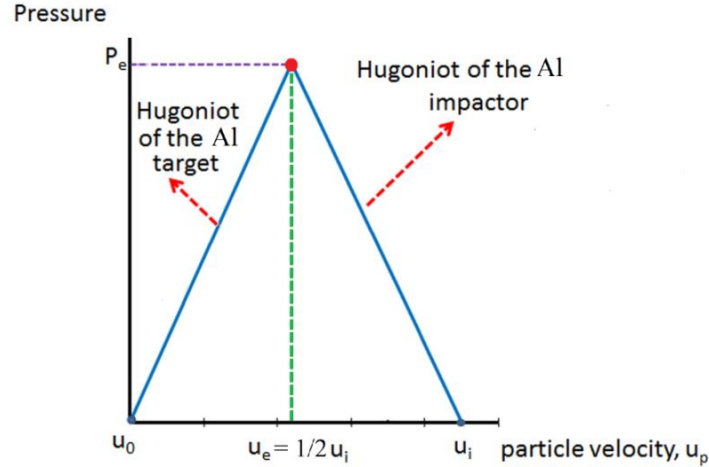


Figure 4.18 Impedance mismatch graph for symmetric impact

Table 4.5 Results of the symmetric impact experiments

Test no	Impact velocity (m/sec)	Equilibrium velocity (m/sec)	Equilibrium/Impact velocity ratio
1	4.64	2.47	0.53
2	4.66	2.39	0.51
3	4.64	2.45	0.53
4	4.60	2.56	0.56
5	4.61	2.42	0.52
6	4.59	2.38	0.52
7	4.60	2.27	0.49
8	4.61	2.59	0.56

#### 4.4.4.3 Particle velocity time histories measured for different porous concretes and normal concrete

The typical particle velocity-time history curves for two types of porous concretes (PRC1 and PRC8) having different static strengths and a moderate strength normal concrete (NC1) using a steel impactor are given in Figure 4.19.

The average static compressive strengths of the PRC1, PRC8 and NC1 mixtures were 34.8 MPa, 15.9 MPa and 26.4 MPa, respectively. When the locations of the plateaus with respect to the impact velocity are compared, the distinctions between the two porous concrete mixtures (PRC1 and PRC8) with different dynamic strengths can clearly be made. The average dynamic strengths of the PRC1 and PRC8 samples, having the particle velocity time histories presented in Figure 4.19, were found to be 66.52 MPa and 26.26 MPa (see Table 4.6), respectively. As in the impact tests of porous concrete samples, also in normal concrete tests, the plateau on the right was very clearly observed, as seen in Figure 4.19, and the samples failed completely in the test. The dynamic

strength was found to be 60.2 MPa for the specific normal concrete (NC1) sample shown in Figure 4.33.

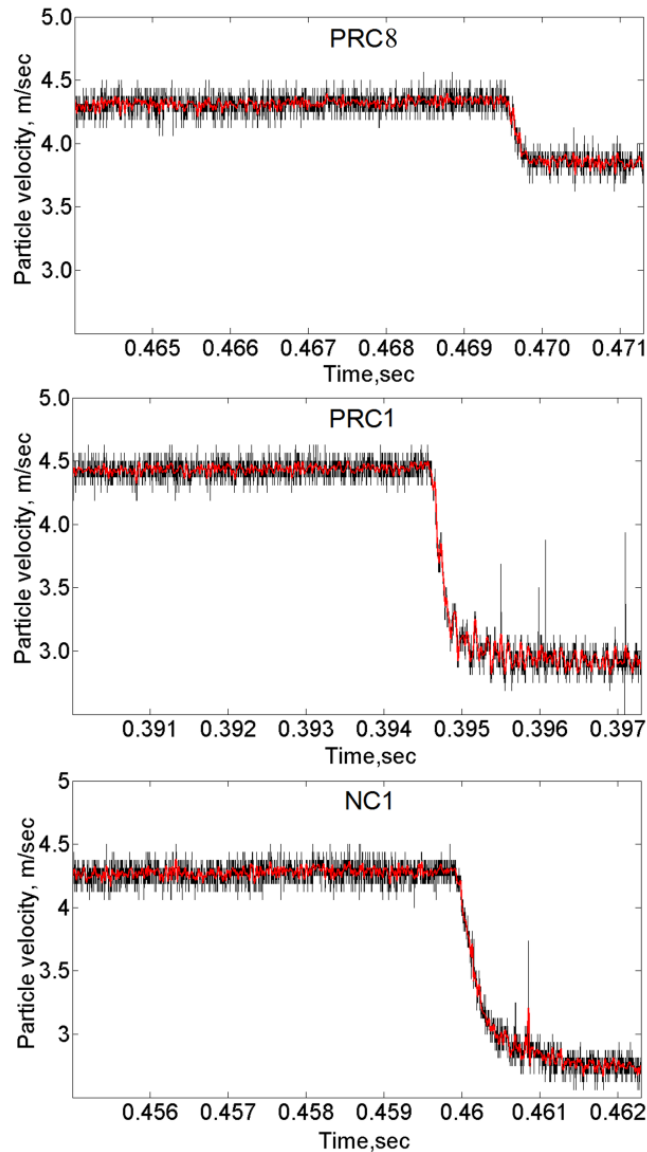


Figure 4.19 Particle velocity time histories for PRC1, PRC8 and NC1 samples

#### 4.4.4.4 Impact test results of different types of porous concretes and normal concrete

The results of the tests applied on porous concretes using steel impactor are presented in Table 4.6. Overall, it can be said that the testing configuration was precise enough to determine the differences between the various mixtures in an accurate way. If the results are evaluated in terms of the dynamic performances of porous concretes, it can be said that aggregate properties such as grading, size, shape, texture and strength have a major influence on the dynamic strength of porous concrete.

Table 4.6 Results of the impact tests conducted on different types of porous concretes

Mix code	Impact velocity (m/sec)	Equil. velocity (m/sec)	Dynamic strength (MPa)	Porosity (%)	Average dynamic strength (MPa)	Average static compressive strength (MPa)	Dynamic Increase Factor DIF
PRC1	4.46	2.93	68.76	21.78	66.52	34.78	1.91
PRC1	4.48	3.01	66.07				
PRC1	4.48	2.98	67.41				
PRC1	4.49	3.00	66.97				
PRC1	4.47	3.06	63.37				
PRC2	4.34	2.71	73.30	20.33	76.78	41.89	1.83
PRC2	4.50	2.73	79.59				
PRC2	4.52	2.83	75.86				
PRC2	4.47	2.78	76.09				
PRC2	4.53	2.77	79.05				
PRC3	4.31	2.42	84.81	18.77	85.99	50.49	1.70
PRC3	4.51	2.71	80.72				
PRC3	4.49	2.68	81.21				
PRC3	4.49	2.35	96.40				
PRC3	4.42	2.49	86.79				
PRC4	4.50	3.16	60.63	17.93	56.22	29.64	1.90
PRC4	4.42	3.22	53.84				
PRC4	4.46	3.12	60.36				
PRC4	4.47	3.40	48.27				
PRC4	4.49	3.20	58.02				
PRC5	4.49	3.24	55.91	21.98	53.09	31.60	1.68
PRC5	4.49	3.17	59.64				

PRC5	4.49	3.30	53.75				
PRC5	4.45	3.43	45.66				
PRC5	4.41	3.29	50.47				
PRC6	4.44	2.67	79.41				
PRC6	4.43	2.62	81.44	20.12	79.69	44.81	1.78
PRC6	4.48	2.63	83.28				
PRC6	4.54	2.88	74.63				
PRC7	4.48	2.79	75.86				
PRC7	4.47	2.47	90.25				
PRC7	4.46	2.73	77.93	18.63	84.37	48.80	1.73
PRC7	4.49	2.40	93.89				
PRC7	4.48	2.62	83.91				
PRC8	4.46	3.90	25.17				
PRC8	4.34	3.72	27.86				
PRC8	4.30	3.67	28.31	24.75	26.26	15.94	1.60
PRC8	4.34	3.73	27.42				
PRC8	4.33	3.84	22.02				
PRC9	4.43	3.95	21.57				
PRC9	4.40	3.88	23.37				
PRC9	4.47	4.02	20.22	-	21.84	13.09	1.73
PRC9	4.49	3.94	24.72				
PRC9	4.55	4.12	19.33				

The test results show that as two sizes of aggregates (2-4 and 4-8 mm) were used instead of single sized aggregates, the dynamic strengths of porous concretes as well as their static strengths increased. Among all the mixtures tested, the mixtures PRC3 and PRC7 with aggregates of two sizes gave the highest dynamic strengths. If their porosity values (18.77% and 18.64%, respectively) are also compared with the porosities of the other mixtures, it is seen that the dynamic strength of porous concretes increases with decreasing porosity. Aggregate grading is coupled with the total porosity which is the main factor that affects the strength.

For mixtures with single sized aggregates, it is seen that, with decreasing aggregate size the dynamic strength of the mixtures increases. The two mixtures PRC1 and PRC2 with single-sized aggregates and the same mixture compositions except their aggregate sizes (which were 4-8 mm and 2-4 mm, respectively), had dynamic strengths of 66.52 MPa and 76.78 MPa, respectively (see Table 4.6). A similar change in strength with the change in grading was seen in PRC5 and PRC6 (with 4-8 mm and 2-4 mm aggregates, respectively). If the porosity values for the mixtures are compared, it is seen that there are slight differences between the porosities of those mixtures. Because the aggregates were irregularly shaped crushed aggregates, smaller sized ones (2-4 mm) did pack slightly better compared to the larger ones (4-8 mm). This affected the porosity. While the total percentages of air pores in single-sized circular-shaped aggregate theoretical mixtures are normally expected to be similar irrespective of the aggregate size, this slight difference in porosity came from the irregularity of the aggregate shapes. The arbitrarily shaped and distributed pores, having more drastic effects on the global behavior when the aggregate size (and therefore the pore size) is greater, can also be a reason behind the differences in the ultimate dynamic strength values. The increase in dynamic strengths can also be explained by the increase in contact or bonding areas with decreasing aggregate size.

The difference in dynamic strengths of the PRC1 and PRC4 can be explained by a combination of several factors. The two mixtures have the same mixture compositions, except that river gravel was used in PRC4 instead of the crushed basalt in PRC1. River gravel tends to have a more equi-dimensional and rounded shape compared to crushed basalt. Crushed basalt also has a rough texture. Due to these differences in shape and texture, the porosity of PRC4 (17.93 %) was considerably lower than that of PRC1 (21.78 %). It is even the lowest among all the mixtures. However, increased aggregate texture and angularity contribute to the strength of porous concrete due to enhanced mechanical interlock, increased total surface area available for the adherence of the cement paste and increased contact points. The strength of basalt being higher than the strengths of most of the different types of aggregates present the river gravel batch is another factor. As a result of all the factors present, the dynamic strength of PRC4 (56.22 MPa) was lower than the dynamic strength of PRC1 (66.52 MPa).

Otherwise than the effect of aggregate properties, the effect of changing the binder composition of cement paste did not have a significant effect on the dynamic strengths. Replacing 15 percent of cement paste by silica fume did not enhance and even slightly decreased the dynamic strengths of the mixtures. The effect of compaction on the impact strengths of porous concrete can be inferred from a comparison of the strength of the mixtures PRC8 and PRC9 with other

mixtures. While intensive compaction was applied to the other mixtures, PRC8 and PRC9 were hand compacted by using a steel cylinder. The drastic decrease in strength of these two mixtures, PRC8 and PRC9, can be attributed to poor particle packing. No set retarder was used in mixtures PRC8 and PRC9, which could have also had an effect on the decreased dynamic strength values. Drop weight impact tests were also applied on a moderate strength normal concrete to compare its impact strength and sizes of fragments with those of porous concretes and also to verify the testing configuration. The results of the tests on normal concrete are presented in Table 4.7.

Table 4.7 Results of the impact tests conducted on normal concrete

Test no	Impact velocity (m/sec)	Equilibrium velocity (m/sec)	Dynamic strength (MPa)
1	4.29	1.34	60.22
2	4.36	1.29	57.98
3	4.08	1.25	56.18
4	4.38	1.39	62.47
5	4.34	1.23	55.28
6	4.29	1.27	57.08
7	4.35	1.26	56.63
Average dynamic strength (MPa)			57.97

The impedance mismatch analyses were again conducted using the particle velocity measurements of the moderate strength normal concrete and the dynamic strength was obtained. The results of normal concrete were compared with porous concretes in terms of their dynamic increase factor (DIF) values which will be explained in the coming section. The DIF values also enabled the normal concrete results to be compared with the literature which will be explained in detail in section 4.4.4.5.

#### 4.4.4.5. Dynamic Increase Factor calculations

Concrete is a highly strain-rate sensitive material (Weerheijm 1992). Dynamic increase factor (DIF), which is the ratio of dynamic strength to static strength, is widely used as an indication of the effect of strain rate,  $\dot{\epsilon}$ , on the strength of cementitious materials. The static compression tests were conducted using a closed loop deformation controlled test set-up at the loading rate of 1 micrometer/sec. Experimental and empirical (using the formula of Comité Euro-International du Béton, CEB) DIF values were also calculated for each mixture to compare the increase in strength under dynamic loading of different porous concretes with those of conventional concretes with the same static strengths. This comparison also gives the opportunity to see how predictable the dynamic strengths of various porous concretes are using the widely used DIF equation of CEB. The CEB relation between DIF and the strain-rate is given in Eq. 4.9. The

bilinear relation between DIF and  $\log \dot{\epsilon}$  has a breakpoint at the strain rate of  $30 \text{ sec}^{-1}$  (Comité Euro-International du Béton, 1993).

$$DIF = \frac{f_{cd}}{f_{cs}} = \left[ \frac{\dot{\epsilon}}{\dot{\epsilon}_s} \right]^{1.026\alpha_s} \quad (\text{for } \dot{\epsilon} \leq 30 \text{ sec}^{-1})$$

and (4.9)

$$DIF = \gamma_s \left[ \frac{\dot{\epsilon}}{\dot{\epsilon}_s} \right]^{1/3} \quad (\text{for } \dot{\epsilon} \geq 30 \text{ sec}^{-1})$$

where  $f_{cd}$  and  $f_{cs}$  are the uniaxial dynamic and quasi-static compressive strengths, respectively. In the equations,  $\dot{\epsilon}_s = 30 \times 10^{-6} \text{ s}^{-1}$ ,  $\gamma_s = 10^{(6.156\alpha_s - 2.0)}$ ,  $\alpha_s = 1/(5 + 9f_{cs}/f_{co})$ ,  $f_{co} = 10 \text{ MPa}$ .

The average static strength of the samples from the same concrete mixture was 26.44 MPa, which corresponds to a dynamic increase factor (DIF) of 2.19. At the average strain rate of  $68 \text{ sec}^{-1}$  (which was measured using high speed photography), the DIF value is calculated to be 2.15 according to Eq. 4.9. This is close to the value of 2.19 that was obtained experimentally for normal concrete.

Table 4.8 Experimental and calculated DIF values for porous and normal concretes

Mixture Code	Static comp. strength	Impact strength	DIF (Experimental)	DIF (Calculated using Eqn.3)
PRC1	34.78	66.52	1.91	1.94
PRC2	41.89	76.78	1.83	1.83
PRC3	50.49	85.99	1.70	1.74
PRC4	29.64	56.22	1.90	2.01
PRC5	31.60	53.09	1.68	2.00
PRC6	44.81	79.69	1.78	1.80
PRC7	48.80	84.37	1.73	1.76
PRC8	15.94	26.26	1.60	2.73
PRC9	13.09	21.84	1.73	3.06
NC1	26.44	57.97	2.19	2.15

The DIF value obtained for normal concrete for the average strain rate of  $68 \text{ sec}^{-1}$ , is consistent with the widely referenced review of Bischoff and Perry on the strain rate sensitivity of concrete as seen in Figure 4.20 (Bischoff and Perry 1991).

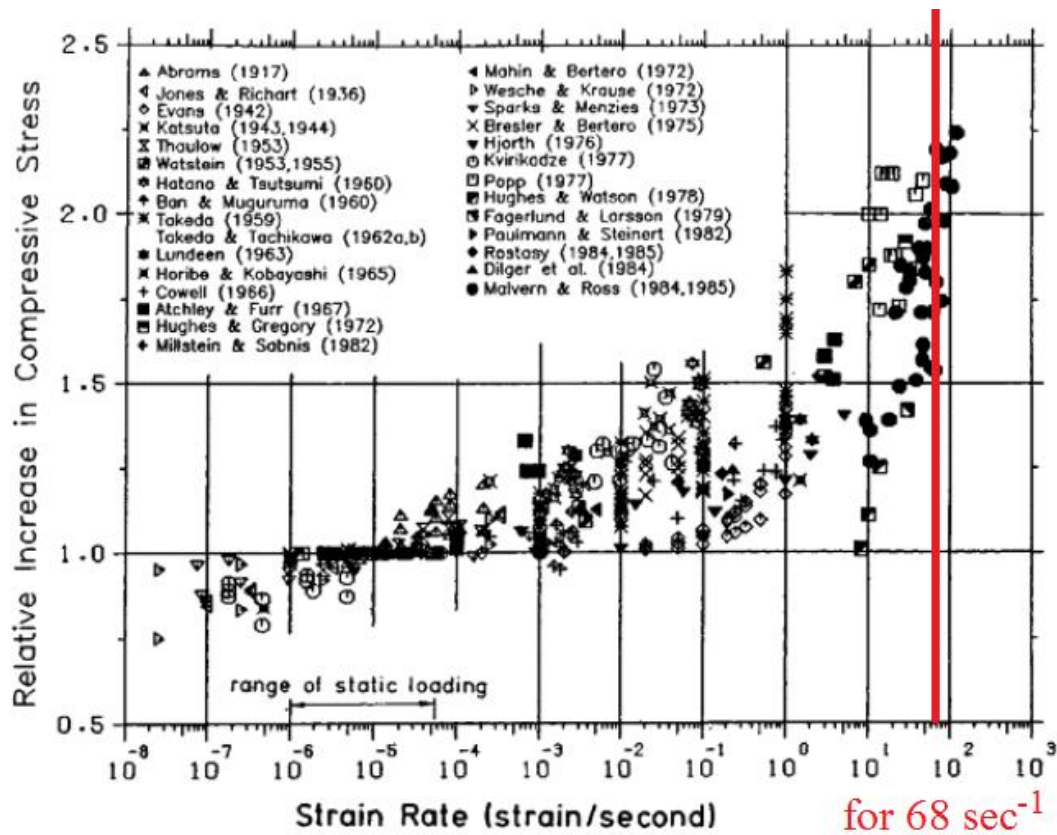


Figure 4.20 Summary of the review of Bischoff and Perry on the strain rate sensitivity of concrete (Bischoff and Perry 1991) (Average strain rate of  $68 \text{ sec}^{-1}$  is valid for the drop weight impact tests conducted in this research)

Similar to normal concretes, porous concretes are strain rate dependent materials due to the presence of the cementitious phases. The DIF values obtained from the experiments compared to the DIF values calculated using the CEB equations that are normally valid for conventional concretes are presented in Table 4.8. The experimental DIF values of the porous concrete mixtures that have high static strengths, in the range of 35-50 MPa, are consistent with the DIF values calculated using CEB equations except for PRC5. The contradicting DIF values obtained for mixtures PRC8 and PRC9, that have not been sufficiently compacted, show that the CEB equations are not valid for low strength, high porosity porous concretes.

#### 4.4.5. Hi-Speed Photography Investigations

A series of experiments was performed on porous concrete samples to measure their impact strengths in an alternative way and observe their fragmentation behaviors using high-speed photography. In high-speed photography measurements, monitoring the displacement of the impactor was the key feature. In order to monitor the motion of the impactor more clearly, a retro-reflective sticker band with a 4 mm thickness (see Figures 4.22, 4.23 and 4.24) was attached on the lateral surface of the impactor. The displacement measurements were taken on



the sticker (see Figures 4.23 and 4.24). The impact strength analyses were again performed using the reverberation application of the impedance mismatch method.

#### 4.4.5.1 Hi-Speed Photography Test Set-up and Instrumentation

In high speed camera measurements, a Phantom V 5.0 digital high speed camera with a sensor size of 1024x1024 pixels was used. It had a variable exposure independent of the sample rate down to 10 microseconds. The framing rate of the camera could be varied between 1000 to 10000 frames per second (fps). Because the total recording time depends on the frame rate and the size of storage medium, at 6134 fps the recording time was about 3 seconds while at 10000 fps it was about 1.85 sec. Since all the collisions had a duration orders of magnitude less than such times, those recording times were sufficient in all tests conducted. In terms of using the available amount of memory for the higher frame rate measurements, taking partial frames was a solution. Therefore, at 10000 fps frame rate, smaller size images are taken compared to 6134 Hz. This can be inferred from a comparison of Figure 4.23 and Figure 4.24.

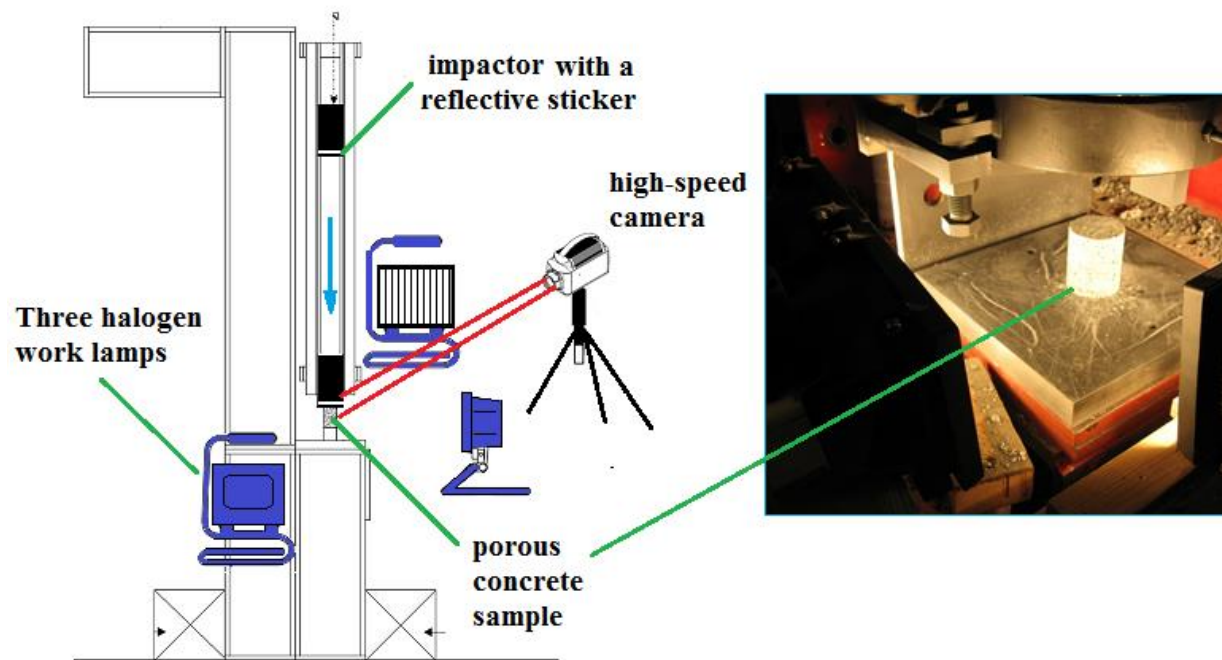


Figure 4.21 High-speed photography test set-up

Light sources are very important in high speed photography. The time that light is exposed to the imaging sensor depends on the frame rate and, therefore, the shutter time, as well as the available light source (Fuller 2009, Chhabildas et al. 2005). Short exposure times require a substantial intensity of illumination. In order to overcome the problems of illumination especially at the frame rate of 10000 fps, three halogen work lamps were placed at three free sides of the test set-up. The high speed camera was located about 1.5 m from the sample. It was placed in a protective container to protect it from the scattering fragments of concrete during testing, while

an opening was left to allow the camera to make recordings. The test set-up is shown in Figure 4.21.

#### 4.4.5.2 Analysis of high-speed photography images

For analyzing the results, the images acquired by the high speed camera were first converted to black and white or binary images by taking a global image threshold as reference using the image processing toolbox of MATLAB. In a black and white image, each pixel has one of the two discrete values (either 0 (black) and 255 (white) or similarly 0 and 1 in binary format). The image that is expressed in pixel coordinates is treated as a grid of discrete elements as shown in the schematic presentation in Figure 4.22.

Pixel coordinates are integer values and range between 1 and the length of the row or column. There is not a one-to-one correspondence between pixel coordinates and the spatial coordinates that show the actual coordinates of the objects. However, by default, the toolbox of the program itself uses its own spatial coordinate system for an image and that coordinate system has a one-to-one correspondence with the pixel indices of the image. This is called the intrinsic coordinate system of the program (Mathworks, 2001).

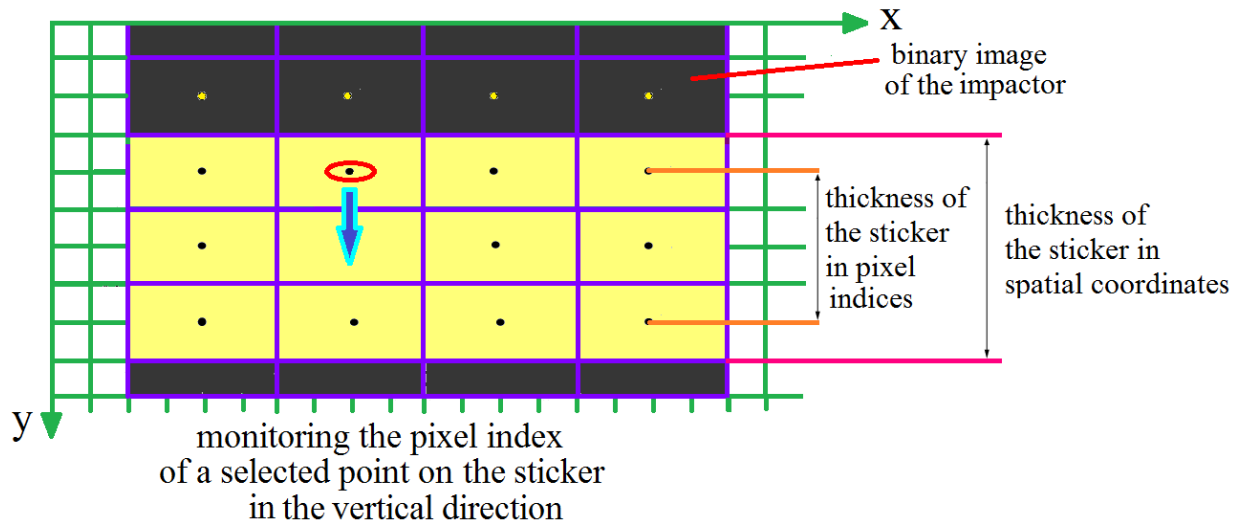


Figure 4.22 Schematic presentation of the impactor image in discrete pixel elements

The x and y coordinates given in the inserts in Figure 4.23 and Figure 4.24, showing the upper and lower edges of the sticker, are the values that belong to that intrinsic coordinate system, which are not the actual spatial coordinates of the sticker. However, since the thickness of the sticker is known (4 mm), a simple conversion factor was calculated between the pixel (or intrinsic) coordinates and the actual spatial coordinates. The conversion factor was found by determining the thickness of the sticker (in pixels) from the image, adding one to it and equating it with the real thickness of 4 mm. Adding one pixel is essential due to the fact that the pixel value is indicated for the middle point of each discrete element as shown in Figure 4.22.

Therefore, there is always one pixel deficit if the thickness is expressed in pixels and directly converted to units of length.

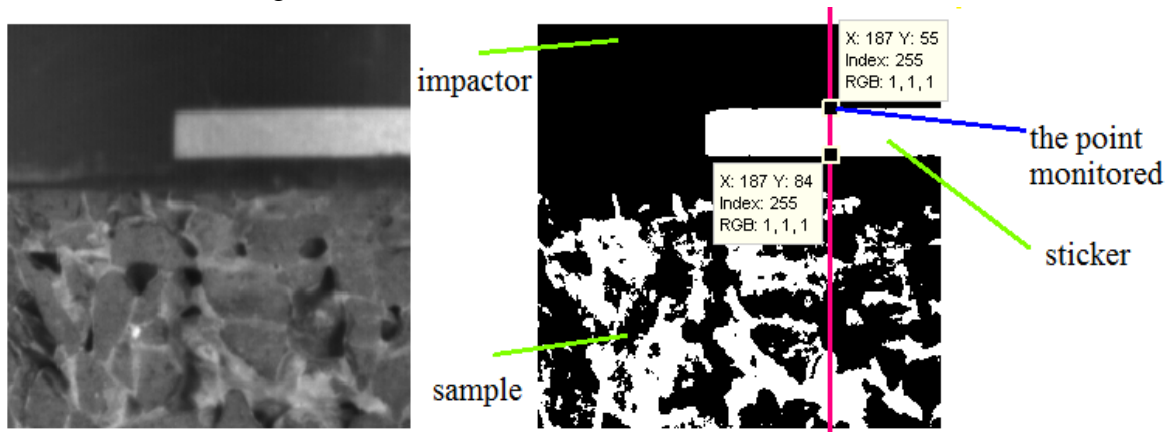


Figure 4.23 High-speed image taken at 10000 fps and its binary version showing measurement points

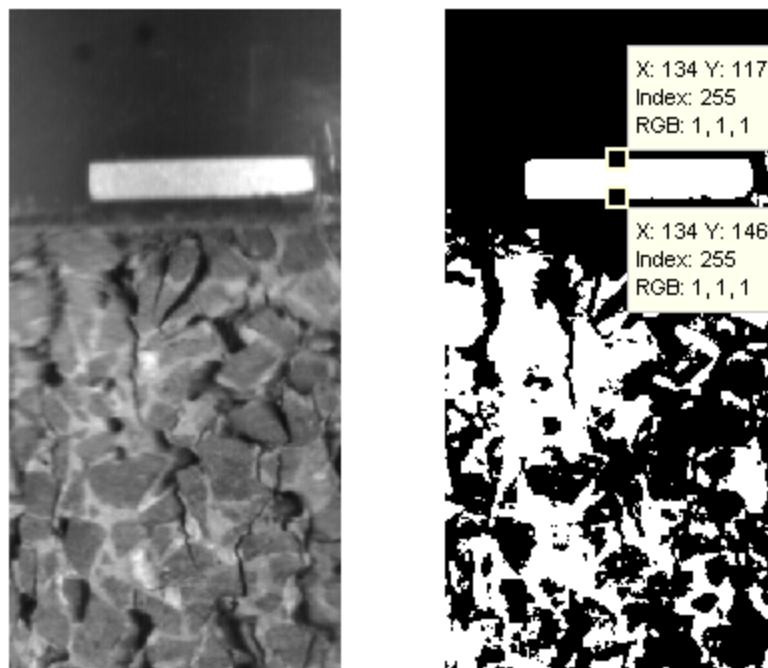


Figure 4.24 High-speed photograph taken at 6134 fps and its binary version showing measurement points

The main objective of the high speed photography measurements is monitoring the displacement of the impactor. For this purpose, a point on the sticker is actually monitored when it moves vertically downwards during the test. The point has a constant pixel coordinate in the horizontal direction (i.e. its intrinsic x coordinate is constant), while its pixel coordinate in the vertical

direction changes. Since before the test the impactor has been painted black, the sticker is the only white area on the impactor. When the image is converted to black and white, this distinction is even clearer. In Figures 4.22, 4.23 and 4.24, it can also be seen that above the sticker, the images are completely in black. Thus for following the motion of the impactor, determining the highest y coordinate with a pixel value equal to 255 (white) in every image (for a fixed x value) was the method used. This type of point selection made it easier to determine the velocity of the impactor using a short code written in MATLAB, that only checks the y-coordinates of the white points in successive images. In Figure 4.23, such a measurement point for a fixed x is indicated. In the analysis, any fixed x coordinate can be selected, provided that it is in the range of the x coordinates of the sticker. The displacement of the point is monitored along with the corresponding frame number and plotted in a displacement (in pixels)-frame number graph as in the plot given in Figure 4.25 for one of the PRC5 samples tested at 10000 fps. No filters were needed due to small noise to signal ratio.

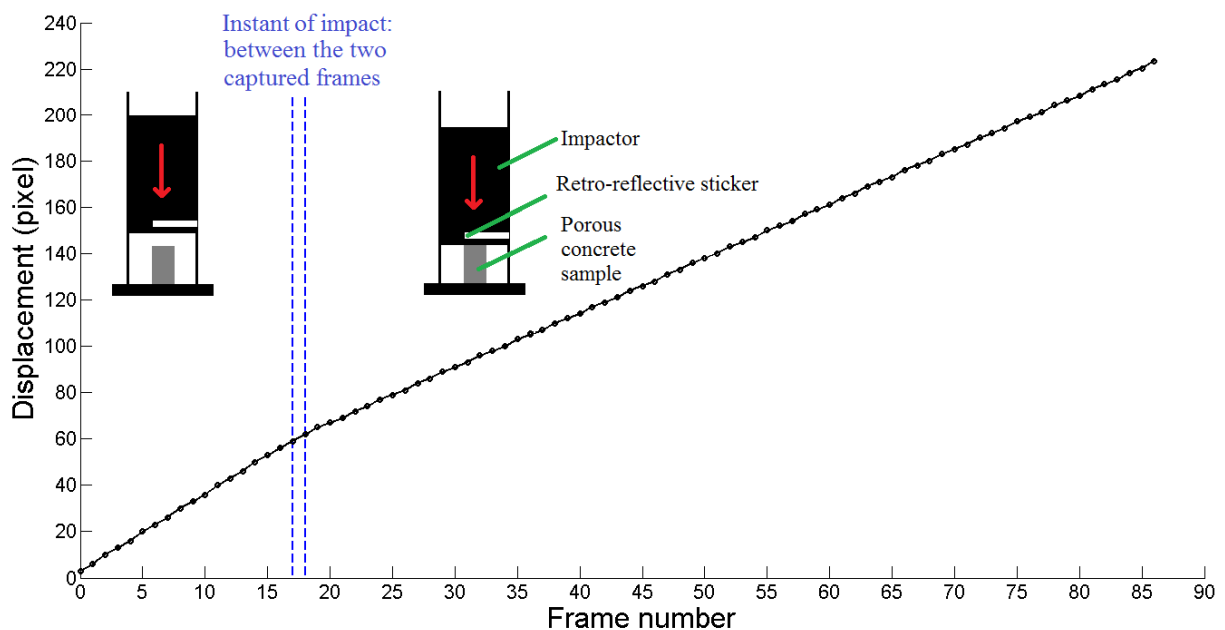


Figure 4.25 Displacement of the impactor (in pixels) vs. frame number graph for PRC5 measured at 10000 fps

The dashed vertical blue lines in the figures represent the frames that have been selected to estimate at what time the collision took place. The first blue line on the left corresponds to the last photo shot that has been captured before the collision while the second line shows the first image captured after the specimen and the impactor are in contact. These two images can be selected when the captured images are observed in a chronological order. Because the time that passes between two frames is  $1/10000$  or  $1/6134$  seconds in the two series of photographs, the exact instant of the collision cannot be known exactly. Therefore, a range of time between the two closest frames is selected.

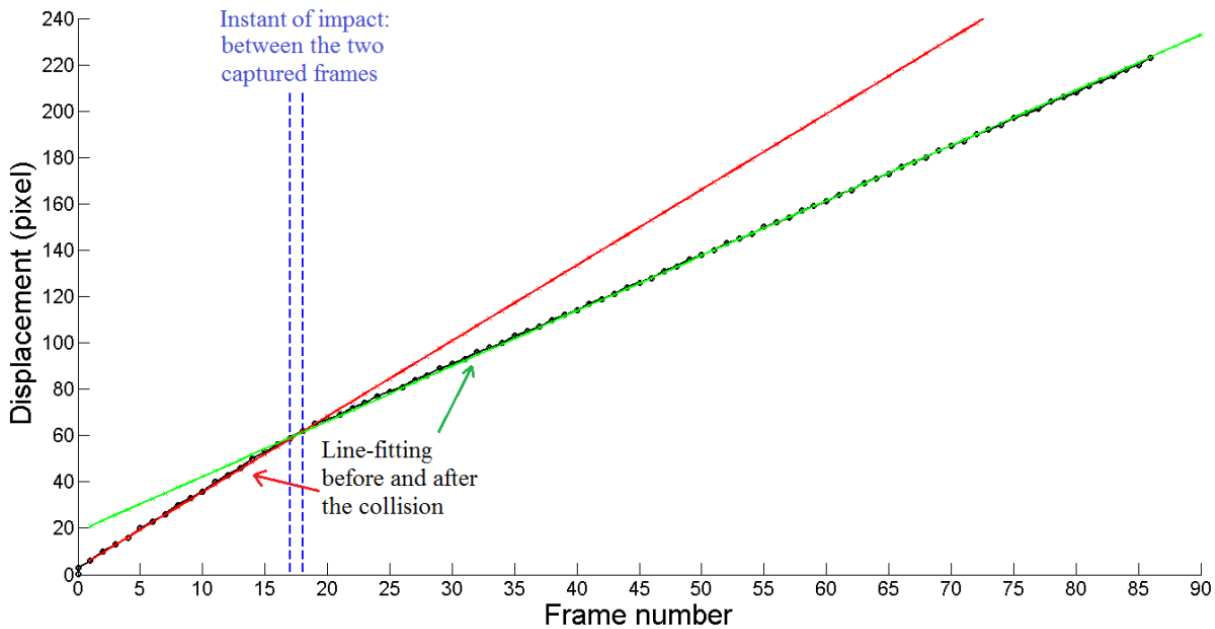


Figure 4.26 Displacement of the impactor (in meters) vs. frame number graph for PRC5 measured at 10000 fps

By converting the pixels into meters and the frame number into time, the same data is plotted again (see Figure 4.26). The experimental displacement-time data is fitted to a bilinear curve consisting of two linear portions of constant slopes. The slopes of the curves represent the particle velocity. A steeper initial rise can be observed in Figure 4.26 due to the impact velocity being obviously higher before the collision. The second portion of the curve (i.e. the second group of experimental data points) has a lower slope showing the velocity of the particles of the steel impactor. This velocity is significantly reduced after the impact when the impactor moves downwards in contact with the porous concrete sample.

#### 4.4.6 High-Speed Photography Results and Discussion

##### 4.4.6.1 Impact strength results

Three different porous concrete mixtures (PRC5, PRC8 and PRC9), that have already been tested with LDV tests, were recorded with the high speed camera at the frame rate of 10000 fps. When the displacement histories of the three mixtures tested at the same sampling rate were compared, it was evident that when the impact strength of the concrete sample was lower, the difference between the two slopes of the bilinear curve decreased (see Figures 4.27, 4.28 and 4.29). This is due to the fact that when the drop weight hits a weaker sample, it decelerates less, compared to hitting a stronger sample. This was clearly observed also during the LDV tests (see Figure 4.19).

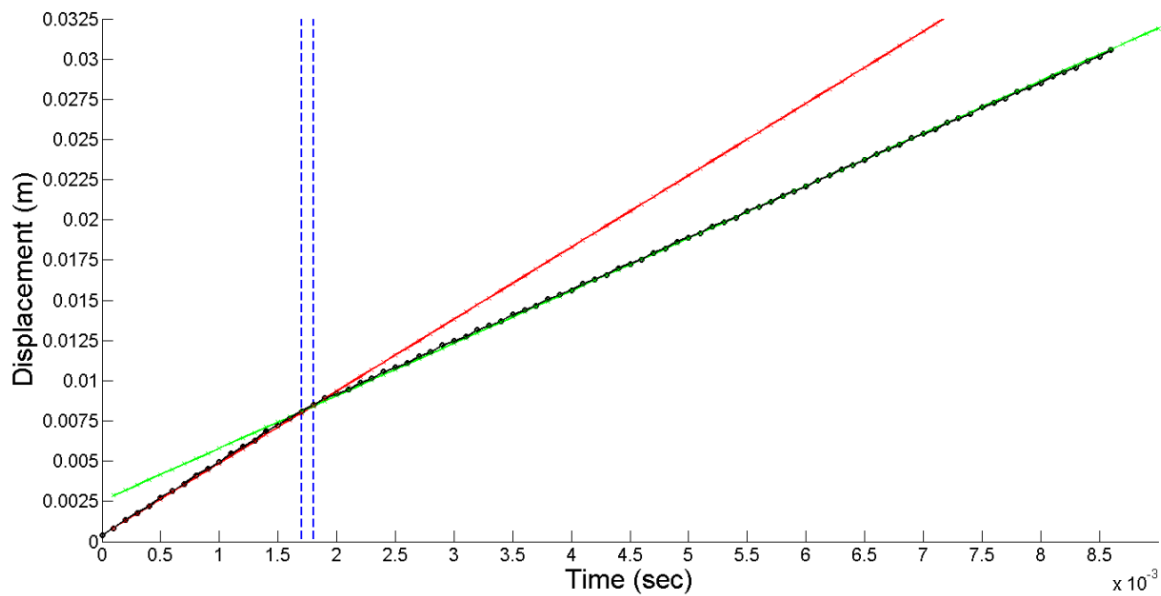


Figure 4.27 Displacement of the impactor (in m) vs. time graph for PRC5 measured at 10000 fps

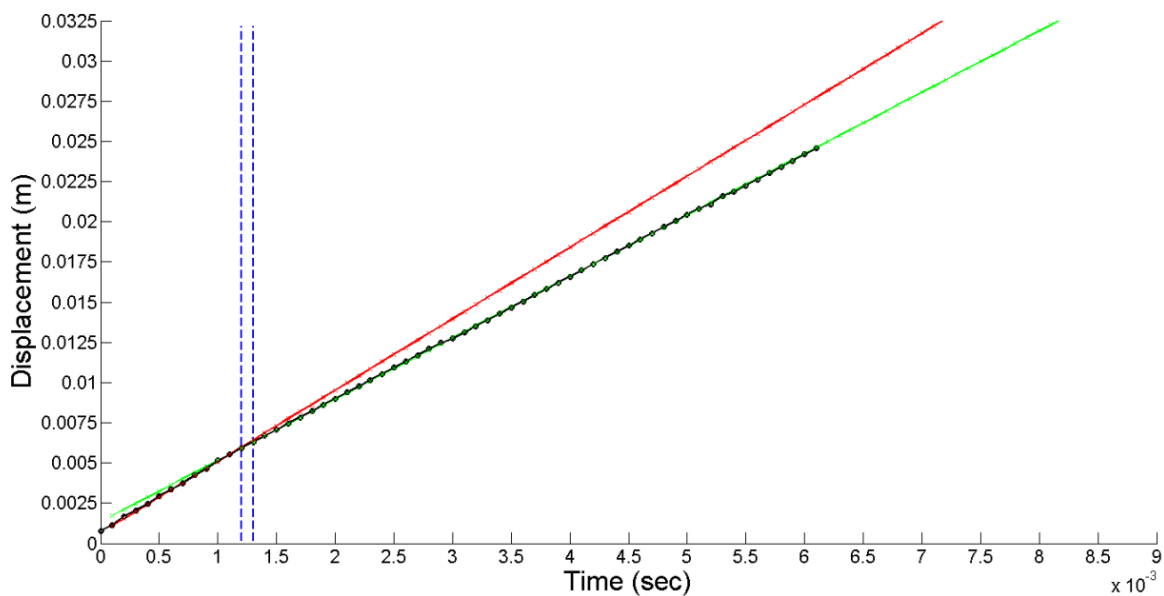


Figure 4.28 Displacement of the impactor (in m) vs. time graph for PRC8 measured at 10000 fps

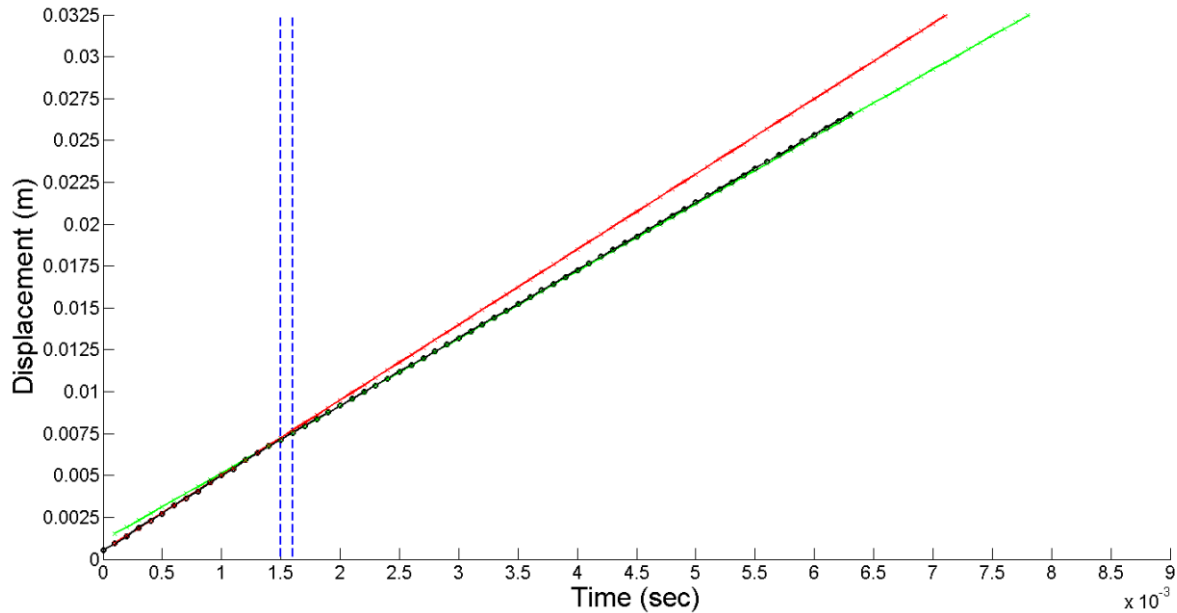


Figure 4.29 Displacement of the impactor (in m) vs. time graph for PRC9 measured at 10000 fps

After the displacement of the selected point on the sticker is monitored and processed, the slopes of the two parts of the fitted bilinear curve were calculated. The slope of the first part of the curve before the collision was the impact velocity while the slope of the second part was the equilibrium velocity. As expected, the equilibrium velocity is always lower than the impact velocity. The values obtained for the impact velocity itself were also a good verification for the monitoring method. The impact velocity of the drop weight impactor is already known from the simple calculations of conversion of potential energy to kinetic energy at free fall. After the impact velocity and equilibrium velocity values are known, the rest of the calculations were done by again using the reverberation application of the impedance mismatch method. The calculations for the impact strength are identical to the ones in the LDV tests. From a comparison of the results of the two tests, it can be concluded that the high speed photography results show a very good agreement with the values obtained from LDV for the same porous concrete mixtures (see also Table 4.9).

Table 4.9 Results of the high-speed photography experiments

Mixture Code	Frame Rate (fps)	Impact Velocity (m/s)	Equilibrium Velocity (m/s)	Impact Strength (MPa)	Average Impact Strength (MPa) (High-speed)	Average Impact Strength (MPa) (LDV)
PRC5_no1	6134	4.49	3.30	53.48	51.86	53.09
PRC5_no2	6134	4.44	3.32	50.34		
PRC5_no3	6134	4.35	3.26	48.99		
PRC5_no4	6134	4.48	3.28	53.93		
PRC5_no5	6134	4.42	3.25	52.58		
PRC8_no1	6134	4.32	3.81	22.92	24.81	26.26
PRC8_no2	6134	4.39	3.78	27.42		
PRC8_no3	6134	4.45	3.95	22.47		
PRC8_no4	6134	4.37	3.79	26.07		
PRC8_no5	6134	4.47	3.91	25.17		
PRC5_no1	10000	4.31	3.07	55.73	53.57	53.09
PRC5_no2	10000	4.49	3.20	57.98		
PRC5_no3	10000	4.47	3.28	53.48		
PRC5_no4	10000	4.50	3.37	50.79		
PRC5_no5	10000	4.45	3.17	57.53		
PRC5_no6	10000	4.41	3.35	47.64		
PRC5_no7	10000	4.46	3.21	56.18		
PRC5_no8	10000	4.49	3.39	49.44		
PRC5_no9	10000	4.33	3.18	51.68		
PRC5_no10	10000	4.47	3.24	55.28		
PRC8_no1	10000	4.35	3.74	27.42	26.52	26.26
PRC8_no2	10000	4.44	3.82	27.86		
PRC8_no3	10000	4.36	3.83	23.82		
PRC8_no4	10000	4.43	3.78	29.21		
PRC8_no5	10000	4.40	3.91	22.02		
PRC8_no6	10000	4.39	3.75	28.76		
PRC9_no1	10000	4.25	3.73	23.37	23.07	21.84
PRC9_no2	10000	4.46	3.97	22.02		
PRC9_no3	10000	4.38	3.95	19.33		
PRC9_no4	10000	4.49	4.02	21.12		
PRC9_no5	10000	4.46	3.83	28.31		
PRC9_no6	10000	4.32	3.78	24.27		



#### 4.4.6.2 Measuring the average strain rate

During the drop weight tests, the strain rates were measured on the samples using a high speed camera at a frame rate of 10000 frames/sec. The displacements of some specific points on the sample were monitored in the first two photographs after the impact. Using these photographs, the strain and subsequently the strain rate were calculated taking the average of the measurements obtained from the different points on each sample. The average strain rate was found to be  $68 \text{ sec}^{-1}$  using the displacement measurements.

#### 4.4.6.3 Fracture patterns of porous concrete under drop weight impact loading

To be able to visualize the fracture patterns of the whole sample, the high speed camera photographs taken at 6134 frames/second were used (see Figures 4.24 and 4.31). The images taken at 10000 fps, do not cover the complete sample (see Figure 4.23). In Figure 4.30, the dotted vertical lines indicate the frequency of the photographs captured. Four representative photographs were presented in Figure 4.31. The moments the photographs were taken are also indicated in Figure 4.30, i.e. points A, B, C and D.

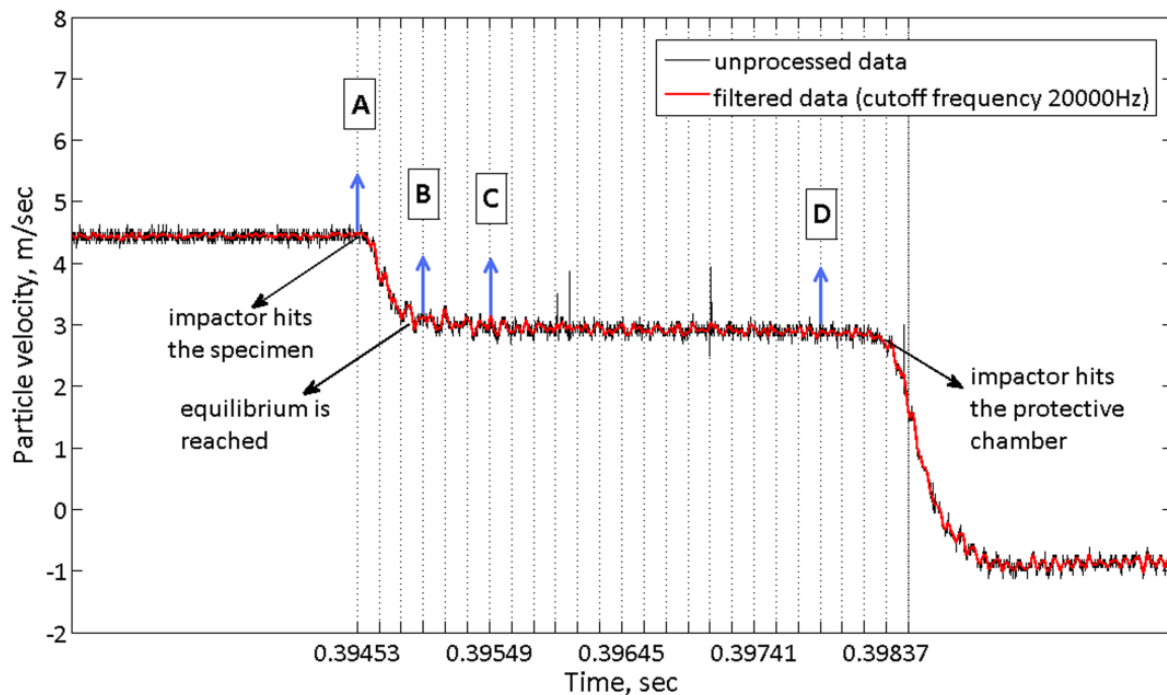


Figure 4.30 Particle velocity history plot indicating the timing of the photographs

The photos in Figure 4.31 were taken from a typical drop weight impact test performed on a PRC5 sample. In the four photographs, it can be seen that under impact loading cracks propagate and coalesce to form small particles due to the stress wave.

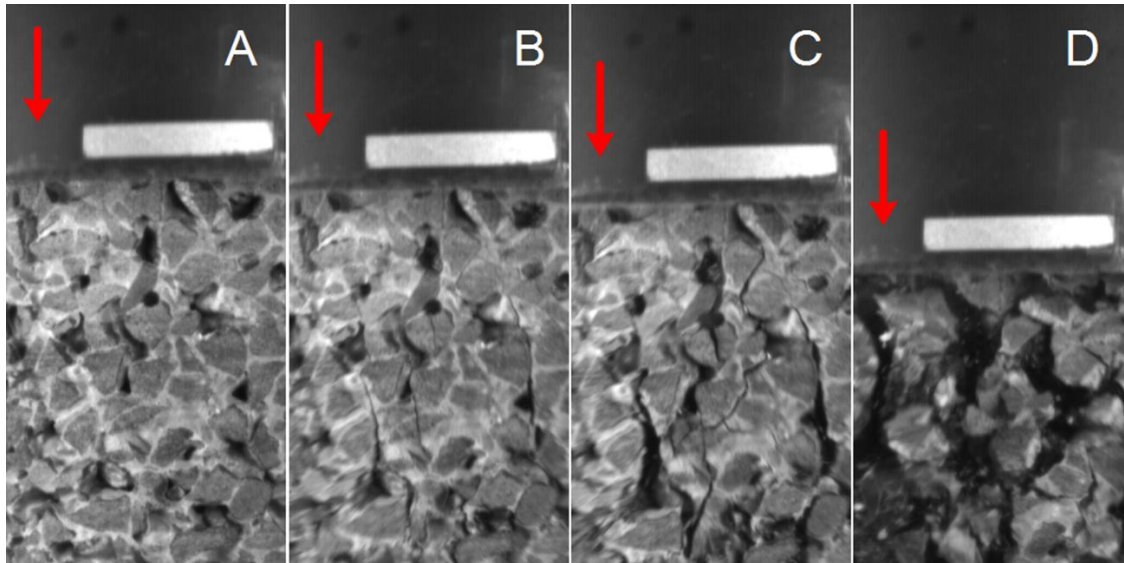


Figure 4.31 Photographs for the impact of PRC5 demonstrating fracture patterns

In porous concrete, similar to normal concrete, microcracks are expected to predominantly initiate from the interface between the aggregate and the bulk cement paste and subsequently propagate into the bulk cement paste. The crack patterns shown in Figure 4.31 are also similar to those of normal concretes in the sense that tensile cracks parallel to the axis of loading and the subsequent shear cones underneath the aggregates can be observed (van Mier 1997). Although this fracturing behavior does experience some effect of restraint due to the friction between the steel plates and the porous concrete specimen during testing as in normal concrete, the characteristics of porous concrete itself are also effective. In porous concretes, the crack patterns are also guided by the pore structure. Differently in porous concretes, cracks also initiate from the upper and lower poles of the pores where tensile stress concentrations are present. These cracks can also be observed in Figure 4.31. This situation was also evident in the numerical results (Figures 5.21, 5.56 and 5.57). Under dynamic loading, as the cracks propagate, they are even forced to go through the aggregates which are the actually the strong phases. It should also be noted that the fracture patterns and the fragments that were examined after failure demonstrate that cracks are not solely located in the cement paste, but are also sometimes forced to propagate through the aggregates. This holds for even high strength basalt aggregates and especially in samples containing river gravel which is a mixture of rocks from very different origins, including particles with very low strength. Fracturing of basalt particles is not as very frequently observed in static loading. In dynamic loading, fast energy transfer from the bulk material into the crack tips, generating crack branching and enhanced energy dissipation, causes instabilities. This eventually causes the cracks to propagate through parts of the material that are not necessarily the weakest phases (Pedersen 2009).

#### 4.4.7 Ultrasonic Wave Velocity Testing of Porous Concretes

Ultrasonic wave velocity tests were also applied to porous concretes to see the general range of their wave velocities. Such information is hardly found in the literature. It should be noted that the sound wave velocity of porous concrete is not required in the impedance mismatch calculations for finding the impact strength. Additionally, EOS relationships between the particle velocities and shock wave velocities of concretes are far from being linear even at moderate shock particle velocities. Therefore, the values obtained were not used in the analyses. The measurements were taken on some selected number of concrete samples just before the samples were drilled for the impact tests. The measurements were performed using a Pundit Plus ultrasonic concrete tester. By measuring the transit time, the velocity of a pulse of longitudinal ultrasonic vibrations travelling in the concrete samples could simply be determined by dividing the sample length by the travel time measured. The measured ultrasonic pulse velocities are given in Table 4.10.

Table 4.10 Ultrasonic pulse velocity results

Mixture Code	Length (mm)	Transit Time ( $\mu$ sec)	Ultrasonic Pulse Velocity (m/sec)	Average Ultrasonic Pulse Velocity (m/sec)	Compressive Strength (MPa)
PRC1_sample1	80.5	19.2	4192.7	4159.4	34.8
PRC1_sample2	80.4	19.5	4123.1		
PRC1_sample3	80.4	19.6	4102.0		
PRC1_sample4	80.6	19.1	4219.9		
PRC5_sample1	82.2	18.8	4372.3	4245.3	31.6
PRC5_sample2	80.0	19.9	4020.1		
PRC5_sample3	81.8	18.8	4260.6		
PRC5_sample4	80.1	18.9	4328.0		
NC1_sample1	75.5	19.1	3963.3	3937.5	26.4
NC1_sample2	75.2	19.2	3906.5		
NC1_sample3	75.8	19.2	3937.7		
NC1_sample4	75.5	19.1	3942.6		

The results seem to be surprising at a first glance because the porous concrete samples that incorporate meso-size air pores would normally be expected to have lower velocity values compared to a normal concrete. However, the normal concrete that has been tested is a moderate strength concrete with a 26.44 MPa static strength, while porous concretes were highly-compressed porous concretes with static strengths at the range of 30-35 MPa. Another reason can be that the normal concrete contained river gravel while porous concretes were prepared using a very high percentage of basalt aggregates. While wave velocity in basalt is between 5000-7000

m/sec (depending on the different types that are present in nature), some of the sedimentary rocks such as sandstone and shale that are present in river gravel have wave velocities at the range of 1500-4600 m/sec and 2000-4600 m/sec, respectively (Zhao 2009). The slightly higher wave velocities obtained for the mixture containing silica fume, i.e. PRC5, may be due to the densifying effect of silica fume. This effect was hardly found in the impact strength results.

#### **4.4.8. Particle Size Analysis of Post-Failure Fragments**

The key objective of this research project was designing a special type of concrete that fractures into small-size fragments under dynamic loading. In order to check whether indeed small size fragments were generated in the impact tests, the fragments of the samples, that were collected in the protective chamber of the drop weight impact test set-up, were analyzed by sieving them using standard sieves (see the protective chamber in Figure 4.32). Note that the presence of the protective chamber prevented the impactor from crushing the post-failure fragments with its self-weight. Various definitions of fragment size are present (Franklin 1996). When grains are not close to being spherical, the size measurements are usually expressed in terms of the diameters of equivalent spheres i.e. fragment size being reduced to the nominal diameter of the corresponding sphere.

##### **4.4.8.1 Sieve analysis results of fragments**

The results of the sieve analyses are presented in Table 4.11. In this table, the nine different types of porous concretes were compared. Fragments of four different specimens (from each mixture) were sieved and the average of those four results was taken for each sieve opening size. The photographs of the fragments of a porous concrete mixture with 4-8 mm aggregates (PRC1) (static compressive strength: 34.78 MPa, impact strength: 66.52 MPa) and that of the normal concrete (NC1) (static compressive strength: 26.44 MPa, impact strength: 57.97 MPa) are presented in Figures 4.32 and 4.33. When the fragments of the two types of concretes are compared, it can confidently be said that a porous concrete having a higher static (and dynamic) strength does act in a much favorable way in terms of fragmentation than moderate strength normal concrete.



Figure 4.32 Photographs of the post-failure fragments of a porous concrete (PRC1)



Figure 4.33 Photographs of the post-failure fragments of a normal concrete (NC1)

It was found that triaxially stressed cones at the end parts of the specimens were formed and remained intact due to the boundary friction between the loading plates and the specimen. The percentage by mass of the two cones that remain were about 20 % in each sample for the sizes of samples that were tested in this study (60 mm diameter-70 mm height). The sieving results of PRC9, one of the weakest mixtures that fractured completely into small size fragments except the mentioned triaxially stressed cones that remained intact, are an indication of those conical parts. These parts constitute approximately 20 % of the mass of a sample as seen in Table 4.11.

Table 4.11 Sieve analysis results of the fragments for different mixtures

Mixture Code	PRC1	PRC2	PRC3	PRC4	PRC5	PRC6	PRC7	PRC9
Aggregate size (mm)	4-8	2-4	50% 2-4, 50% 4-8	4-8	4-8	2-4	50% 2-4, 50% 4-8	4-8
Sieve size (mm)	% Fragment Passing							
32	79	67	73	82	80	64	79	80
16	72	60	60	70	72	56	62	73
8	47	48	42	45	49	47	41	48
4	10	29	19	15	10	26	18	10
larger than 16	72	60	60	70	72	56	62	73

The sieve analysis also showed that the fragments were slim in shape having one dimension very different from the others due to the fragment patterns that can also be observed in Figures 4.31



where the vertical tensile cracks cause the formation of slender fragments. If the fragments are taken as spheres with equivalent diameters (taking the area as reference) the diameter of the circle, with the same area as the maximum projected profile of a fragment, is taken as the fragment size.



Figure 4.34 Post-failure fragment and its maximum projected profile

If this is applied, as an example, to one representative large-size fragment shown in Figure 4.34, it is found that a fragment that has a length of 22.3 mm (remaining on the 16 mm sieve) has a corresponding equivalent diameter of 12.6 mm. It is not possible to evaluate each fragment through such a calculation, but when quantifying fragmentation, the evaluation of the sieve analysis should actually be done also taking the shapes of the fragments into consideration.

In Table 4.11 the fragments larger than 32 mm was mostly caused by the confined cones formed at the ends of the samples. This was clearly observed during the sieving process. If the percentages of the fragments that are smaller than 16 mm are taken as reference, the mixtures PRC1, PRC4 and PRC5 (mixtures with aggregates at the size of 4-8 mm) showed a good performance in terms of fracturing into small fragments. If PRC6 and PRC7 are compared it appears that even though PRC7 had a lower porosity and higher dynamic strength than PRC6, it fractured into smaller fragments. The same can also be said for mixtures PRC2 and PRC3. Meanwhile, PRC9, which generated the smallest fragments, had a very low static strength. From further evaluation of the values presented in Table 4.11 it can be learned that the distributions of fragments smaller than 16 mm also differ in the different mixtures. In mixtures PRC2 and PRC6, the number of fragments smaller than 4 mm are consistently higher than those of other mixtures PRC1 and PRC5. The sizes of fragments of the latter mixtures were mostly concentrated in the range of 4-8 mm. This can surely be explained by their aggregate sizes.

It can be concluded that the fragmentation performance of the different mixtures strongly depend on the aggregate size. The common feature of mixtures PRC1, PRC4 and PRC5, i.e. the mixtures that gave the smallest amount of fragments larger than 16 mm, was the grading of their aggregates (4-8 mm). These mixtures had the coarsest grading of all the mixtures. The same phenomenon is also apparent when PRC6 and PRC7 (or PRC2 and PRC3) are compared. Due to their contents of 4-8 mm aggregates the mixtures PRC3 and PRC7, which actually have lower porosity and higher strength values than PRC 2 and PRC6, gave equal and even a slightly lower

amount of fragments larger than 16 mm. This can be explained by the fact that when the aggregate grading is finer, the amount of contact surface (per aggregate volume) between the neighboring aggregates is higher. Therefore, each aggregate is bonded more strongly to its neighbors. On the other hand, when the finer portion of the fragment size distribution is considered, the amount of finer fragments ( $< 4$  mm) is higher in mixtures containing 2-4 mm aggregates compared to the mixtures with 4-8 mm aggregates. However, the percentage of larger size fragments ( $> 16$  mm) being higher, which is the main concern in terms of safety applications, make the fragmentation performance of those mixtures less favorable. For selecting a mixture to be used in safety structures, this selection should be done in view of the service loads and the amplitude of impact stress the concrete is expected to be exposed to in that specific application. Mixtures PRC1, PRC4 and PRC5 (mixtures with sufficient static strengths and small-size fragments) and PRC2, PRC3, PRC6 and PRC7 (having higher static strengths, but generating slightly larger fragment sizes) should be evaluated according to the specific design requirements such as static strength and fragment size.

#### **4.5. Conclusions**

In this dynamic testing and evaluation part of the research, different experimental configurations were introduced or applied for determining the dynamic response of porous concretes in a drop weight impact test. Nine different types of porous concretes and one mixture of normal concrete were produced and subjected to drop weight impact tests in order to investigate the dynamic properties. Different alternatives of porous concretes that have sufficient static and dynamic strengths as well as a fragmentation performance were designed and tested.

When mixtures containing different shapes and types of aggregates were compared, it was seen that increased texture and angularity contributed to the impact strength of porous concrete. When two sizes of aggregates were used instead of using single sized ones, the dynamic strengths of porous concretes were also increased. This was due to the aggregates having different sizes performing a more efficient packing. For mixtures having single-sized aggregates, as the size of the aggregates decreased, the dynamic strength was enhanced due to the increase in contact and bonding areas. Compaction is another factor that also had an important effect on the impact strength properties because it directly affects the porosity. While aggregate properties drastically affected the strength properties, changing the cement paste composition did not have a significant effect on the impact strengths of the samples.

In the research, different experimental methods were used and compared. While these comparisons provided information on the feasibility of using those methods in designing and testing porous concretes, they were also needed in validating the different methods. From the evaluation of the experimental configurations, it was found that stress gauge measurements have the advantage of being direct ways of measuring. No additional analyses were needed afterwards to obtain the impact strength data. Provided that the calibration of the gauges is done properly, the method directly provides the correct impact stress. It is emphasized, however, that the testing system requires a long and laborious installation process for each sample. This is not feasible for

testing a large number of samples. In addition, about fifty percent of the samples exhibited too much damage immediately after being loaded by the impact load to make any recordings. This further reduces the efficiency.

Among the other two monitoring and measuring techniques (LDV and high speed photography) that have been applied, LDV proved to be more accurate because of its higher sampling rate (400000 Hz) compared to high speed photography (10000 Hz). It also has the advantage of being independent of factors such as the light source that is used in the photography measurements. High speed photography however has its own advantage of also facilitating the visualization of the fracture process. This provides important qualitative information such as characterization of the propagation and coalescence of cracks and shapes of fracture patterns. This information is not generated in other types of testing. On the other hand, both LDV and high speed photography techniques have the advantage of being non-contact methods with no need to install sensors on the sample. The applied reverberation technique for analysis also has the advantage of involving only the well-known dynamic impedance properties and the velocity measurements of the impactor, while the target specimen that is tested is not directly involved in the measurements or the analysis. While measurements with gauges always require the presence of other materials such as capping materials, rubber and steel plate to protect the sensors, both LDV and high-speed photography also enable to have a direct collision between the impactor and the concrete without any interruptions.

The reverberation application of the impedance mismatch method, used in analyzing LDV and high-speed photography results, proved to be sufficient in investigating the drop weight impact behavior by making the assumption of one-dimensional wave propagation.

## References

Agar Ozbek A.S., Weerheijm J., Schlangen E., van Breugel K. (2012), *Drop weight impact strength measurement method for porous concrete using laser Doppler velocimetry*, Journal of Materials in Civil Engineering, 24(10), 1328-1336.

Agar Ozbek A.S., Weerheijm J., Schlangen E., van Breugel K. (2013), *Investigating the dynamic properties of porous concretes through drop weight impact testing*, Cement and Concrete Composites, 39, 1-11.

Antoun T., Seaman L., Curran D. R., Kanel G. I., Razorenov S. V., Utkin A. V. (2003), *Spall Fracture*, Springer-Verlag, New York, USA.

Appleby-Thomas G. J., Hazell R. J., Stennett C. (2009), *The variation in lateral and longitudinal stress gauge response within an RTM 6 epoxy resin under one-dimensional shock loading*, Journal of Materials Science, 44, 6187–6198.



Asay J. R., Shahinpoor M. (1993), *High-pressure shock compression of solids*, Springer-Verlag, New York, USA.

Barker L. M., Hollenbach R. E. (1972), *Laser interferometer for measuring high velocities of any reflecting surface*, Journal of Applied Physics, 43, 4669-4675.

Bhargava J., Rehnström A. (1975), *High-speed photography for fracture studies of concrete*, Cement and Concrete Research, 5(3), 239-248.

Birch R.S., Jones N. (1990), *Measurement of impact loads using a laser Doppler velocimeter*, Proceedings of the Institution of Mechanical Engineers Part C, Mechanical engineering science.

Bischoff P.H., Perry S.H. (1991), *Compressive behavior of concrete at high strain rates*, Materials and Structures, 24(6), 425-450.

Bourne N. K., Rosenberg Z., Field J. E. (1995), *Highspeed photography of compressive failure waves in glasses*, Journal of Applied Physics, 78, 3736-3739.

Chen X., Chandra N., Rajendran A. M. (2004), *Analytical solution to the plate impact problem of layered heterogeneous material systems*, International Journal of Solids and Structures, 41(16-17), 4635-4659.

Chhabildas L. C., Grady D. E., Hall C. A., Reinhart W. D. (2002), *Dynamic properties of concrete through particle velocity profile measurements*, Sandia National Labs, Livermore, USA.

Chhabildas L.C., Davison Lee, Horie Y. (Eds.). (2005), *High-Pressure Shock Compression of Solids VIII*, Springer, Berlin, Germany.

Comité Euro-International du Béton (1993), *CEB-FIP Model Code 1990*, Redwood Books, Wiltshire, UK.

Crouch L.K., Pitt J., Hewitt R. (2007), *Aggregate effects on pervious portland cement concrete static modulus of elasticity*, Journal of Materials in Civil Engineering, 19(7), 561-568.

Duffy J. (1991), *Experimental studies of shear band formation through temperature measurements and high speed photography*, Journal de Physique IV, 1, 645-652.

Drumheller D. S. (1998), *Introduction to wave propagation in nonlinear fluids and solids*, Cambridge University Press, Cambridge, UK.

Espinosa H. D. (2000), *Low-velocity impact testing*, ASM handbook, 8(6), 539-559.

Field J.E., Walley S.M., Proud W.G., Goldrein H.T., Siviour C.R. (2004), *Review of experimental techniques for high rate deformation and shock studies*, International Journal of Impact Engineering, 30, 725–775.

Franklin J., Katsabanis T. (1996), *Measurement of blast fragmentation*, A.A.Balkema Publishers, Rotterdam, the Netherlands.

Fuller P.W.W. (2009), *An introduction to high speed photography and photonics*, The Imaging Science Journal, 57, 293-302.

Furnish M. D., Chhabildas L.C., Reinhart W. D. (1999), *Time-resolved particle velocity measurements at impact velocities of 10 km/s*, International Journal of Impact Engineering, 23, 261-270.

Furnish M.D., Alexander C. S., Brown J. L., Reinhart W. D. (2014), *2169 steel waveform measurements for equation of state and strength determination*, Journal of Applied Physics, 115, 1-9.

Gebbeken N., Greulich S., Pietzsch A. (2001), *Equation of State Data For Concrete Determined by Full-Scale Experiments and Flyer-Plate-Impact Tests*, European Conference on Computational Mechanics, Poland.

Gebbeken N., Greulich S., Pietzsch A. (2006), *Hugoniot properties for concrete determined by full-scale detonation experiments and flyer-plate-impact tests*, International Journal of Impact Engineering, 32, 2017-2031.

Ghafoori N., Dutta S. (1995), *Laboratory investigation of compacted no-fines concrete for paving materials*, Journal of Materials in Civil Engineering, 7(3), 183-191.

Grady D. E. (1996), *Shock equation of state properties of concrete*, Proceedings of Structures under Shock and Impact IV, Southampton, UK.

Grady D. E. (1998), *Shock-wave compression of brittle solids*, Mechanics of Materials, 29, 181-203.

Gupta Y. M. (1983), *Analysis of manganin and ytterbium gauge data under shock loading*, Journal of Applied Physics, 54(11), 6094-6098.

Gustavsen R. L., Sheffield S. A., Alcon R. R., Hill L. G. (1999), *Shock initiation of new and aged pbx 9501 measured with embedded electromagnetic particle velocity gauges*, Los Alamos National Laboratory, New Mexico, USA.

Hall C. A., Chhabildas L.C. and Reinhart W.D. (1999), *Shock Hugoniot and release in concrete with different aggregate sizes from 3 to 23 GPa*, International Journal of Impact Engineering, 23, 341-351.

Hereil P. L. and Buzaud E. (2006), *An analysis of the propagation of front shock in concrete*, Journal de Physique IV, 134, 133-138.

Hodgkinson J. M., Vlachos N. S., Whitelaw J. H., Williams J. G. (1982), *Drop-weight impact tests with the use of laser-Doppler velocimetry*, Proceedings of the Royal Society of London, London.

Ishiguchi M., Yoshida M., Nakayama Y., Matsumura T., Takahashi I., Miyake A., Ogawa T. (2000), *A study of the Hugoniot of mortar*, Journal of the Japan Explosives Society, 61, 249-253.

Jordan J.L., Baer M. R. (2012), *Mixture model for determination of shock equation of state*, Journal of Applied Physics, 111, 1-10.

Kajberg J., Sundin K.G., Melin L.G., Stahle P., (2004), *High strain-rate tensile testing and viscoplastic parameter identification using microscopic high-speed photography*, International Journal of Plasticity, 20, 561–575.

Kanel G. I., Razorenov S. V. , Fortov V. E. (2004), *Shock-wave phenomena and the properties of condensed matter*, Springer-Verlag, New York, USA.

Kondo K., Yasumoto Y., Sugiura H., Sawaoka A. (1981), *A multiple shock reverberations in a layer structure observed by particle velocity and pressure gauges*, Journal of Applied Physics, 52, 772-776.

Lee S. F. , Swallowe G. M. (2004), *Direct measurement of high rate stress–strain curves using instrumented falling weight and high-speed photography*, The Imaging Science Journal, 52, 193-201.

Lee D., Tippur H., Kiruguilige M., Bogert P. (2009), *Experimental study of dynamic crack growth in unidirectional graphite/epoxy composites using digital image correlation method and high-speed photography*, Journal of Composite Materials, 43(19), 2081-2108.

- Luoa X., Chung D. L. (2000), *Concrete-concrete pressure contacts under dynamic loading, studied by contact electrical resistance measurement*, Cement and Concrete Research, 30(2), 323-326.
- Lysne P.C., Boarde R.R., Percival C.M., Jones O.E., (1969), *Determination of release adiabats and recented Hugoniot curves by shock reverberation techniques*, Journal of Applied Physics, 40, 3786-3795.
- Majzoub R., Chaudhri M. (2000), *High-speed photography of low-velocity impact cracking of solid spheres*, Philosophical Magazine Letters, 80(6), 387-393.
- Mathworks Inc. (2001), *MATLAB image processing toolbox*, User Manual.
- Meyers M. A. (1994), *Dynamic behavior of materials*, John Wiley & Sons, New York, USA.
- Millett J., Bourne N., Rosenberg Z. (1998), *Observations of the Hugoniot curves for glasses as measured by embedded stress gauges*, Journal of Applied Physics, 84(2), 739-741.
- Mindess S., Bentur A. (1985), *A preliminary study of the fracture of concrete beams under impact loading using high speed photography*, Cement and Concrete Research, 15(3), 474-484.
- O'Neil E. F., Jennings H., Thomas J., Shen W., Cummins T. (2004), *Safety Concrete - Development of a Frangible Concrete to Reduce Blast-Related Casualties*, Northwestern University, Infrastructure Technology Institute, Illinois, USA.
- Pan B., Qian K., Xie H., Asundi A. (2009), *Two-dimensional digital image correlation for in-plane displacement and strain measurement: a review*, Measurement Science and Technology, 20, 1-17.
- Pedersen R.R. (2009), *Computational modelling of dynamic failure of cementitious materials*, Faculty of Civil Engineering, Delft University of Technology, Delft, PhD.
- Perez-Castellanos J. L., Cortes R., Fernandez-Saez J., Navarro C. (1997), *Numerical simulation of the impact of projectiles on thin aluminium plates*, Journal de Physique IV, 7, 711-716.
- Ramesh K.T. (2009), *High strain rate and impact experiments*, Handbook of experimental solid mechanics, Springer, Massachusetts, USA.

Reinhart W. D., Chhabildas L. C., Kipp M. E., Wilson L. T. (1999), *Spall strength measurements of concrete for varying aggregate sizes*, Proceedings of 15th US Army Symposium on Solid Mechanics, USA.

Rosenberg Z., Yaziv D., Partom Y. (1980- I), *Calibration of foil-like manganin gauges in planar shock wave experiments*, Journal of Applied Physics 51(7):3702-3705.

Rosenberg Z., Yaziv D., Partom Y. (1980-II), *Direct measurement of strain in plane impact experiments by a longitudinal resistance gauge*, Journal of Applied Physics, 51(9), 4790-4798.

Rosenberg Z. (1981), *The use of Manganin gauges in shock reverberation experiments*, Journal of Applied Physics, 52(6), 4000-4002

Rosenberg Z., Meybar Y., Yaziv D. (1981), *Measurement of the Hugoniot curve of Ti-6Al-4V with commercial manganin gauges*, Journal of Physics D: Applied Physics, 4, 261-266.

Rosenberg Z., Partom Y., Keren B. (1983), *Calibration of commercial manganin stress gauges under static uniaxial strain conditions*, Journal of Applied Physics, 54(5), 2824-2826.

Rosenberg Z., Partom Y. (1985-I), *Longitudinal dynamic stress measurements with in-material piezoresistive gauges*, Journal of Applied Physics, 58(5), 1814-1818.

Rosenberg Z., Partom Y. (1985-II), *Lateral stress measurement in shock loaded targets with transverse piezoresistance gauges*, Journal of Applied Physics, 58(8), 3072-3076.

Sharma A., Shukla A., Prosser R. A. (2002), *Mechanical characterization of soft materials using high speed photography and split hopkinson pressure bar technique*, Journal of Materials Science, 37, 1005–1017.

Sukontasukkul P., Nimityongskul P., Mindess S. (2004), *Effect of loading rate on damage of concrete*, Cement and Concrete Research, 34(11), 2127-2134.

Unosson M., Nilsson L. (2006), *Projectile penetration and perforation of high performance concrete: experimental results and macroscopic modelling*, International Journal of Impact Engineering, 32, 1068-1085.

Van Mier J.G.M. (1997), *Fracture processes of concrete: Assessment of material parameters for fracture models*, CRC Press, USA.

Weerheijm J. (1992), *Concrete under impact tensile loading and lateral compression*, Faculty of Civil Engineering, Delft University of Technology, Delft, PhD.

- Wu E., Sheen H. J., Chen Y. C., Chang L. C. (1994), *Penetration force measurement of thin plates by laser Doppler anemometry*, *Experimental Mechanics*, 34, 93-99.
- Xu R., Rosakis A. J. (2003), *An experimental study of impact-induced failure events in homogeneous layered materials using dynamic photoelasticity and high-speed photography*, *Optics and Lasers in Engineering*, 40, 263–288.
- Xu L. R., Rosakis A. J. (2005), *Impact damage visualization of heterogeneous two-layer materials subjected to low-speed impact*, *International Journal of Damage Mechanics*, 14, 215-232.
- Yaziv D., Rosenberg Z., Partom Y. (1980), *Release wave calibration of manganin gauges*, *Journal of Applied Physics*, 51(12), 6055-6057.
- Yeh Y., Cummins H. Z. (1964), *Localized Fluid Flow Measurements with AN He-Ne Laser Spectrometer*, *Applied Physics Letters*, 4, 176-178.
- Zhao J. (2009) *Rock Mechanics for Civil Engineers Lecture Notes*, Swiss Federal Institute of Technology, Zürich, Switzerland.
- Zukas J. A. (1990), *High velocity impact dynamics*, John Wiley & Sons, New York, USA.

## **CHAPTER 5**

### **EXPLICIT FINITE ELEMENT ANALYSIS OF THE IMPACT BEHAVIOR OF POROUS CONCRETE**

#### **5.1. Introduction**

Numerical simulation techniques play an increasingly important role in designing and investigating new cementitious materials. Various different numerical methods are used by researchers for simulating the behavior of the cementitious materials in a realistic way and for verifying the outcome with experimental results (Qian et al. 2011). The aim of conducting numerical simulations was predicting and better understanding the dynamic as well as fragmentation properties of porous concrete. The analyses also enabled parameter studies, which are not possible to conduct experimentally due to the presence of too many coupled parameters. Therefore, numerical analyses were undertaken to investigate the separate and combined effects of different parameters that dominate the dynamic behavior of the porous concrete material. In the numerical analyses the distinctive properties of porous concrete were the presence of arbitrary shaped meso-scale air pores and the coalescence of the free surfaces of the pores as the loading proceeds.

This chapter summarizes the numerical analyses conducted on porous concrete. First, the effect of individual parameters, such as aggregate particle size, porosity, pore size and distribution are studied by analyzing virtual (model) porous concretes. Next, real porous concrete mixtures were analyzed. The numerical output was compared with experimental results. The numerical work comprises (i) the mesh and aggregate particle distribution generations performed by the codes written in MATLAB and (ii) the finite element analyses conducted with general purpose finite element programs, ABAQUS. The dynamic analyses performed using ABAQUS were conducted with the explicit central difference time integration method provided in ABAQUS/Explicit.

#### **5.2. Explicit Finite Element Analysis**

The explicit finite element method has been developed as an alternative to the widely used implicit finite element methods for mainly nonlinear transient dynamic analyses. It is currently adopted for various applications that involve highly nonlinear systems with large deformations and rotations, extensive contact and/or impact. The explicit scheme is an alternative problem solving method, which is incremental, but not iterative (Wu and Gu 2012, De Borst et al. 2012). In general, each type of integration, implicit or explicit, has its own advantages and disadvantages. Implicit methods require a much larger computational effort per time step compared with explicit methods, mainly due to the required iterations. On the other hand, implicit methods usually have unconditional stability. This enables the selection of a time step size appropriate for the specific problem to be solved, not on any limit due to stability. Explicit methods, using a diagonal mass matrix, require much simpler calculations. Hence, the

computational cost per time step is much lower. However, an explicit method can only be conditionally stable. Therefore, such methods may be more efficient when the time step size required by the stability limit is close to the time step size needed to describe the physical problem. This is usually the case in wave propagation analyses (Wu and Gu 2012, De Borst et al. 2012, Noh and Bathe 2013, Tarque 2012).

In this study explicit time integration has been selected as the analysis method because of the high nonlinearity of the system as well as the short duration of the loading. Among the explicit time integration schemes, the central difference method is a widely used one. In a central difference scheme, displacements and velocities are calculated in terms of quantities that are already known at the beginning of each time step. This procedure does not require iterations. The displacements at time  $(t+\Delta t)$  are calculated by using the matrices calculated at the previous time  $(t)$  and the deformations obtained at times  $(t-\Delta t)$  and  $(t)$  (Chopra 2000, Huebner et al. 2001). This is a very important computational advantage compared to implicit methods. Converging solutions are reached when the total energy equilibrium criteria are satisfied. In order to take into account the geometric and material nonlinearities, the matrices are updated at every step. Small time increments are selected in order to avoid large differences in matrices between two successive analysis steps. The stability limit (the largest time increment that can be selected in the analysis) is a critical value that is related to the time required for a stress wave to cross the smallest-sized element in the model. If the model contains only one type of material, the initial time increment is directly proportional to the size of the smallest element in the mesh. If the model contains multiple material descriptions, the element with the highest wave speed will dominate the determination of the needed time increment. An approximation of the stability limit for selecting the time increments is often given as the smallest transit time of a dilatational wave (with wave speed of  $c_d$ ) across any of the elements in the mesh (with smallest element dimension  $L_{min}$ ) as given below.

$$\Delta t \approx \frac{L_{min}}{c_d} \quad (5.1)$$

In case the time increments are not small enough, an unstable solution is reached where the time history responses of variables, such as displacement, oscillate with increasing amplitudes. The energy balance of the system is also drastically affected (Simulia\_1 2013, Chen et al. 2012, Sun et al. 2000, Noels et al. 2004, Dhanasekar 2008, Siad 2008). Since no iterations are performed, small time increments are required to ensure acceptable results. As a consequence of this, the total dynamic response time that can be modeled should be limited. For dynamic analyses of short duration incidents explicit methods are appropriate (Noh 2013, Farooq 2010, Huang 2009, Elmer 2012).

### 5.3. Fracture Behavior of Porous Materials

Porous concretes are designed for an intentionally high volume of meso-size air pores. Pores, in return, are among the major determinants of the mechanical properties of porous materials. Researchers have focused on the influence of various different properties of pores on the



mechanical behavior of different porous materials (Rehder et al. 2014). In the numerical part of this project, the effect of porosity, pore size and pore size distribution were analyzed separately and collectively to see the effects of those parameters.

According to Timoshenko and Goodier, the overall elastic stress distributions in an infinitely wide plate subjected to tensile (or compressive) loading (see Figure 5.1), can be described with the following equations (Timoshenko and Goodier 2001, Green 1998).

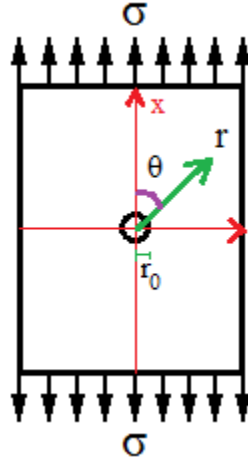


Figure 5.1 Infinitely wide plate containing a single circular hole (Green 1998)

$$\begin{aligned}\sigma_{rr} &= \frac{\sigma}{2} \left[ 1 - \frac{r_0^2}{r^2} + \left( 1 + 3 \frac{r_0^4}{r^4} - 4 \frac{r_0^2}{r^2} \right) \cos 2\theta \right] \\ \sigma_{\theta\theta} &= \frac{\sigma}{2} \left[ 1 + \frac{r_0^2}{r^2} - \left( 1 + 3 \frac{r_0^4}{r^4} \right) \cos 2\theta \right] \\ \sigma_{r\theta} &= -\frac{\sigma}{2} \left( 1 - 3 \frac{r_0^4}{r^4} + 2 \frac{r_0^2}{r^2} \right) \sin 2\theta\end{aligned}\tag{5.2}$$

Therefore, at the surface of the circular hole where  $r = r_0$ , the only stress that exists can simply be derived as:

$$\sigma_{\theta\theta} = \sigma_0(1 - 2 \cos 2\theta)\tag{5.3}$$

which has a value of  $3\sigma$  at  $\theta = \pm \pi/2$  and  $-\sigma$  at  $\theta = 0$  and  $\pi$ . Hence, the stress concentration factor (SCF, the ratio of the maximum local stress to the far field stress) for this geometry is equal to 3 and -1 at the specified locations. This holds for both tension and compression loading. Stress

concentrations are known to cause the formation of not only very high stresses near the inclusion, but also very low stresses at the rest of the section (Leguillon and Piat 2006).

A similar explanation was also given in another work where crack growth from a cylindrical hole in a brittle plate (or a spherical hole in a brittle solid) under compression was modelled considering an infinite elastic plate containing a hole of radius  $a$ . Differently in that research, the distance  $X=x/a$  is measured radially outward from the surface of the hole as seen in Figure 5.2. In the figure, it is again seen that the stress at the north and south poles of the hole is tensile and equal in magnitude to  $|\sigma_1|$  (equal to 1 when normalized by  $\sigma_1$ ). How this normalized tensile stress falls rapidly with distance  $X=x/a$  from the surface of the hole and becomes compressive when  $X \geq 2/3$  is also shown in the figure (Sammis and Ashby 1986).

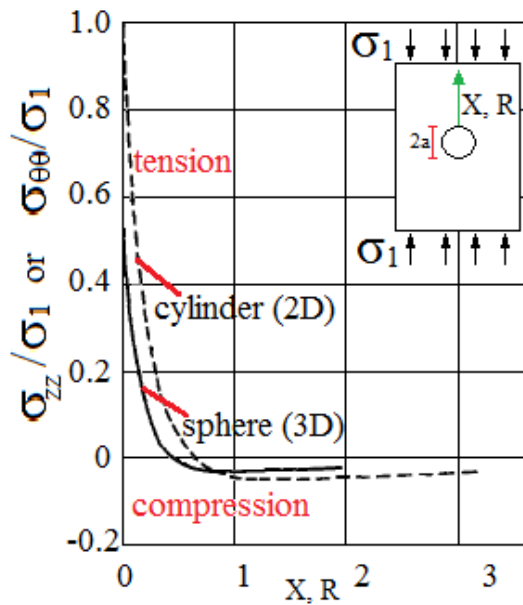


Figure 5.2 Tensile and compressive stress distributions around a circular (or spherical) hole (Sammis and Ashby 1986)

Stress concentrations and their locations are very important because these amplified stresses are usually the causes of the failure initiation at those locations and most materials, which are in a state of compression, undergo a tensile failure in the vicinity of pores. Additionally, because in real materials, pores are usually not bounded by a smooth surface, the stress concentrations are expected to be even much higher (Green 1998).

In a related study focusing on the behavior of materials containing pores, a series of uniaxial compression tests on samples containing a single hole with different diameters and sample widths were conducted to investigate the crack growth and failure modes. In the study, it was again found that for all samples that have been investigated, the tensile stresses were always greatest at the poles. When these stresses reached a critical value to initiate cracking, a pair of cracks emanated from the poles. The magnitude of the stresses around the hole was also greatly influenced by the location and the diameter of the hole and the sample width. When a narrow

sample was loaded and cracks started to form, a clear outward bending deformation of the ligaments on either side of the growing cracks occurred. Two ‘columns’ could be distinguished with also a constraining effect of the loading platens at the two ends of the sample. Bending displacements were formed when the crack length became comparable with the sample width. The bending then gave an additional contribution to the stress at the crack tips and made it propagate further which caused the cracks to extend unstably to the ends of the sample. When the sample was long enough compared to its width, the splitting was sometimes linked to buckling (as seen in the experimental results of the narrow sample in the top row of images in Figure 5.3). When the sample became wider, the resistance to bending was larger than in small samples with the same hole. In those samples, buckling was prevented. It was also noted that, due to the heterogeneity that existed in the rock samples tested, cracks were sometimes affected by those defects and did not emanate exactly from the points of north and south poles. Their propagation was also influenced which caused kinking (Wong et al. 2006).

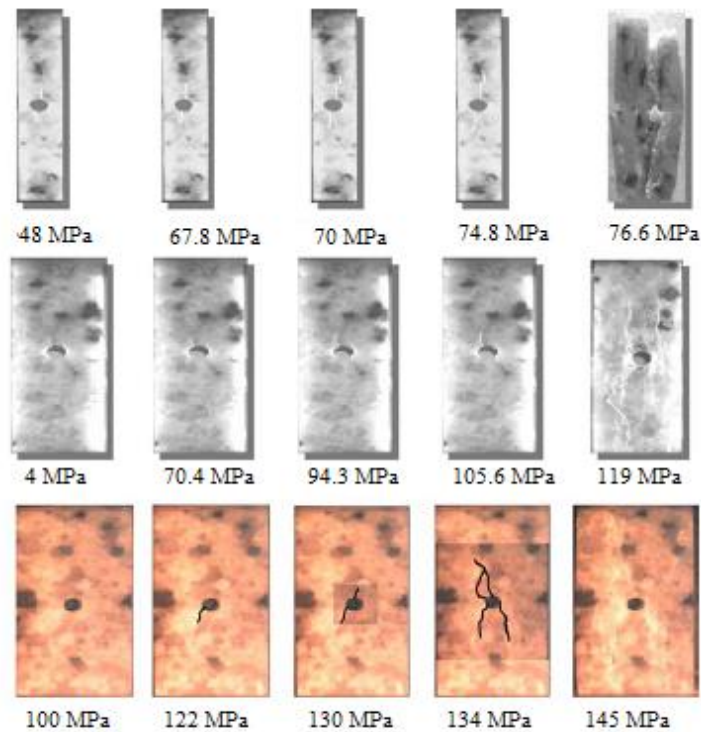


Figure 5.3 Failure behavior of samples having different widths (3.5, 7 and 10 mm, from top to bottom) (Wong et al. 2006)

In a numerical study of samples under compressive loading, the growth of cracks from a single hole (with diameters of 10, 15, 20 mm) was numerically modeled. In the study, the influence of hole diameter on the crack growth behavior was examined. The simulation results, showing in sequence the stress distribution along with the ultimate failure modes (in the last column on the right), are shown in Figure 5.4.

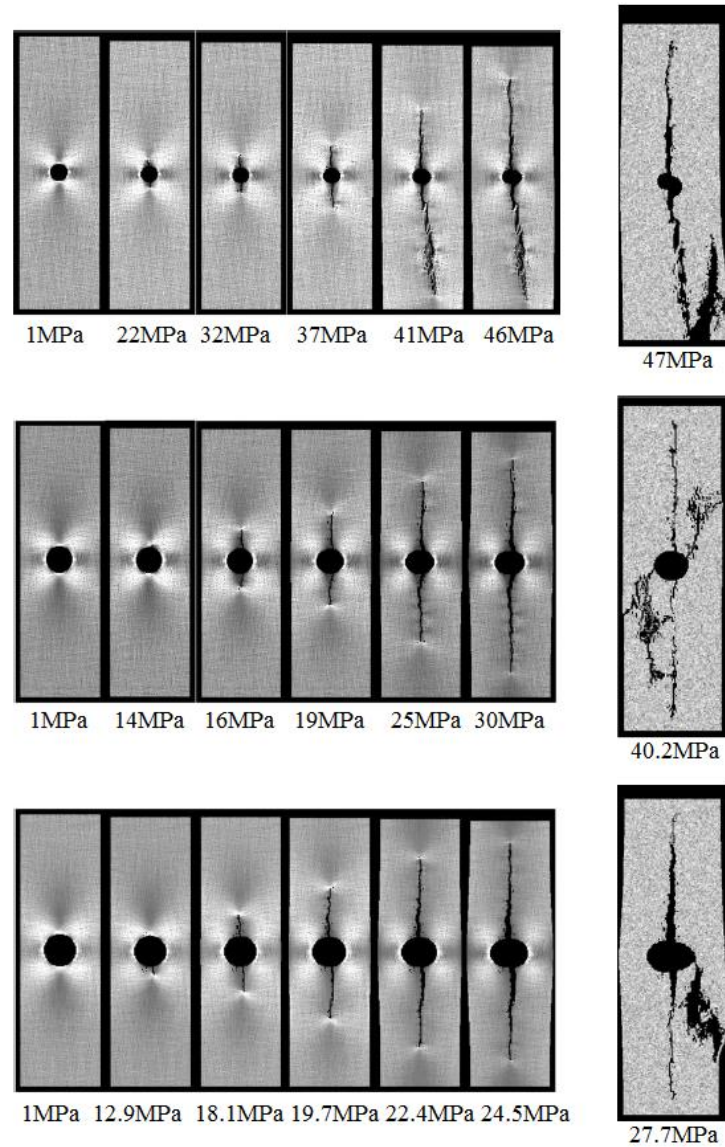


Figure 5.4 Numerical results on the failure of samples having different pore sizes (Tang et al. 2005)

The results show that the crack initiation and growth in the specimen with the smallest hole ( $2a=10$  mm) is much more difficult at the early stage of loading. For the specimens containing larger holes the cracks initiate earlier and have a higher growth rate at the beginning. as can be seen in Figure 5.4 (Tang et al. 2005). In another study, it was also seen that the interaction between the growing cracks and the specimen boundaries caused shear stress in the area between the hole and the free boundary of the specimen and failure when the shear stress reached sufficiently high values (Zhao et al. 2011).

In the pioneering work of Ashby and Sammis, it was stated that in brittle porous solids, unconfined samples tend to fail by ‘vertical slabbing’, where microcracks propagate and

percolate to form failure planes parallel to the loading direction as in parts (a) and (d) of Figure 5.5. At low or intermediate confining pressures, as in (b), a failure band, which is also sometimes called a shear band, forms because of the confining pressure. At high confining pressures, as in (c), a single failure surface does not form. The sample deforms in a pseudo-ductile mode and large scale deformation is taken up by many, homogeneously distributed cracks (Ashby and Sammis 1990).

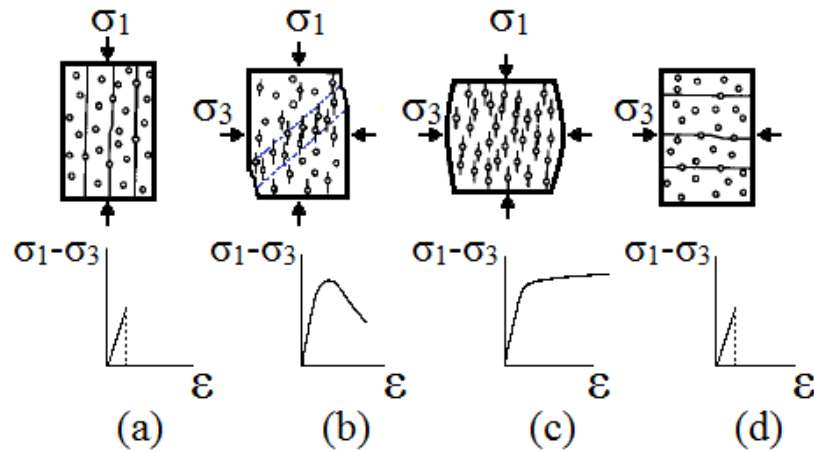


Figure 5.5 Different failure modes of a porous material (Ashby and Sammis 1990)

In another study, where again the fracture of porous materials is investigated, a fracture criterion involving both toughness and strength was proposed. In the study, the controversy between the crack blunting due to pores, resulting in an apparent toughness enhancement and the weakening effect caused by an increasing volume fraction of pores was emphasized (Leguillon and Piat 2006). In case of two neighboring pores ahead of the primary crack, as depicted in Figure 5.6, there are two major effects. There is the effect leading to an apparent toughness enhancement with increasing pore size. On the other hand, there is the weakening effect caused by the decreasing width of ligament between pores, where  $d$  is the pore diameter,  $a$  is the ligament width between the two pores and  $\zeta$  is the dimensionless ( $a/d$ ) ratio.

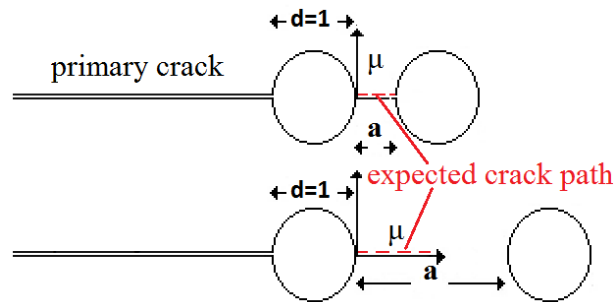


Figure 5.6 Two pores and the expected crack path (Leguillon and Piat 2006)

For  $d=0.1$  mm, the toughening effect due to the blunting was found for  $\zeta = a/d \geq 0.4$  ( $a \geq 0.04$  mm) in PMMA and  $\zeta \geq 1$  ( $a \geq 0.1$  mm) in Alumina. This effect diminished as the pore diameter decreased, while for pores as small as  $d=0.001$  mm, no toughness enhancement was seen. When the distance between the pores is small, the crack jumps from one pore to the next one, leading to a weakening effect. Reversely, when the ligament width is more than about  $6d$ , as in the bottom of Figure 5.6, the pore can be assumed to behave as a single pore, without a strong influence of the next pore. In four-pore systems, there is also the competition between the straight propagation of the crack along the symmetry axis and the crack kinking toward the nearest collateral pore. The straight propagation is valid except for collateral pores being very close to the primary (blunted) crack tip. However, it was also noted that even if the structure is perfectly symmetric, a random distribution of micro flaws (at a smaller scale than the pore diameter) induces a non-symmetric deflection rather than symmetric ones causing a crack kink.

In a research study, the compressive strengths of porous ceramics, having different macro-pore sizes, were found. The porous ceramics were fabricated by adding a pore-forming material at three different particle sizes to the same ceramic. The relation between compressive strength, porosity and macro-pore size is presented in Figure 5.7. The figure shows that, the compressive strength increases with decreasing macro-pore size (Liu 1997).

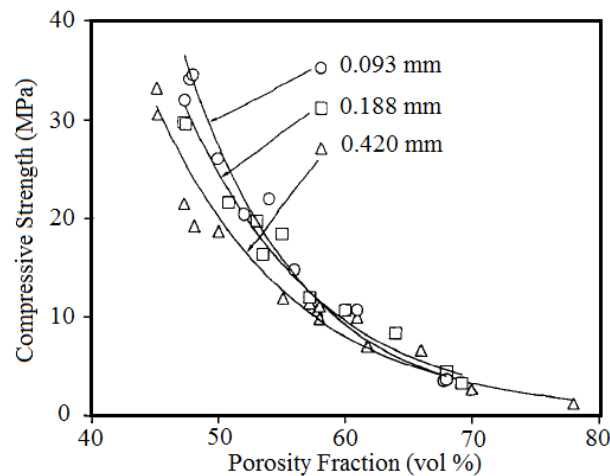


Figure 5.7 Porosity-compressive strength behavior of porous ceramics in terms of different sizes of pore-forming particles corresponding to different macro-pore sizes (Liu 1997)

Similar results were found by Zhao et al. (2004), who found that cracks nucleate more readily from larger cavities than from smaller ones and the compressive strength decreased with increasing cavity size.

The effect of the orientation of holes on the mechanical behavior has been studied by Tang et al. (2005). They found that, under uniaxial compression, holes in a diagonal array are more conducive to interaction than the holes arranged in either a horizontal or a vertical array. It was also emphasized that in the diagonal orientation of holes, the crack extension initially nucleated from the poles of the hole and then coalescence occurred between the holes along the diagonal line (in high shear stress zones). In models where the holes were horizontally oriented however,

the existence of the nearby holes sometimes even decreased the tensile stress around the central hole. In a study of Ashby and Sammis (1990) it was found that the cracks and pores being aligned in the sample causes anisotropy in the material even when the matrix material is originally isotropic e.g. the modulus of elasticity in the principal compression direction differs from that in the other directions. This also affects all the other mechanical properties and makes the situation more complex to analyze (Ashby and Sammis 1990).

Fracture behavior of composite materials under compressive loading, where cracks nucleate from the existing inhomogeneities, such as hard or soft inclusions and microcracks, has been investigated intensely by Ashby and Sammis (1990) and Tasdemir et al. (1998). Porous concrete contains both “hard” inclusions, i.e. aggregates and “soft” inclusions, i.e. the air pores of arbitrary shape and size distribution. In order to investigate the influences of those inclusions, the effects of selected parameters were investigated individually by making analyses first on model porous concretes. In these studies, the effect of only one parameter was considered while trying to keep the rest constant. This cannot be possible in case real porous concrete is considered, where many parameters are actually coupled. Testing of the real porous concrete samples from different mixtures were also simulated and compared with the experimental results

#### **5.4. Finite Element Analyses of the Impact Behavior of Porous Concrete**

The challenging factors in a numerical analysis of porous concrete are the presence of the arbitrary shaped meso-scale air pores and the contacts between the pore surfaces as the loading proceeds. In a nonlinear analysis, the main sources of nonlinearity are usually known to be the geometry, the materials involved and the boundaries and contacts between concrete surfaces especially when friction should be defined (Simulia\_2 2013). The analyses conducted on porous concretes can, be considered as highly nonlinear since all the mentioned factors of nonlinearity are present.

In the analyses conducted in the scope of this project, the finite element analysis software ABAQUS was used. In order to get input for the finite element meshes, the actual aggregates that were present in the mixtures were determined through 3D computed tomography. A mesh generation program was developed to use this data in generating a finite element mesh, which also includes arbitrary shaped air pores that are present in the porous concrete. In the analyses, concrete was considered as a four-phase material consisting of aggregates, bulk cement paste, interfacial transition zones (ITZ) and meso-size arbitrary shaped air pores.

The objective of the modelling part of this project was simulating and assessing the dynamic behavior of different porous concretes under impact loading in order to understand the effect of various control parameters on the impact behavior of those porous concretes. The following numerical analyses were performed and are reported in the next sections (see also Tables 5.1-5.5). Initially, to be able to see and better understand the behavior of a brittle plate with a single hole under compression, some static analyses were conducted that clearly demonstrated the stress distributions around a hole. The same analysis was also conducted for a cementitious material for comparison. Dynamic analyses were conducted on plain concrete material (modelled

as a one phase material with average concrete properties) containing a single hole, containing regularly distributed multiple holes and containing randomly distributed multiple holes. To see the effect of aggregate size without the effect of aggregate shape and packing, model porous concretes with circular aggregates at different diameters were also analyzed. The results of the analyses on the model porous concrete materials were very useful for better understanding the effects of factors such as pore size, pore distribution and aggregate size. In order to analyze the real porous concrete material itself, the mixtures that have been tested in the experiments have also been investigated by simulating the conducted drop weight impact tests.

#### **5.4.1. Finite Element Model**

In the numerical part of this research project, finite element analyses were conducted to investigate the responses of different types of porous concretes. In the analyses, finite element software ABAQUS (dynamic explicit analysis module) was used. In choosing an approach to a nonlinear dynamic problem, the length of time of the response, the sources of nonlinearity as well as the size of the problem are considered. The explicit time integration was chosen over the implicit analysis especially due to the short duration of impact, the large deformations and the nonlinear material response. The explicit integration method also carries the advantage of efficiently solving highly discontinuous events and is, therefore, often selected because of its efficiency in solving complicated contact problems (Susila and Hryciw 2003). Contact, which is a very important feature of the porous concrete material due to the presence of numerous pores, can be considered as extremely nonlinear (Simulia\_1 2013).

As previously pointed out at the Explicit Finite Element Analysis section of this chapter, the maximum time step to be used in the explicit analysis is very critical in terms of the stability of the solution. The results in an explicit dynamics analysis are not automatically checked for accuracy. However, in most cases this is not of concern, because the stability condition imposes a very small time increment such that the solution changes only slightly in a time increment (Simulia\_1 2013). While the analysis may take a very large number of increments, each increment is relatively inexpensive, resulting in an economical solution. In the explicit analyses conducted on porous concretes, the time steps were typically at the scale of  $10^{-14}$ - $10^{-15}$  sec.

In the analyses, the aggregate phase was identified as linear elastic. The Concrete Damaged Plasticity (CDP) model, which is a plasticity-based damage model for concrete, was used to define the material properties of the cementitious phases that are present in the analyses, i.e. the interfacial transition zone (ITZ) and the bulk cement paste. The Concrete Damaged Plasticity Model, that has been developed by Lubliner et al. and modified by Lee and Fenves, is an alteration and revision of the Drucker-Prager model (Lubliner et al. 1989, Lee and Fenves 1998, Hillerborg et al. 1976). It is a material model generally used for analyzing cementitious materials (Chaudhari and Chakrabarti 2012). A detailed description of the model is also available in ABAQUS manuals (Simulia\_1 2013).

The model is based on the concepts of isotropic damaged elasticity and isotropic tensile and compressive plasticity to represent the inelastic behavior of concrete. In the model two main



mechanisms are present, i.e. tensile cracking and compressive crushing. Different degradations of the elastic stiffness in tension and compression are considered. Rate sensitivity is also present. Especially an increase in the peak strength with strain rate can be captured (Jankowiak and Lodygowski 2005, Kmiecik and Kaminski 2011, Sun et al. 2000, Martin 2010, Simulia\_1 2013). For providing input data for the Concrete Damaged Model, experimental stress-strain data (beyond the elastic range) of the cementitious phases can be used. The experimental stress-strain data cannot be directly used as input because small fluctuations in the graph may sometimes cause error. Therefore, the strain data is slightly modified according to the format accepted by the program which will be explained in more detail in the next paragraph (Jankowiak and Lodygowski 2005, Lubliner et al. 1989, Simulia\_1 2013). The input data used to define the stress-strain behavior of each phase will also be explained in more detail in the coming respective sections of this chapter. The damage-inelastic strain relations were obtained by scaling the data given in the work of Jankowiak and Lodygowski in accordance with the experimental data from cementitious phases used in the analyses conducted for this research (Jankowiak and Lodygowski 2005).

Inelastic strains that have to be given as input for the model are determined by deducting the elastic part from the total strains recorded at the uniaxial tests. For both the compression and the tension data the same procedure is applied. The stress-strain relationship under uniaxial compression or tension is therefore defined as the initial undamaged modulus of elasticity, inelastic strain in compression or tension and damage. The program automatically converts the inelastic strain values to plastic strain using the relationship described in Figure 5.8. In that figure “pl” and “in” denote plastic and inelastic, respectively. The input data, that is directly obtained from the inelastic parts of the experimental stress-strain curves (both compressive and tensile) of the materials, frequently gives the error of “the calculated plastic strain being negative or decreasing with increasing inelastic strain”. Therefore, all the user-provided experimental stress versus inelastic strain data should be checked and adjusted if needed, in accordance with Figure 5.8 and the equations below. When generating tensile and compressive damage-inelastic strain input data, the work of Jankowiak and Lodygowski was taken as reference (Jankowiak and Lodygowski 2005, Simulia\_1 2013).

$$\tilde{\varepsilon}_C^{pl} = \tilde{\varepsilon}_C^{in} - \frac{d_c}{(1-d_c)} \frac{\sigma_C}{E_0} \quad (\text{for compression})$$

$$\tilde{\varepsilon}_C^{in} = \varepsilon_C - \varepsilon_{0C}^{el} \quad (5.4)$$

$$\varepsilon_{0C}^{el} = \frac{\sigma_C}{E_0}$$

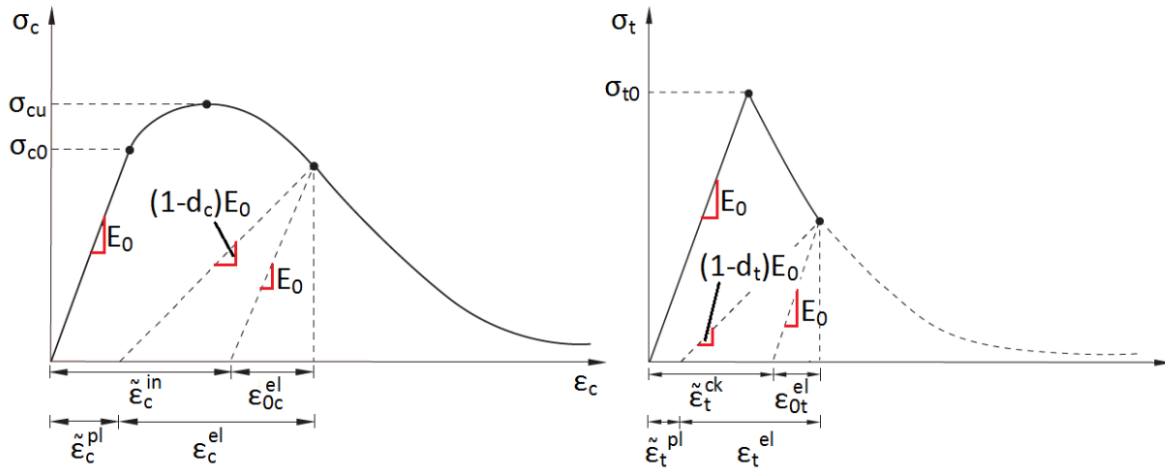


Figure 5.8 Compression and tension behavior in CDP model (Simulia\_1 2013)

The response is linear until the value of initial yield in both tension and compression. Cracking tension and crushing compression are then represented in the model by hardening (softening) variables. The CDP model does not include failure criteria. The failure should therefore be evaluated by the user, based on the state of damage. In order to introduce strain rate dependence, microscale inertia is incorporated in the model. The inertial forces acting at the micro-scale provide resistance against the micro-scale crack growth and therefore, increase the peak strength of the material.

The analysis of the impact behavior of a cylindrical porous concrete sample is actually a three dimensional problem. However, because the number of elements for representing a two dimensional section reaches about 200000 elements (including the impactor and the steel base structure), an axisymmetric analysis had to be preferred considering the limitations of computer power as well as the restrictions due to 2D mesh generation. Axisymmetric models represent a slice that is revolved around the y axis of the reference Cartesian coordinate system. All the included geometry must lie in the positive x portion of the xy plane. The geometry used in the analyses was a section taken from the porous concrete impact testing setup. This section represents the complete setup i.e. the cylindrical steel impactor, sample and the steel base structure at the bottom, as the section taken is rotated 360 degrees around the vertical axis. The dimensions of the mesh representing the concrete sample was 30 mm in width, 75 mm in height (corresponding to 60 mm diameter and 75 mm height sample when rotated axisymmetrically). The mesh of the steel impactor had 55 mm width and 220 mm height (corresponding to the 110 mm diameter and 220 mm height sample when rotated).

The drop weight impact test setup that is defined in the simulations consisted of a stationary steel base structure at the bottom, the concrete sample and the steel impactor. A typical finite element mesh for a porous concrete impact computation is shown in Figure 5.9. It is recommended to have similar size elements at the two surfaces of contact with friction, in order not to have additional convergence problems due to contacts (Simulia\_1 2013). For that purpose, the meshes

for the steel components of the setup were also selected to be approximately as fine as the meshes for the concrete sample (see Figure 5.10).

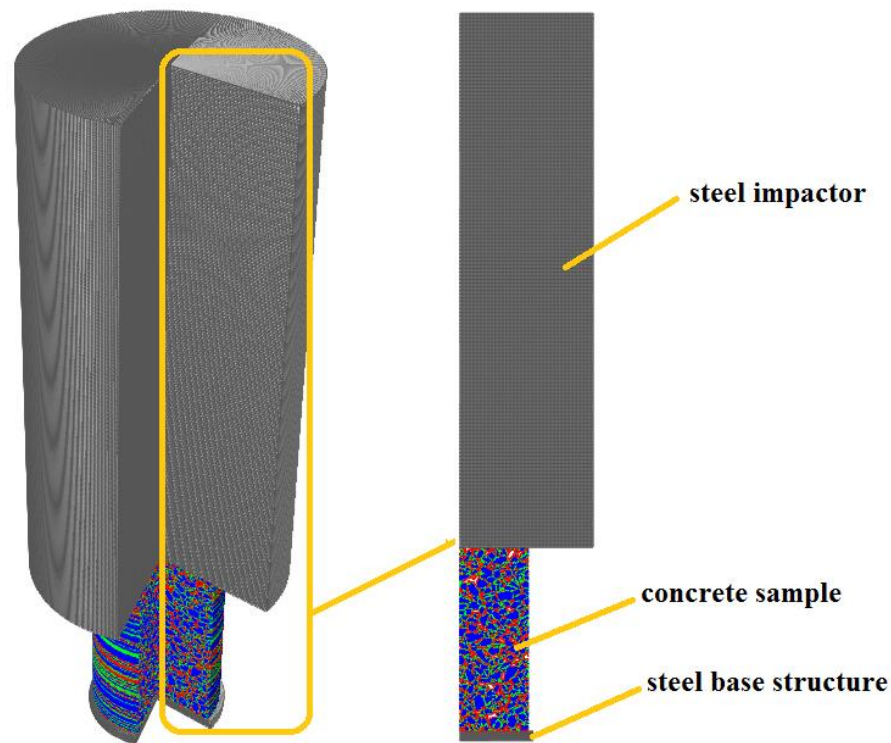


Figure 5.9 A typical finite element mesh for the impact analysis of porous concrete

The final meshes were exported to the preprocessing software ABAQUS/CAE. A fixed boundary was defined at the bottom surface of the steel base structure. The displacement in x-direction and the rotation of the impactor were constrained in order to facilitate a purely vertical movement. In the drop weight experiments the same situation is valid because the drop weight travels down in a tube. The two (steel-concrete) contacts formed between the steel base structure and the bottom surface of the concrete sample and between the steel impactor and the top surface of the sample. These surface-to-surface contacts had a friction coefficient of 0.3 in tangential direction. The (concrete-concrete) contacts formed between the surfaces of the porous concrete sample were defined as “self-contact” with a friction coefficient of 0.5 (Gorst et al. 2003, DIN 1982, BS 1997. Self-contact is used when a deformable layer comes into contact with itself. The axial impact loading applied to the concrete sample is defined as an initial impact velocity that has been assigned to the impactor (initial velocity of 4.5 m/sec), which is approximately the velocity that had been measured during the Doppler laser velocimetry experiments. The parameters that were focused on in the analysis, were mainly the impact strengths and crack patterns estimated by the damage contours. These parameters enabled the evaluation of different porous material options in terms of strength and fragmentation behavior. In the analyses, a sudden snap-back behavior after the peak was observed in the materials that contain an aggregate phase. Because the

aggregates were defined as linear elastic, an evaluation that also includes the deformation behavior especially after the peak could not be performed.

For a simple verification of the propagation time of the induced stress wave, a numerical impact test on a plain concrete was conducted. The time needed for the compressive stress to cross the height of the sample can be computed in the simulations (see Figure 5.10).

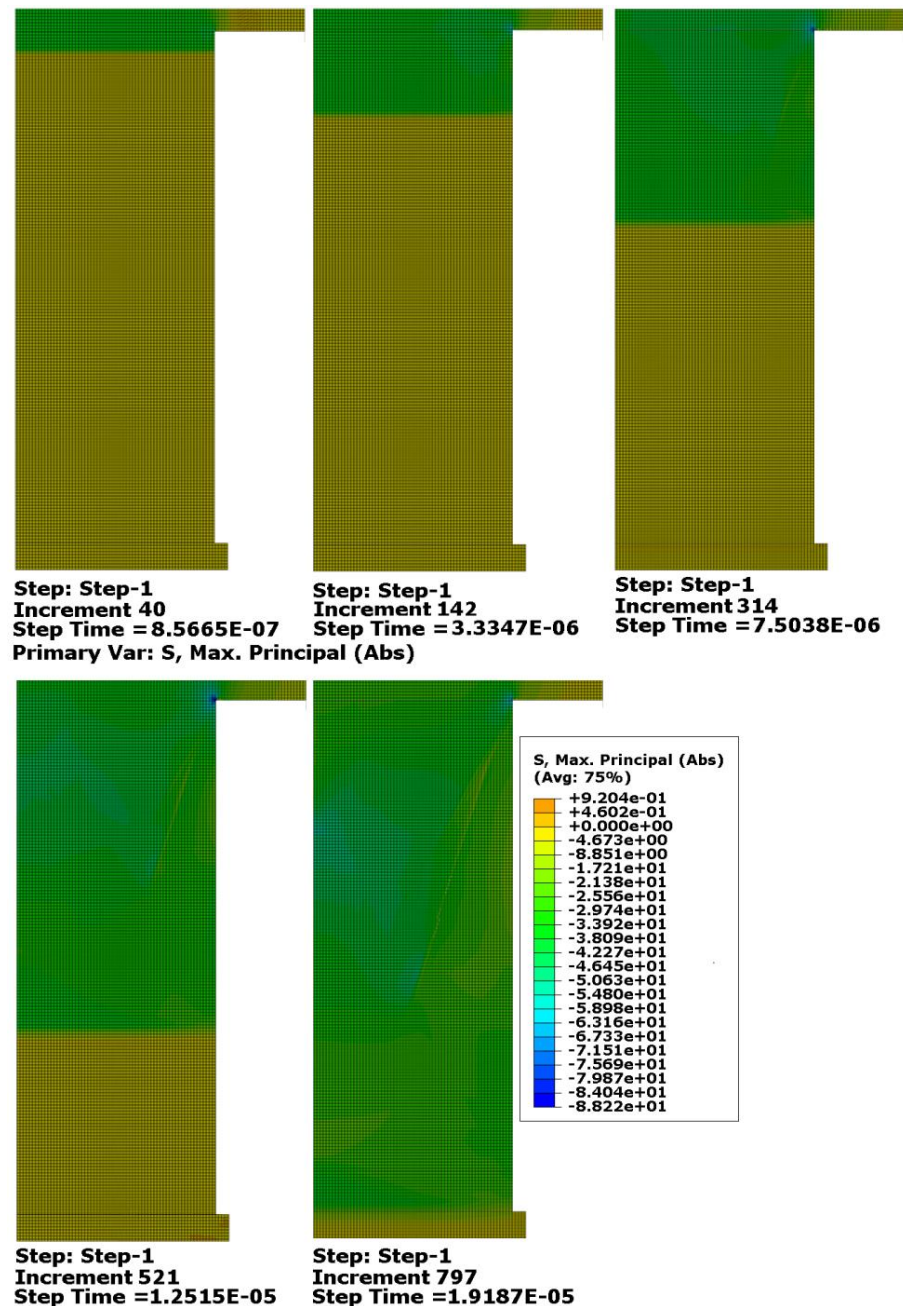


Figure 5.10 Shock response time verification for the impact test of plain concrete

Using that, an approximate wave speed for plain concrete is also calculated. The calculated wave speed can be compared with the reference wave speed values in literature, which is an important validation in terms of timing. In the simulation, plain concrete was defined using CDP model. The material property input was the same as for the plain concrete used in the model concretes with circular pores (for details, see Figure 5.18). The height of the sample in the simulations was 75 mm. It was found that it takes approximately  $1.9 \times 10^{-5}$  sec for the compressive stress to cross the whole height of the sample. This corresponds to a wave speed of about  $(75/1.9 \times 10^{-5}) = 3950$  m/sec. Because the speed of sound in plain concrete is about 3100 - 3700 m/sec (Grondzik et al. 2010, Dann and Dann 2012), the time calculated in the simulations was found to be close to the real impact response time.

### 5.4.2 Mesh Generation

Mesoscopic analysis of porous concrete requires the generation of a random aggregate structure in which the size, shape and spatial distributions of the coarse aggregates resemble that of real porous concretes. Because the properties of the meso-size pores are also critically important for both the static and the dynamic properties of the porous concretes, defining the pores in the most realistic way possible in the numerical analyses was also a necessity. For that purpose, a mesh generation code was written in MATLAB for generating realistic meshes for porous concretes. Computed tomography (CT) was used in mesh generation both in determining the aggregate distribution (see Figure 5.11) and in quantifying the porosity of the porous concrete specimens (see section 3.2.3.2.). In the CT analysis, three-dimensional images of the specimens are acquired. The three-dimensional image can then be separated into digital CT slices enabling the analysis of the specimen at any section taken both vertically and horizontally at any angle. In the CT image, different materials are indicated by different shades of gray due to the change in density. For obtaining the particle distribution and shapes of the aggregates, all porous concrete mixtures that were numerically analyzed were cast again using epoxy resin instead of cement paste keeping the aggregate content and the compaction method the same as the real mixtures. The epoxy was used to provide a greater difference between the densities of the matrix and the aggregates in the CT image, in order to have a clearer distinction between the two. Because the specimens were large, they were cut into smaller portions to be able to capture the whole specimen with a high enough resolution. The pieces of images were then combined using an imaging software in order to have the complete images of the selected sections. By converting the gray scale images to binary (purely black and white) and then by finding the coordinates of the borders of aggregates, each aggregate was defined one by one in the program. Having the coordinates of the aggregates, the program creates three sets of borders for each aggregate, representing the borders between the four phases i.e. aggregate, ITZ, bulk cement paste and air (see Figure 5.11). Each aggregate grain was defined individually and numbered. The boundaries of the phases surrounding it were also defined one by one following the same sequence of grain numbers assigned to each grain.



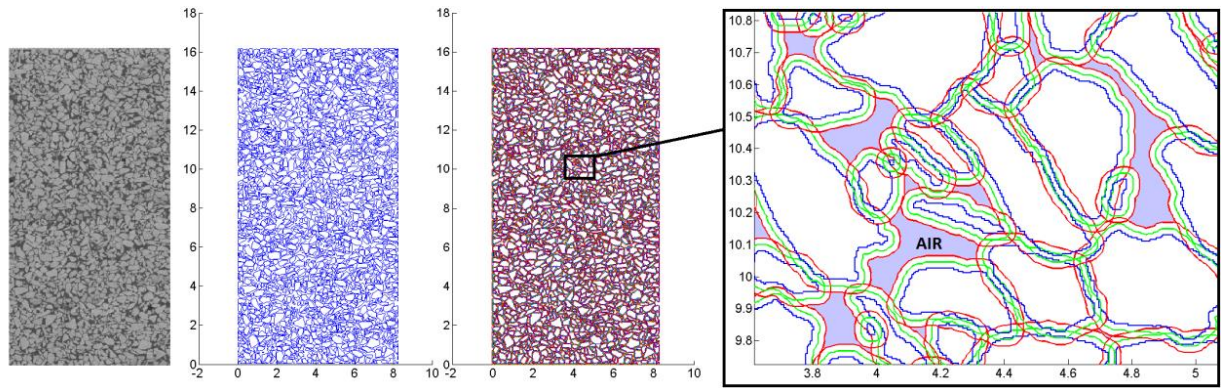


Figure 5.11 (Left) CT scan of a 2-4 mm basalt aggregate epoxy porous concrete, (middle) the detected borders of the aggregates, (right) borders of the phases: aggregates (blue), ITZ (green) and bulk cement paste (red)

The nodes, and consequently the elements of a background mesh of specified dimensions, were then sorted by the program according to the material phase they were included in as shown in Figure 5.12.

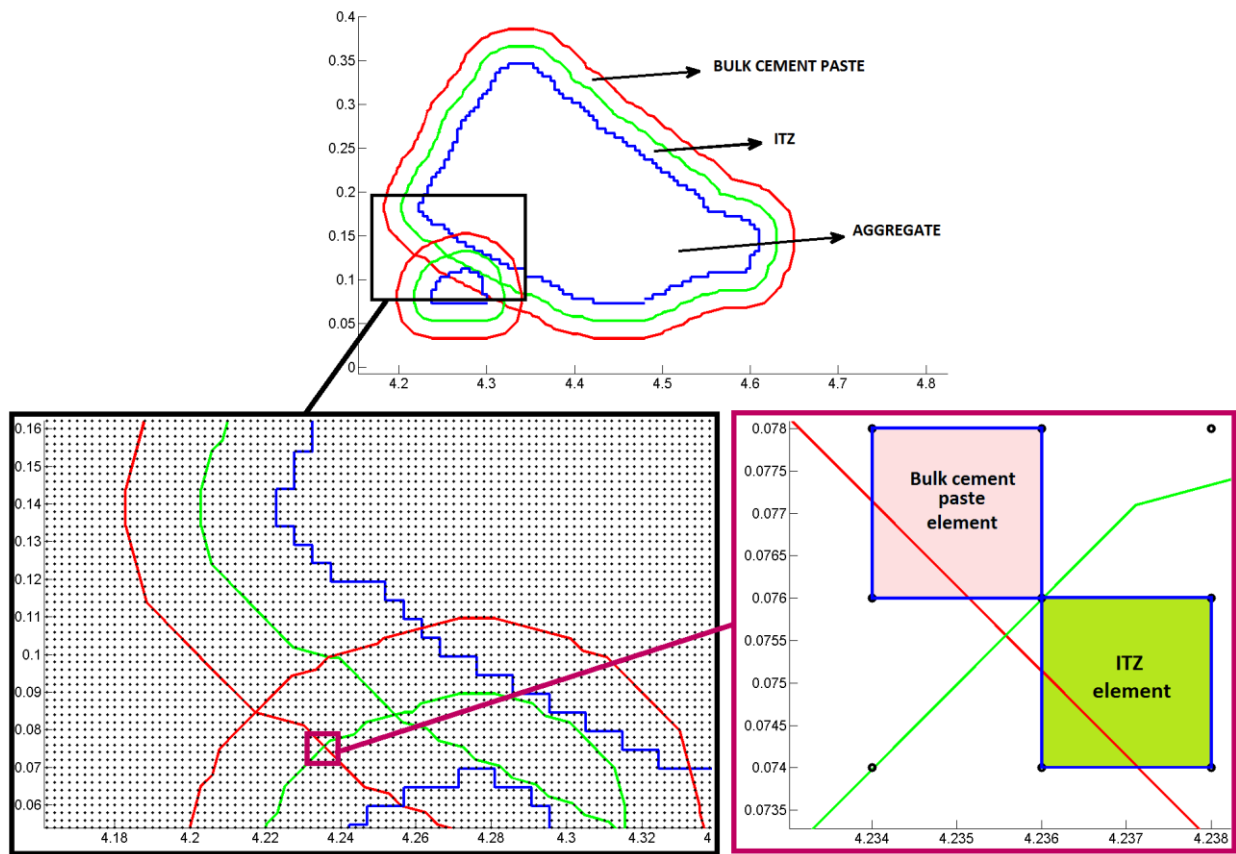


Figure 5.12 Mesh generation- categorizing the elements of a background mesh

The mesh program generates the porous concrete mesh taking those boundaries as reference and defining the rest of the mesh as air. The elements and the corresponding nodes that were situated in the air phase were then removed from the mesh after which the mesh was reorganized. The procedure is repeated iteratively by varying the cement paste layer thickness until the porosity that is aimed at is obtained. The finite element mesh representing a section of the porous material (to be used in either a 2D or an axisymmetric 3D analysis) was generated as in Figure 5.13. It should be noted that because the mesh in the figure is very fine, the borders of the elements are not fully visible.

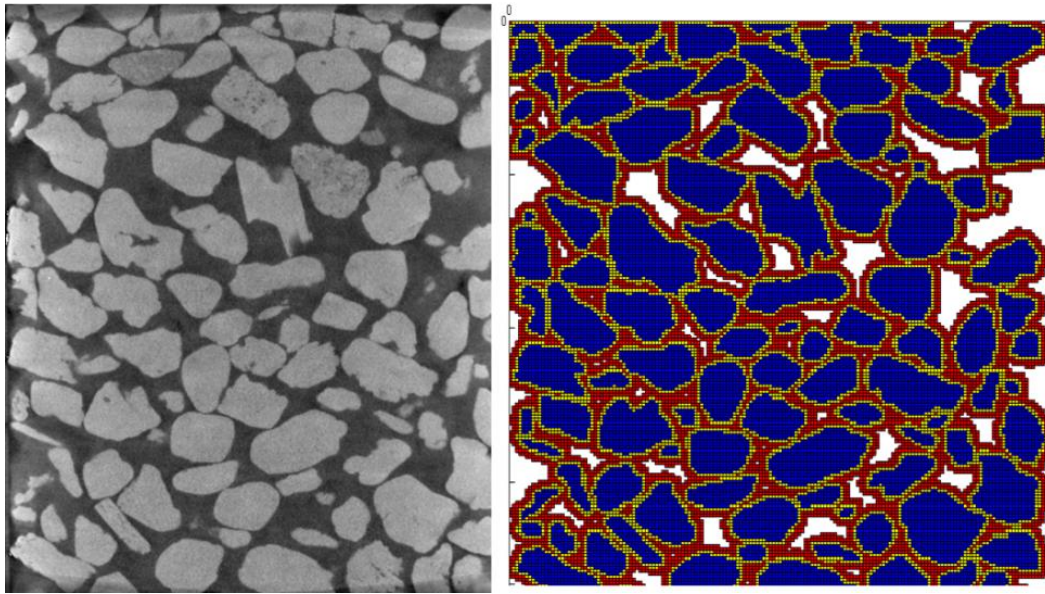
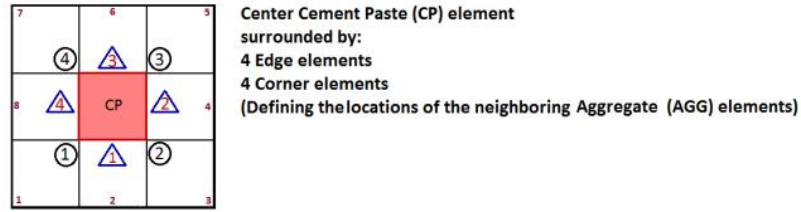


Figure 5.13 Mesh generation using CT scan: a) (left) CT image of a hand-compacted porous concrete with 4-8 mm gravel aggregates, b) (right) the respective porous concrete mesh generated

Mesh refinement at specific locations was needed because damage can be more localized at specific regions especially at weak phases such as ITZ. Therefore, a finer mesh is preferred for the ITZ regions. For mesh refinement, a similar mesh generation procedure is followed as presented at the beginning of this section. Differently, an ITZ layer is not initially generated, i.e. only a bulk cement paste layer (CP) is defined around the aggregates. Subsequently, the CP elements that are neighboring to the aggregates are refined by partitioning. The partitioning method that is designed for mesh refining is briefly explained in Figure 5.14 where the main types of element partitions are demonstrated.



MAIN TYPES OF NEIGHBORHOODS TO THE CP ELEMENT  
(combinations and variations of these main types are used in defining all CP elements)

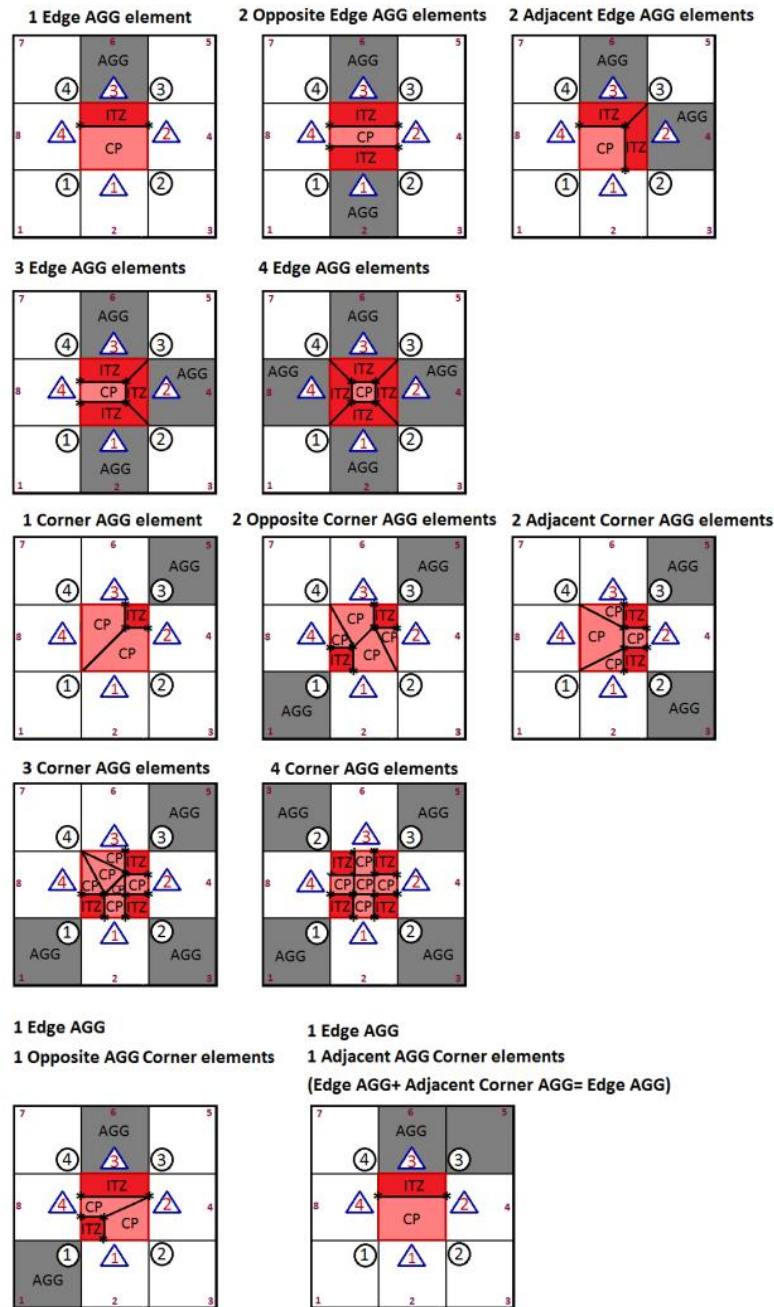


Figure 5.14 Element partitioning for mesh refinement



In partitioning, a partition ratio is selected depending on the aimed element size for the phase (see Figure 5.15). In order for the refined elements not to have high aspect ratios, a partition ratio less than  $1/3$  is not feasible. In addition, in the explicit analyses the smaller the elements, the smaller is the stability limit (see section 5.2) (Tarque 2011). Therefore, mesh refinement should be done in a controlled way.

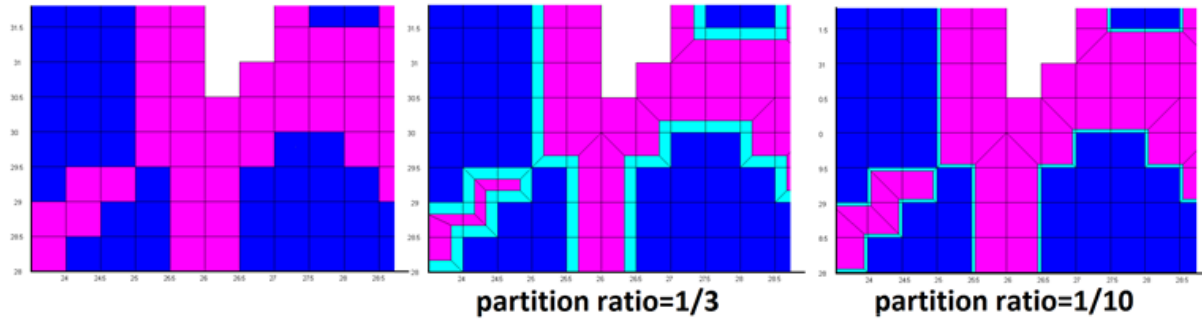


Figure 5.15 Examples of mesh refinement with different partition ratios

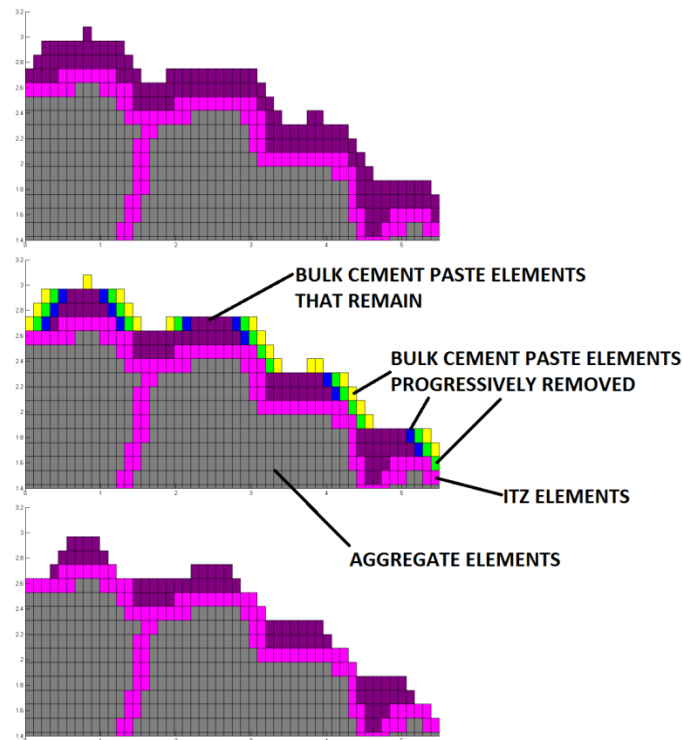


Figure 5.16 Trimming of the cement paste elements

Another feature that was added to mesh generation was trimming of the outer layer of cement paste elements (quadrilateral elements having two or more than two free surfaces) in order to adjust the porosity as well as to form a realistic distribution of cement paste phase. At each step, only the outermost elements are removed, e.g. starting from the yellow elements to the ones in

green and then the ones in blue, while the porosity is checked at each step. The bulk cement paste elements are removed progressively until the aimed porosity is reached. Similarly, in real porous concretes the actual thickness of cement paste is not uniform around the aggregates. At free surfaces that are not in contact with each other the cement paste layer gets slightly thinner. The removal of such idle elements may not significantly affect the mechanical properties. They are important, however, in modifying and quantifying the porosity in a realistic way. This is illustrated in Figure 5.16, where the original mesh at the top is trimmed by progressively removing the colored elements step by step.

### 5.4.3. Numerical Analyses on a Single Pore

Numerical analyses were initially conducted on plates with one pore, loaded in static compression. In the analyses, a linear elastic material (glass) and a cementitious material (concrete) were considered in order to be able to compare the behaviors of these two materials. Then, the performances of concrete cylinders with and without a single pore under impact loading were also analyzed. The main features of the ‘single pore analyses’ are given in Table 5.1.

Table 5.1 Single pore analyses

SINGLE PORE ANALYSES			
Material Phases Present: Aggregates + Bulk Cement Paste + Air			
Analysis Label	Specimen (mm)	Pore Radius (mm)	Material Phases
GLASS1PORE_STA	Plate	15	Glass+Air
CONC1PORE_STA	Plate	15	Concrete + Air
CONC_DYN	Cylinder	-	Concrete
CONC1PORE_DYN	Cylinder	8	Concrete + Air

As mentioned in section 5.3 already, stress concentrations at the vicinity of a pore in a brittle plate have been widely investigated analytically, experimentally and numerically. Therefore, this was also a good verification of the results of this numerical analysis. Thus, basic analyses were conducted first on a plate of a typical brittle material (defining the material properties of glass). Then, similar analyses on a concrete plate with hole were carried out to approximately see the stress concentrations, before going into the analyses of model and real porous concretes under impact loading. In Figure 5.17, the calculated stress distributions around a hole in glass (under a static compressive stress of 30 MPa) are shown. Tensile stresses about 32.17 MPa at the poles and compressive stresses about 90.86 MPa at the two sides of the hole were obtained. To check the stress concentrations altogether, the absolute maximum principle stress was selected to see the largest value of the minimum and maximum principals regardless of their signs. The numerical results of a linear-elastic material (glass, defined with  $E = 60$  GPa and  $\nu = 0.22$ ) were found to be agreeing with the results in literature where tensile stresses are formed at the poles and compressive stresses are concentrated at the sides of a pore while their ratio (absolute) is

close to three (Timoshenko and Goodier 2001). Because there is no damage or failure of elements defined in this basic model, the stresses progressively increase around the hole in a perfectly linear elastic material.

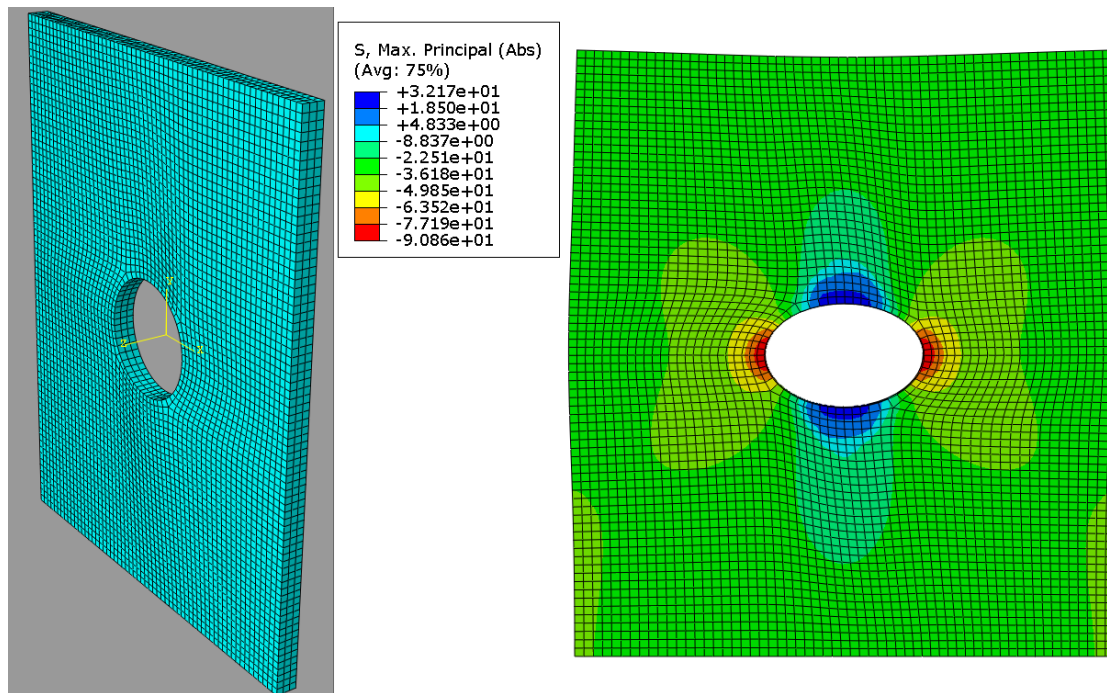


Figure 5.17 Stress concentrations around a hole in a linear elastic material (under static compression)

In Figure 5.19, the stress distributions around a hole in a concrete plate (again under a static compressive load of 30 MPa) are shown. In the analyses, a type of concrete that resembles the general behavior of a porous concrete was defined, by taking the experimental data as reference, using the Concrete Damaged Plasticity (CDP) material model in ABAQUS. As also previously described in section 5.4.1 on the finite element model, the input for the CDP material model to define the cementitious phases can be extracted from experimental data. Inelastic strains that have to be given as input for the model are determined by deducting the elastic part corresponding to the undamaged material from the total strains recorded at the uniaxial tests. Modified inelastic strain input was used by taking the work of Jankowiak and Lodygowski as reference in order not to receive strain input error (see also section 5.4.1). The input data to define the compressive and tensile behavior of the concrete material used in the analyses of a single pore described above are given in Figure 5.18. It should be noted that only the stress-inelastic strain values are provided as input to the model. The linear elastic parts of the uniaxial tensile and compressive stress-strain responses are not included in the input. Thus, the curves in Figure 5.18 do not start from the origin. This is also valid for the input data that have been defined for the cement paste and ITZ phases presented in the respective sections of this chapter. The damage-inelastic strain data were also taken from the paper by doing scaling (Jankowiak and

Lodygowski 2005, Simulia\_1 2013). This same input data for concrete were also used for representing the material properties of the concrete material phase in the model porous concretes containing (regularly and randomly distributed) circular pores in section 5.4.4.1 as well as the porous concrete with a single pore under impact loading. In the model, the following parameters were also defined:  $E=35$  GPa (taking approximately the  $E$  value obtained from the high strength porous concrete mixtures as reference),  $\nu=0.19$ . The modulus of elasticity of porous concrete is high due to the high percentage of aggregates in the material and the low ITZ content due to the lack of fine aggregates. The rest of the parameters needed for the model that cannot be commonly measured in experiments (such as dilation angle and viscosity parameter) were again taken from the widely referenced work of Jankowiak and Lodygowski given for a concrete class B50 (Jankowiak and Lodygowski 2005).

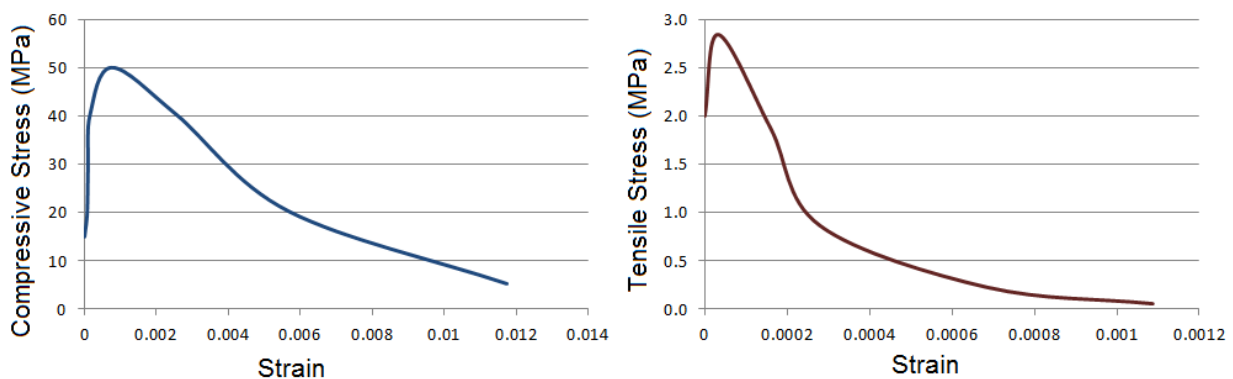


Figure 5.18 Compressive and tensile stress versus strain input data for concrete (for single and multiple pore model porous concrete analyses)

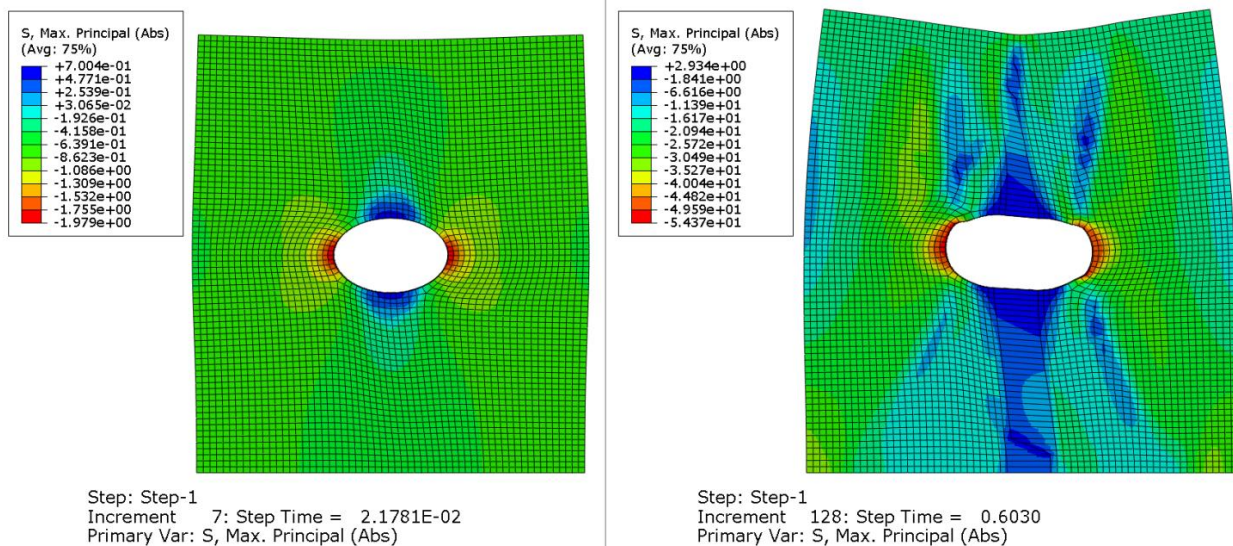


Figure 5.19 Stress concentrations around a hole in concrete plate (under static compression).  
Left: elastic response phase, right: beyond the elastic stage



For low stress levels, when the material is still in the elastic range, the stress distribution around a hole in concrete is very similar to those of a glass specimen. However, when the stresses increase and the material starts to deform plastically, the distributions and magnitudes of tensile and compressive stresses around the hole become completely different. This is illustrated in the second stress contour presentation in Figure 5.19. Although the magnitude of the stresses and deformations significantly vary, the general rule of high tensile stresses at the poles and compressive stresses at the two sides of the pore is still valid.

After analyzing the stress distributions in a plate with a hole under static compression, the behavior of concrete having a single hole (axisymmetric analysis) under drop weight impact loading (with an impact velocity of 4.5 m/s) was investigated. In Figure 5.20, the general view of the mesh and the maximum (absolute) principal stress distribution are shown. In the analysis, the height of the sample was 75 mm and the radius was 30 mm, taking the dimensions of the experimental concrete specimens used in impact testing as reference. It can again be observed in the stress distributions that there are tensile stress concentrations at the top and bottom borders and a compressive stress concentration at the sides of the pore under compressive dynamic loading.

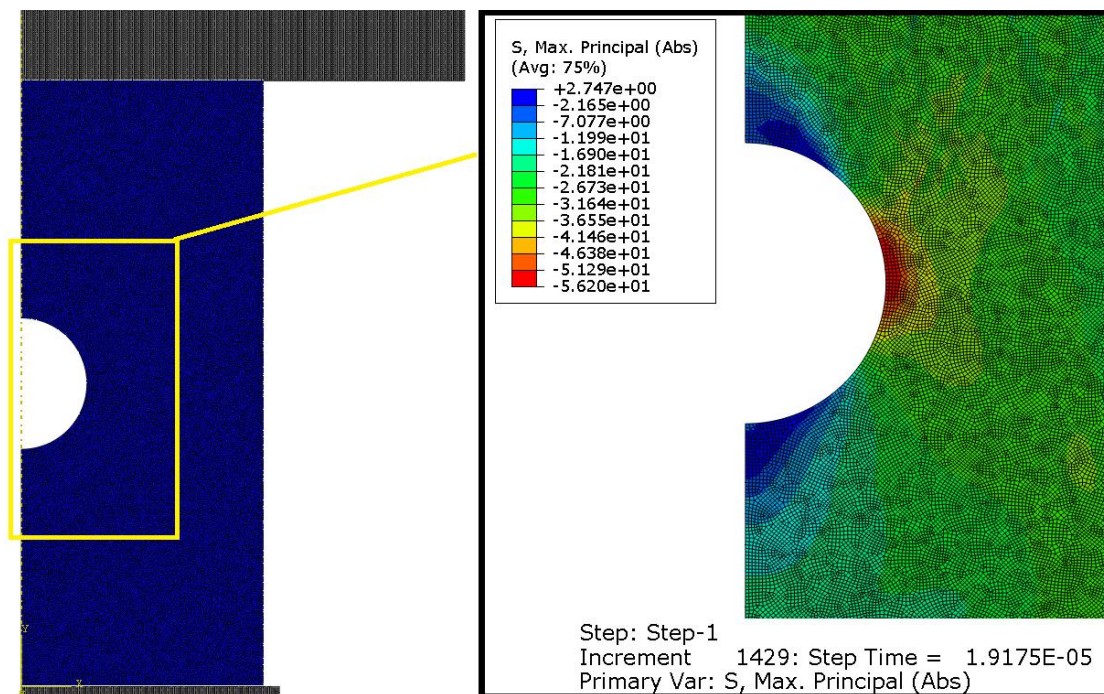


Figure 5.20 Stress concentrations around a hole in a concrete cylinder (under impact)

In the analyses, the crack growth under impact loading is visualized using the compressive and tensile damage variable contours (DamageC and DamageT). The cracks generated in the specimen are presented for two subsequent time steps in Figure 5.21. Because cementitious materials show different responses in tension and compression, the occurrence of damage due to compression is usually observed later in time compared to damage due to tension. The

compressive and tensile damage contour plots were checked at the time ( $1.91 \times 10^{-5}$  seconds) presented in Figure 5.20. It was seen that there was tensile damage incurred at the top and bottom poles (see Figure 5.21). At the same time step, no compressive damage was observed. At a later time (approximately around  $4.5 \times 10^{-5}$  seconds), damage due to compression was visible in the DamageC contours presented in Figure 5.21. As it will also be observed in the damage contours of circular pore model concretes (see section 5.4.4.1), the cracks originating from the pores due to tension or compression are then guided by not only material based, but also structural effects such as restrained lateral deformations due to boundary conditions. Due to the friction between the steel base structure at the bottom and the bottom surface of the concrete specimen as well as the friction between the top surface of the specimen and the bottom surface of the impactor, the initial cracks become inclined and curved wing cracks develop from the crack-tips. This mechanism is also observed in numerous studies performed on homogeneous brittle materials such as PMMA (van Mier 2013).

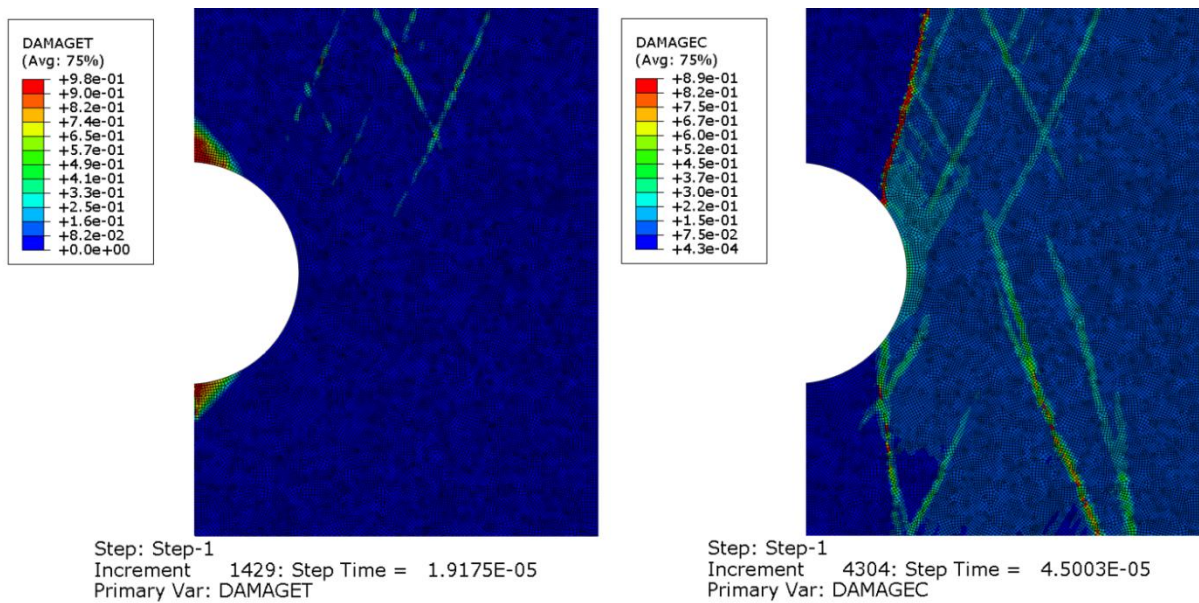


Figure 5.21 Tensile and compressive damage contours in a concrete cylinder (under impact) at  $t = 1.917 \times 10^{-5}$  s and  $t = 4.5003 \times 10^{-5}$  s.

#### 5.4.4. Numerical Analyses on Model Porous Concretes

The influences of the different parameters such as pore and aggregate size distributions and total porosity, on the performance of concrete are usually coupled. Therefore, it is hardly possible to quantify the sole effect of each parameter. Even when several different types of porous concretes are analyzed and compared, it is not easy to reach a conclusion on the effect of individual parameters. To overcome this problem, virtual or model porous concretes were also analyzed in the scope of this research. In those analyses, the size, amount and distribution of the pores as well as the aggregate sizes were individually varied. The numerical simulations were conducted using an axisymmetric geometry as discussed in section 5.4.1. 30 mm radius, 75 mm height

samples with circular pores and 36 mm radius, 75 mm height samples with circular aggregates were analyzed. The samples were impacted with a steel drop weight of 55 mm radius and 220 mm height with an impact velocity of 4.5 m/sec representing the drop weight experiments. The primary concerns of the analyses were computing the dynamic strengths of the analyzed porous concretes as well as examining their fragmentation behaviors.

Self-contact with a friction coefficient of 0.5 was adopted for the tangential behavior of the concrete surfaces coming into contact. Self-contact can be defined as a type of contact where a deformable layer comes into contact with itself. Hard contact was defined for the normal direction in which no penetration of the (slave) nodes to the opposite (master) surface is allowed on the interface. The friction at the boundaries, i.e. the friction between the steel base at the bottom of the specimen and the specimen itself as well as the friction between the steel impactor and the specimen, were incorporated into the model as surface-to-surface contact with a friction coefficient in the tangential direction of 0.30. The presence of complex contact properties substantially decreases the time increment in the explicit computations. However, contacts are essential in conducting a realistic simulation for materials such as porous concrete, which involve complex contact properties. Frictional restraint at the borders is also an important structural factor that significantly affects the fracture behavior of the specimen.

#### 5.4.4.1. Model Porous Concretes with Regularly Distributed Circular Pores

Model porous cementitious materials having circular pores of different radii, pore size distribution and total porosity, were analyzed to see the effect of those parameters individually.

Table 5.2 Analyses conducted on model porous concretes with regularly distributed circular pores

MODEL POROUS CONCRETES WITH REGULARY DISTRIBUTED CIRCULAR PORES Material Phases: Plain Concrete + Air			
Analysis Label	N. of Pores	Pore Radius (mm)	Porosity
REGPORE8NO1	8	3.0	0.1005
REGPORE8NO2		4.0	0.1786
REGPORE8NO3		5.0	0.2791
REGPORE23NO1	23	1.7693	0.1005
REGPORE23NO2		2.3591	0.1786
REGPORE23NO3		2.9488	0.2791
REGPORE77NO1	77	0.9670	0.1005
REGPORE77NO2		1.2893	0.1786
REGPORE77NO3		1.6116	0.2791
REGPORE281NO1	281	0.5062	0.1005
REGPORE281NO2		0.6749	0.1786
REGPORE281NO3		0.8436	0.2791

The main features of the analyses conducted on model porous concretes with regularly distributed circular pores are given in Table 5.2. In the analyses, concretes with four different numbers of pores (8, 21, 77 and 281) were investigated (see Figure 5.22). The effects of pore size and the number of pores on the behavior of porous cementitious materials were elaborated. The Concrete Damaged Plasticity model was again used to define the plain concrete phase. The input data used for the model porous concretes were the same as in the single pore analyses as defined in section 5.4.3 (see Figure 5.18).

In the first sets of analyses, samples with regularly distributed circular pores were investigated. Initially, the effect of pore size was analyzed while the total porosities were kept constant. A representative set of meshes (total porosity 0.1005) is presented in Figure 5.22.

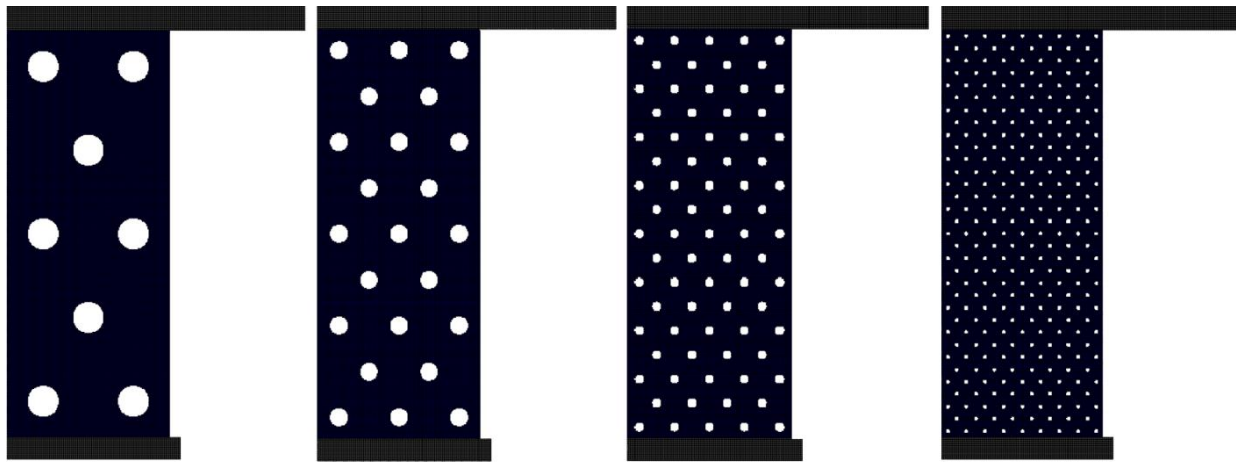


Figure 5.22 Porous concretes with circular pores at different sizes (total porosity 0.1005)

The impact responses of model porous concretes with pores of different sizes and constant total porosities of 0.1005, 0.1786 and 0.2791 are compared. Results are presented in Figures 5.23, 5.24 and 5.25, respectively. From the figures, it can be concluded that the impact strength increases as the pore size decreases, provided that the total porosity is kept constant. It was also found that this trend was valid for all the total porosities analyzed.



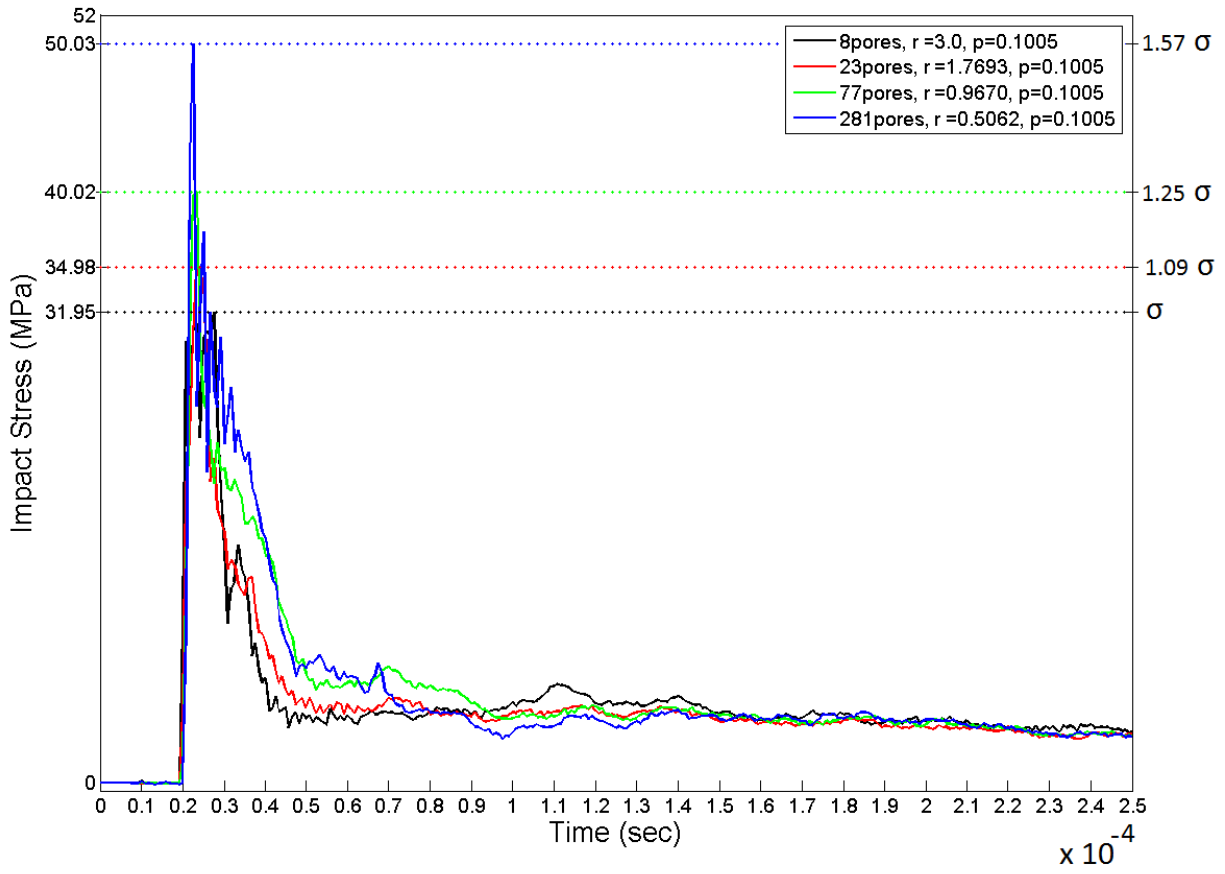


Figure 5.23 Impact stress time histories of model porous concretes with different pore sizes (total porosity 0.1005)

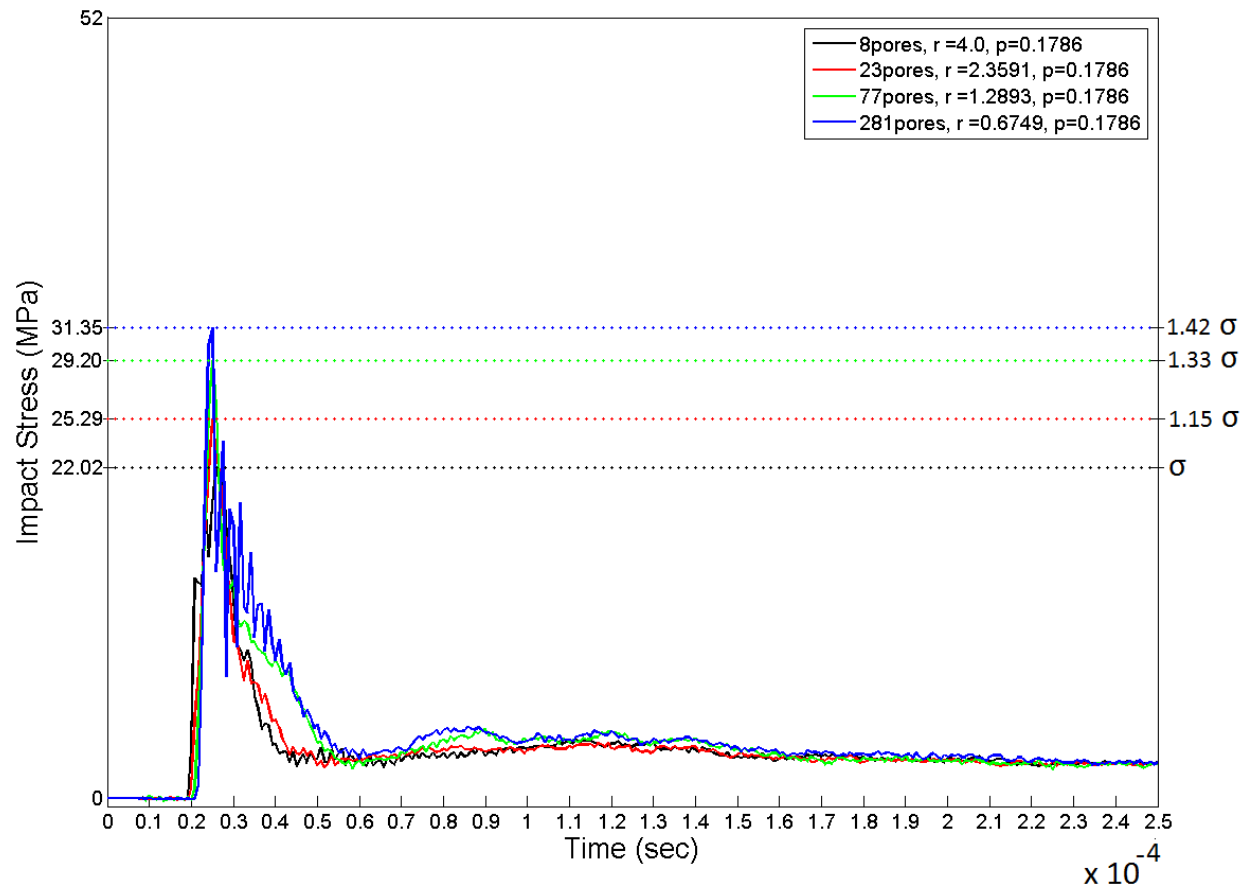


Figure 5.24 Impact stress time histories of model porous concretes with different pore sizes (total porosity 0.1786)

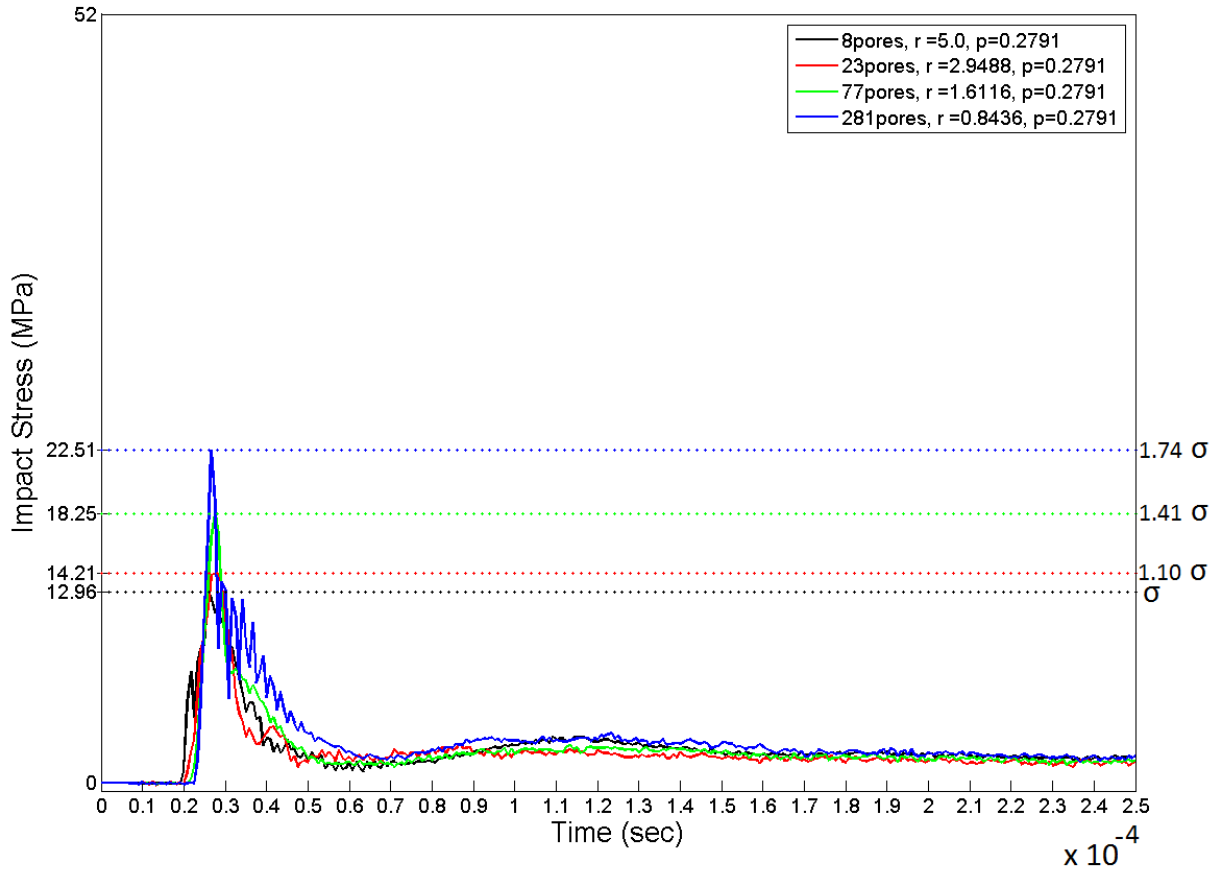


Figure 5.25 Impact stress time histories of model porous concretes with different pore sizes (total porosity 0.2791)

Along with the dynamic strengths, the fragmentation behaviors of the different mixtures are also important. The crack patterns formed under impact loading were again visualized using the compressive and tensile damage variables. While all regularly distributed circular pore model concretes were examined in terms of damage, the two extremes (8 pores and 281 pores) were selected for detailed presentation in Figures 5.26 and 5.27. In the figures, the compressive and tensile damage evolution contours are shown separately. The elements with a damage value of 0.9 or higher were removed by the program. This enabled the visualization of the crack patterns. The images showing the results at some selected instances:  $3.5 \times 10^{-5}$  sec corresponding to approximately the peak and  $5.0 \times 10^{-5}$  sec which is approximately the end of the descending branch (see Figures 5.23-5.25), were presented in Figures 5.26 and 5.27. Because the finite element mesh is very fine, the colored contours are not visible in the images that show the whole mesh. Therefore, a piece of zoomed image showing a close up view was also added to the figure. At the zoomed image, elements with damage values of 0.9 or higher were not removed. The last contour plot in each figure gives the combination of tensile and compressive damage contours (for  $5.0 \times 10^{-5}$  sec), which reflects a more realistic crack pattern.

The dynamic fracturing behaviors observed in these analyses involve both material and structural aspects. The cracks that originate from the top and bottom poles of the pores in the tensile damage graphs are clearly seen in both Figures 5.26 and 5.27. They are the typical tensile damage locations that can be expected at the vicinity of the pores. Additional tensile splitting cracks emanating from those locations are also visible. In the compressive damage contours, the cracks that originate from the sides propagate further by making inclinations. State of triaxial compression exists due to boundary effects in impact testing. Friction between the concrete sample and the steel impactor or the steel base structure of the setup causes lateral compression additional to the uniaxial compression component. Therefore, limited and sometimes no damage can be seen in the triaxially loaded zones at the border of the samples.

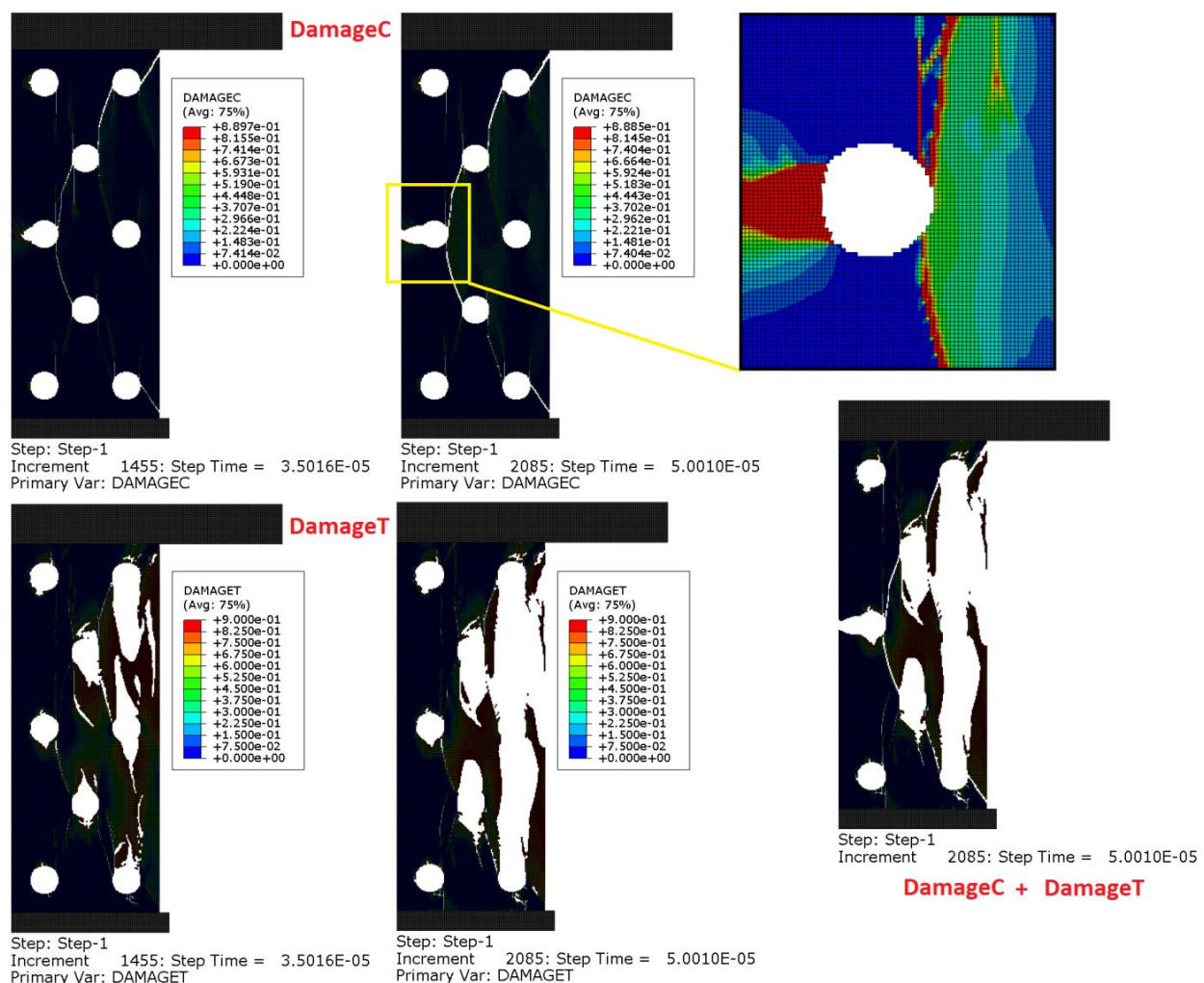


Figure 5.26 Compressive (upper part) and tensile damage (bottom part) contours and their combination for estimating the crack propagation in model porous concrete under impact loading (8 pores, r=3 mm, porosity=0.1005)

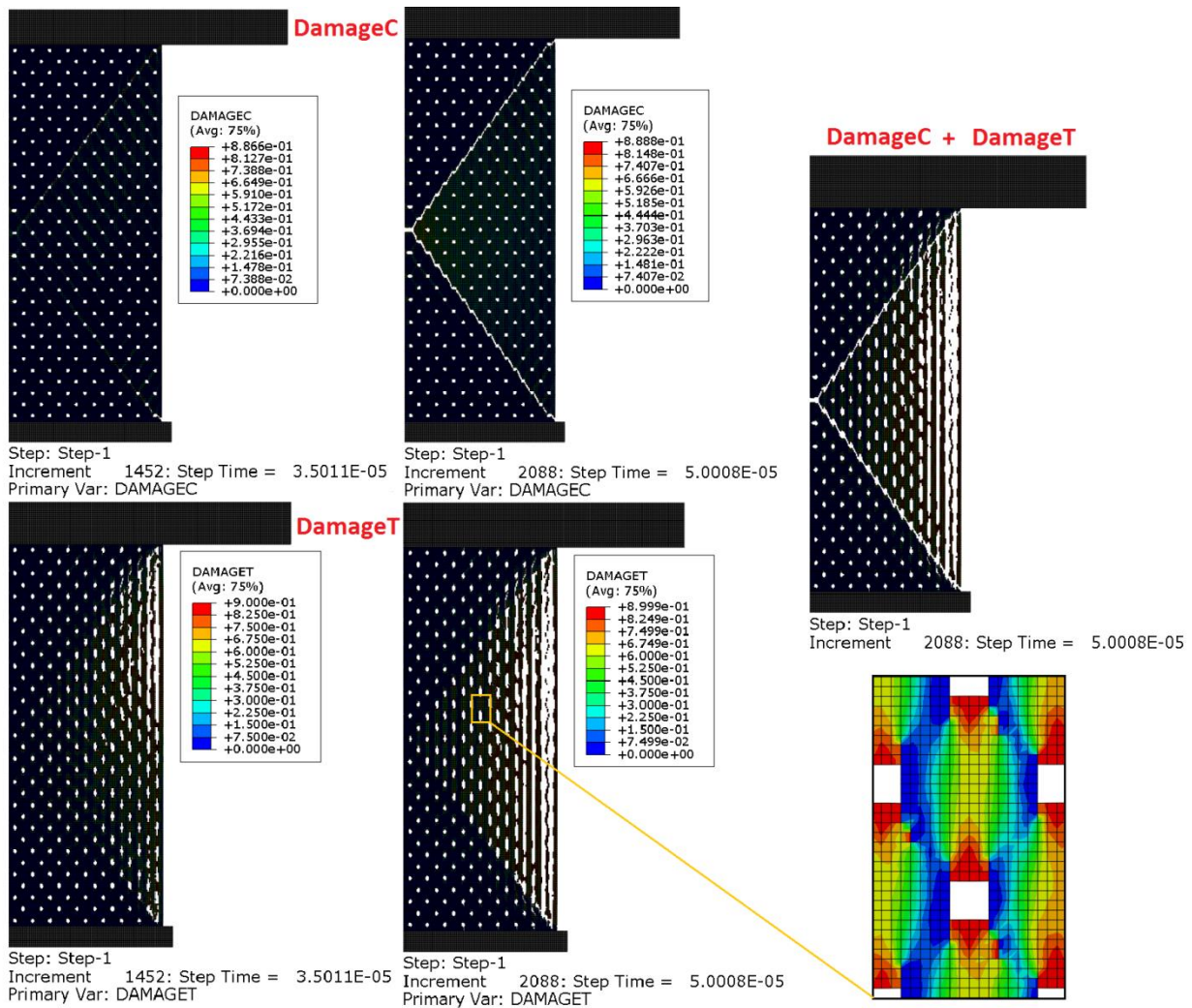


Figure 5.27 Damage contours for estimating crack propagation in model porous concrete (281 pores,  $r=0.5062$  mm, porosity=0.1005)

When the fragmentation behaviors of the two model porous concretes with 8 and 281 pores are compared, an important difference can be observed. A multiple crack pattern has developed in the model concrete with 281 pores. This facilitated the formation of more small-sized fragments, except in the triaxially confined zones (see Figure 5.27). On the contrary in the concrete with 8 pores, due to the presence of cracks at a very limited number of specific locations, comparatively large fragments can be estimated from the damage results (see Figure 5.26). It should additionally be noted that even though the total porosity in both analyses was constant (0.1005), the impact strength of 281 pore concrete was 50.03 MPa, while that of the 8 pore concrete was 31.95 MPa. Therefore, as an important trend that can be used for designing an enhanced strength porous concrete fracturing into small fragments, as the pore size decreases, the sizes of the fragments also drastically decrease. Meanwhile, the dynamic strength increases. Considering the objective of the research, this trend is highly favorable.

In Figures 5.28, 5.29, 5.30 and 5.31, it can be seen that increasing the pore size and consequently increasing the porosity, highly decreases the dynamic strength, as expected. The extent of that decrease in relation to the different pore sizes are also evaluated by comparing the four figures. Decreasing the porosity from 0.2791 to 0.1005 in model concretes having 8 pores (decreasing the pore radius from 5 to 3 mm) enhances the impact strength 2.47 times (see Figure 5.28). In case of samples with 281 pores the same decrease in porosity (by decreasing the pore radius from 0.8436 to 0.5062 mm) increases the dynamic strength 2.22 times (see Figure 5.31). Similarly, for the other two pore sizes (see Figures 5.29 and 5.30), the ratios of dynamic strengths were 2.46 and 2.19, respectively. Therefore, it can be said that changing the porosity affects the strength as expected. This effect is nearly independent of the pore size, as can be seen in the relative increases in strength on the right y axes.

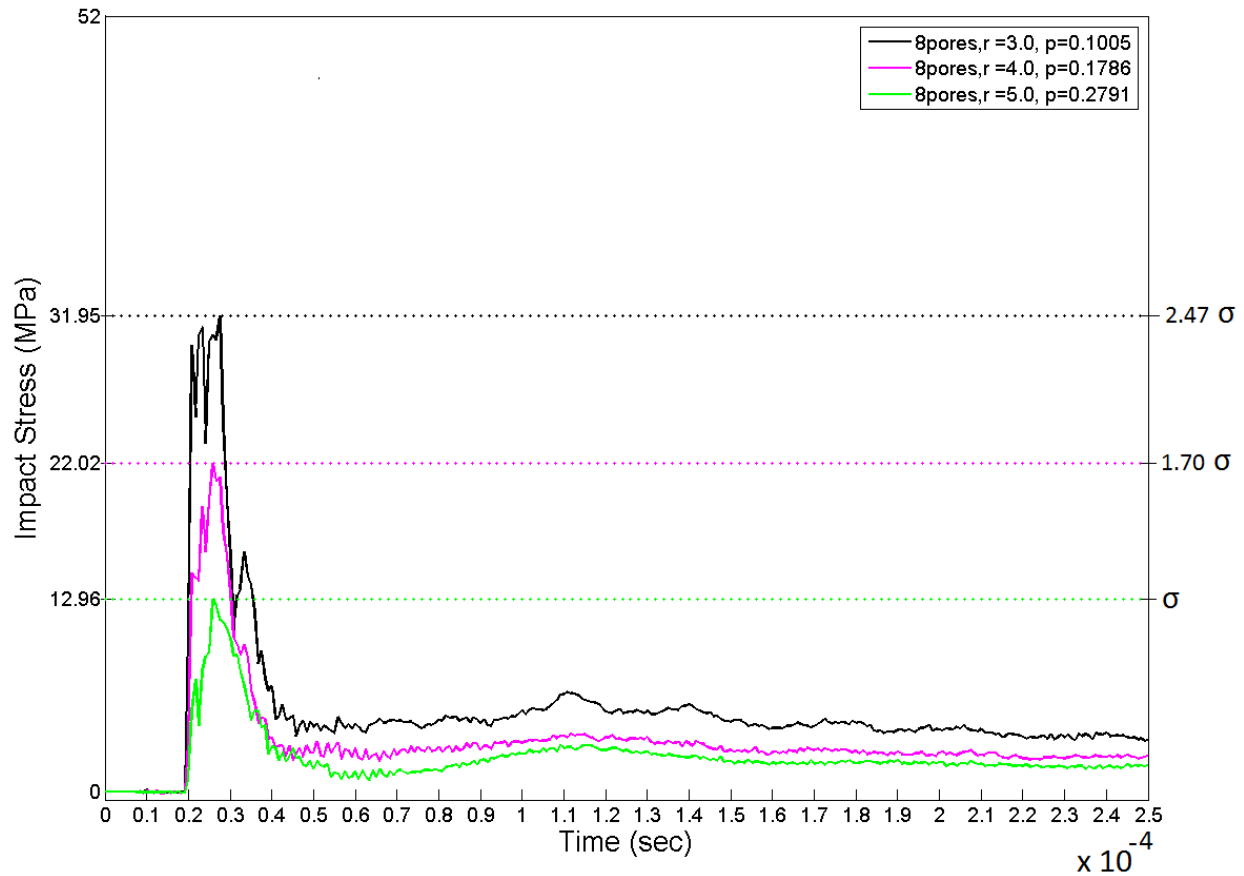


Figure 5.28 Impact stress time histories of 8 pore model concretes with different pore sizes

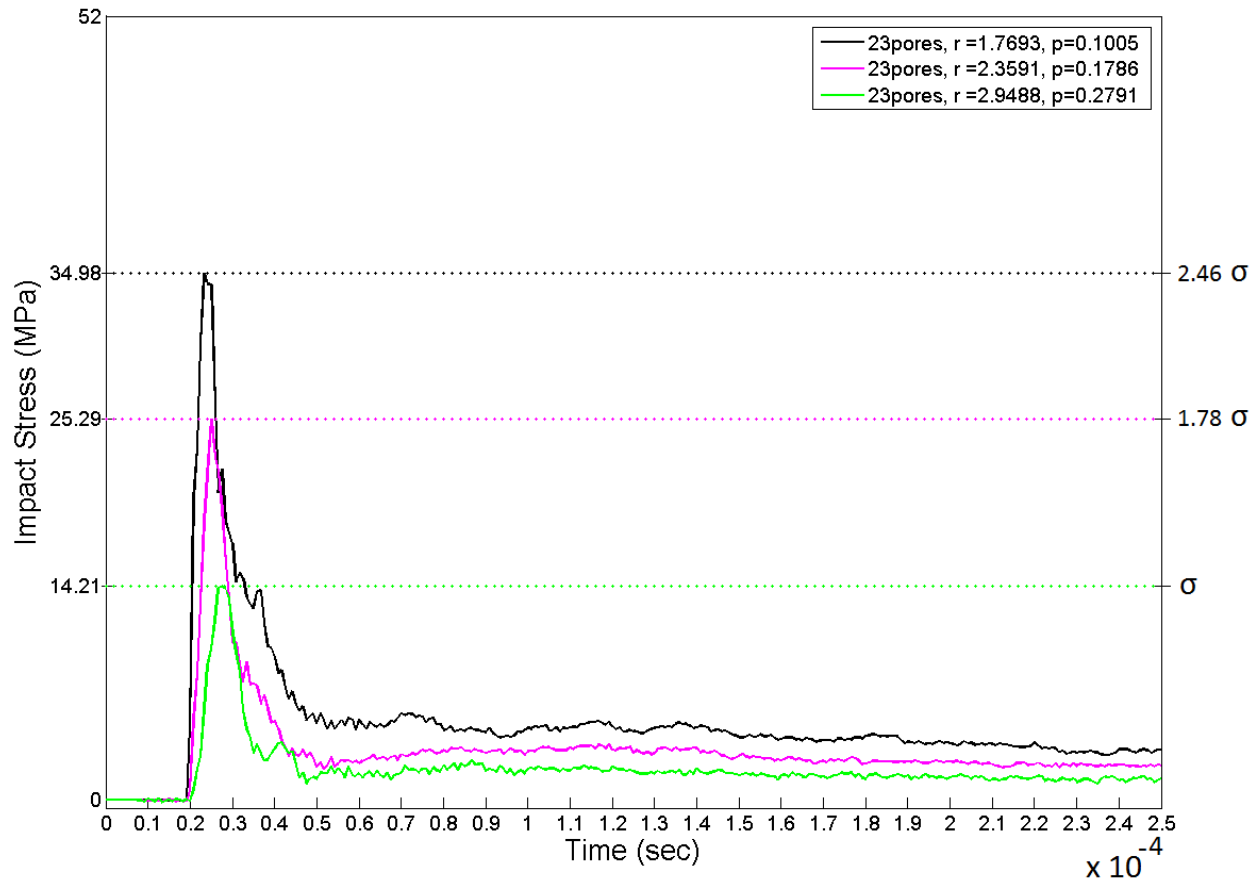


Figure 5.29 Impact stress time histories of 23 pore model concretes with different pore sizes

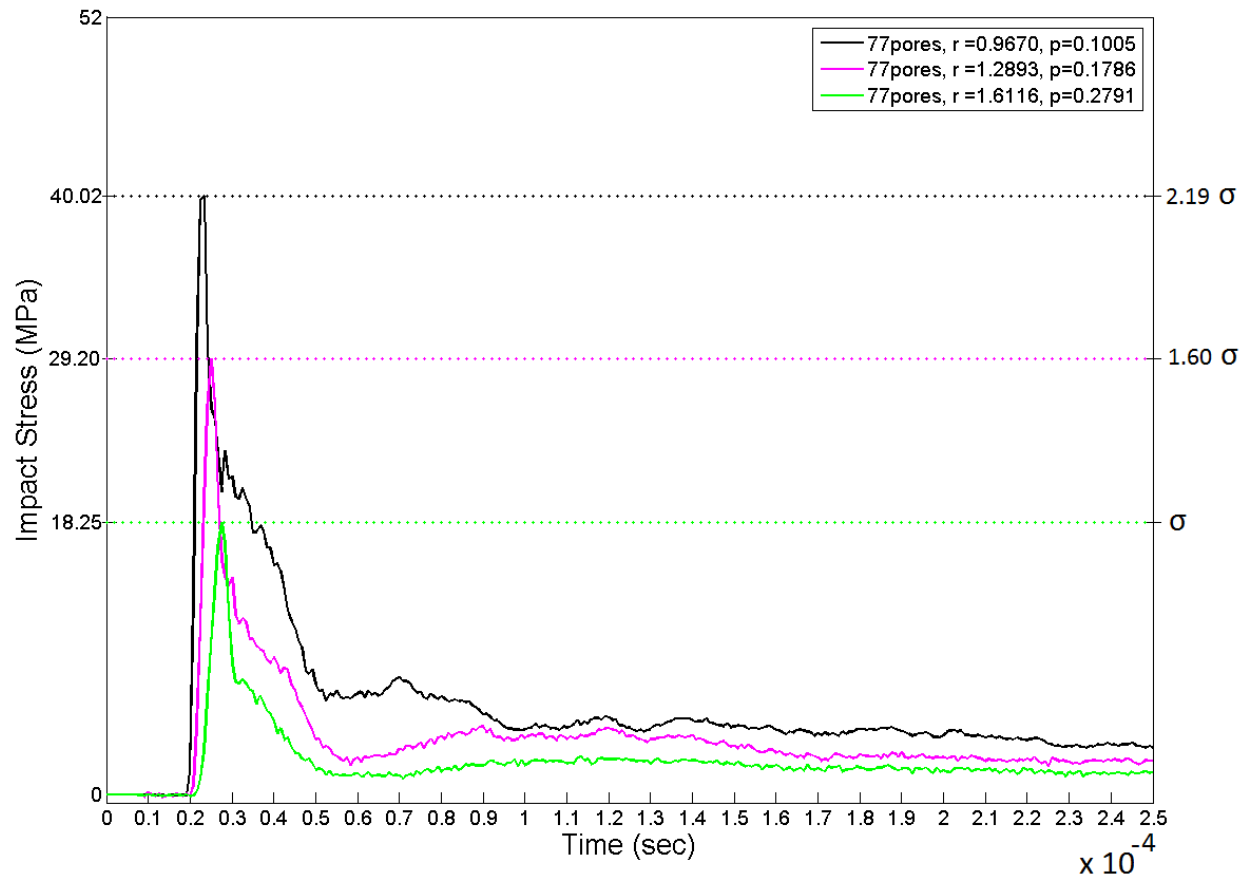


Figure 5.30 Impact stress time histories of 77 pore model concretes with different pore sizes



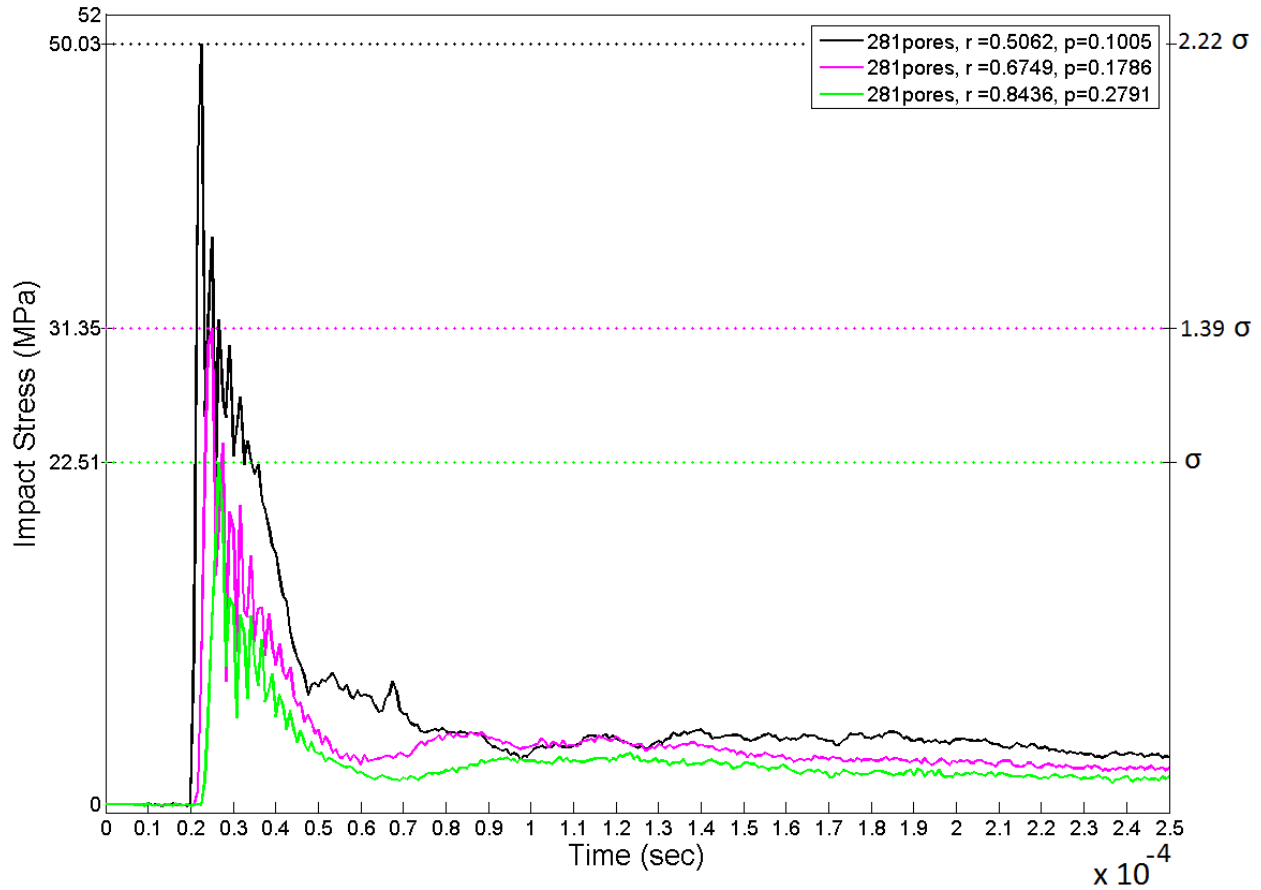


Figure 5.31 Impact stress time histories of 281 pore model concretes with different pore sizes

In the damage contour plots, the detrimental effect of increasing the pore size and increasing the porosity is clearly seen in all four figures (see Figures 5.32, 5.33, 5.34 and 5.35). It should be noted that in the plots, elements with compressive damage (DamageC) or tensile damage (DamageT) values greater than 0.9 are removed from the mesh to be able to visualize the crack patterns. When the porosity reaches 27.91 %, the weakening of the material reaches a level where even the zones of the mesh close to the specimen boundaries were fractured. This is probably due to poor triaxial confinement because of the presence of too much porosity in the zone, ruining the integrity of the material. A comparison of the images of Figures 5.32-5.35 vertically down for the same porosity reveals the effect of changing the pore size on the size of the fragments. It should also be noted that even though the pores were placed regularly in the sample, when the number of pores decreases, e.g. when it reaches 8 pores as an extreme, the material becomes highly anisotropic. This effect is more pronounced in concretes having randomly oriented pores, which will be explained in more detail in section 5.4.4.2.

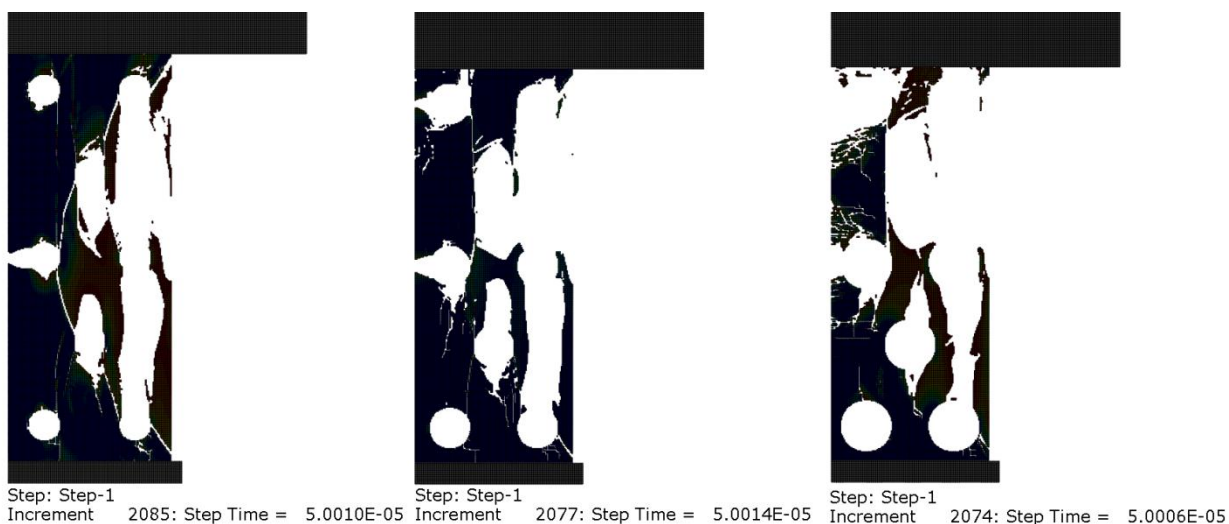


Figure 5.32 Damage contours (combination of compressive and tensile damage) of 8 pore model concretes with increasing porosity ( $p=0.1005, 0.1786, 0.2791$ )

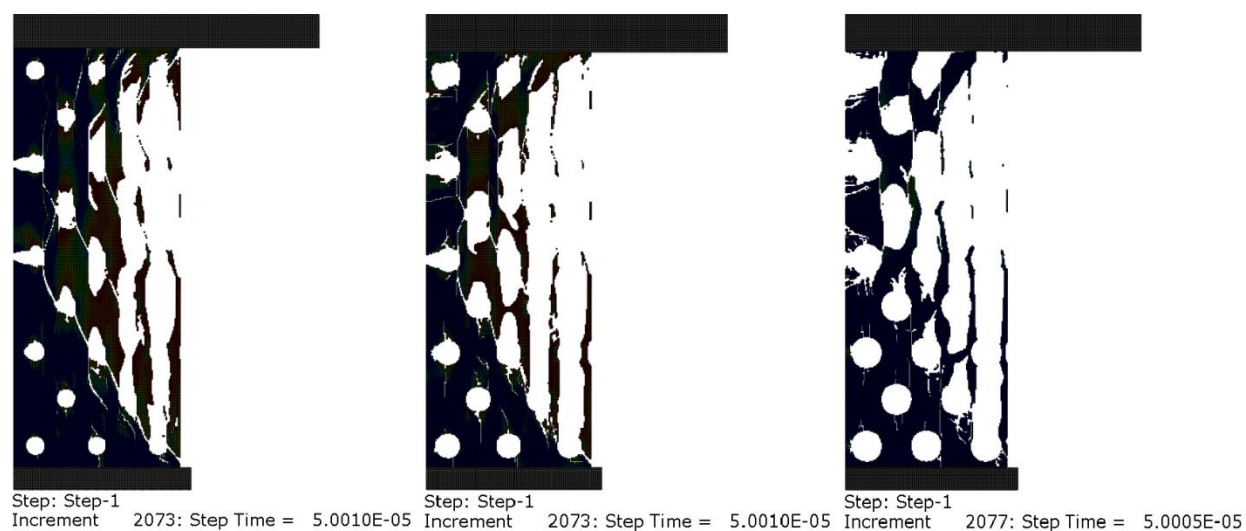


Figure 5.33 Damage contours (combination of compressive and tensile damage) of 23 pore model concretes with increasing porosity ( $p=0.1005, 0.1786, 0.2791$ )

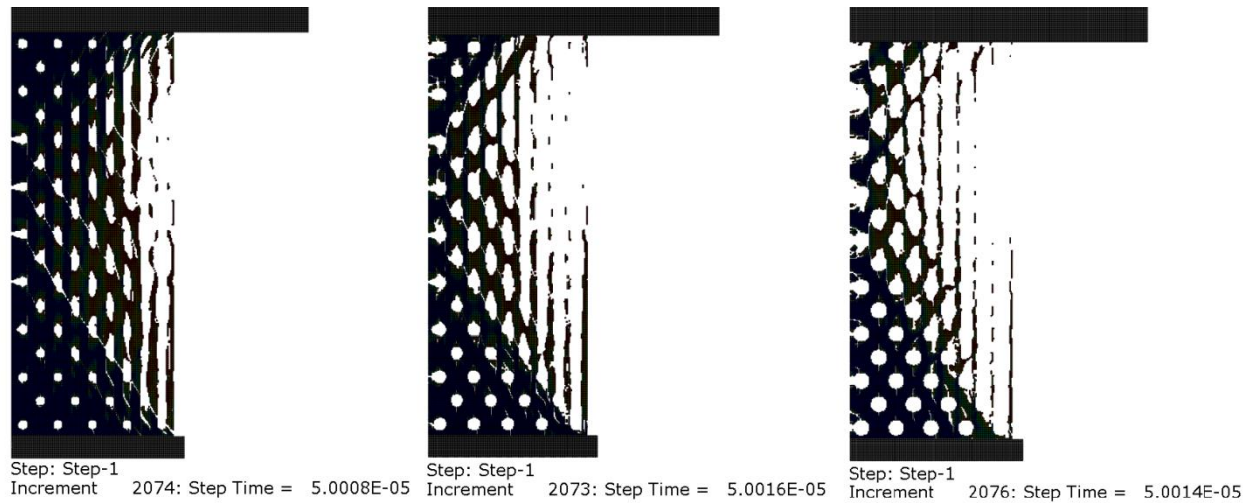


Figure 5.34 Damage contours (combination of compressive and tensile damage) of 77 pore model concretes with increasing porosity ( $p=0.1005, 0.1786, 0.2791$ )

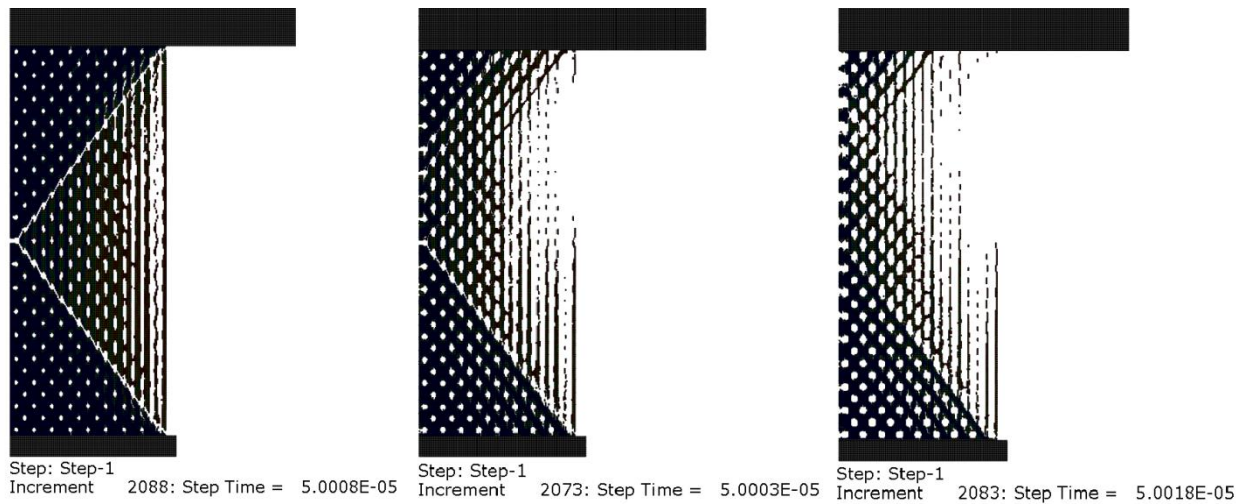


Figure 5.35 Damage contours (combination of compressive and tensile damage) of 281 pore model concretes with increasing porosity ( $p=0.1005, 0.1786, 0.2791$ )

#### 5.4.4.2. Model Porous Concretes with Randomly Distributed Circular Pores

After investigating the individual effects of pore size and porosity on the performance of model concretes, irregularity should also be introduced in the model as an influencing parameter as in real porous concretes. The main features of the analyses conducted on model porous concretes with randomly distributed circular pores are given in Table 5.3.

Table 5.3 Analyses conducted on model porous concretes with randomly distributed circular pores

<b>MODEL POROUS CONCRETES</b> <b>WITH RANDOMLY DISTRIBUTED CIRCULAR PORES</b> (Each analysis repeated also for the no end friction option) Material Phases: Plain Concrete + Air				
Analysis Label	N. of Pores	Pore Radius (mm)	Porosity	Pore Distribution
RANDPORE8NO1	8	3.0	0.1005	Random1
RANDPORE8NO2				Random2
RANDPORE8NO3				Random3
RANDPORE8NO4				Random4
RANDPORE23NO1	23	1.7693	0.1005	Random1
RANDPORE23NO2				Random2
RANDPORE23NO3				Random3
RANDPORE23NO4				Random4
RANDPORE77NO1	77	0.9670	0.1005	Random1
RANDPORE77NO2				Random2
RANDPORE77NO3				Random3
RANDPORE77NO4				Random4
RANDPORE281NO1	281	0.5062	0.1005	Random1
RANDPORE281NO2				Random2
RANDPORE281NO3				Random3
RANDPORE281NO4				Random4

In the analyses of model porous concretes with randomly distributed pores, again four mixtures with different numbers of pores options, namely 8, 21, 77 and 281 pores, were investigated. This time one pore size was analyzed for each number of pores ( $r=3$  mm, 1.7693 mm, 0.97670 mm and 0.5062 mm, respectively). Total porosity was kept constant at 0.1005. For each number of pores, four different random pore distributions were generated. The x and y coordinates of the center of random pores were determined by using the random number generator in MATLAB. By also defining circles of specified radii around the generated center coordinates one by one, the intersection is checked. In case of an intersection, the generated center coordinates were simply eliminated. It was clearly seen in the experiments and in the model concretes with regularly distributed pores that the boundary conditions have a strong effect on the fragmentation behavior. Therefore, in these analyses two different friction conditions were defined at the specimen boundaries. Friction coefficients of 0.3 (the same as in the analyses of model concretes with regularly distributed pores) and 0 (ideal testing with no friction) were used. The no friction analyses were conducted to especially monitor the fragmentation behavior of the material itself, where no structural effects due to constraining near the specimen boundaries are present.

The impact stress-time histories of the four random and one regularly distributed 8, 23, 77 and 281 pore concretes (in Figures 5.36, 5.38, 5.40 and 5.42, respectively) are examined along with the standard deviations of the peak values. It was found that when the pore size increases, the effect of randomness on the results, i.e. the variance of the impact strength, increases. At constant total porosity, when the sizes of the pores decrease (as the number of pores increases, e.g. at 281 pores, see Figures 5.42 and 5.43) the material becomes more isotropic (compared to e.g. 8 pore options in Figures 5.36 and 5.37). Even when there is a random pore distribution, this trend does not change. Consequently, the impact strength shows less scatter. A standard deviation in impact strength of 2.26 MPa was found for samples with 281 pores compared to 5.44 MPa for samples with 8 pores. When the boundary effect is eliminated by removing the friction, it was surprising to see that the impact strength results were not significantly affected and stayed approximately the same.

From an analysis of the damage contours presented in Figures 5.37, 5.39, 5.41 and 5.43 for samples with 8, 23, 77 and 281 pores, respectively, it is observed that, when there is no friction, more tensile cracks oriented parallel to the compressive loading direction are formed. This kind of cracking is significantly different from the former inclined cracks caused by triaxial compression at the specimen boundaries. While there are no zones under triaxial confinement, the extensive tensile splitting also causes the formation of small concrete columns that buckle and behave as columns fixed at both ends (Schulson et al.1999). The splitting subsequently causes excessive dilation and ultimate failure. If the damage contour plots are compared, it is observed that for smaller pore size (i.e. the number of pores increases), the fracture takes place in a similar way as in concretes having different random pore distributions. Consequently, the shapes and the sizes of the fragments that are formed are more or less similar (see Figures 5.41 and 5.43). This is not the case for samples with large pores where, samples with different random pore distributions show very different fracture patterns, depending on the location of the pores (see Figure 5.37). A similar trend is seen in the impact strength results. For samples with smaller pores, the impact strength values of samples with randomly distributed pores are closer to each other (see Figure 5.42) compared to those found for samples with larger pores (see Figure 5.36).

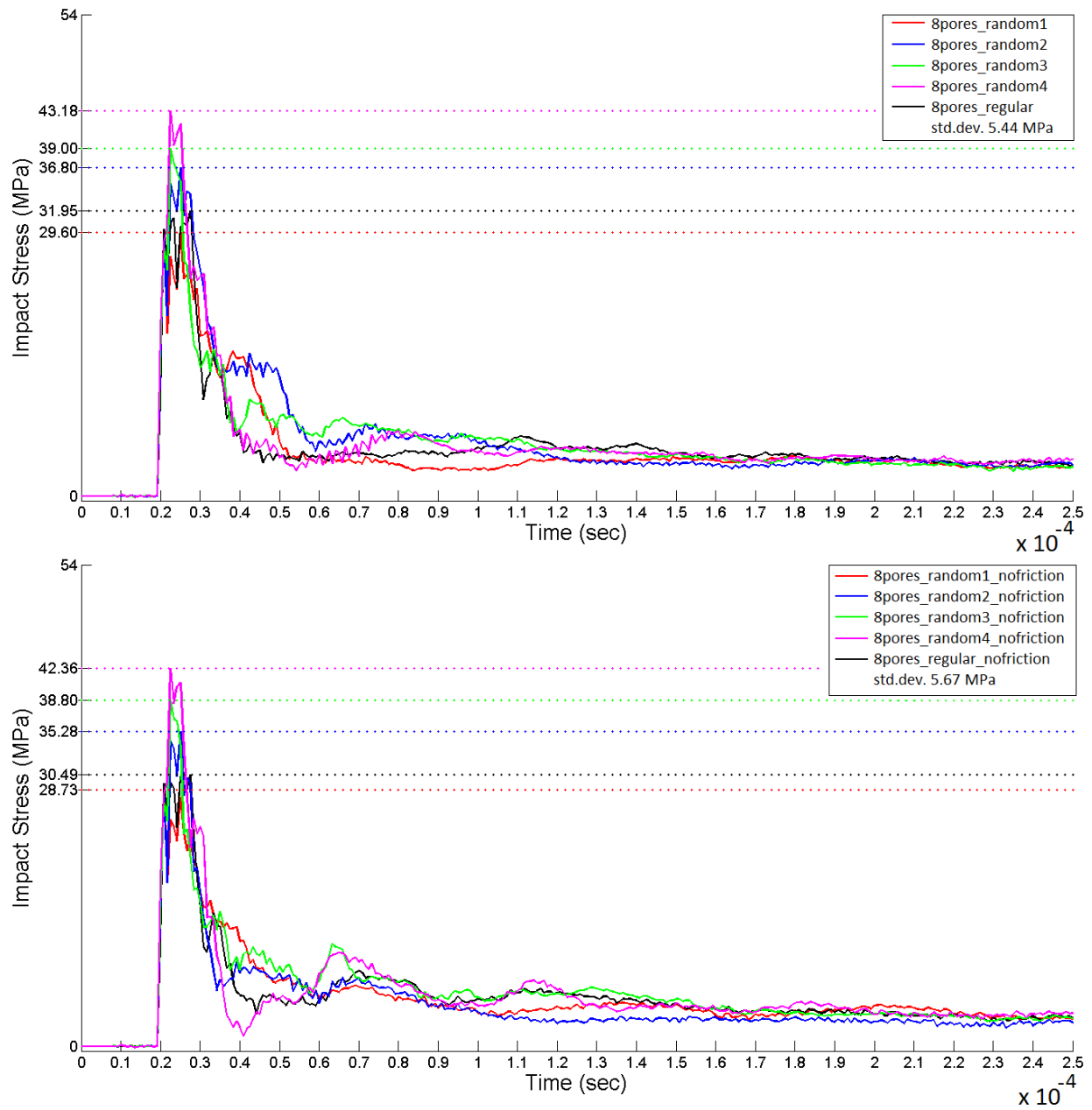


Figure 5.36 Impact stress time histories of model concretes with 8 pores with four random distributions analyzed with and without boundary friction

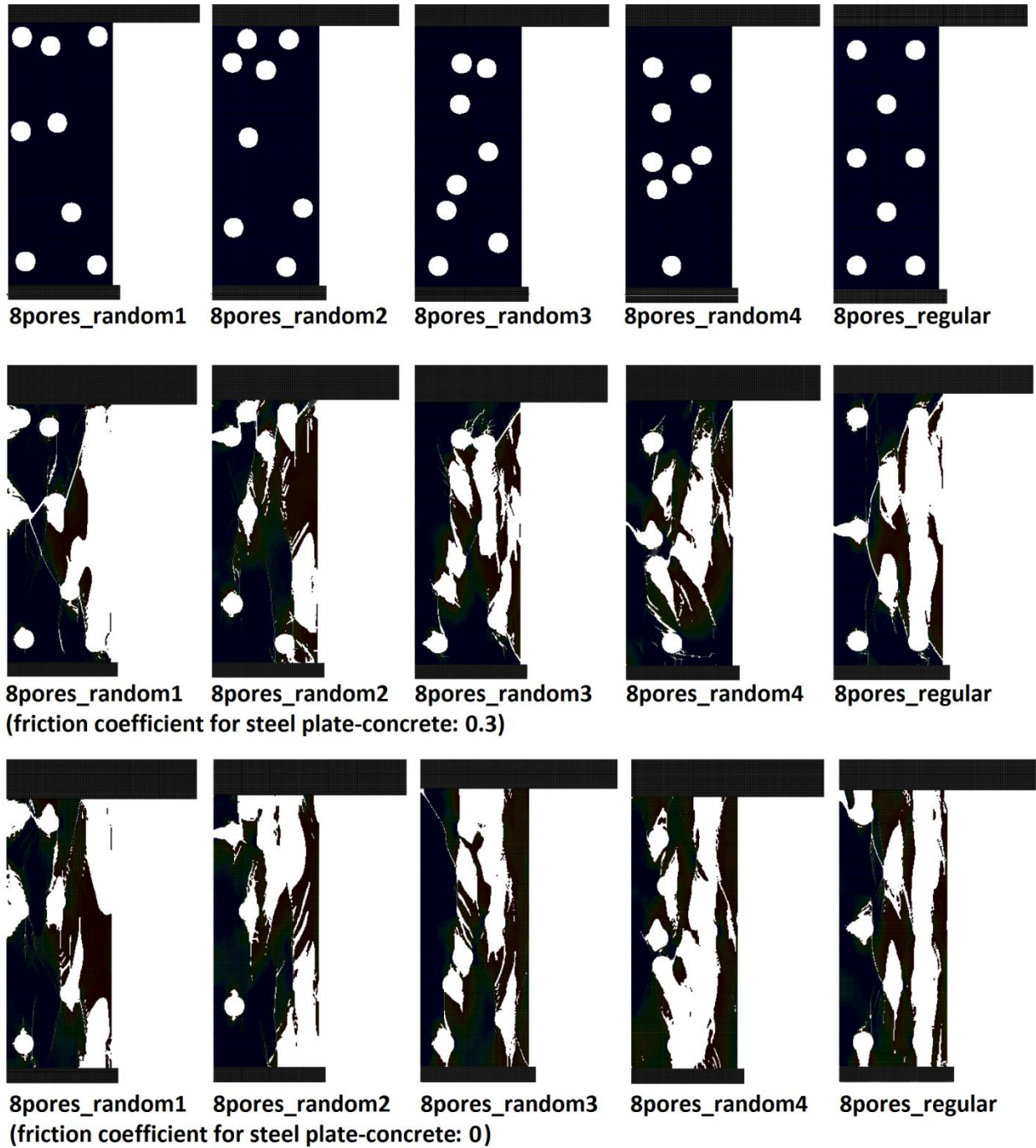


Figure 5.37 Damage contours of model concretes with 8 pores with four random distributions analyzed with and without boundary friction



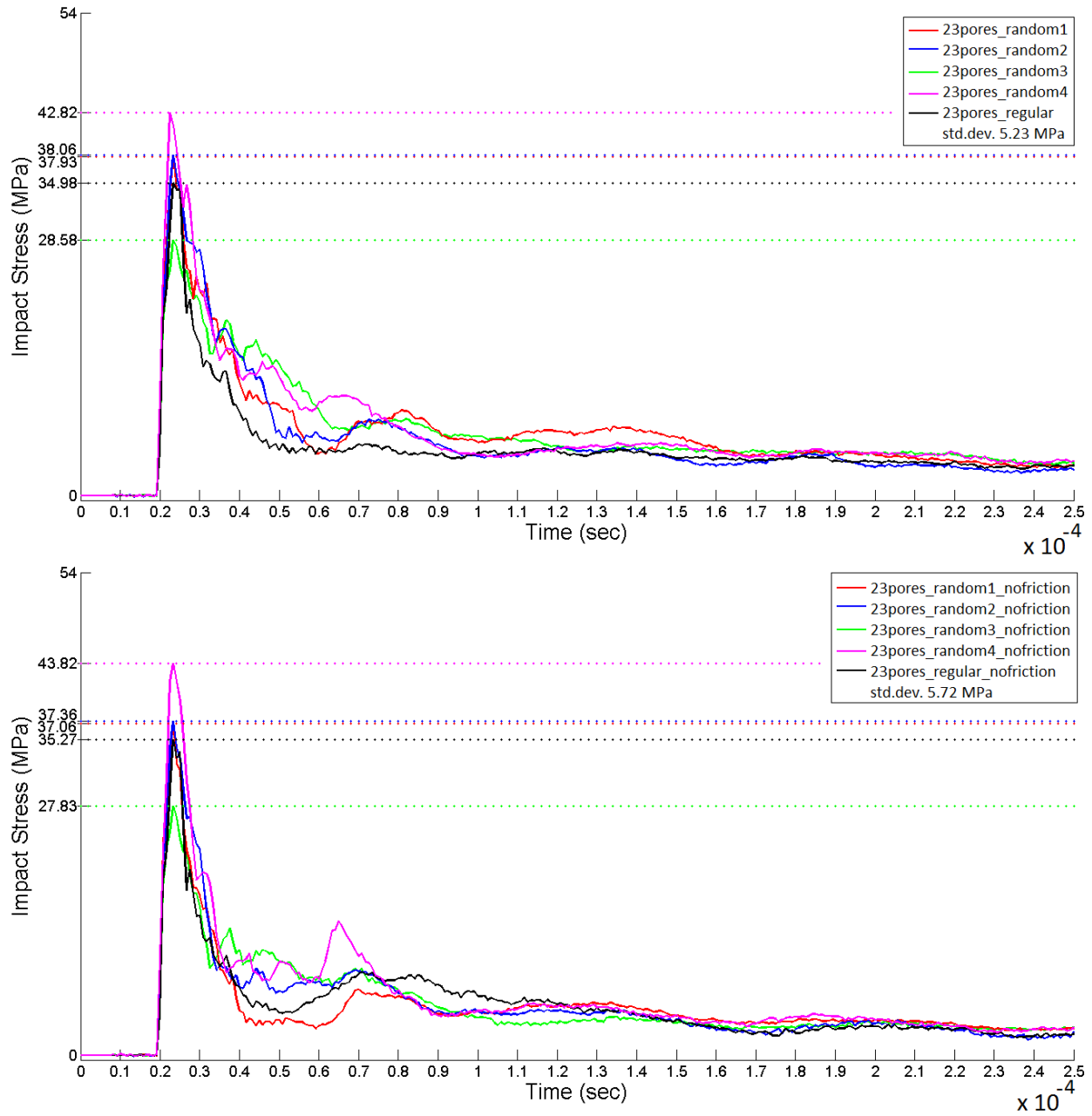


Figure 5.38 Impact stress time histories of model concretes with 23 pores with four random distributions analyzed with and without boundary friction



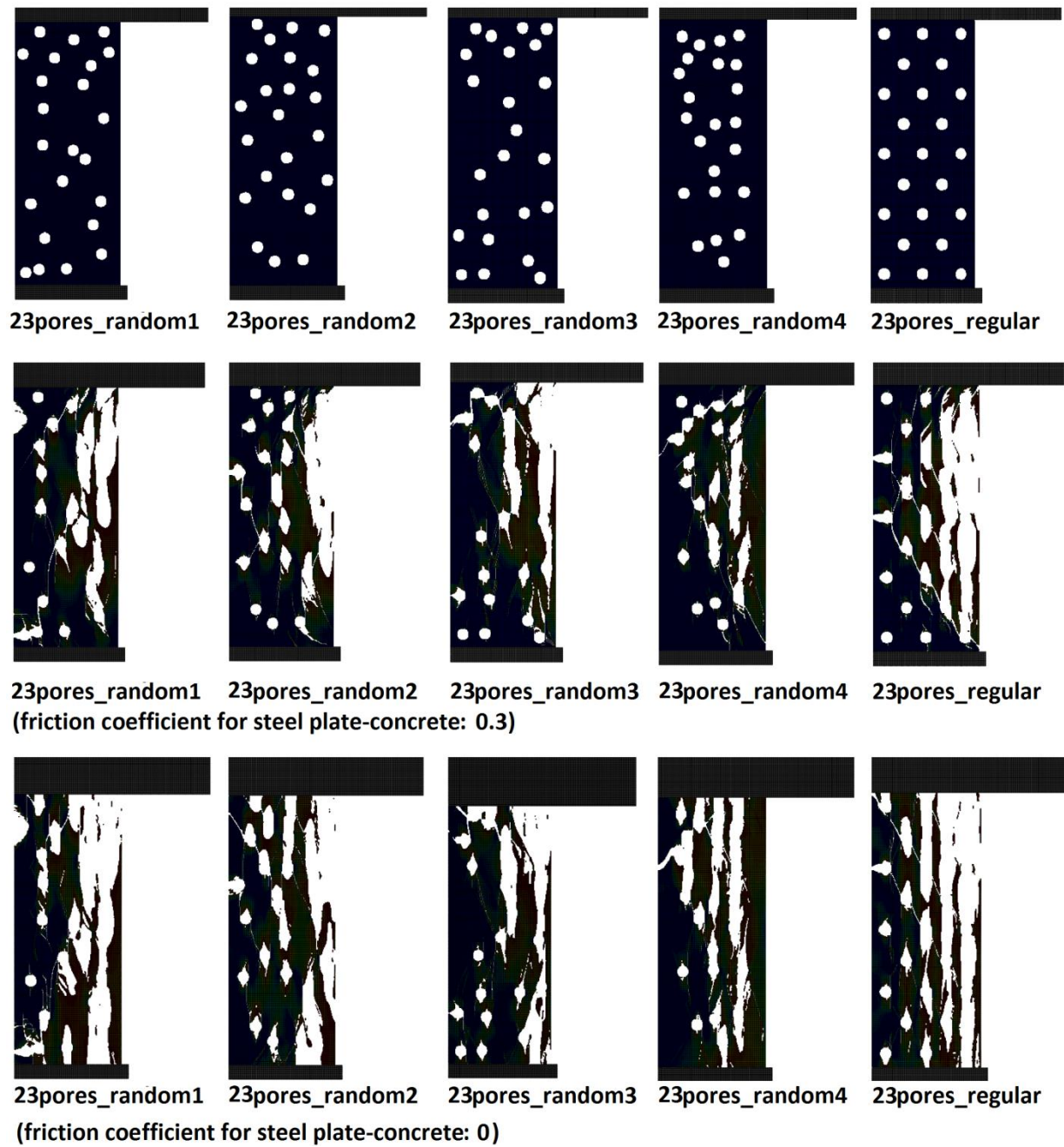


Figure 5.39 Damage contours of model concretes with 23 pores with four random distributions analyzed with and without boundary friction

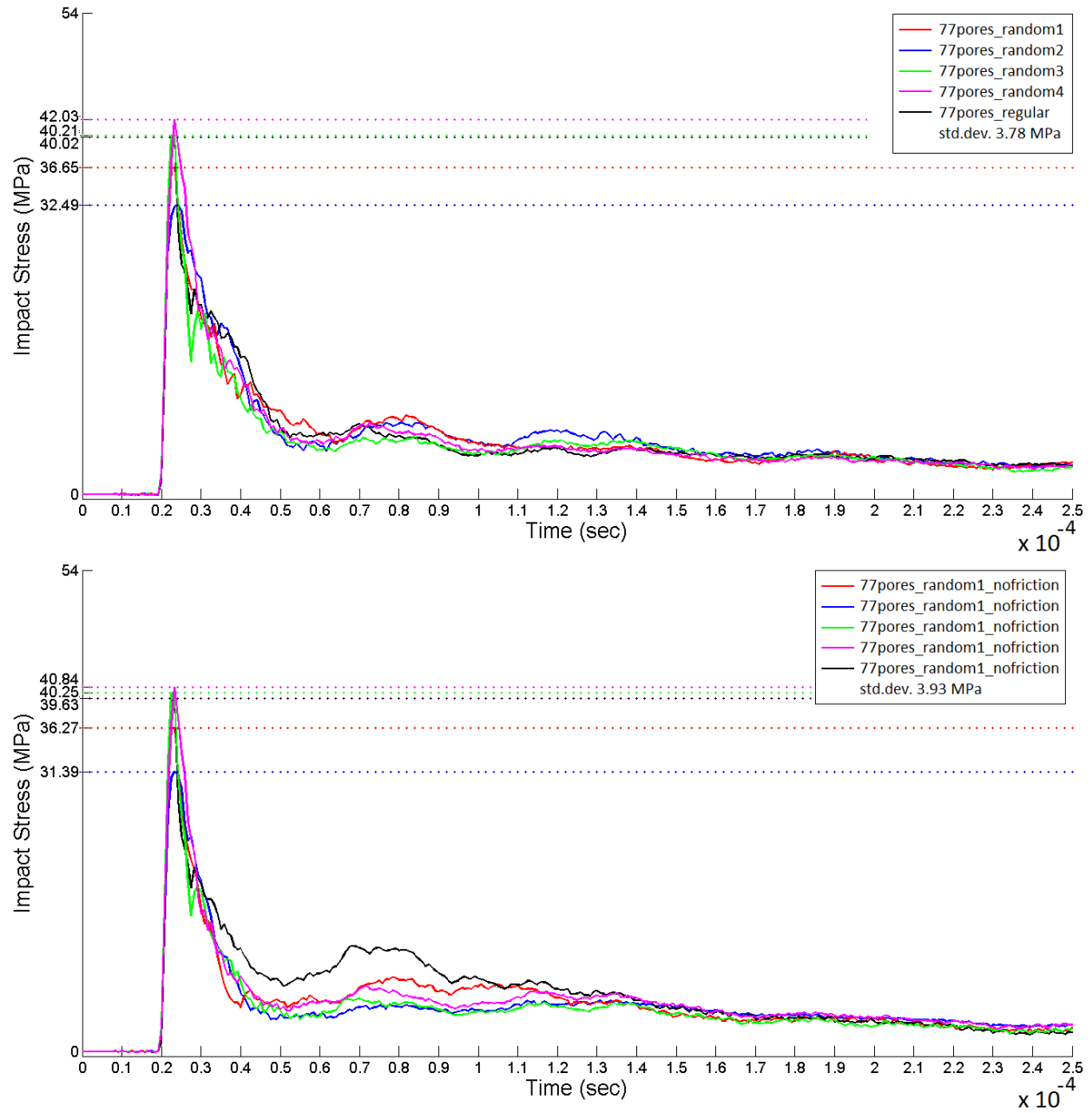


Figure 5.40 Impact stress time histories of model concretes with 77 pores with four random distributions analyzed with and without boundary friction

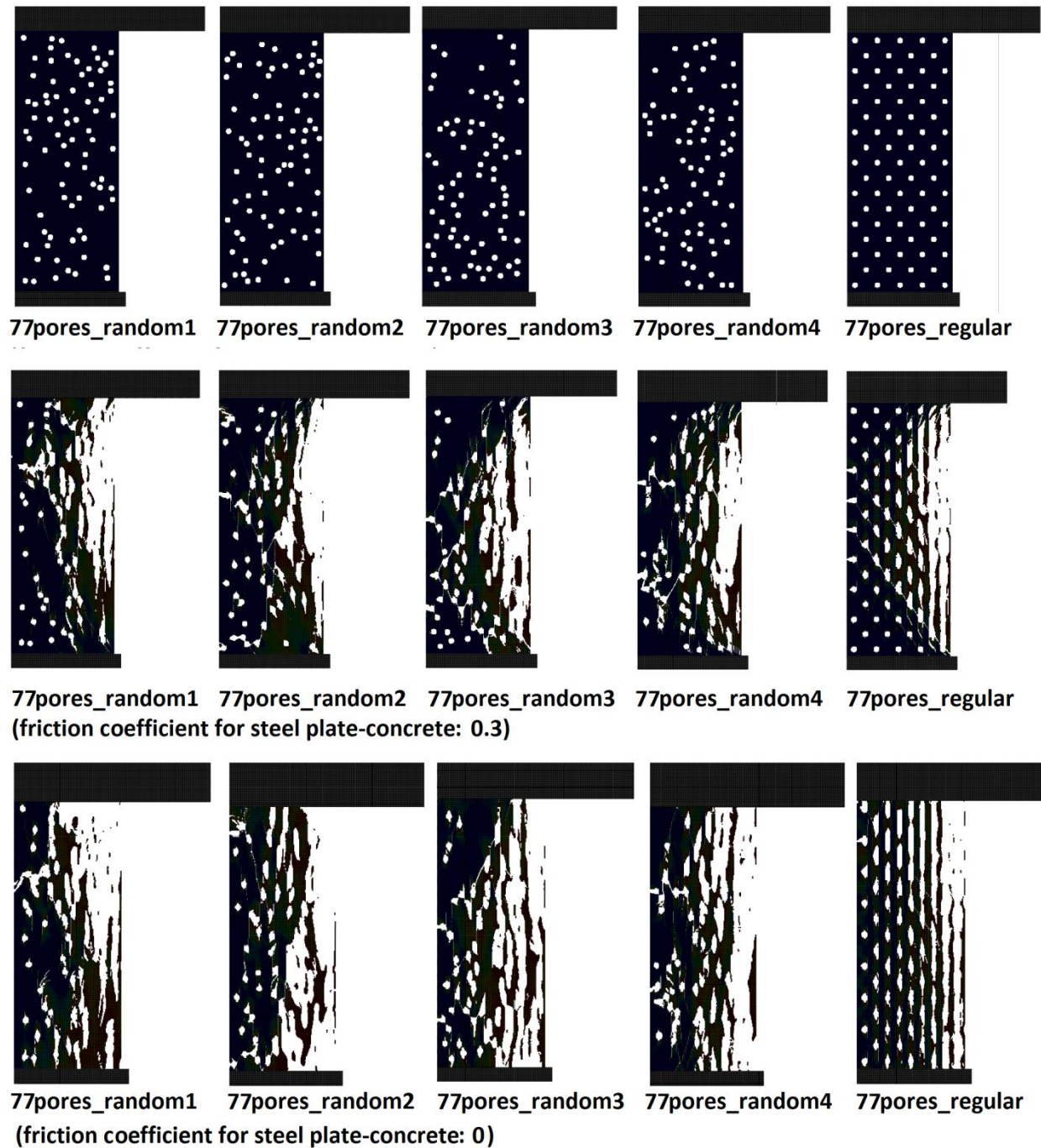


Figure 5.41 Damage contours of model concretes with 77 pores with four random distributions analyzed with and without boundary friction

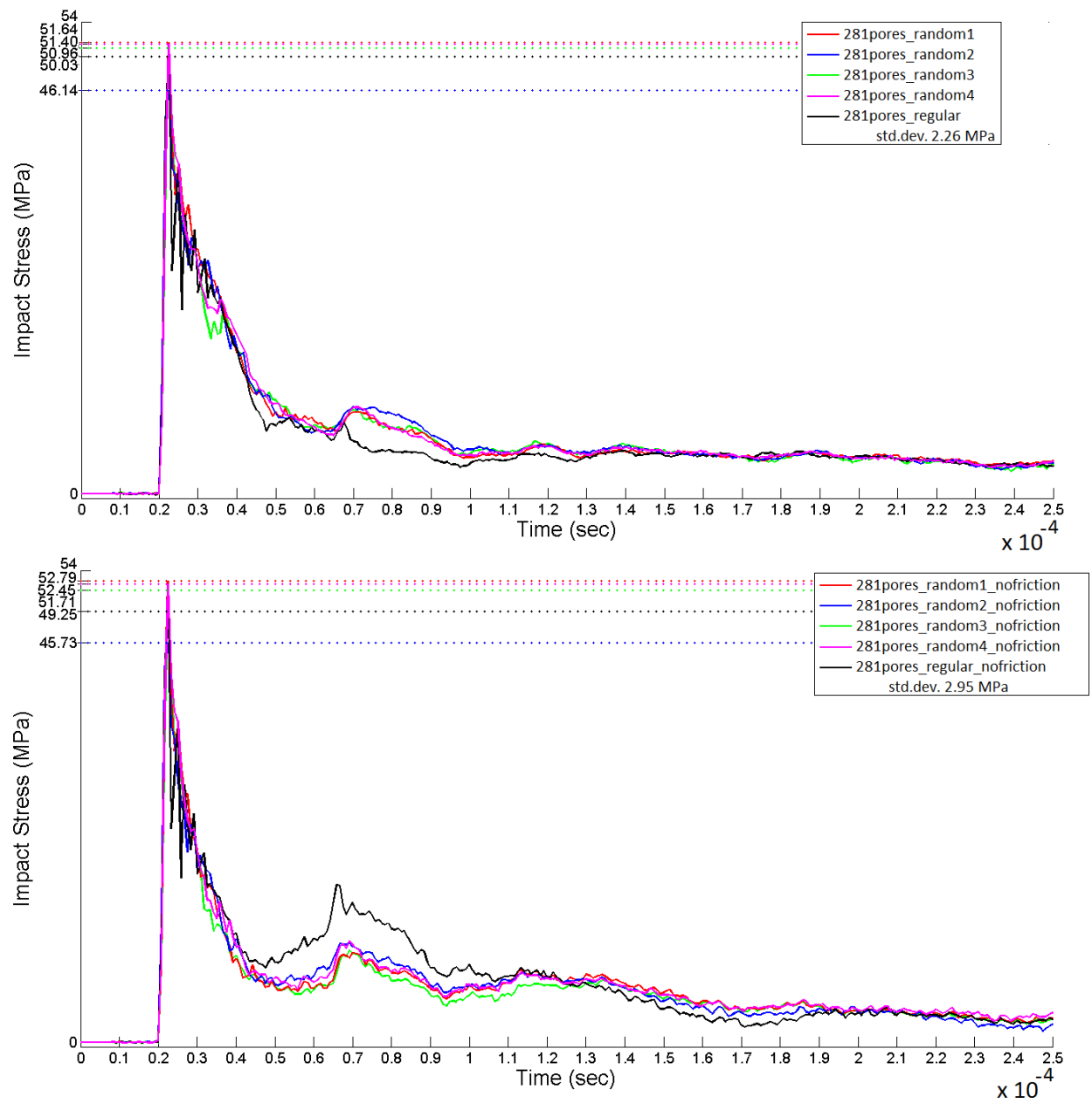


Figure 5.42 Impact stress time histories of model concretes with 281 pores with four random distributions analyzed with and without boundary friction



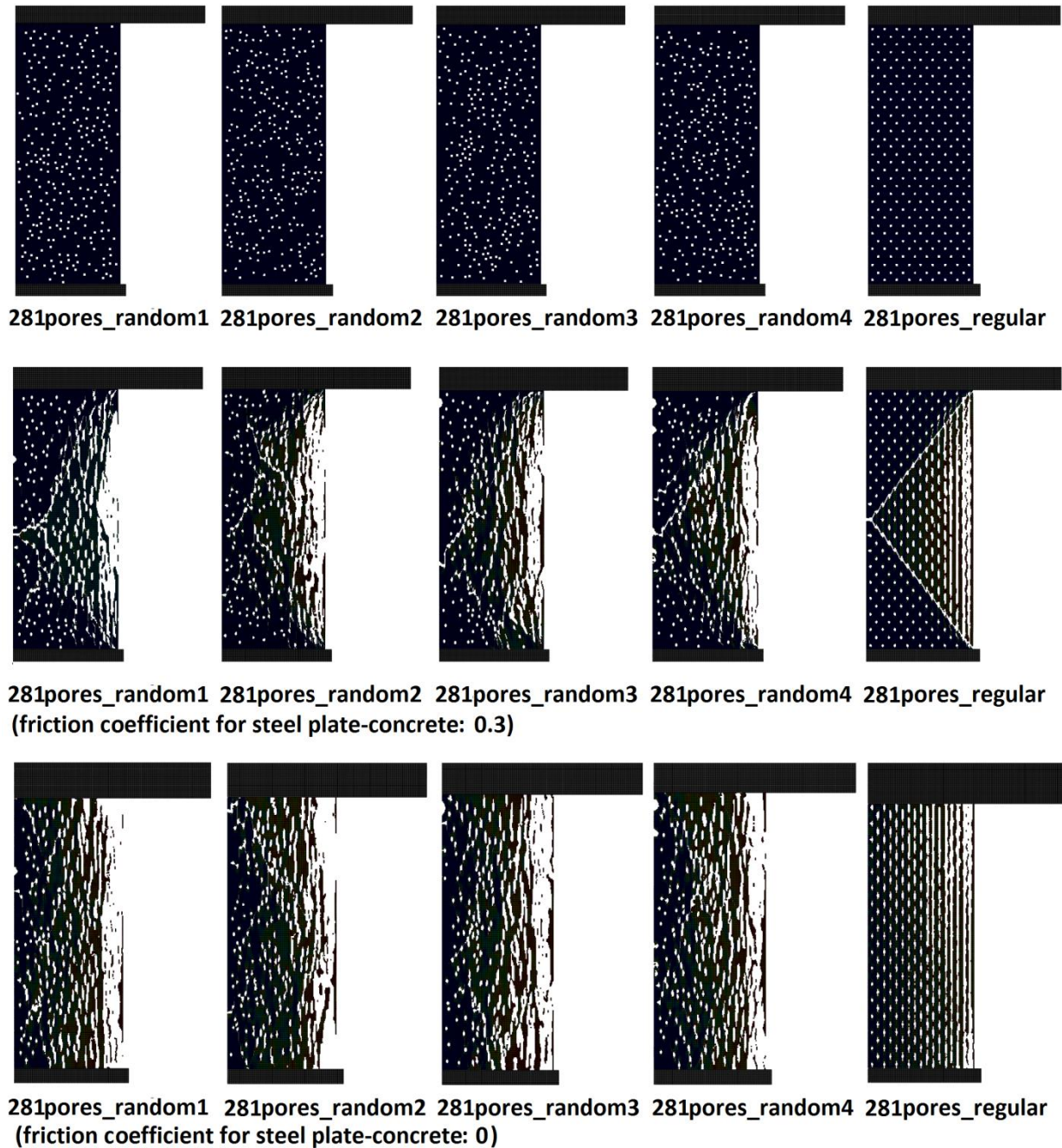


Figure 5.43 Damage contours of model concretes with 281 pores with four random distributions analyzed with and without boundary friction

#### 5.4.4.3. Model Porous Concretes with Circular Aggregates

Model porous concretes with circular aggregates were analyzed to understand the effect of aggregate size on the porous concrete properties without the influence of the packing density. When the particles are circular and are distributed according to the same structure (in all the three samples analyzed, it is hexagonal close packing), the packing density and therefore the

porosity stays the same. In real porous concretes with irregularly shaped particles however, particle size highly affects the packing density. The main features of the analyses conducted on model porous concretes with circular aggregates are given in Table 5.4.

Table 5.4 Analyses conducted on model porous concretes with circular aggregates

MODEL POROUS CONCRETES WITH CIRCULAR AGGREGATES Material Phases: Aggregates + Bulk Cement Paste + Air		
Analysis Label	Aggregate Diameter (mm)	Cement Paste Thickness (mm)
AGG2	$2.0-(2*0.1)=1.8$	0.1
AGG4	$4.0-(2*0.1)=3.8$	0.1
AGG8	$8.0-(2*0.1)=7.8$	0.1

In these analyses, porous concrete is represented with equally sized circular aggregates covered with a thin layer of cement paste. Starting point is a 2D structure, which is then rotated axisymmetrically. The cement paste layers around the aggregate particles are only partially in contact as shown in Figure 5.44. The particles in real porous concretes definitely do not have equal sizes, even not in the same standard size range such as 2-4 mm or 4-8 mm. Since identical circular particles oriented in the same structure have the same packing density even when the radius is varied, the effect of packing density as well as porosity can be ruled out. Meanwhile, it will be explained in more detail later in this section that pore size and the contact surfaces, which are directly related with aggregate size, are important parameters in this set of analyses.

In the analyses, samples with three different sizes of circular aggregates were investigated. To be able to keep the packing and the porosity constant and to have the same pattern of circles, aggregate particles were chosen with diameters 2, 4 and 8 mm. The size of the aggregates includes a 0.1 mm thickness cement paste layer. Hence, the diameters of the aggregate particles themselves were 1.8 mm, 3.8 mm and 7.8 mm, respectively. Each sample had approximately the same porosity ( $p$ ):  $p=0.1093$  (45 particles with 8 mm diameter including the cement paste layer, sample dimensions 70.5 mm x 36.0 mm),  $p=0.1029$  (180 particles of 4 mm diameter, sample dimensions 69.8 mm x 36.0 mm) and  $p=0.1092$  (700 particles of 2 mm diameter, sample dimensions 70.5 mm x 36.0 mm).

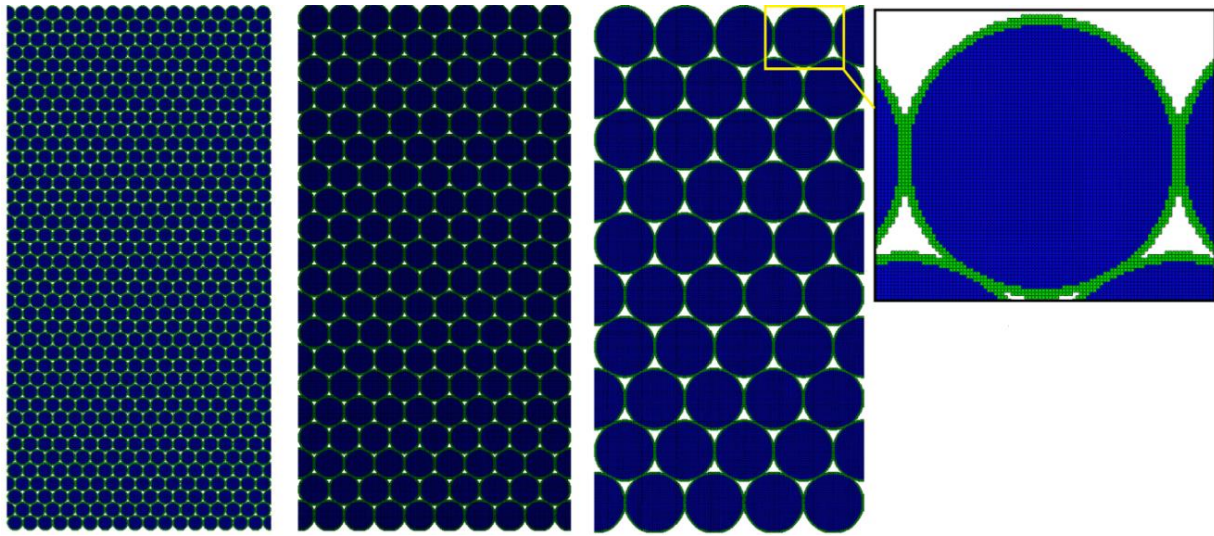


Figure 5.44 Finite element meshes of model porous concretes with 2 mm, 4 mm and 8 mm (aggregate+cement paste) particles

In the analyses the aggregates were defined as elastic (with  $E=50$  GPa,  $\nu=0.3$ ). The cement paste phase around the aggregates was defined using the CDP model. The input data for the compressive and tensile behavior of the cement paste are given in Figure 5.45. For the stress-strain relationship, the modification of the strain was again done by taking the work of Jankowiak and Lodygowski as reference (Jankowiak and Lodygowski 2005, Simulia\_1 2013). The damage-inelastic strain data were taken from the same source. Scaling was done to the strain data by taking the strain data obtained during the experiments as reference. In the model, the following parameters were also defined:  $E=19.7$  GPa,  $\nu=0.19$ . This input data for cement paste will also be used for the material properties of the cement paste phase of real porous concrete mixtures described in section 5.4.6.

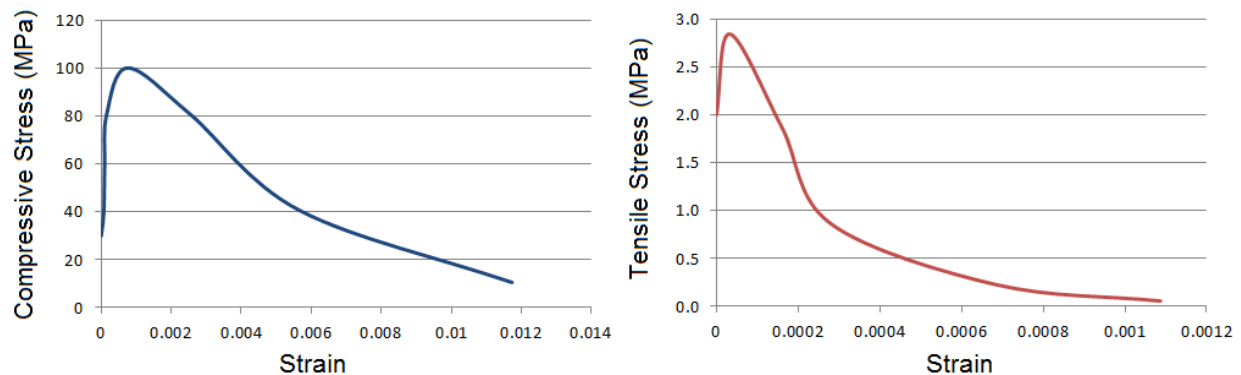


Figure 5.45 Compressive and tensile stress versus strain input data for the cement paste phase (for circular aggregate model concrete and real porous concrete analyses)



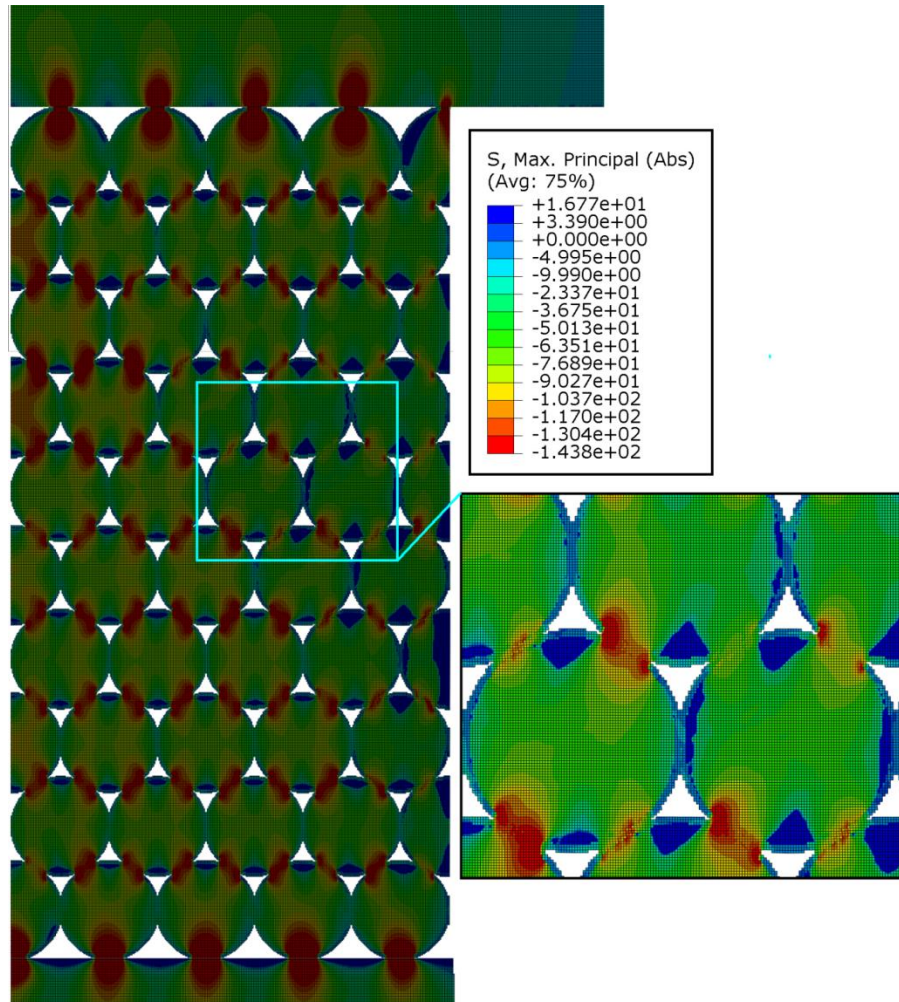


Figure 5.46 Stress distribution in a circular aggregate model porous concrete under impact (8 mm particles)

If the stress distributions in porous concretes with 8 mm diameter particles under impact are examined, large tensile stress concentrations at the top and bottom of the pores are observed. Tensile splitting stresses vertically oriented at the contact points between two particles (see Figure 5.46) can also be seen. Compressive stress concentrations at the diagonal contact points between the particles can also be observed.

According to the numerical results, the impact strengths of porous concretes with 8 mm and 4 mm particles were approximately the same, while the impact strength of the model porous concrete with 2 mm particles was much lower as seen in Figure 5.47.



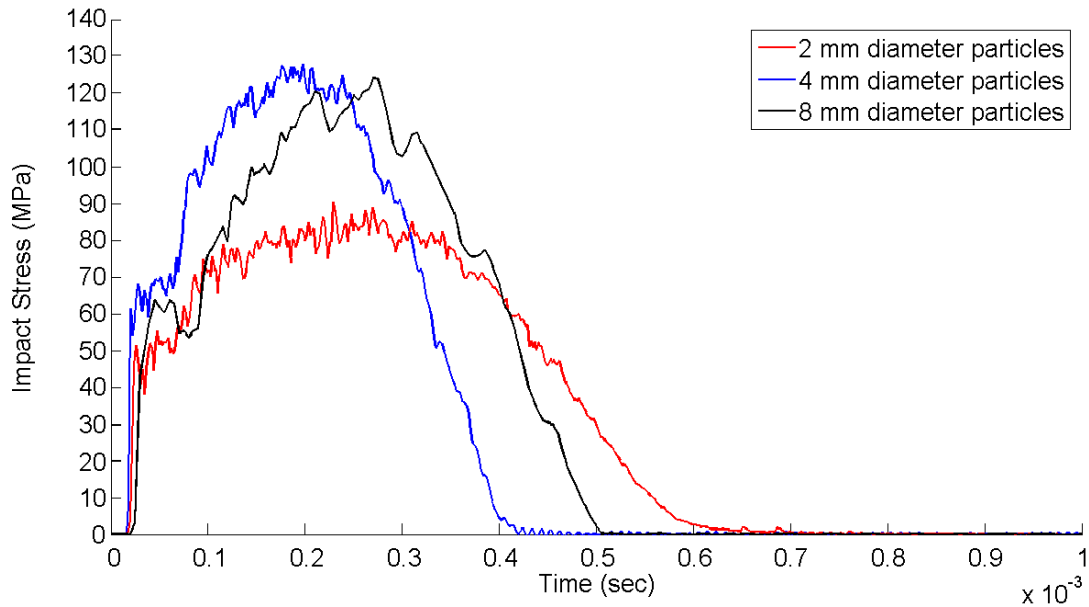


Figure 5.47 Impact stress time history of model porous concretes with 2 mm, 4 mm and 8 mm particles

These results were not expected. In both the static and the dynamic compression (impact) experiments, it was found that compressive strength increases as the aggregates get finer (see Table 3.2 and Table 4.6). The experimental results on impact strengths were also supported by the numerical results on the corresponding real porous concretes (see section 5.4.6). Porous concretes with finer aggregates gave higher dynamic strengths. Therefore, the results obtained in these numerical analyses on model porous concretes with circular aggregates are contradicting with those results.

Compressive strengths of the normal concretes have been mentioned to increase as the maximum sizes of coarse aggregates increase up to an extent (Wolinski et al. 1987, Meddah et al. 2010). For porous concretes, however, there is a lack of consensus in literature on whether increasing the aggregate size has an increasing or decreasing effect on the compressive strength. There are research articles in the literature that report their findings on aggregate size having an increasing (Chindaprasirt et al. 2009) and decreasing (Deo and Neithalath 2010) effects on the compressive strength of porous concretes. In porous concretes, the aggregates covered with cement paste are only locally in contact. Therefore, the total number of contact points between the aggregates drastically decreases with increasing particle size. This, in return, decreases the strength of the material because contact points facilitate the assembly of the particles. Similarly, different from normal concrete, aggregates in porous concrete are gap graded or usually single-sized. Therefore, even though changing the maximum aggregate size may not have such a detrimental effect on the packing of normal concrete, it may have a drastic effect on the packing of real porous concretes. Additionally, when the aggregate particles are larger, cracks are forced more to propagate through the aggregate phase compared to samples with smaller size aggregates, which enhances the dynamic strength.

Another factor is that, the numerical results of circular pore model concretes have clearly shown that decreasing the pore size at constant total porosity increases the impact strength (see Figures 5.23, 5.24 and 5.25). The pores in small size circular aggregate porous concretes are definitely smaller compared to larger aggregate porous concretes. This, therefore, should directly affect the impact strength values as well. Another effect that should be considered is the better interlocking of smaller size irregularly shaped aggregates compared to larger ones. Since the aggregates in the current analyses are circular, there is no interlocking. However, in the analyses of real porous concretes, and in the experiments, interlocking is an important factor too. When all the factors are considered, the reasons behind the impact strengths staying the same (for 8 and 4 mm particles) or decreasing (for 2 mm particles) with decreasing aggregate size can be attributed to several factors (such as aggregate size, pore size, contact points) acting in opposite directions.

Another aspect that will have affected the numerical results obtained with the circular particle model concretes concerns the modelling of the interfacial transition zone (ITZ). In the model, this zone was not considered. It is a fact that as the aggregates get finer, the amount of ITZ, which is the weakest phase in concrete, increases. Thus, in case a weaker ITZ would have included in the analyses, the decrease in strength with decreasing aggregate size would even be larger. On the other hand, the dimensions of the particles (aggregate plus 0.1 mm cement paste) were taken to be 2, 4 and 8 mm i.e. the aggregate particle diameters were 1.8 mm, 3.8 mm and 7.8 mm, respectively. Because the cement paste thickness was kept constant at 0.1 mm while the aggregates get larger, the ratio of cement paste to aggregates is higher in the finer aggregate model porous concretes compared to larger aggregate ones. Since the aggregates phase is a mechanically stronger phase compared to cement paste that could have also affected the results.

Therefore, because there are several factors working in opposite directions, it is not possible to make a definite statement on the effect of aggregate size on the strength of model porous concretes with circular aggregates. In each individual sample, several factors dominate over each other differently and unexpected results can be obtained.

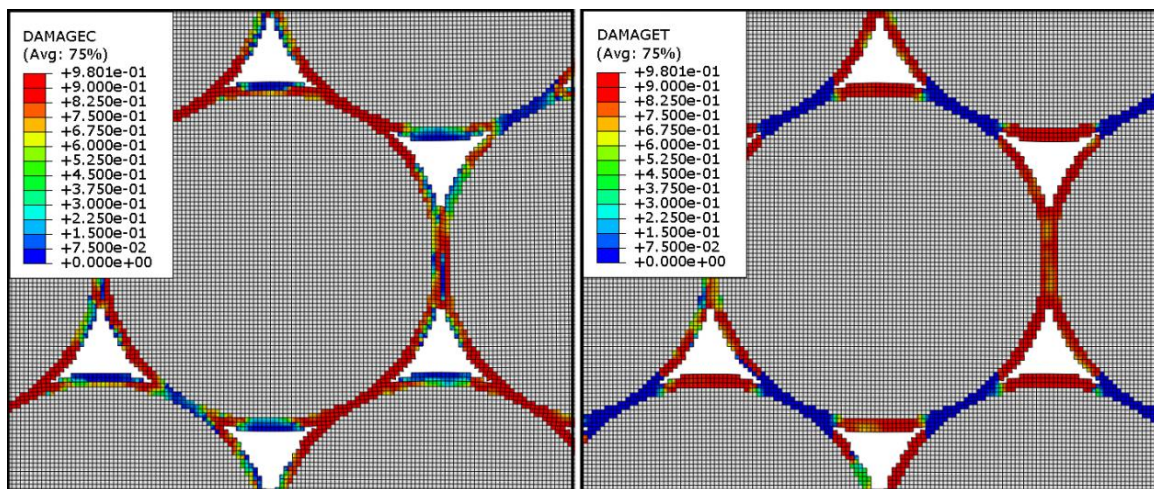


Figure 5.48 Damage contours in 8 mm aggregate model porous concrete (a) DamageC, (b) DamageT

When the compressive and tensile damage contours are examined for the 8 mm circular aggregate porous concrete, it was seen that tensile damage is concentrated at the top and bottom of the pores, as well as at the contact locations at the two sides of the particles (see Figure 5.48). This was consistent with the stress distributions observed. On the other hand, compressive damage concentrates at the diagonal contact points between the particles.

#### 5.4.5. Numerical Analyses on Real Porous Concretes

In the following numerical analyses on real porous concretes, the finite element software ABAQUS/Explicit was used. In the analyses, porous concrete was again defined as a four-phase material consisting of aggregates, bulk cement paste, interfacial transition zones (ITZ) and meso-size arbitrarily shaped air pores. In order to get an appropriate mesh for a realistic representation of the porous concretes used in the experimental program, 3D computed tomography was used. The features of mesh generation were described in detail in section 5.4.2.

For the numerical analyses, the mixtures that have given the highest static and dynamic strengths while maintaining the multiple fragmentation behavior were selected. Three porous concrete mixtures with basalt aggregates with different gradings were analyzed, i.e. gradings of 4-8mm, 2-4 mm and 50% 4-8 mm-50% 2-4 mm, a full concrete with 4-8 mm basalt aggregates and a 4-8 mm gravel aggregate porous concrete. The main features of the numerical analyses conducted on real porous concretes and their experimental strength results are presented in Table 5.5.

Table 5.5 Analyses conducted on real porous concretes and the experimentally obtained strength results

REAL POROUS CONCRETES				
Material Phases: Aggregates + ITZ + Bulk Cement Paste + Air (except FULL4-8)				
Analysis Label	Aggregates	Experimental Static Strength (MPa)	Experimental Impact Strength	Mixture Code in Table 3.1 and Table 4.6
BASALT2-4	2-4 mm Basalt	41.89	76.78	PRC2
BASALT4-8	4-8 mm Basalt	34.78	66.52	PRC1
BASALT2-8	50% 2-4 mm – 50% 4-8 mm Basalt	50.49	85.99	PRC3
FULL4-8	4-8 mm Basalt	61.10	-	FC1
GRAVEL4-8	4-8 mm River Gravel	29.64	56.22	PRC4

The input data for the cementitious phases (ITZ and cement paste) were defined taking experimental data as reference as explained in sections 5.4.1 and 5.4.3. The results of the



numerical analyses were compared with the experimental results. The simulations were conducted using an axisymmetric geometry where a drop weight impacted the porous concrete sample with an impact velocity of approximately 4.5 m/sec.

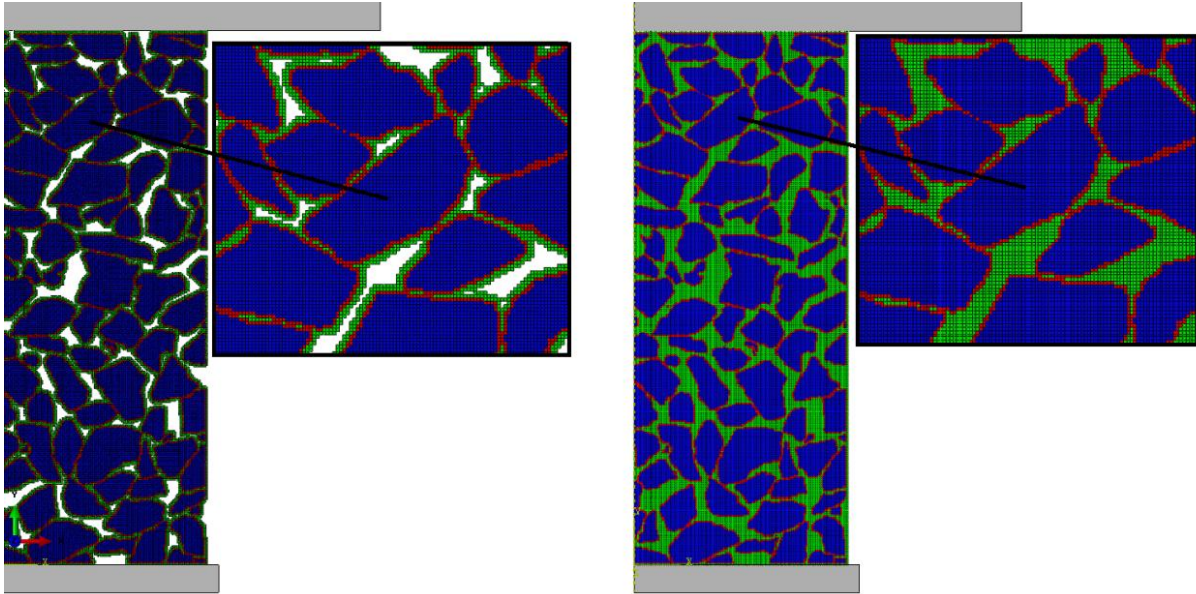


Figure 5.49 Finite element meshes for 4-8 mm basalt porous concrete (PRC1) and 4-8 mm basalt full concrete (FC1)

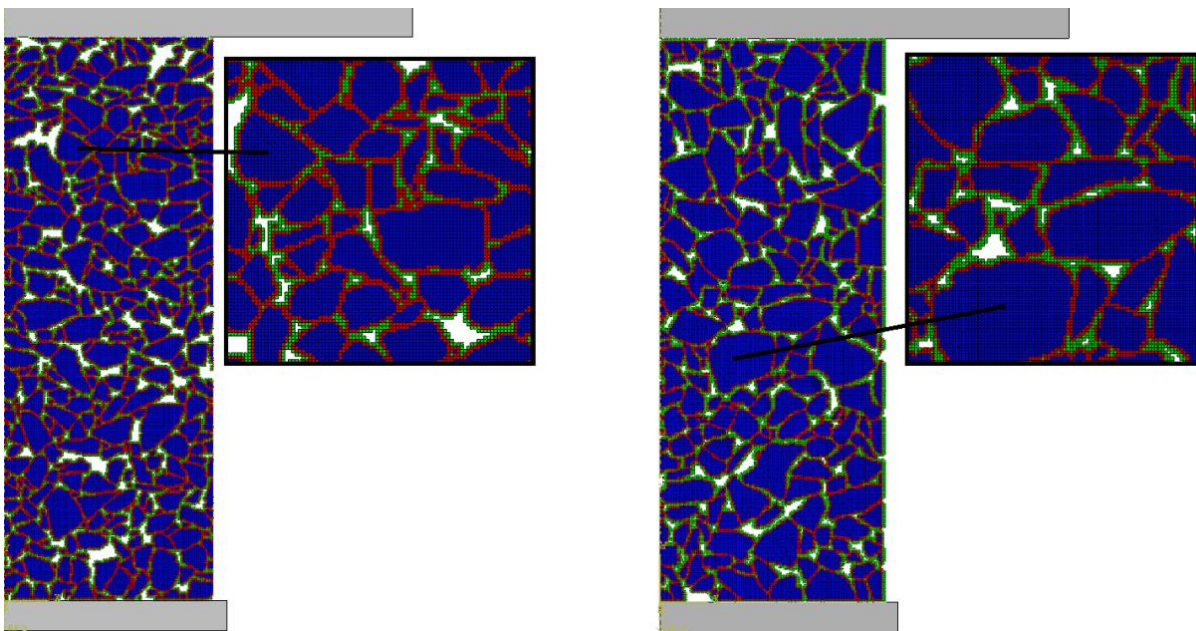


Figure 5.50 Finite element meshes for 2-4 mm (PRC2 in Chapter 4) and 50% 4-8 mm-50% 2-4 mm basalt (PRC3 in Chapter 4) porous concretes

The samples used in the simulations were 75 mm in height and 30 mm in diameter. In Figures 5.49-5.51, half of the section, that is rotated axisymmetrically, is shown. The steel impactor part of the mesh is mostly cropped from the image. It was noted in section 3.3.3 that in the meso-scale tests conducted on the composite gravel samples, the properties of the ITZ phases were found to be highly varying depending on the type of gravel aggregate. Therefore, in the numerical analyses on gravel porous concrete, different mechanical properties were assigned to the ITZ phases formed with different gravel aggregates (see Figure 5.51). Similarly, it was observed during concrete casting and compaction that some gravel aggregates were very weak compared to the others and that they even fractured during the compaction process. Therefore, different types of gravel aggregates with different properties were considered. Some of them (such as chalk) were given very low mechanical properties.

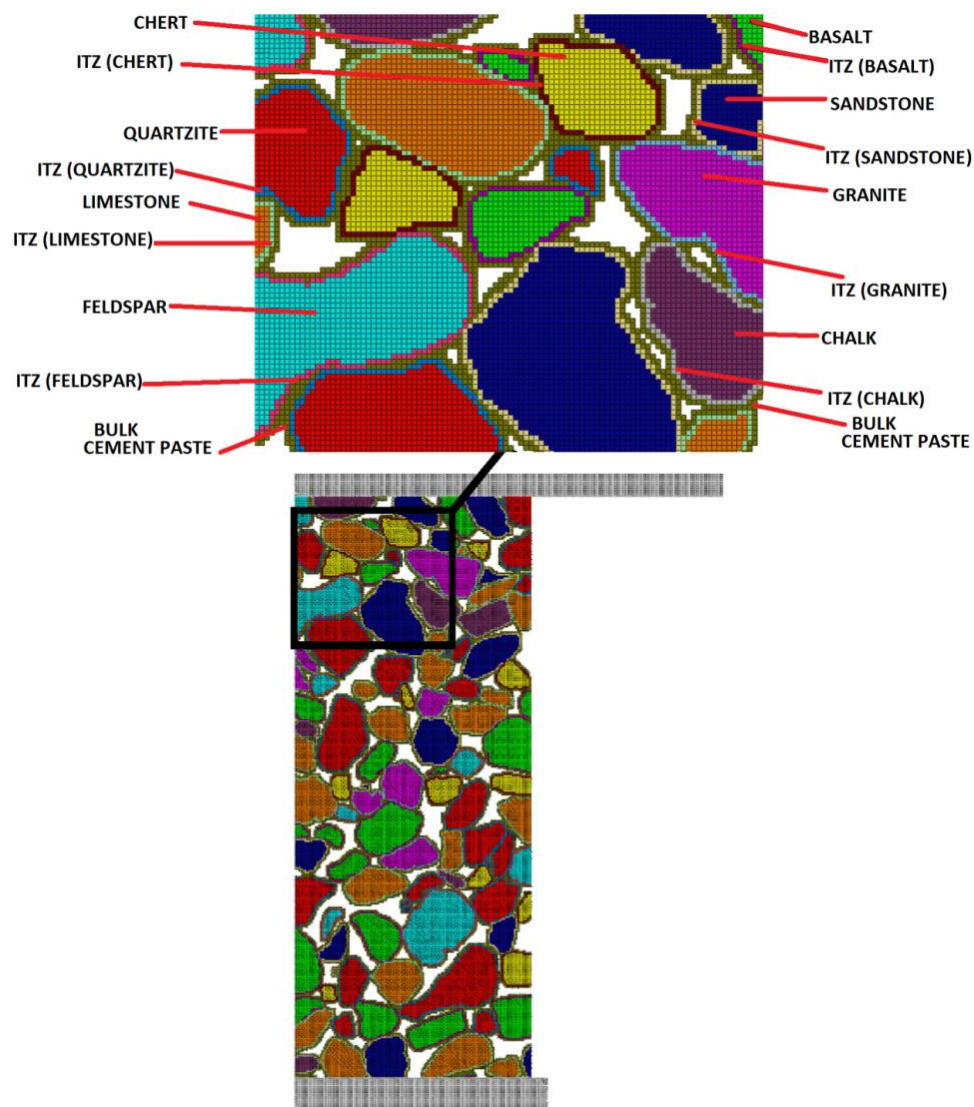


Figure 5.51 Finite element mesh for 4-8 mm gravel porous concrete containing different types of gravel aggregates (PRC4 in Chapter 4)

In the analyses of basalt-based porous concrete, the aggregates were defined as elastic (with  $E=50$  GPa,  $\nu=0.3$  for basalt) and no failure mechanism was defined for the aggregates. The cement paste and ITZ phases around the aggregates were defined using the CDP model in ABAQUS. The input data to define the compressive and tensile behavior of the cement paste phase were previously provided in section 5.4.4.3. The input data to define the compressive and tensile behavior of the ITZ phase were given in Figure 5.52 (also taking  $E=19.7$  GPa,  $\nu=0.19$ ). The percentages and material parameters of different gravel aggregates can be found in Table 5.6. By taking the meso-scale ITZ tests conducted on gravel aggregates as reference, peak tensile strengths between 0.45-1.30 MPa were defined for the different ITZ phases of gravel samples. The respective compressive strength input data were estimated by taking the tensile data as reference.

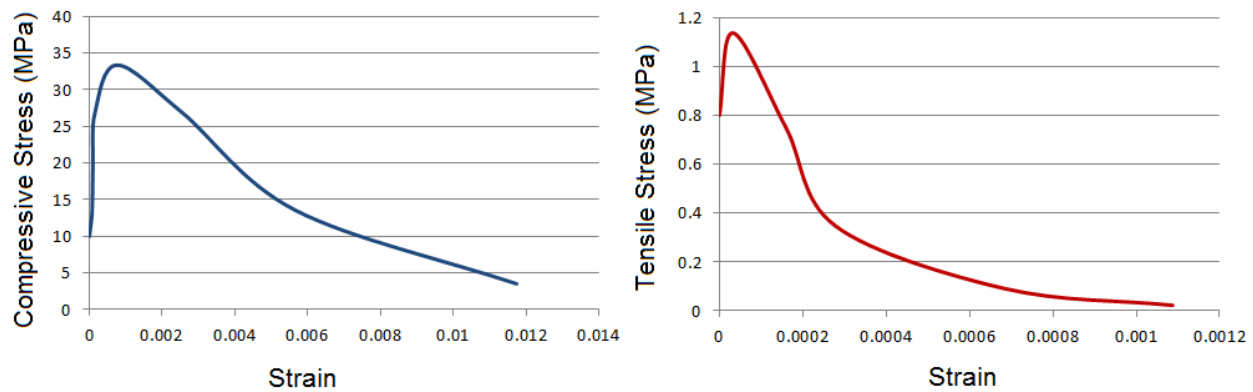


Figure 5.52 Compressive and tensile stress versus strain input data for the ITZ phase (for real porous concretes with basalt aggregates)

Table 5.6 Percentages and material parameters of different gravel aggregates

Aggregate Type	Percentage (%) (based on number of elements)	E (GPa)	$\nu$
Sandstone	14.03	20	0.30
Feldspar	8.94	40	0.30
Limestone	19.56	27	0.25
Chert	6.22	65	0.20
Chalk	4.65	18	0.25
Quartzite	22.83	65	0.25
Granite	6.87	70	0.23
Basalt	16.88	50	0.25

The frictional properties at the boundaries and at the free surfaces coming into contact were defined as explained in detail in section 5.4.4. The (concrete-concrete) contacts formed between the surfaces of the porous concrete sample were defined as “self-contact” with a friction

coefficient of 0.5. Self-contact is used when a deformable layer comes into contact with itself. In the analyses, it was seen that defining self-contact with high friction (friction coefficient 0.5) significantly decreased the time steps in the explicit analyses. Therefore, removing the self-contact was attempted and the results were compared with those of the analyses that include the contacts. The impact stress graphs for the same analyses with and without self-contact for a 4-8 mm basalt porous concrete are shown in Figure 5.53. In Figure 5.54 (a) no self-contact is defined (b) self-contact with friction is defined. In Figure 5.54 (b), the drastic effect of not defining contacts in the analysis can clearly be seen. If proper contact properties are not defined, when the elements located on the free surfaces come into contact, they deform uncontrollably and even become highly distorted. Even then, the explicit analysis provides output, as can be seen in Figure 5.53 (brown curve). However, the results obtained highly deviate from reality.

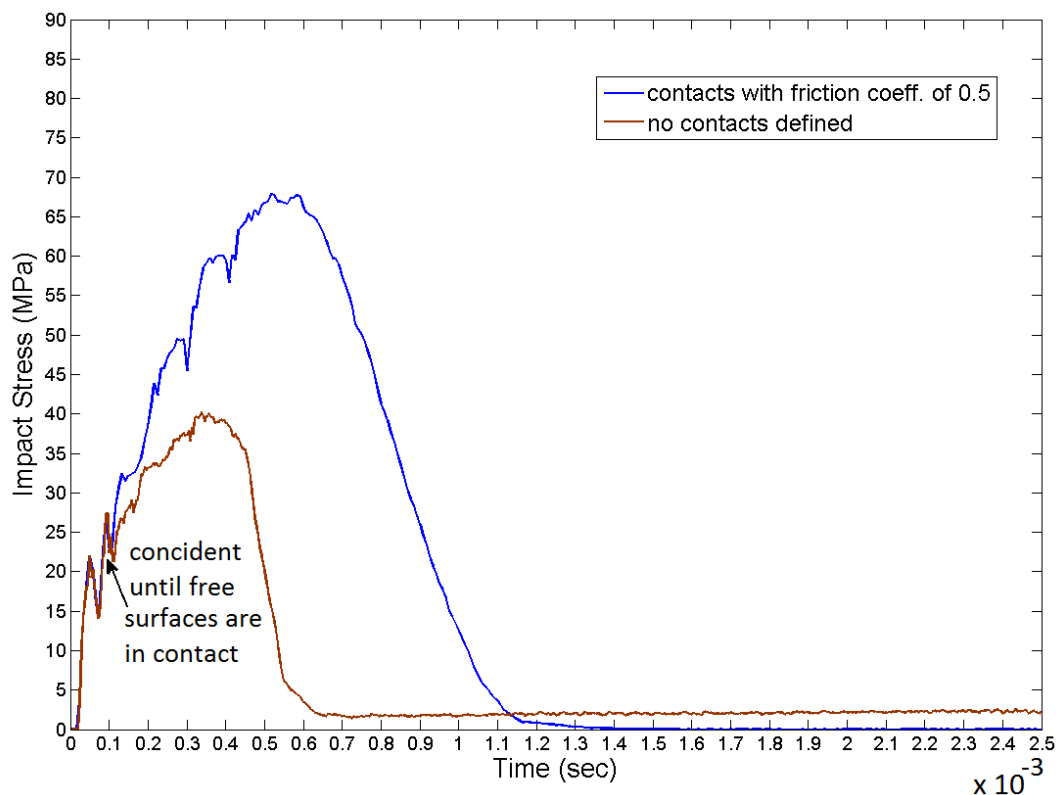


Figure 5.53 Impact stress graphs of 4-8 mm basalt porous concrete with and without self-contact



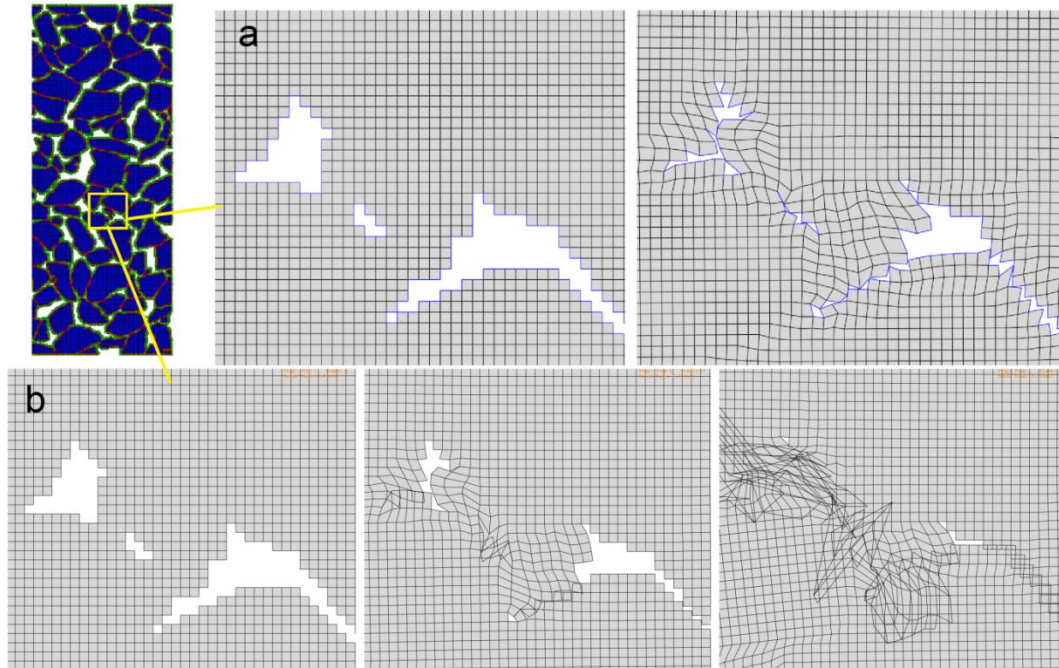


Figure 5.54 Pore collapse in porous concrete (a) with self-contact and (b) without self-contact

In Figure 5.55, the impact stress time histories of the three porous concrete mixtures with basalt aggregates having gradings of 4-8mm (PRC1), 2-4 mm (PRC2) and 50% 4-8mm-50% 2-4 mm (PRC3), a 4-8 mm gravel aggregate porous concrete (PRC4) and a full concrete with 4-8 mm basalt aggregates (FC1) are presented. Full concrete specimens were experimentally produced by completely filling and vibrating the porous concrete sample with cement paste just after compaction, at the fresh state as described in section 3.3.1. Therefore, the sample is different from normal concrete in the sense that there is no fine aggregates involved. It is essentially a porous concrete sample where all the meso-scale air pores are filled with cement paste. This mixture was used in investigating the effect of the lack of pores in the behavior of the material by comparing the evolution of impact stresses as well as the fracture patterns.



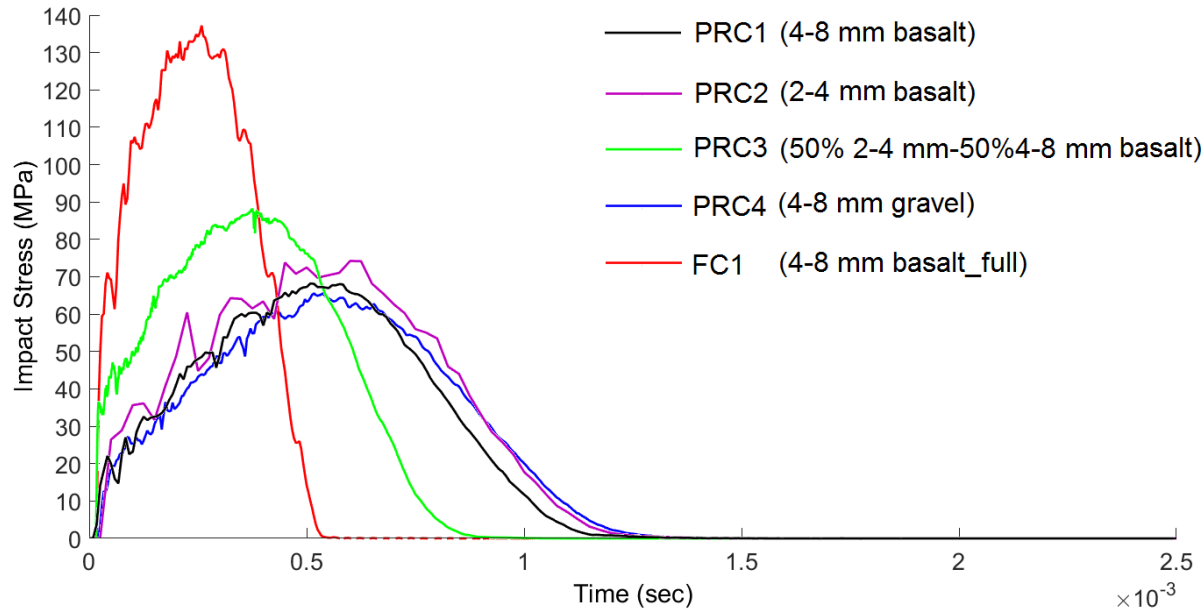


Figure 5.55 Impact stress time histories for different porous concretes and a full concrete

When the peak values of the impact stress-time histories are checked and compared with the experimental results of the corresponding mixtures in Chapter 4, it can be said that impact strengths of the samples obtained numerically are in a good agreement with the experimental results (see Table 5.5). The simulations are considered realistic in the sense that the generated finite element meshes resembling the phase distributions of the materials and the input data for the different components in the materials were taken from experimental data. Similar to the experiments, highest impact strength was reached for 50% 4-8mm-50% 2-4 mm basalt porous concrete (PRC3). While the results of PRC 1 and PRC2 are also close to the experimental results, the numerically computed impact strength of PRC4 (gravel concrete) was slightly higher than the experimentally found value (see Table 4.6). This can be attributed to the fact that in the analyses of real porous concretes with basalt as aggregate, the same material parameters were used while in porous concrete with gravel very different and varying material parameters had to be taken. Some of those parameters might be different from the real values. In addition, the percentages of the different types of gravel aggregates were intuitively selected in the analysis. The actual exact composition of the gravel aggregate batch could not be determined. When all the curves obtained from different mixtures are compared, it can be observed that in full concrete, the peak stress is reached in a shorter time and a faster failure is evident.

Since one of the main objectives of the numerical research was estimating the fragmentation behavior of porous concrete, the damage contours of the analyzed concretes were also evaluated. When the compressive and tensile damage contours of a 2-4 mm basalt aggregate porous concrete are examined by zooming into one of the pores (see Figure 5.56), it can be seen that the top and bottom poles of the pores suffer from tensile damage. This is similar to observations in model porous concretes (see section 5.4.3, Figures 5.20, 5.21, 5.26 and 5.27). Compressive

damage occurs more on the sides of the pores and at the triaxially confined zones above and below the aggregates. At those locations, similar to the triaxially confined zones at the specimen borders, the lateral expansion of cement paste is restraint by the aggregates and triaxial compression develops at the top and bottom of the aggregates (Stroeven 1973, van Mier 2013).

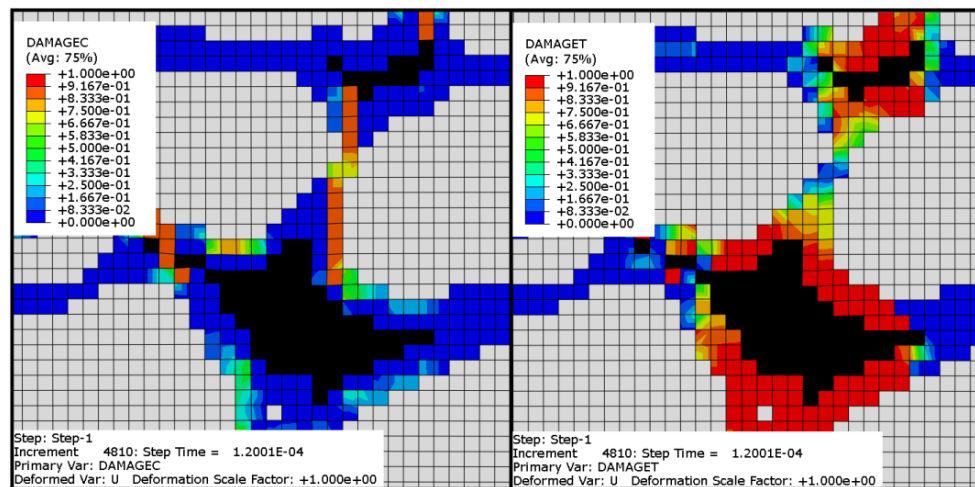


Figure 5.56 Compressive and tensile damage contours around a hole (PRC3)

When a larger piece of the mesh is analyzed, the same types of damage are seen throughout the concrete (see Figure 5.57). Additional concentrations of splitting tensile damage can also be seen between the aggregates in the vertical direction. Immediately above and below the aggregates and also at the diagonal contact points, the compressive damage is also evident.

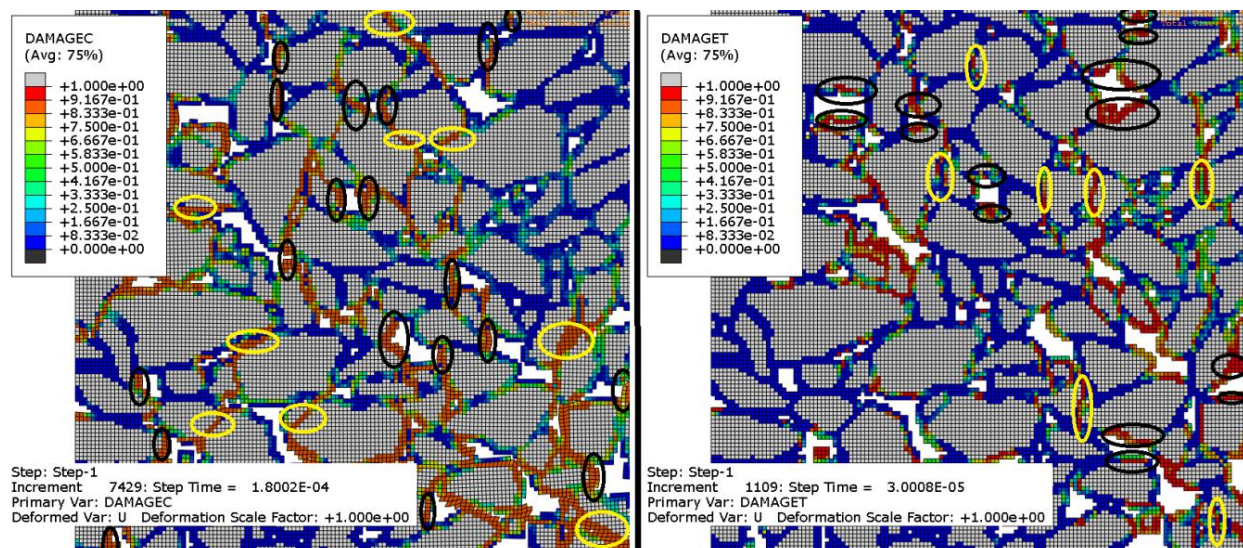


Figure 5.57 Distributions of compressive and tensile damage contours (PRC3)

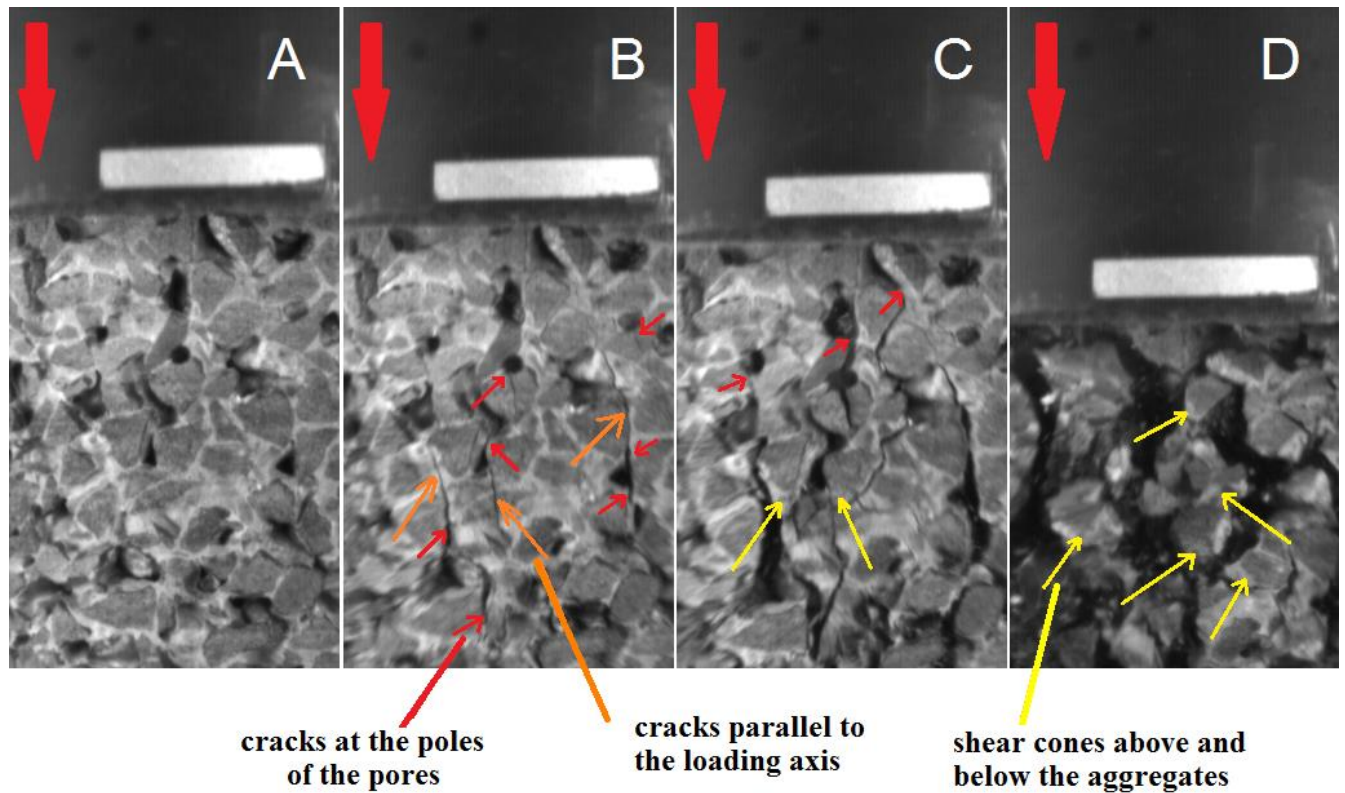


Figure 5.58 High speed photographs for the impact test of a 4-8 mm basalt aggregate porous concrete sample demonstrating the fracture patterns

The numerical results can be compared with the images acquired using high speed photography. In Figure 5.58 (also Figure 4.31), crack patterns such as tensile cracks parallel to the axis of loading (indicated by orange arrows in Figure 5.58) and the subsequent shear cones underneath the aggregates (indicated by yellow) can be observed. On the other hand, due to the porous structure, cracks initiating from the upper and lower poles of the pores (indicated by red arrows in the figure), where tensile stress concentrations are present, are also evident. Similar crack distributions were also observed in the numerical results (in Figures 5.21, 5.56 and 5.57).

After examining the locations of tensile and compressive damage concentrations separately in zoomed images, the complete samples were examined at different times. Two pictures from each mixture were presented ( $2.5 \times 10^{-4}$  sec which is much earlier than the peak and  $1.5 \times 10^{-3}$  sec which is after the peak) in Figures 5.59-5.63. From the images it is evident that some cracks start to appear (at  $2.5 \times 10^{-4}$  sec) much earlier than the peak strength. The elements that correspond to a tensile or compressive damage value of 0.9 or higher were removed as previously done in order to estimate the crack patterns and fragment sizes.



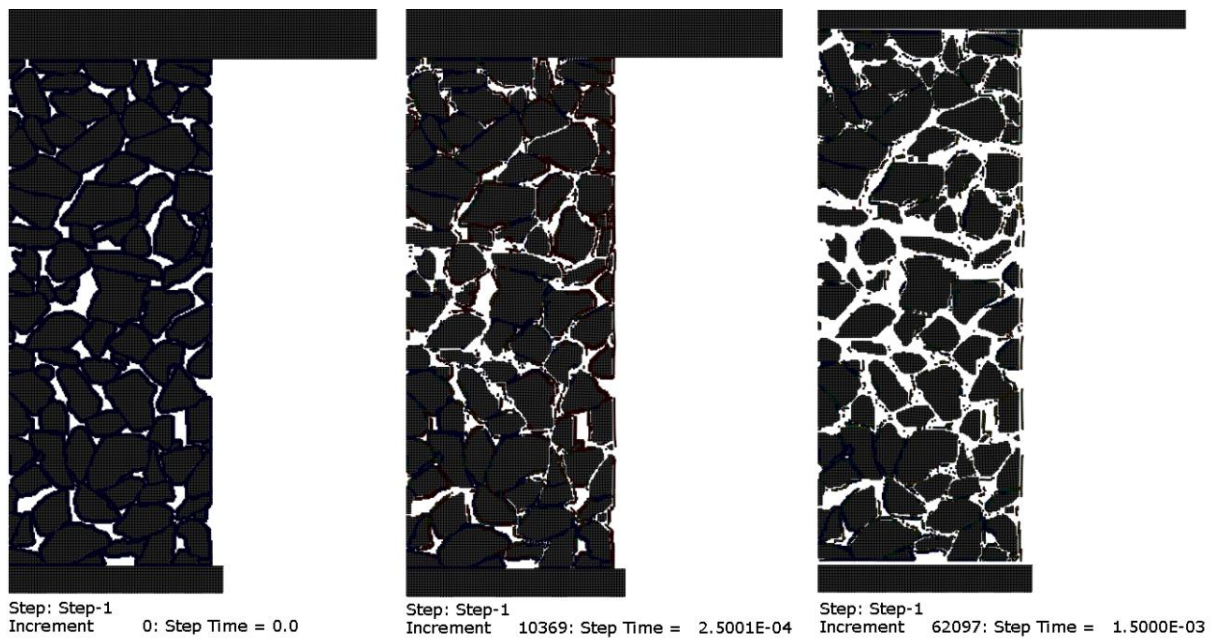


Figure 5.59 Compressive + tensile damage variable contours in PRC1 (with 4-8 mm basalt aggregates) (elements having DamageC or DamageT  $\geq 0.9$  removed.)

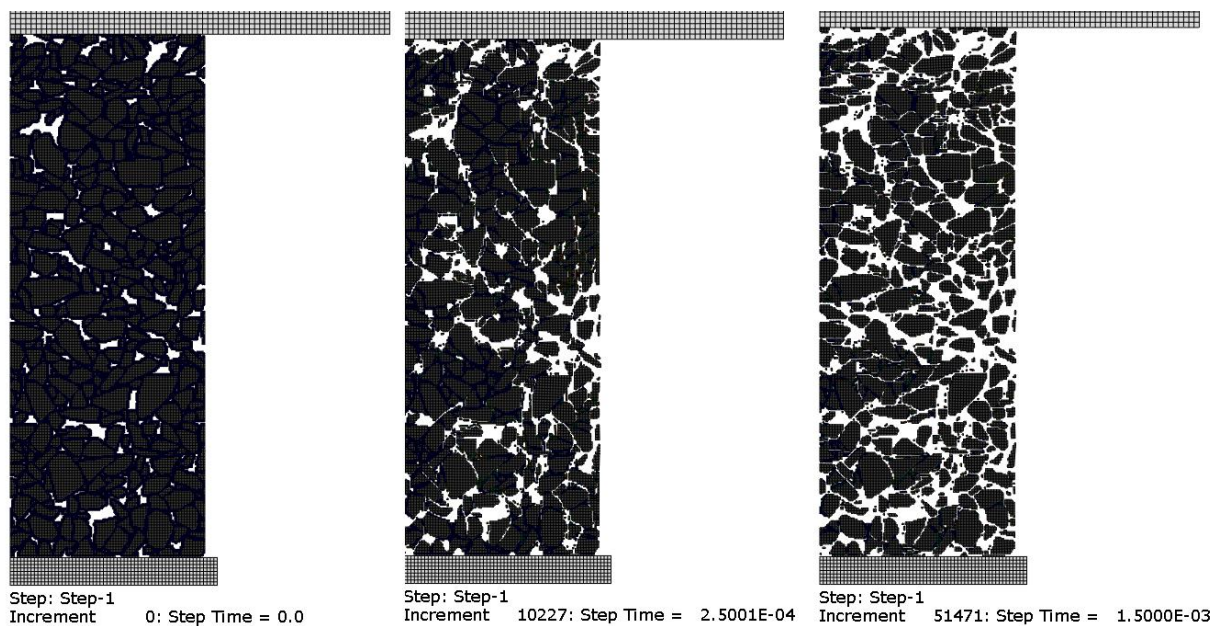


Figure 5.60 Compressive + tensile damage variable contours in PRC2 (with 2-4 mm basalt aggregates)

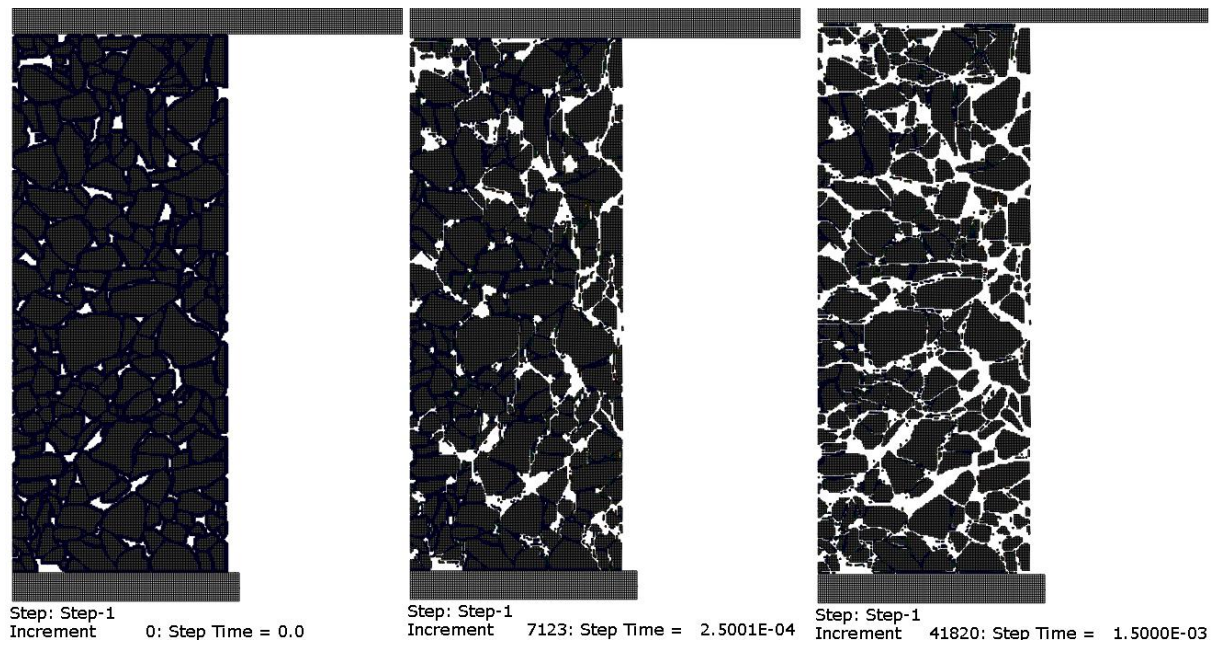


Figure 5.61 Compressive + tensile damage variable contours in PRC3 (with 50% 2-4 mm-50% 4-8 mm basalt aggregates)

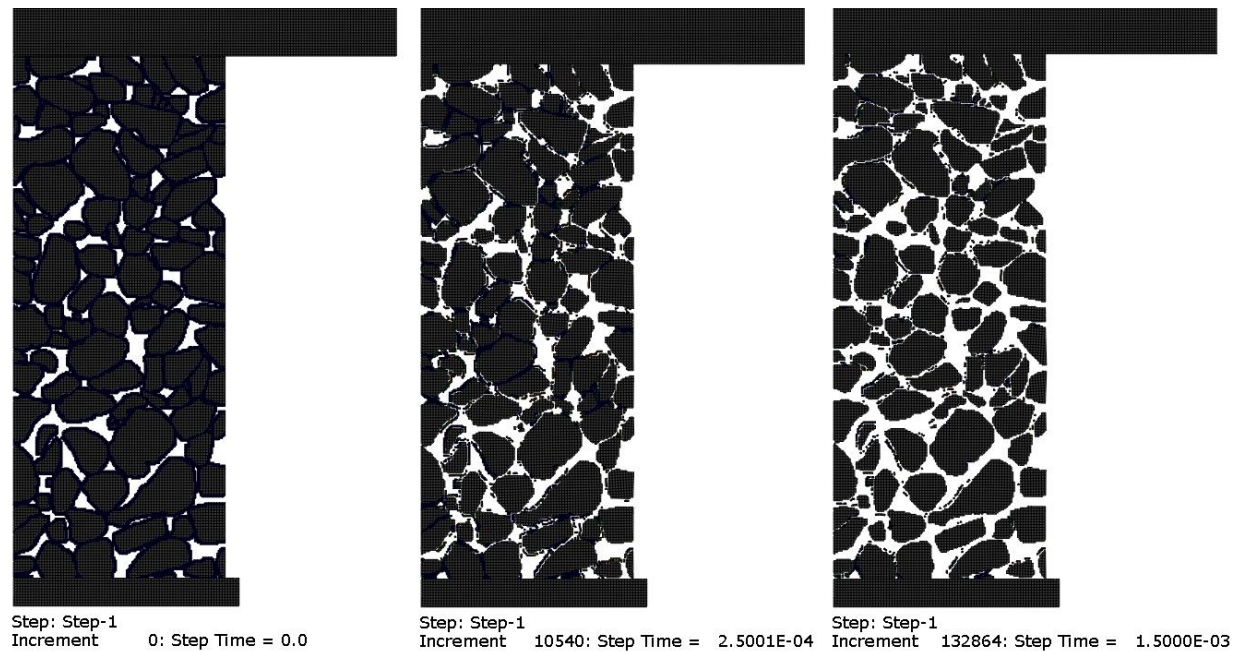


Figure 5.62 Compressive + tensile damage variable contours in PRC4 (with 4-8 mm gravel aggregates)



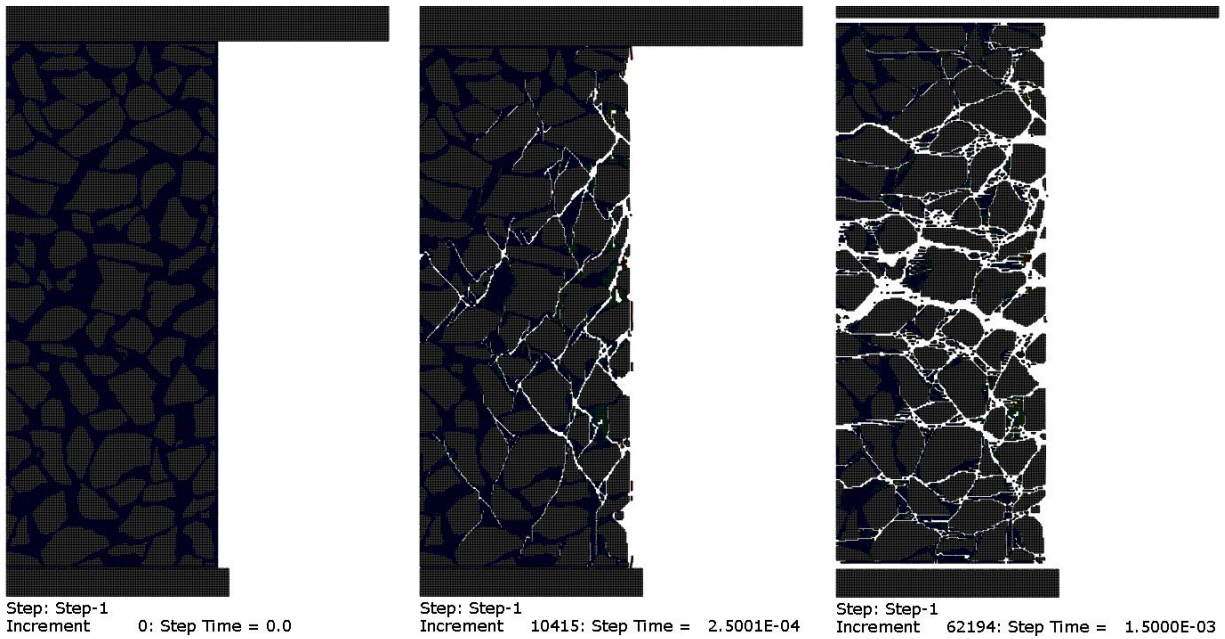


Figure 5.63 Compressive + tensile damage variable contours in FC1 (4-8 mm basalt aggregate full concrete)

If the images are compared, it is clear that the mixtures with 4-8 mm (basalt or gravel) aggregates (PRC1 and PRC4) fracture into fragments nearly in the size of their aggregates. This is similar to what was also observed during the experimental impact tests and discussed in Chapter 4. When the porous concretes are compared (Figures 5.59-5.62) with the full concrete (Figure 5.63), the multiple fracturing performance of porous concretes can be distinguished. The small bridges that assemble the aggregates in porous concretes were easily broken and the samples fractured into fragments nearly as small as their aggregates. Whereas full concrete fractured into larger size fragments.

It should be noted that a weaker effect of boundary friction and triaxial confinement was observed in these analyses compared to those performed on model porous concretes even though the same friction coefficient of 0.3 was used. While triaxially confined zones near the sample boundaries stayed undamaged in model porous concretes (see for example Figures 5.32-5.35), such intact zones could not clearly be observed in real porous concrete analyses. (Note: It was slightly more observable for full concrete (FC1) and PRC1.) This was actually unexpected. The boundary effect is slightly more visible at time  $2.5 \times 10^{-4}$  sec. However, at time  $1.5 \times 10^{-3}$  sec, where the general level of damage is very high throughout the sample, it is obviously much less pronounced. A similar trend was also observed in the third image in Figure 5.32 where a model porous concrete with high porosity (0.2791) was analyzed. In that example, the triaxially confined zones were also fractured and the effect of confinement due to friction was not evident. Therefore, a possible explanation is for this can be the presence of a high percentage of large size pores and consequently less strengthening due to confining pressure.

#### 5.4.6. Determination of Pore Size Distribution

Determining the pore size distribution was important for providing complementary information in view of understanding the behavior of porous concretes. Image analysis techniques were used to determine the pore sizes of the mixtures that have been numerically analyzed and a small program was written for the purpose. Similar to the analyses performed for determining the real aggregate distributions of porous concretes, the meshes were converted to binary images. The borders of all the pores were defined by checking the black pixels that are neighbors to white pixels (see Figure 5.64). Subsequently, each border pixel is again checked in terms of being neighbors this time with other black pixels to continue tracing the complete border of each pore. When all the pores are separately detected one by one, their areas are also calculated in terms of pixels and converted to metric units.

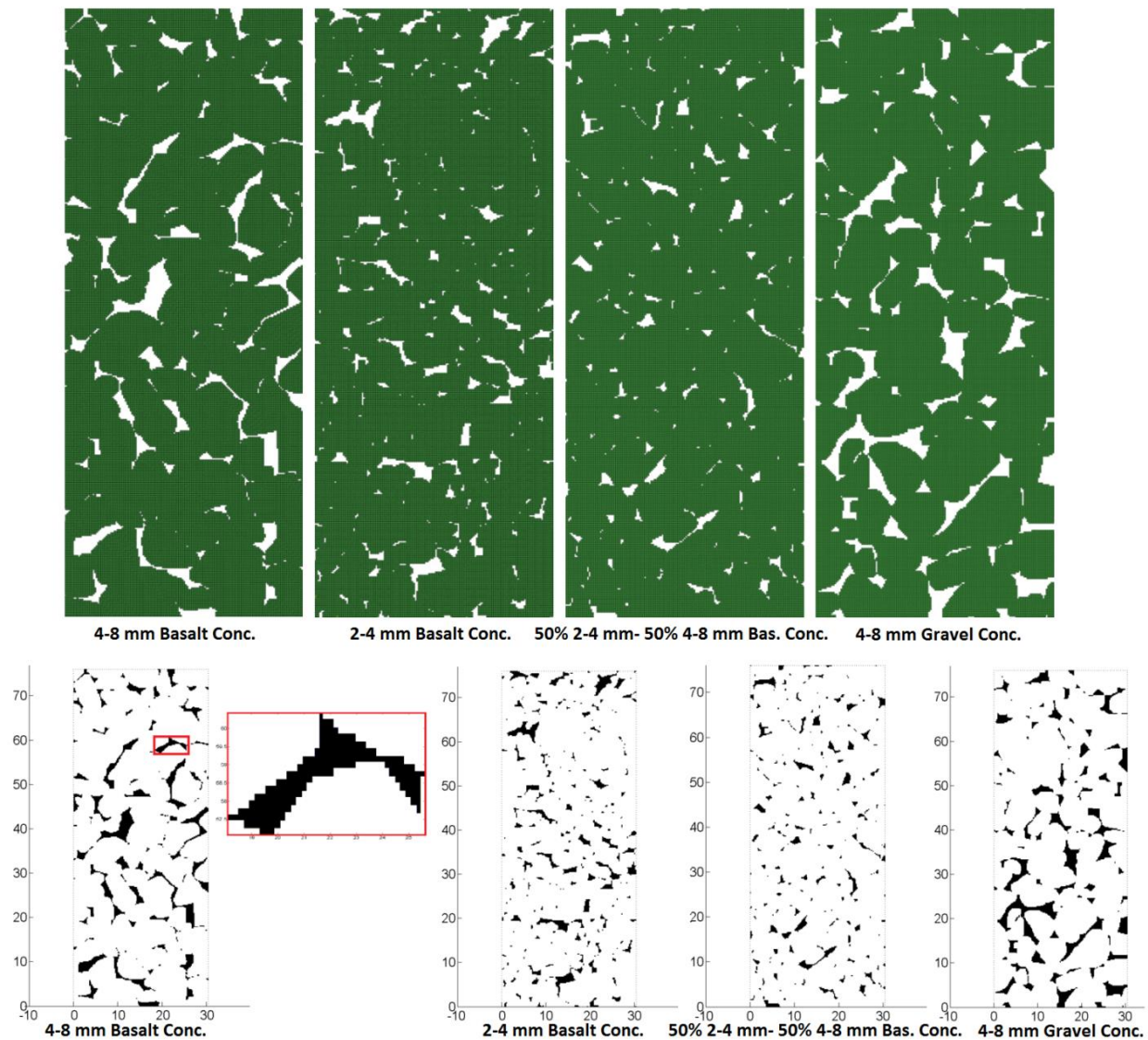


Figure 5.64 Determination of pore size distribution



The areas of the pores were plotted one by one in a graph (see Figure 5.65) for the four different types of porous concretes. The curves are also zoomed in to show that the parts that seem to go horizontal with the pore size value of 0 actually have values other than 0. Since those pores are very small compared to the rest, they are not clearly visible in the collective graph. It should also be noted that because in the program, each pore is selected and numbered one by one, each data point in Figure 5.65 indicates the size and pore number of a specific pore. Therefore, the x-axis shows the pore numbers of all the pores present in a sample.

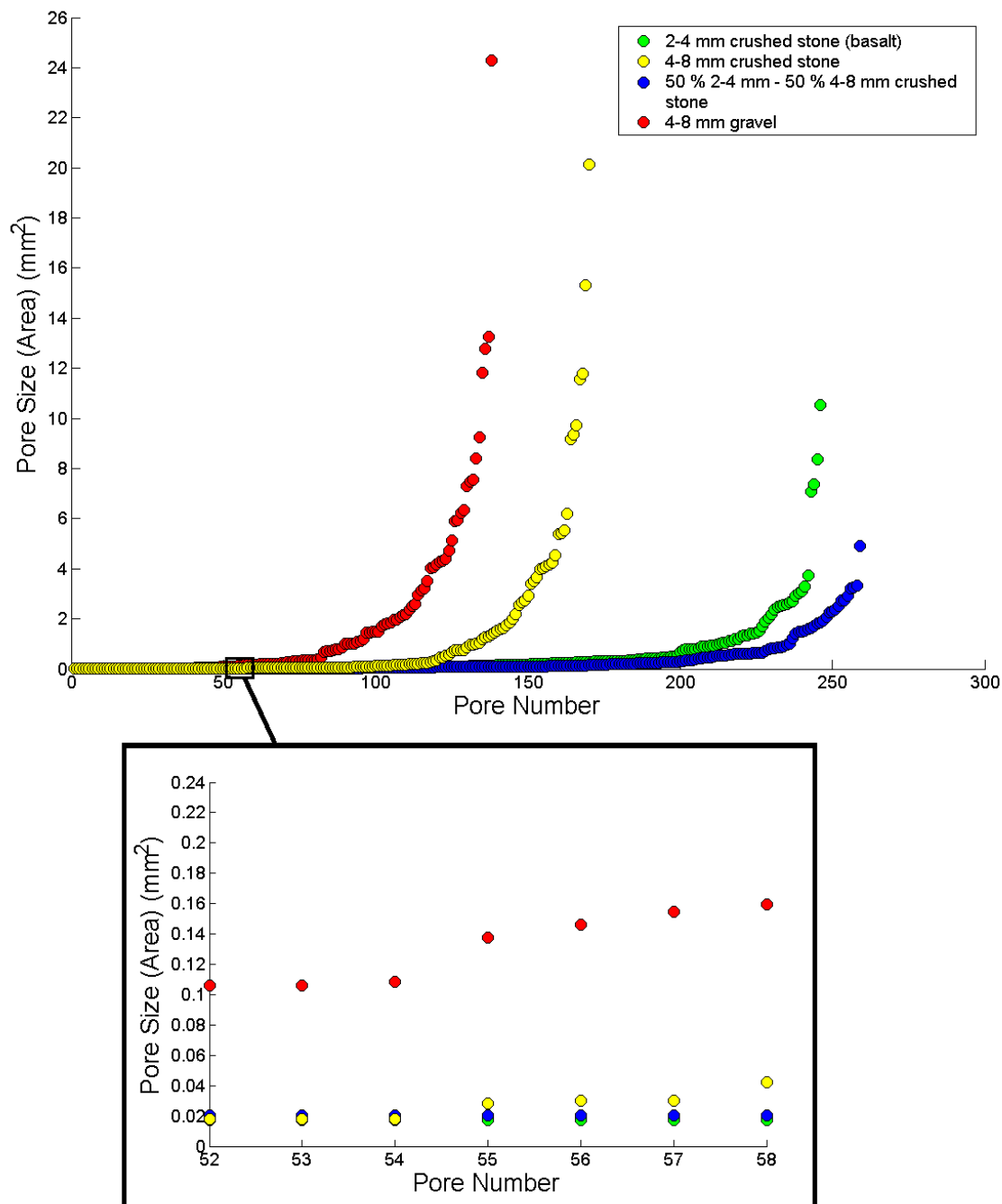


Figure 5.65 2D pore size versus pore number graph for PRC1, PRC2, PRC3 and PRC4

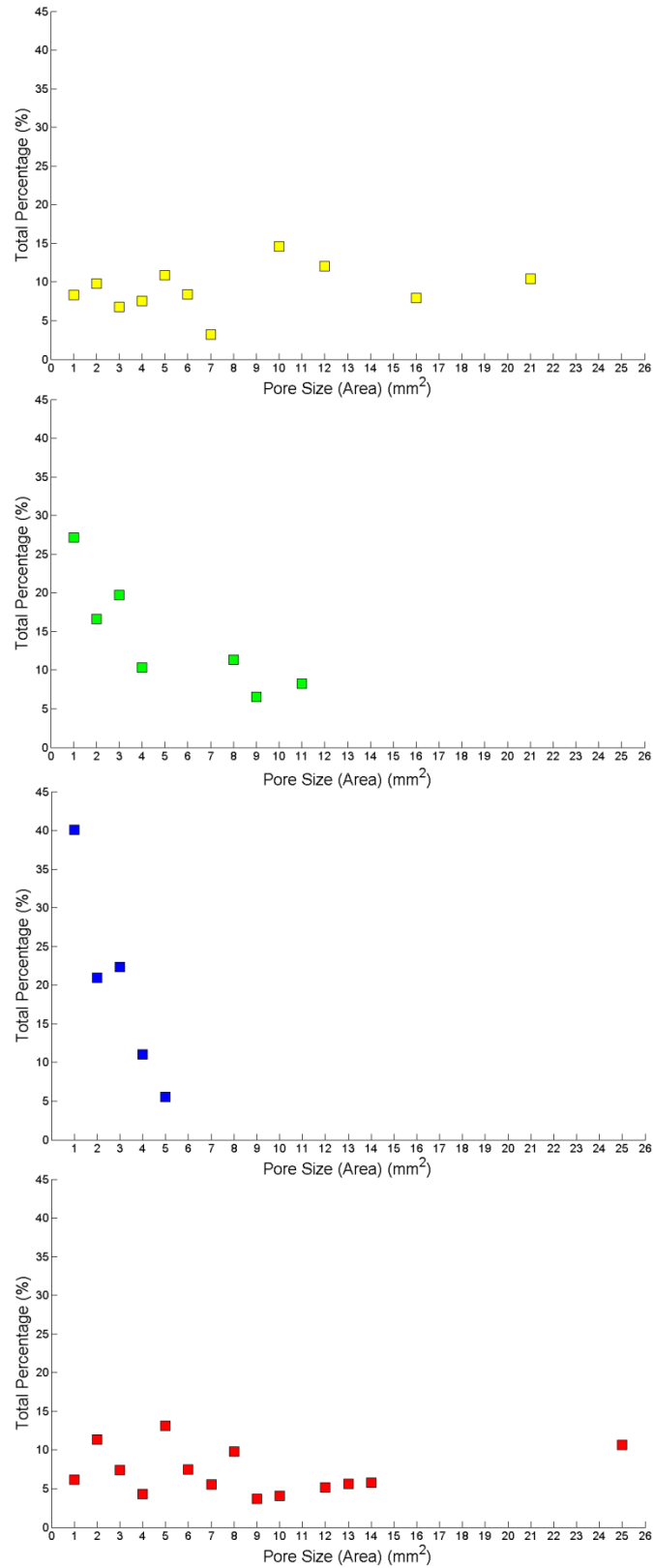


Figure 5.66 2D pore size intervals versus cumulative percentage graph for PRC1, PRC2, PRC3 and PRC4 (from top to bottom)

To have a clearer overview of the size distributions, the pores are grouped into size intervals. For example, pores with a size between 4 and 5 mm<sup>2</sup> are added up and collectively presented at pore size 5 in the graphs as seen in Figure 5.66. The graphs demonstrate the pore size distributions of different mixtures. It can clearly be seen that PRC1 and PRC4 with 4-8 mm aggregates have larger pores compared to PRC2 and PRC3 with 2-4 mm and 50% 2-4 mm-50% 4-8 mm aggregates, respectively. The graphs clearly demonstrate the effect of aggregate size on the pore size distribution of different mixtures.

#### **5.4.7. Determination of Fragment Size Distribution**

The crack patterns predicted by the damage evolution contours (see Figures 5.59-5.62) were generally observed to be good estimations of the real crack patterns observed with the high speed photography videos and the fragments collected during impact testing. In the analyses, highly damaged (damage parameter  $\geq 0.9$ ) elements were again removed (see also Figure 5.59). Quantifying the sizes of the fragments was also important in terms of the research project objectives. Therefore, the same analysis that was conducted on pores were conducted on the fragments of PRC1 (4-8 mm basalt porous concrete). An example is given in Figure 5.67. Because an axisymmetric analysis was performed, where the mesh was rotated 360 degrees around the y-axis, the areas of the fragments that are intersecting the axis of symmetry (y-axis or  $x=0$ ) were doubled (see the red bordered fragments indicated by green in Figure 5.68). Meanwhile, the rest of the fragments (see the blue bordered fragments Figure 5.68) were taken to be present two times. This is because in the mirror image, those separate fragments are again present (i.e. two separate fragments with the same area each). It should also be noted that the mesh images in Figure 5.67 and 5.68 are plotted by slightly shifting to the right to better demonstrate the borders of fragments touching the y-axis. In the analyses, the mesh is located between  $x=0$  and  $x=30$  mm. The 2D fragment sizes versus fragment number curve for PRC1 is presented in Figure 5.69.

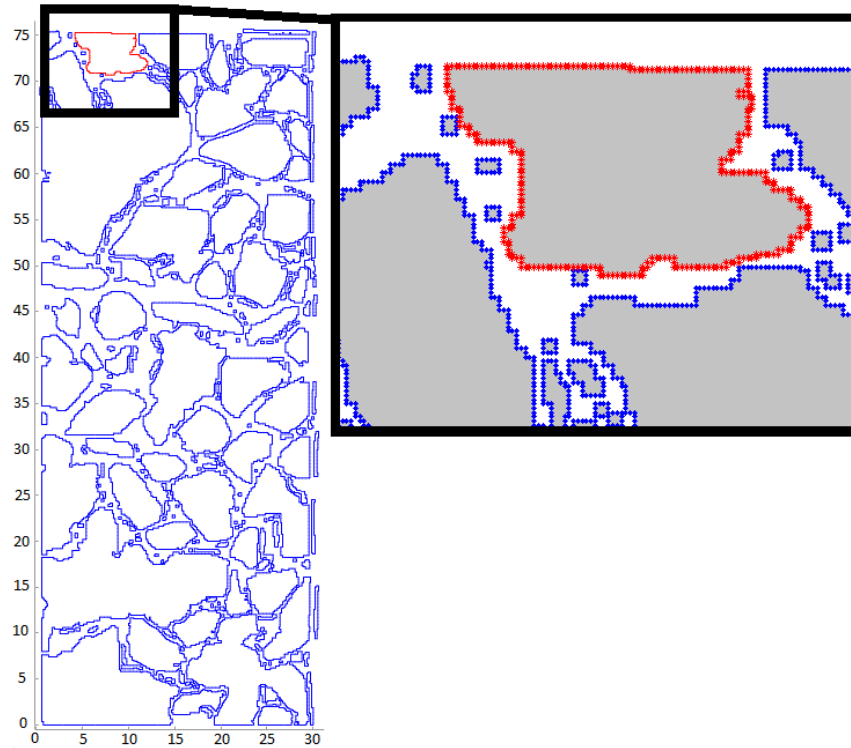


Figure 5.67 Determination of fragment sizes

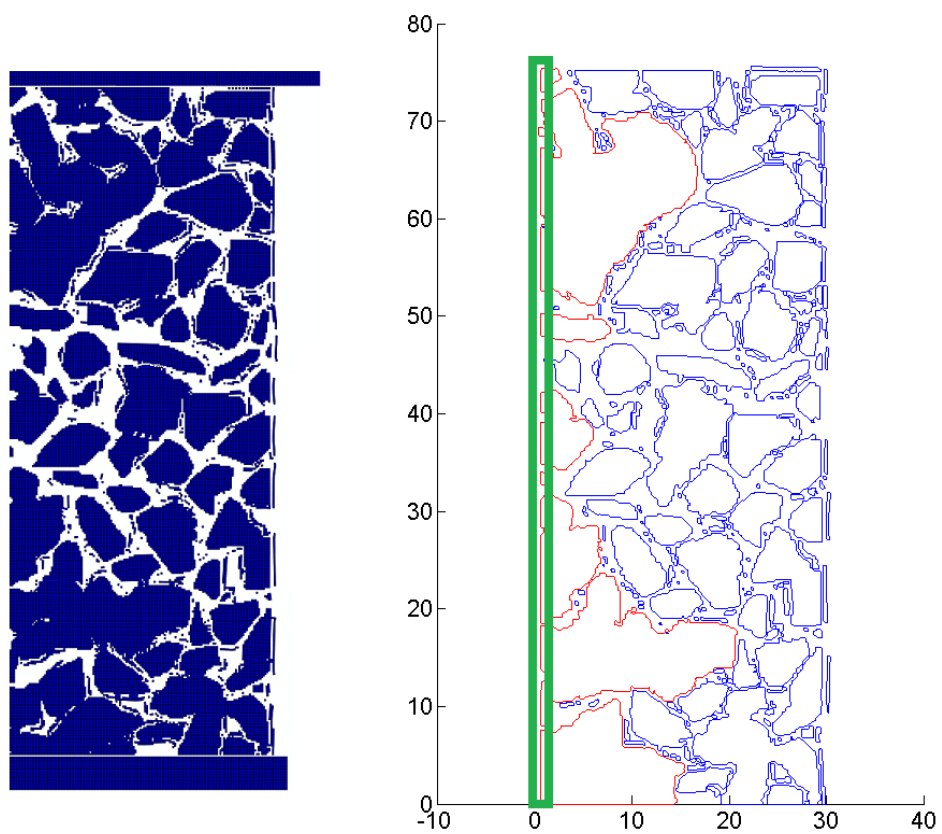


Figure 5.68 The fragments with doubled areas (red) due to axisymmetry (intersecting the y-axis)

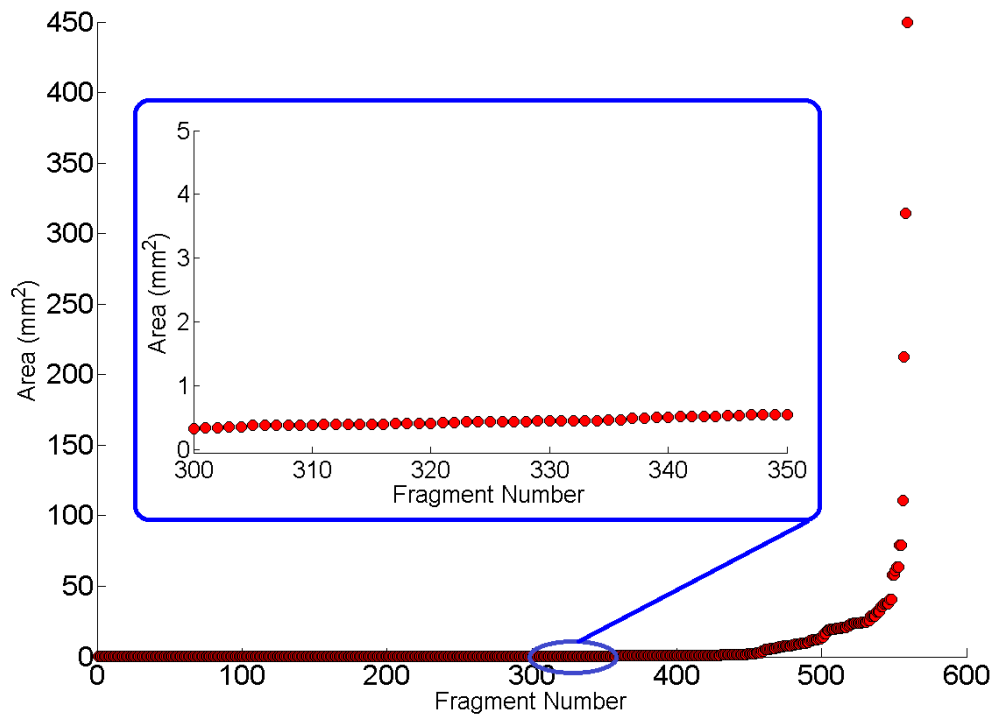


Figure 5.69 2D fragment size versus fragment number graph for PRC1

The individual 2D sizes were again grouped into size intervals as previously done in pore size analyses (see Figure 5.70). During the impact experiments, the fragments were collected and sieved as described in detail in section 4.4.8.1. The numerical results could therefore be compared with the sieve analysis results by converting the 2D sizes (areas of the fragments) from the numerical analysis to standard sieve sizes. This was done by calculating the diameters of the circles having the same corresponding areas and again grouping them in terms of the sizes of the standard sieves starting from 4 mm (4, 8, 16 and 32 mm). The bar graph in Figure 5.71 shows the two sets of results. The numerical fragment size analysis seems to estimate the fragment sizes quite sufficiently up to 16 mm, but deviates from the experimental results at the larger size fragments.

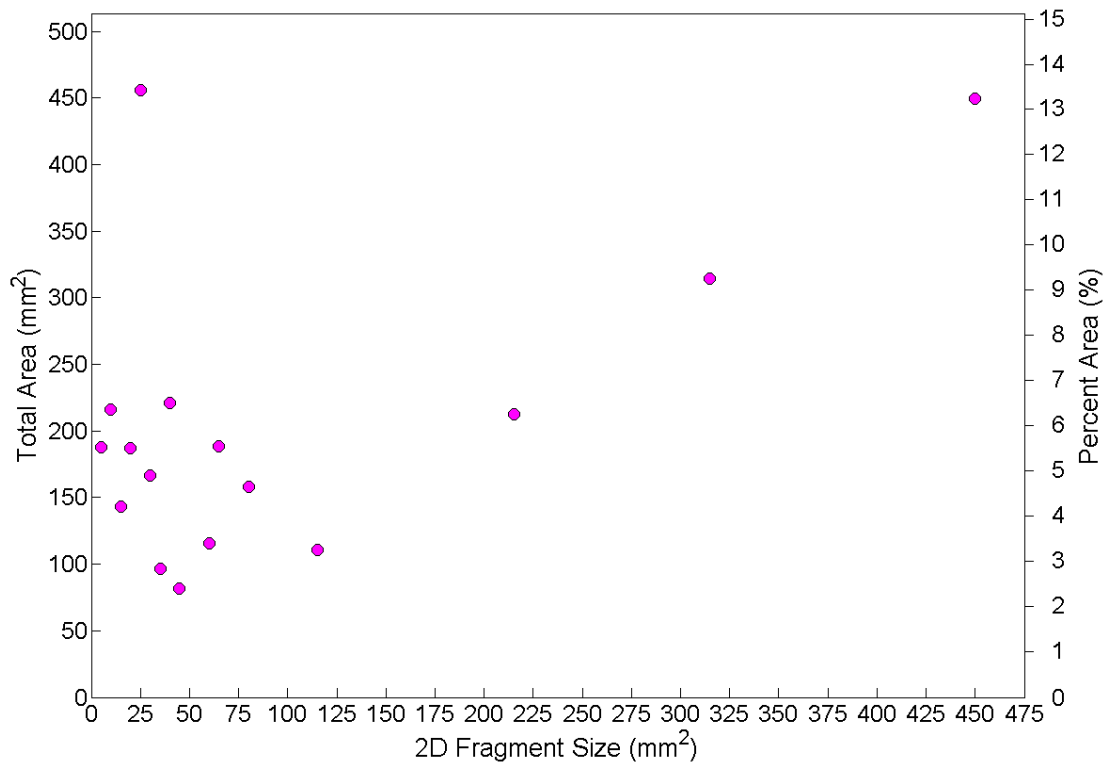


Figure 5.70 2D fragment size intervals versus cumulative area and percentage graph for PRC1

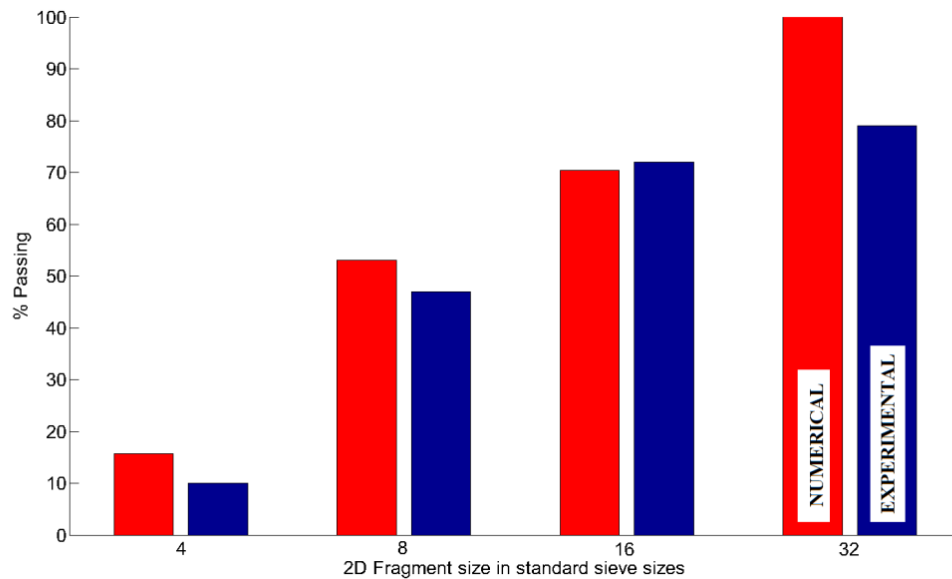


Figure 5.71 Comparison of the numerical and experimental fragment sizes

#### 5.4.8. Conclusions

The focus of the numerical part of this research project was simulating and assessing the dynamic behavior of different porous concretes under impact loading in order to understand the effect of various control parameters on their impact behavior. To achieve this purpose, analyses were also conducted on fictitious (model) porous materials. Analyses on model porous concretes better demonstrated the individual factors which affect the porous concrete properties. The following conclusions can be drawn regarding the numerical part of this research study.

Explicit finite element methods are efficient numerical methods for impact research, especially when the time step size complying with the stability limit is feasible, to describe the physical problem in a reasonable time. In this research, explicit time integration has been selected as the analysis method because of the high nonlinearity of the system and the short duration of the dynamic interaction. It should also be noted that in the attempts to use implicit analysis techniques for analyzing porous concrete, convergence problems were encountered due to extensive element distortions.

For a realistic representation of the real porous concretes that have been tested, the aggregates were directly determined through 3D computed tomography. A mesh generation program was developed for realistically generating finite element meshes including the arbitrary shaped air pores. In the analyses, porous concrete was considered as a four-phase material consisting of aggregates, bulk cement paste, interfacial transition zones (ITZ) and meso-size air pores.

A Concrete Damaged Plasticity (CDP) model, which is a plasticity-based, damage model for concrete, was used to define the material properties of the different cementitious phases in the paste i.e. the interfacial transition zone (ITZ) and the bulk cement paste. For conducting realistic numerical analyses, input data for the model were inferred from the experimental tensile and compressive test results for cement paste phase and plain concrete. Experimental tensile strength data were used to define the strength properties of the ITZ phase. It could be concluded that the CDP model was capable to represent the cementitious phases present in porous concrete, enabling to capture a realistic behavior for the material under impact loading.

The analyses of samples with only one pore provided helpful information on the stress and damage distributions at the vicinity of a pore. Model porous concretes with regularly and randomly distributed circular pores were used to better understand the effects of individual parameters associated with pores. From a comparison of the impact responses of model porous concretes with different size pores (constant total porosity), it could clearly be concluded that, with decreasing pore size, the impact strength of the concretes increased. In the analyses the crack patterns formed under impact loading were visualized using the compressive and tensile damage variables. By removing the elements that correspond to damage values of 0.9 or higher, the estimation of the crack patterns was possible. (For the definition of the damage variable please see section 5.4.1). From damage output, it could be concluded that with decreasing pore



size (and hence an increase of the number of pores in order to keep the total porosity constant), the sizes of the fragments that are formed drastically decreased. It was also seen in the analyses that increasing the pore size, and consequently increasing the porosity, highly decreased the dynamic strength, as expected.

In the analyses of porous concretes with randomly distributed circular pores, for each different total number of pores, four random pore distributions were investigated with and without boundary friction. The analyses with and without end friction revealed that restrained deformations due to boundary conditions have a major effect on the fragmentation behavior. This was also clear from the plot of the damage contour. In case of no friction, no triaxially confined zones were seen while tensile splitting became a more dominant factor. However, such a drastic effect could not be observed in the peak stress values. According to the results obtained from the analyses on the concretes with randomly distributed pores, it could be concluded that when the pore size increased the effect of randomness on the results, i.e. the variance, also increased.

Circular aggregate porous concretes were also analyzed to understand the effect of aggregate size on the porous concrete properties without the influence of packing density. In the analyses, the packing density was kept constant. According to the results, the impact strengths of porous concretes with 4 and 8 mm particles were approximately the same. The impact strength of the model porous concrete with 2 mm particles was lower. This was an unexpected trend, because it contradicts with both the experimental and the numerical results on real porous concretes, where finer aggregate mixtures gave higher impact strengths. This result of circular aggregates also contradicted with the circular pore model concretes in which the impact strengths significantly increased as the pore size decreased. Meanwhile, there is no agreement in the literature on whether increasing the aggregate size has an increasing or decreasing effect on the compressive strength of porous concretes. The contradiction between the experimental (and numerical results) on real porous concretes and the results on circular aggregate porous concretes can be attributed to the presence several factors acting in opposite directions. Among the various factors, aggregate size and pore size act in opposite directions dominating over each other in different situations. The better interlocking of smaller size irregularly shaped aggregates compared to larger ones in real porous concrete simulations, which is not valid for circular shaped aggregates, is another factor. The amount of cement paste, which is the weak phase, being higher in smaller size aggregate porous concretes also has an important effect. All those different factors acting simultaneously affect the numerical as well as the experimental results, sometimes causing contradicting outcomes.

For real porous concretes, when the peak values of the impact stress time histories are compared with the experimental results of the respective mixtures, it can be said that impact strengths of the samples obtained numerically were in a good agreement with the experimental results except for the gravel mixture. It could be concluded that the simulations conducted were realistic. This

can be attributed to the finite element meshes resembling the phase distributions of the actual materials and the input data for the different phases being generated based on experimental data. Numerical analysis of the pore and fragment size distributions also provided complementary information to better understand the dynamic behavior of the different mixtures.

The numerical model proves to be a versatile tool for the analysis of porous concrete. The mesh generating part of the model represents the porous material in a realistic way. With the definition of contacts with friction and the use of CDP model supported by experimental input, different types of porous concretes were modeled at a level of detail that was necessary to capture the characteristic impact properties of the material.

## References

- Qian, Z., Schlangen, E., Ye, G. and Breugel van, K. (2011), *3D Modeling of Fracture in Cement-Based Materials*, Key Engineering Materials, 452-453, 69-72.
- Wu, S.R. and Gu, L. (2012), *Introduction to the Explicit Finite Element Method for Nonlinear Transient Dynamics*, Wiley.
- De Borst, R., Crisfield M. A., Remmers J.J.C. and Verhoosel C.V. (2012), *Non-linear Finite Element Analysis of Solids and Structures*, Wiley.
- Noh, G. and Bathe K.J. (2013), *An Explicit Time Integration Scheme for the Analysis of Wave Propagations*, Computers and Structures, 129 (2013), 178–193.
- Tarque, N.S. (2011), *Numerical modelling of the seismic behavior of adobe buildings*, PhD Thesis, University of Pavia, Italy.
- Chopra, A.K. (2000), *Dynamics of Structures: Theory and Applications to Earthquake Engineering*, Prentice Hall.
- Huebner, K.H., Dewhirst, D.L., Smith, D.H. and Byrom T.G. (2001), *The Finite Element Method for Engineers*, Wiley.
- Simulia\_1 (2013), *ABAQUS Analysis User's Manual 6.13*.
- Chen, Z., Shin, M. and Adrawes, B. (2012), *Numerical Simulation of Prestressed Concrete Crosstie and Fastening System*, PCI Convention.
- Sun J.S., Lee, K.H. and Lee, P.H. (2000), *Comparison of Implicit and Explicit Finite Element Methods for Dynamic Problems*, Journal of Materials Processing Technology, 105(1-2), 110-118.

Noels, L., Stainier, L. and Ponthot, J.P. (2004), *Combined Implicit/Explicit Time-Integration Algorithms for the Numerical Simulation of Sheet Metal Forming*, Journal of Computational and Applied Mathematics, 168(1-2), 331–339.

Dhanasekar, M. and Haider, W. (2008), *Explicit Finite Element Analysis of Lightly Reinforced Masonry Shear Walls*, Computers and Structures, 86(1-2), 15–26.

Siad, L., Ouali, M.O. and Benabbes, A. (2008), *Comparison of Explicit and Implicit Finite Element Simulations of Void Growth and Coalescence in Porous Ductile Materials*, Materials and Design, 29(2), 319–329.

Farooq, U. and Gregory, K. (2010), *Explicit Dynamic Simulation of Drop-Weight Low Velocity Impact on Carbon Fibrous Composite Panels*, ARPN Journal of Engineering and Applied Sciences, 5(3), 50-61.

Huang, C.C. and Wu, T.Y. (2009), *A Study on Dynamic Impact of Vertical Concrete Cask Tip-over Using Explicit Finite Element Analysis Procedures*, Annals of Nuclear Energy 36(2), , 213–221.

Elmer, W. VII, Taciroglu, E. and McMichael, L. (2012), *Dynamic Strength Increase of Plain Concrete From High Strain Rate Plasticity with Shear Dilation*, International Journal of Impact Engineering, 45, 1–15.

Rehder, B., Banh, K. and Neithalath, N. (2014), *Fracture Behavior of Pervious Concretes: The Effects of Pore Structure and Fibers*, Engineering Fracture Mechanics, 118, 1–16.

Timoshenko, S and Goodier, J.N. (2001), *Theory of Elasticity*, Prentice-Hall.

Green, D.J. (1998), *An Introduction to the Mechanical Properties of Ceramics*, Cambridge University Press.

Sammis, C.G. and Ashby, M.F. (1986), *The Failure of Brittle Porous Solids under Compressive Stress States*, Acta Metall, 34(3), 511-526.

Leguillon, D. and Piat, R. (2006), *Fracture of Porous Materials – Influence of the Pore Size*, Engineering Fracture Mechanics, 75(7), 1840-1853.

Wong, R.H.C., Lin, P. and Tang, C.A. (2006), *Experimental and Numerical Study on Splitting Failure of Brittle Solids Containing Single Pore under Uniaxial Compression*, Mechanics of Materials, 38, 142-159.

Tang, C.A., Wong, R.H.C., Chau, K.T. and Lin, P. (2005), *Modeling of Compression-Induced Splitting Failure in Heterogeneous Brittle Porous Solids*, Engineering Fracture Mechanics, 72, 597-615.

Zhao, C., Matsuda, H., Morita, C. and Shen, M.R. (2011), *Study on Failure Characteristic of Rock-Like Materials with an Open-Hole under Uniaxial Compression*, Strain: An international Journal for Experimental Mechanics, 47(5), 405-413.

Ashby, M.F. and Sammis C.G. (1990), *The Damage Mechanics of Brittle Solids in Compression*, Pure and Applied Geophysics, 133(3), 489-521.

Liu, D.M. (1997), *Influence of Porosity and Pore Size on the Compressive Strength of Porous Hydroxyapatite Ceramic*, Ceramics International, 23, 135-139.

Zhao, X, Zhang, H. and Zhu, W (2004), *Fracture evolution around pre-existing cylindrical cavities in brittle rocks under uniaxial compression*, Transactions of Nonferrous Metals Society of China, 24(3), 806-815.

Tasdemir, M.A., Tasdemir, C., Akyuz, S., Jefferson, A.D., Lydon, F.D and Barr, B.I.G. (1998), *Evaluation of Strains at Peak Stresses in Concrete: A Three-Phase Composite Model Approach*, Cement and Concrete Composites, 20, 301-318.

Simulia\_2 (2013), *Obtaining a Converged Solution with ABAQUS*.

Susila, E. and Hryciw, R.D. (2003), *Large Displacement FEM Modelling of the Cone Penetration Test (CPT) in Normally Consolidated Sand*, International Journal for Numerical and Analytical Methods in Geomechanics, 27(7), 585–602.

Lubliner, J., Oliver, J., Oller, S. and Oñate, E. (1989), *A Plastic-Damage Model for Concrete*, International Journal of Solids and Structures, 25(3), pp. 229-326.

Lee, J. and Fenves G.L. (1998), *A Plastic Damage Model for Cyclic Loading of Concrete Structures*, ASCE Journal of Engineering Mechanics, 124, 892–900.

Chaudhari, S.V. and Chakrabarti, M.A. (2012), *Modeling of Concrete for Nonlinear Analysis Using Finite Element Code ABAQUS*, International Journal of Computer Applications, 44(7),14-18.

Jankowiak, T. and Lodygowski T. (2005), *Identification of Parameters of Concrete Damage Plasticity Constitutive Model*, Foundations of Civil and Environmental Engineering, 6, 53-69.

Kmiecik, P. and Kaminski, M. (2011), *Modelling of Reinforced Concrete Structures and Composite Structures with Concrete Strength Degradation Taken into Consideration*, Archives of Civil & Mechanical Engineering, 11(3), 623-636.

Martin, O. (2010), *Comparison of different constitutive models for concrete in ABAQUS/Explicit for missile impact analyses*, JRC European Commission.

Hillerborg, A., Modeer M. and Petersson P. E. (1976), *Analysis of crack formation and crack growth in concrete by means of fracture mechanics and finite elements*, Cement and Concrete Research, 6, 773–782,

Grondzik, W.T, Kwok, A.G., Stein, B. and Reynolds, J.S. (2010), *Mechanical and Electrical Equipment for Buildings*, Wiley.

Dann, J.H. and Dann J.J. (2012), *CK-12 Basic Physics*, CK-12 Foundation.

Mier van, J.G.M. (2013), *Concrete Fracture: A Multiscale Approach*, CRC Press

Schulson, M., Iliescu D. and Renshaw C.E. (1999), *On the initiation of shear faults during brittle compressive failure: A new mechanism*, Journal of Geophysical Research, 104, 695-705.

Wolinski, S., Hordijk, D.A., Reinhardt, H.W. and Cornelissen, H.A.W. (1987), *Influence of aggregate size on fracture mechanics parameters of concrete*, International Journal of Cement Composites and Lightweight Concrete 9(2) 95-103.

Meddah, M.S., Zitouni, S. and Belaabes, S. (2010), *Effect of content and particle size distribution of coarse aggregate on the compressive strength of concrete*, Construction and Building Materials, 24(4), 505-512.

Chindaprasirt, P., Hatanaka, S., Mishima, N., Yuasa, Y. and Chareerat, T. (2009), *Effects of binder strength and aggregate size on the compressive strength and void ratio of porous concrete*, International Journal of Minerals, Metallurgy and Materials, 16(6), 714-719.

Deo, O. and Neithalath, N. (2010), *Compressive behavior of pervious concretes and a quantification of the influence of random pore structure features*, Materials Science and Engineering: A, 528(1), 402-412.

Stroeven, P. (1973), *Some aspects of the micromechanics of concrete*, PhD Thesis, Delft University of Technology, the Netherlands.

Gorst, N.J.S., Williamson, S.J., Pallett, P.F. and Clark, L.A (2003), *Friction in temporary works*, Research Report, University of Birmingham, U.K.

Deutsches Institut für Normung (1982), *Falsework calculation, design and construction* DIN 4421:1982, Beuth Veriag GmbH, Berlin, Germany.

British Standards Institution (1997), *Falsework performance requirements and general design*, Draft prEN 12812, London, U.K.

## CHAPTER 6

### HIGHLIGHTS AND GENERAL CONCLUSIONS

#### 6.1 Highlights of the Thesis

With the aim to obtain a cementitious material with sufficient static strength, but fracturing into small size fragments when subjected to an explosion load, different types of porous concretes were designed and investigated. Production of the porous concretes was accomplished by modifying the mixture design and the compaction technique.

- Experiments at different scales (macro and meso-scale tests supported by microscopical observations) were performed to determine the effect of the type of aggregate, cement paste and pore structure properties on the performance of porous concretes, while the outcome of the tests also guided the design process of the material.
- Computed tomography observations of partly fractured samples provided very important information in view of understanding the fracturing behavior of porous concretes
- Meso-scale ITZ testing provided specific information on the effects of cement paste composition and aggregate type on the mechanical properties of the ITZ.
- In order to quantify the impact stress in drop weight experiments conducted on porous concretes, two experimental measurement techniques, using LDV and high speed photography as the monitoring methods, were developed. The techniques were applied on porous concretes with different dynamic strengths.
- The instrumented test set-ups can be used to test a large number of samples in a short time. The test set-ups provide noncontact measurement methods that do not require any sensors to be installed on the target samples.
- The velocity measurements were analyzed with a special reverberation application of the impedance mismatch method.
- The goal of the numerical part of this research project was simulating and assessing the dynamic behavior of different porous concretes under impact loading in order to understand the effect of various control parameters related to aggregate and pore structure properties. To reach this goal, analyses were also conducted on fictitious (model) porous materials that better demonstrate the individual effects of the control parameters involved.
- For a realistic representation the real porous concretes, the aggregates that were present in the mixtures were directly determined through 3D computed tomography. The porous concrete was considered as a four-phase material. A mesh generation program was developed for generating finite element meshes that also include arbitrary shaped air pores in the porous concrete.
- Explicit time integration calculations were efficient in analyzing the highly nonlinear behavior of porous concretes under drop weight impact.

- Pore size and fragment size distributions were also estimated using the output of numerical analyses.

## 6.2. General Conclusions

The following general conclusions can be drawn from this thesis:

- By modifying the mixture composition as well as the method of compaction, porous concretes with substantial static strengths (at the range of 30–50 MPa) were obtained.
- Among all the parameters that have been investigated, aggregate properties have a dominant effect on the static properties of porous concrete since the coarse aggregate particles are very effective in the formation of the skeleton structure of the material. The cement paste bridges in between the aggregates appear not that effective in this type of concrete.
- Intense compaction in thin (2.5 cm) layers, which directly affects the orientation and the packing of the particles and the porosity, is very important for producing porous concretes with substantial strength. It turned out that controlling the setting time of cement paste with a set retarder is also critical for ensuring that the compaction process is not jeopardized.
- The computed tomography (CT) scans of fractured samples revealed that in porous concretes, crack patterns are very much influenced by the distinct porous structure. The cracks are forced to propagate into locations guided by the geometry of the skeleton structure determined by the aggregate grading.
- Mesoscale test results clearly showed that silica fume had an effect of enhancing the ITZ strength. This effect is less pronounced in porous concretes, where the amount of ITZ phase present in the material is much smaller compared to normal concrete.
- The meso-scale testing of composite samples containing gravel aggregates showed that a batch of river gravel contained various types of aggregates, forming bonds of very different strengths with the cement paste.
- From particle velocity measurements and subsequent analyses of these velocities, the dynamic strengths of different porous concretes and a moderate strength normal concrete could be obtained with high precision.
- The velocity measurement technique was proved to be valid by testing the same type of porous concrete specimens using both steel and aluminum impactors. The results showed that although the dynamic impedance of the impactor was varied, the same stress results were obtained.
- Among the two monitoring and measuring techniques (LDV and high speed photography), LDV proved to be more accurate due to its higher sampling rate (400000 Hz) compared to high speed photography (10000 Hz). It also has the advantage of being independent of factors such as the right light source that is needed in photography measurements. High speed photography, however, has its own advantage of facilitating the visualization of the fracture process. This provides important qualitative information, such as characterization of the propagation and coalescence of cracks and shapes of fracture patterns.



- The impact test results showed that the aggregate properties and the compaction effort are the main factors that affect the dynamic performance of porous concrete. The results are in line with the static results.
- The results of numerical analyses of porous concretes were in good agreement with the experimental results provided that real aggregate distributions were used. Both the impact strength and the crack pattern formation for the types of porous concretes could be simulated reliably.
- As the impact responses of model porous concretes with different pore sizes (and constant total porosity) were compared, it was concluded that for the three porosities analyzed, the impact strength of the concretes was higher for mixtures with smaller pores while the total porosity was kept constant.
- Numerical analysis of concretes with randomly distributed pores showed that in mixtures with larger pore size, the variance of the impact strength also became higher.
- In general, a comparison of the results of analyses of the impact test with and without end friction of the test specimen showed that structural effects such as restrained deformations due to boundary conditions have a significant effect on the fragmentation behavior.

### **6.3. Further Research**

This thesis presents promising results for designing porous concretes with substantial strength (30-50 MPa) as a multiple fragmenting building material, to be used in safety structures. Further research is recommended on the following subjects:

- Intensive compaction is an essential feature of moderate strength porous concrete. However, due to the compaction of the concrete in one direction, anisotropy in the material was inevitable. Designing a multi-axial compaction method can be an important contribution in mitigating the anisotropy of the material.
- Porous concretes with aggregates such as basalt may suffer from durability threats such as ASR. While the superior mechanical properties of basalt are important for both the static and the dynamic properties of the material, different alternatives that comply with both the mechanical requirements, but are also less vulnerable to durability threats can be investigated.
- While in porous concretes pores are intentionally incorporated in the material as weak phases, because their properties are affected by several parameters at the same time (such as aggregate grading, cement paste layer thickness, compaction etc.), they cannot be completely controlled. Research options of adding other weak phases (instead of pores), such as polymers that can be well controlled and engineered, in a more homogeneous matrix such as cement paste or mortar instead of concrete can also be investigated.
- Numerical techniques, which facilitate the removal of highly distorted elements from the analysis, may be used to overcome the convergence problems that are faced when analyzing porous concretes using implicit finite element methods.

## ACKNOWLEDGEMENTS

I would like to express my sincere gratitude to my promotor Prof. Klaas van Breugel for providing me with the opportunity to conduct my PhD at TU Delft and for guiding the research with his deep knowledge and experience. Working in his group, I have also had the chance to admirably observe how he can always see the big picture in every research and make key suggestions that shape the research projects. Owing to Klaas and Jaap, I also finally learned to make sentences shorter than four lines. I gratefully acknowledge my copromotor Dr. Jaap Weerheijm, who has contributed to every step of this research with his valuable perspective. I feel very lucky that I could ask for his opinion, whenever I needed a suggestion about my research, and he always guided me to the right track. I am also thankful to Prof. Erik Schlangen, who together with Jaap supported me to be admitted to TU Delft as a PhD student, also always kindly offered his valuable suggestions and time whenever I needed help concerning my research. Special thanks to Prof. van Breugel and Dr. Weerheijm also for the Dutch translations of the propositions and the summary.

I would like to thank the members of the Doctoral Committee, Prof. Viktor Mechtcherine, Prof. Bert Sluys, Prof. Andrei Metrikine, Prof. Mehmet Ali Taşdemir and Prof. J.A. Mulder, for their time, interest and valuable comments. I would like to express my special thanks to Prof. Mehmet Ali Taşdemir and Prof. Canan Taşdemir also for encouraging me to conduct a PhD, to choose an academic life and to go to the Netherlands. Their advices on both research as well as on my career have been priceless.

I would like to acknowledge the Nederlandse Defensie Academie and TNO for supporting this research and Prof. Edwin Dado for his contributions. I would also like to thank the Engineering Dynamics Section of the Faculty of 3ME for providing the LDV and high speed photography equipment.

I am thankful to Ger Nagtegaal and Gerard Timmers for always kindly giving a hand, regardless of what the experiment is, and for solving the problems with their great experimental experiences. Without their help, none of the experiments would be realized. I would like to thank Ronnie Pedersen for his great support in modeling and for the collaboration. I would like to thank Arjan Thijssen for his contributions to the ESEM analyses as well as for conducting the CT scans. The technical colleagues in the Stevin Laboratory are acknowledged for always being willing to kindly help and for their hospitality. Special thanks to Kees van Beek and Paul Vermeulen for their contributions to the meso-scale and dynamic test setups. I would also like to thank Zheng Tian and his friends who have greatly helped the casting and compaction of the porous concrete samples until late hours in the lab. I am grateful to Iris Batterham, Nynke Verhulst and Claudia Baltussen for their kind help in all administrative matters.

My special thanks go to Lupita Sierra Beltran (also my paranymph) for being a very valuable friend along with being a supportive colleague. Together with Dennis, I hope you always stay as our good friends no matter how far we live now. I would like to thank Emine and Oğuzhan Çopuroğlu for their sincere friendship and for teaching me a lot about living in the Netherlands. I am thankful to Sonja Scher for sharing good memories also outside the university and for being very friendly and helpful since my very first day at TU Delft. Thanks to Sonja and Pascal also for our nice trips and their hospitality. I would like to thank all my colleagues and friends from TU Delft (especially Jie Zhao, Virginie Wiktor, Henk Jonkers, Alvaro Garcia Hernandez, Daijiro Tsutji, Maria Luisa Ripoll, Tuan Rang and Ying Wang) for the enjoyable lunch and coffee breaks and dinners which have left very nice memories from my life in the Netherlands.

I would like to thank all the good friends in Delft (Begüm, Şenol, Hilal, Emrah, Aylin, Anıl B., Tolga, Pervin, Anıl S., Çağrı, Gülay, Atilla and Nejla), who have made our life in the Netherlands very colorful and enjoyable. A special word for Elif-Senlav and dear Nihal Teyze who were our family in the Netherlands. Thank you for the uncountable good memories and for always being our great friends both in the Netherlands and luckily also in Turkey.

I would like to thank all my colleagues at Istanbul Technical University for their kind support. Special thanks to Müge Balkaya and Burcu Akçay Aldanmaz for being much more than colleagues, but real friends. I would like to thank all my friends in Istanbul, who have encouraged me to finish this thesis.

Lastly, I would like to thank my dear family... I am grateful to Beril, Handan and my late uncle İlhan Özcanlı for always wishing the best for me. I am thankful to my parents-in-law, my brothers-in-law and my sister-in-law for really making me feel like their daughters and their sisters. A special thanks to my sister, my best friend, for always supporting me and even spoiling me as her “little” sister. Words cannot express how grateful I am to my dear mother and father, for their endless care and understanding. I am very lucky to be your daughter. I am thankful to my husband Muammer for always being there for me in both good and bad days. Without you, none of it would be possible. I am grateful to my beloved little daughter Selen for bringing much more meaning to my life. You are such a precious gift...

## **CURRICULUM VITAE**

Name: Ayda Şafak Ağar Özbek  
Date of Birth: 14 November 1976  
Place of Birth: Istanbul, Turkey  
Email: [sagar@itu.edu.tr](mailto:sagar@itu.edu.tr)

### *Work Experience*

2012-current Teaching and research assistant, Faculty of Civil Engineering, Istanbul Technical University, Istanbul, Turkey  
2006 – 2010 Ph.D. researcher, Delft University of Technology, Faculty of CiTG, Microlab, Delft, The Netherlands.  
2003-2006 Ph.D. researcher and teaching and research assistant, Faculty of Civil Engineering, Istanbul Technical University, Istanbul, Turkey

### *Education*

2003 M.Sc. in Civil Engineering, Boğaziçi University, Istanbul, Turkey  
2003 Executive MBA., Istanbul Technical University, Istanbul, Turkey  
1999 B.Sc. in Civil Engineering, Boğaziçi University, Istanbul, Turkey